Towards an Integrated Foreign Body Response: Multi-Modal Investigation of Glial, Vascular, and Disease-associated Factors at the Electrode-Tissue Interface

by

Steven Michael Wellman

B.S., University of Florida, 2015

Submitted to the Graduate Faculty of the

Swanson School of Engineering in partial fulfillment

of the requirements for the degree of

Doctor of Philosophy

University of Pittsburgh

2022

UNIVERSITY OF PITTSBURGH

SWANSON SCHOOL OF ENGINEERING

This dissertation was presented

by

Steven Michael Wellman

It was defended on

November 8, 2022

and approved by

Franca Cambi, M.D., Ph.D., Professor
Department of Neurology, School of Medicine

Xinyan Tracy Cui, Ph.D., Professor
Department of Bioengineering, Swanson School of Engineering

Xiaoming Hu, M.D., Ph.D., Associate Professor
Department of Neurology, School of Medicine

Alberto L. Vazquez, Ph.D., Associate Professor
Department of Radiology, School of Medicine

Dissertation Director: Takashi D.Y. Kozai, Ph.D., Associate Professor
Department of Bioengineering, Swanson School of Engineering

Towards an Integrated Foreign Body Response: Multi-Modal Investigation of Glial, Vascular, and Disease-Associated Factors at the Electrode-Tissue Interface

Steven Michael Wellman, PhD

University of Pittsburgh, 2022

The success of neural electrode technology to understand brain function and restore lost motor or sensory control is dependent on a reliable and robust recording of neuronal signals. However, the ability to detect extracellular potentials within the brain over long periods of time using penetrating recording electrodes is impeded by a gradually progressive and insurmountable biological reaction to a foreign body. The brain's immune response to intracortical microelectrodes is traditionally characterized as an early onset of neuroinflammation due to activated microglia and astrocytes resulting in the formation of an encapsulating glial scar and neurotoxic microenvironment, ultimately leading to end-stage neuron loss. Attempts at correlating these biological events with electrode recording performance are complicated by a high variability in tissue response outcomes. This may be attributed to a currently incomplete representation of all the biological constituents that are impacted by electrode implantation within the brain, such as other essential glial and vascular cell populations also present near microelectrode implants.

In this dissertation, we apply a multi-modal approach involving two-photon microscopy, electrophysiology, and immunohistology to discern the fate and function of historically understudied cells at the electrode-tissue interface, such as oligodendrocytes, oligodendrocyte precursor cells, and perivascular pericytes. We demonstrate that oligodendrocyte precursor cells react spatiotemporally to penetrating microelectrodes in a manner which is distinct from activated microglia cells. We also reveal that myelinating oligodendrocytes, the differentiated target of

oligodendrocyte precursors, are critical for the robust detection and electrophysiological firing of neurons around chronically implanted recording electrodes. Furthermore, we reveal alterations in the structure and function of brain pericytes over the course of device implantation. Lastly, we offer new insights on the accumulation of pathological tissue factors related to aging and neurodegenerative disease around chronic brain implants. In sum, our findings provide multiple new perspectives towards a more accurate description of the integrated foreign body response at the electrode-tissue interface. A more holistic understanding of the potential adverse tissue reactions occurring within the microenvironment of chronic brain implants will better inform innovative electrode designs and give rise to more targeted clinical therapies for improving the bio-integration of neural interfacing technology in the future.

Table of Contents

List of Tables

List of Figures

Preface

Over the course of 6 years in graduate school, I had the honor and privilege of working with a group of remarkable individuals who have contributed significantly to my academic and professional success and so I would like to take the opportunity to acknowledge them here.

First, I would like to acknowledge my graduate advisor, Dr. Takashi Kozai, for realizing the potential within me which I could not yet see within myself and ensuring I develop into a fully independent, self-sustainable academic researcher. I would also like to acknowledge my co-mentor, Dr. Alberto Vazquez, for the abundance of technical expertise, professional wisdom, and sage advice which I will carry on with me throughout my academic career as well as the remainder of my life. I would like to acknowledge my co-worker, Dr. Franca Cambi, for helping me foster a collaborative spirit for research and taking the time to develop a genuine friendship outside of our professional working relationship. I would also like to acknowledge my mentor and grand-PI, Dr. Tracy Cui, for continuous support and guidance during my academic and professional development as I navigated through the different trials and tribulations of graduate school. Finally, I would like to acknowledge my dissertation committee member, Dr. Xiaoming Hu, for generously offering unique advisory insight during the final stages of my graduate research career.

Next, I would like to acknowledge my extraordinary BIONIC Lab lab mates, Kevin Stieger, Keying Chen, Fan Li, Jazlyn Gallego, Olivia Coyne, Nicholas Michelson, Dr. James Eles, Dr. Naofumi Suematsu, Camila Garcia, Adam Forrest, Lehong Li, Guangfeng Zhang, and Ingrid McNamara, for consistently bringing new life into the lab and being an endless source of support and camaraderie. I would also like to acknowledge the amazing cohort of BioE Ph.Ds whom I have had the pleasure of starting the program with, watching each other grow, and transition on to

bigger and better endeavors. Finally, I would like to acknowledge my small yet steadily growing D-SPAN family, who continually support, motivate, and inspire me daily to become an independent and successful researcher in STEM.

Next, I want to acknowledge my day-one, Dr. Sally Zheng, who I am proud to consider a dear friend-turned-family and who has taught me the value of living a life separate from my work which can be just as rich and full of wonderful opportunities. I also want to acknowledge my dear friend and former roommate, Dr. Chris Hughes, for being a constant source of merriment and companionship which helped keep me sane during my tenure throughout graduate school. Finally, I want to acknowledge my dear friend, Dr. Michelle Heusser, for ultimately convincing me to join the Bioengineering PhD program at Pitt and showing me that grad school can certainly be "all fun and games."

Next, I would like to acknowledge my wonderful parents, Marilyn and Scott Wellman, who have granted me the greatest gift a son could ask for: a life full of endless love, hope, and the opportunity to succeed. I would also like to acknowledge my beautiful siblings, Vanessa and Richard Anon, for being an infinite source of unconditional love, support, and encouragement. I would like to acknowledge my paternal grandparents, Drs. Keith and Nancy Wellman, for investing wholeheartedly into my childhood and education and helping me develop into the individual I am today. Lastly, I would like to acknowledge my maternal grandparents, Antonio and Carmela Rodriguez, for showing me that hard work, laughter, and humility are the greatest defenses in the face of adversity.

Lastly, I would like to acknowledge my dear and loving fiancé, Nathan, for whom none of this could have been accomplished without. Thank you for being my constant ray of sunshine.

1.0 Introduction

This chapter was adapted from a first authorship review published in Advanced Functional Materials titled, "A materials roadmap to functional neural interface design" (S. M. Wellman et al., 2018); *from a first authorship review published in ACS Chemical Neuroscience titled, "Understanding the inflammatory tissue reaction to brain implants to improve neurochemical sensing performance"* (S. M. Wellman & T. D. Kozai, 2017a); *from a first authorship manuscript published in the journal Frontiers in Neuroscience titled, "Revealing spatial and temporal patterns of cell death, glial proliferation, and blood-brain barrier dysfunction around implanted intracortical neural interfaces"* (S. M. Wellman, L. Li, Y. Yaxiaer, I. McNamara, & T. D. Kozai, 2019a); *and from a first authorship review published in Biomaterials, titled "The role of oligodendrocytes and their progenitors on neural interface technology: a novel perspective on tissue regeneration and repair"* (S. M. Wellman, F. Cambi, & T. D. Kozai, 2018).

1.1 Clinical Applications, Common Failure Modes, and Current Challenges of Neural Interfacing Technology

1.1.1 Clinical Application of Neural Interfaces for Brain-Computer Interfaces (BCIs)

Implantable neural interfaces are important tools for capturing and modulating the sophisticated computations of the nervous system. This technology has seen an explosion in research, innovation, and potential applications. In order to better understand plastic changes in

neural networks, these interface components must maintain stability over the long time periods associated with memory formation and learning (Huber et al., 2012). Clinical scientists have also applied knowledge gained from basic neuroscience studies to develop interfaces with the nervous system for therapeutic or assistive purposes in patients with injury and disease (Collinger et al., 2014; J. L. Collinger et al., 2013; L. R. Hochberg et al., 2006). For example, electrical stimulation using implantable neural interfaces –or neuromodulation devices– have received FDA market approval for the treatment of a diverse set of conditions including epilepsy, depression, Parkinson's Disease, sleep apnea, blindness, deafness, obesity, urinary and fecal incontinence, and hypertension. Patients have also used similar devices to detect and direct brain signals to control robotic limbs, bypassing their injured or degenerated spinal cord (J. L. Collinger et al., 2013; L. R. Hochberg et al., 2006). While these clinical successes highlight the potential of these technologies, concerns over large variability in therapeutic/assistive efficacy, long-term reliability, and health risks (J. C. Barrese et al., 2013; C. A. Chestek et al., 2011; Takashi D. Y. Kozai, Zhanhong Du, et al., 2015; T. D. Y. Kozai, A. Jaquins-Gerstl, A. L. Vazquez, A. C. Michael, & X. T. Cui, 2015) prevent these devices from reaching their full potential.

1.1.2 Common Failure Modes of Intracortical Microelectrode Arrays

The capabilities of neural interfaces as assistive devices for disabled or neurologically impaired individuals are limited by the gradual degradation in recording or stimulating performances over time (J. L. Collinger et al., 2013; Leigh R. Hochberg et al., 2012; Polikov, Tresco, & Reichert, 2005; Ward, Rajdev, Ellison, & Irazoqui, 2009). Failure modes of intracortical microelectrodes can be divided into three major categories: mechanical, material, and biological sources of device failure (J. C. Barrese et al., 2013; T.D.Y. Kozai et al., 2015). Mechanical failures

involve a perturbation in the external connectors of the device that are responsible for transmitting signal from the implanted electrode to an external computer. Examples include electrode displacement from the tissue or severing of connector cables. Material failures include the degradation of the conductive, insulating, or specially coated interface that impedes the exchange of information between the electrode and surrounding tissue. This type of failure manifests in the conductor and insulating material chosen, as well as the size, geometry, and mechanical characteristics of the device which have respective influences on the severity of tissue inflammation. Biological failures are the result of endogenous tissue reactions to the physical implantation or presence of the device. Failure in either of these categories is not exclusive; for example, while delamination of the insulation results in recording failures, subsequent exposure of the underlying electroactive material can also lead to electrode dissolution, which negatively impacts tissue viability. The persistence of a degenerative foreign body response afflicts both biological tissue as well as the material interface, reducing the long-term recording quality of chronically implanted devices.

1.1.3 Current Challenges in Implementation of Neural Interfacing Technology

Current challenges with chronically implantable neural interfaces can largely be categorized into performance *reliability* and *variability* issues. Invasive surgical procedures to implant chronic neural interfaces carry inherent risks, such as brain infection, surgery related hemorrhaging, blood clots, edema, etc. As such, these interfaces would ideally be designed to minimize tissue trauma, remain both functional and biocompatible for the lifetime of the patient to avoid corrective surgery or re-implantation, and be removable in the event of unforeseen complications. Across all neural implant classes, there is an average decline of the signal-to-noise

ratio (SNR) in the communication between the nervous system and neural interfaces over time. The resulting decline in neural interface *reliability* is believed to be, in part, due to the inflammatory tissue response triggered by the surgical implantation procedure. This initial reaction can progress into a chronic immune response, ultimately turning into a foreign body response and even leading to migration of the tissue or implant (Takashi D. Y. Kozai, Zhanhong Du, et al., 2015; P. J. Rousche & R. A. Normann, 1998). While the details of the biological challenges with chronic neural interfaces have been discussed elsewhere (Takashi Daniel Yoshida Kozai et al., 2015), this reactive tissue response degrades the electrical characteristics of the interface by forming a high impedance encapsulation sheath in conjunction with neural degeneration. This response decreases the amplitude of the detected neural signals by increasing the minimum distance from the electrode to the nearest neuron firing action potentials, thereby increasing the applied current necessary for exciting nearby neurons, and limiting the precision of activation via electrical stimulation (G. C. McConnell, H. D. Rees, et al., 2009; Roitbak & Sykova, 1999). A number of acute and delayed stab wound studies show that the tissue can recover to some extent when the device is removed (Biran, Martin, & Tresco, 2005; T. D. Kozai, Z. Gugel, et al., 2014; G. C. McConnell, H. D. Rees, et al., 2009; K. A. Potter, Buck, Self, & Capadona, 2012), suggesting that certain physical properties of chronically implanted neural interfaces are responsible for this tissue reaction (T. D. Kozai, Z. Gugel, et al., 2014).

The focus on minimizing the foreign body response has increased the emphasis on studying advanced materials to overcome specific design parameters hypothesized to attenuate the inflammatory tissue response (see reviews (Jeong et al.; Jorfi, Skousen, Weder, & Capadona, 2015; T. Kozai et al., 2014; Takashi Daniel Yoshida Kozai et al., 2015; Lacour, Courtine, & Guck, 2016; J. H. Lee, Kim, Kim, & Lee, 2016; Patil & Thakor, 2016; Thompson, Zoratti, Langhals, & Purcell,

2016)). However, large histology and recording performance *variability* (T. D. Kozai, A. S. Jaquins-Gerstl, A. L. Vazquez, A. C. Michael, & X. T. Cui, 2016; T. D. Kozai et al., 2010; Takashi Daniel Yoshida Kozai et al., 2015; T. D. Y. Kozai et al., 2014; Rousche et al., 2001; J. C. Williams, J. A. Hippensteel, J. Dilgen, W. Shain, & D. R. Kipke, 2007; J. C. Williams, R. L. Rennaker, & D. R. Kipke, 1999) have made it difficult to disentangle contributions from the many physical properties of these devices to the myriad of observed multi-modal failure modes (J. C. Barrese et al., 2013; Gilgunn, Xiao Chuan, Flesher, Schwartz, & Gaunt, 2013; T.D.Y. Kozai et al., 2015; Takashi Daniel Yoshida Kozai et al., 2015; D. McCreery, S. Cogan, S. Kane, & V. Pikov, 2016). These complex failure modes produce histological outcomes that, in isolation, are poor predictors of actual performance outcomes as measured by brain-machine neural communication with high degrees of freedom and SNR (T.D.Y. Kozai et al., 2015; T. D. Y. Kozai et al., 2014). Similarly, for stimulation electrode sites, small amounts of platinum particulates expelled over the course of stimulation, and the resulting foreign body response, have not been linked to any additional clinically adverse tissue reaction beyond those of a recording electrode (Clark et al., 2014; Clark, Clark, & Furness, 2013; Nadol, O'Malley, Burgess, & Galler, 2014; Spiers et al., 2016).

1.2 Current Understanding of Brain Tissue Response to Neural Interfacing Technology

Normal physiology in the brain involves a variety of active signaling between neurons, glia, and vascular cells in order to perform functional activity and maintain tissue homeostasis. These sensitive connections are altered or compromised during injury, influencing neuronal output and tissue health (Takashi Daniel Yoshida Kozai et al., 2015). The critical pathways that lead to the neurodegenerative insult induced by electrode implantation have been a subject of debate,

however, major influences such as glial cell activation and blood-brain barrier permeability are widely accepted contributors to declining neuronal health (T. D. Y. Kozai et al., 2010; B. D. Winslow, Christensen, Yang, Solzbacher, & Tresco, 2010b). A brief review of the major constituents that exist within the parenchyma (neurons, glia, and the cells that support the blood-brain barrier) and their currently known involvement in the foreign body response to inserted devices is required in order to contextualize the impact of implantation injury to other understudied cell types within the brain.

1.2.1 Blood-Brain Barrier Disruption on Activation of the Inflammatory Tissue Response

The blood-brain barrier (BBB) actively regulates influx of nutrients and oxygen and efflux of waste products between central nervous system (CNS) tissue and peripheral blood while providing protection to neuronal cells from toxins and pathogens that circulate throughout the body (Serlin, Shelef, Knyazer, & Friedman, 2015). The insulating nature of this vascular membrane is the result of endothelial cells forming continuous intracellular tight junctions with one another, supported by astrocytes and pericytes that provide additional mechanical and trophic support to the blood-brain interface (Muoio, Persson, & Sendeski, 2014). During brain injury, disrupting the endothelial cell-cell barrier can lead to vasogenic edema, loss of perfusion, activation of glia, and neurodegeneration (Venkat, Chopp, & Chen, 2017). Additionally, compromising the integrity of the BBB exposes the parenchyma to inflammatory plasma proteins and allows for the infiltration of inflammatory peripheral immune cells (Venkat et al., 2017). A review detailing the biochemical mechanisms behind the impacts of BBB disruption on degrading signal sensitivity of neural implants has been published previously (Takashi Daniel Yoshida Kozai et al., 2015). Considering that microelectrode arrays constantly shift due to breathing and pulsating micromotions within the

body, random tears to the BBB can occur at any time throughout the lifetime of the implant. As a result, maintaining BBB integrity is required to minimize the impact of glial cell activation and surrounding tissue inflammation during chronic implantation.

1.2.2 Glial Cells on Noise

Gliosis is commonly observed in the context of chronically implanted microelectrodes which hinders recording and stimulating performances over time (Marin & Fernandez, 2010; McConnell, Butera, & Bellamkonda, 2009; Szarowski et al., 2003; J. C. Williams et al., 2007). Glial scarring can interfere with the exchange of ions and charged solutes between neurons and the conductive surface of the electrode which increases the noise and impedes signal detection, ultimately leading to a decreased signal-to-noise ratio (SNR). *In vivo* imaging has been used to characterize the acute and immediate activation and encapsulation of microglia cells in response to microelectrode insertion (Kozai, Vazquez, & Weaver, 2012). The astrocytic scarring response is commonly characterized by an upregulation in glial fibrillary acidic protein (GFAP) around the device-tissue interface. As a result, the compacted glial scar creates a membrane-bound barrier that inhibits transmission of signal across the electrode-tissue interface. Gliosis can persist at chronic time points in part due to the continual secretion of pro-inflammatory factors and repeated disruption of the BBB whose ability to heal may be impaired by the implant, negatively impacting the viability of the surrounding neurons.

1.2.3 Neuronal Sources of Signal Loss

Blood-brain barrier disruption, glial cell activation, and inflammation influence neuronal physiology and, ultimately, neuronal function. Direct correlations between increased BBB leakage and decreased neuronal activity have been observed at chronic time points (Saxena et al., 2013). The presence of a glial scar prevents the transmission of electrical signals and displaces nearby neurons further from the electrode interface. This effectively increases the distance to the nearest neuron making it difficult for an electrode to record or discriminate between single units due to the voltage drop off from increasingly distant neurons (Mechler & Victor, 2012). Furthermore, neurons are particularly susceptible to oxidative stress events which may occur when the BBB is disrupted, creating an ischemic event, or production of reactive oxygen species (ROS) from activated glia. Finally, reactive oxygen species and pro-inflammatory cytokines secreted by activated immune cells are notably toxic to neurons and have been characterized in other neurodegenerative disorders (Lewis, Manning, Rossi, & Krieger, 2012; W. Y. Wang, Tan, Yu, & Tan, 2015). Therefore, implementation of successful therapeutic strategies or improved device design could mitigate the blood-brain barrier or glial-induced insult on neuronal loss, improving the performance of chronically implanted neural electrodes (T. D. Kozai, N. B. Langhals, et al., 2012).

1.2.4 Summary and Current Limitations on an Integrated Tissue Response

The influence of blood-brain barrier disruption and activated glia on neuronal health are not mutually exclusive; effects of one insult can trigger inflammatory events in the other. Potential strategies aimed at mitigating the currently known biological reactions to improve the

biocompatibility of neural interfaces have been suggested and published elsewhere (Takashi Daniel Yoshida Kozai et al., 2015; Mehdi, John, Christoph, & Jeffrey, 2015; Steven M. Wellman et al., 2017). However, recent studies have proven that increased neuronal viability, decreased glial cell activation, or reduced BBB leakage are not exclusively accurate predictors of functional electrode performance (T. D. Y. Kozai et al., 2014). A majority of investigations of the biological component of the electrode-tissue interface characterize the microglial and astrocyte reactivity around inserted devices and their impact on neural health (see review (J. W. Salatino, K. A. Ludwig, T. D. Y. Kozai, & E. K. Purcell, 2017)). However, these studies neglect a variety of other cellular factors in the brain such as oligodendrocyte precursor cells, mature oligodendrocytes and their myelin components, mural cells such as pericytes and endothelial cells, and other potential neurodegenerative tissue factors that can be expressed during injury or disease. Since each of these cellular populations have their respective roles in maintaining brain health and may potentially deviate from their responsibility in homeostasis during disease and injury, careful characterization of their distribution and behavior around inserted neural devices is required to work toward effective device design.

1.3 Alternative CNS Effectors of Tissue Health and Function during Device Implantation

The performance of biosensors in the brain depends primarily on the state of neuronal health in the tissue. The overall health and activity of neurons can be greatly influenced by non-neuronal cells including microglia, astrocytes, and the BBB. The pathology of microglia, astrocytes, and neurons are well characterized in the context of intracortical electrodes; however, other potential CNS contributors to the dynamic tissue response in the brain such as

oligodendrocyte lineage cells, myelinating oligodendrocytes, and pericytes are relatively understudied.

1.3.1 Oligodendrocyte Precursor Cells

Distributed ubiquitously throughout the central nervous system, oligodendrocyte precursor cells are essential in maintaining physiological support of neurons and act as a reservoir for myelinating oligodendrocytes in the event of oligodendrocyte loss or demyelinating injury (Joel M Levine, Reynolds, & Fawcett, 2001). In regards to glial inflammation, they are known to respond to injury in a similar vein as microglia and react similarly to astrocytes through secretion of axon growth-inhibiting chondroitin sulfate proteoglycans, such as neural/glia antigen 2 (NG2)—thus, they are commonly referred to as NG2 glia (Nishiyama, Yang, & Butt, 2005b; Tan, Zhang, & Levine, 2005). NG2 glia also possess the ability to differentiate into reactive astrocytes under specific conditions of injury (Figure 1-1) (Komitova, Serwanski, Richard Lu, & Nishiyama, 2011). Using two-photon microscopy, the acute *in vivo* dynamics of microglia (T. D. Y. Kozai, A. L. Vazquez, C. L. Weaver, S.-G. Kim, & X. T. Cui, 2012) and, more recently, NG2 glia (S. M. Wellman & T. D. Y. Kozai, 2018) have been observed following microelectrode implantation, revealing a sequence of process extension and cell body migration in a specific spatiotemporal pattern of reactivity. However, beyond acute implantation, the distribution and proliferating patterns of NG2 glia have yet to be characterized around intracortical microelectrode arrays.

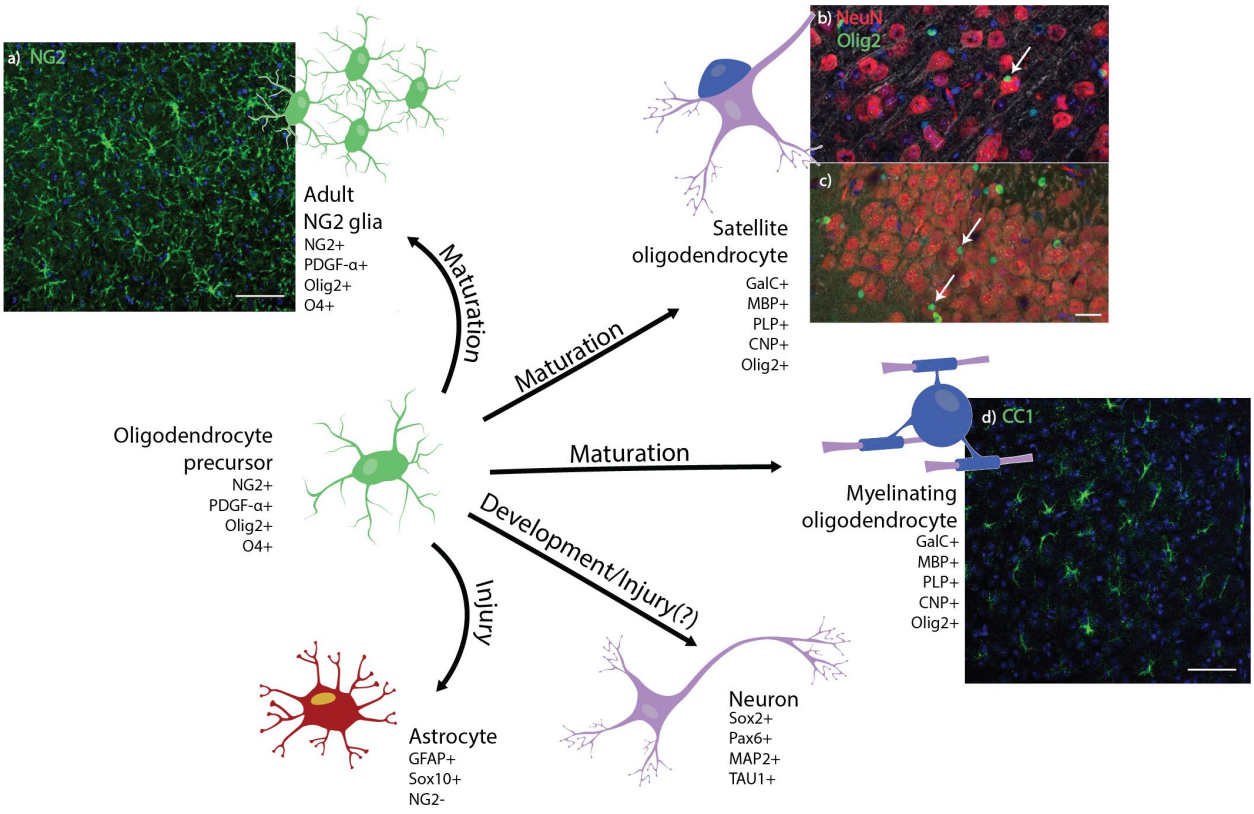

Figure 1-1 Development and cell fate of oligodendrocyte precursor cells. Oligodendrocyte precursor cells maintain various paths of cell fate depending on tissue conditions. (a) Histological stain of NG2+ glia (green) and cell nuclei (blue) in horizontal sections of the adult mouse cortex. Scale bar = 100 µm. Olig2+ oligodendrocytes (green) can be perineuronal (white arrow), residing in close proximity to NeuN+ neuron cell bodies (red) in both the (b) cortex and (c) dentate gyrus of coronal sections of the adult mouse brain. Scale bar = 25 µm. (d) Confocal image of cortical CC1+ myelinating oligodendrocytes (green) and cell nuclei (blue) in horizontal sections of the adult mouse. Scale bar = 100 µm. Oligodendrocyte precursors have been observed in certain regions of the brain to transdifferentiate into neurons and, under specific injury conditions, into reactive astrocytes.

NG2 glia have been implicated as participatory elements in the formation of the glial scar due to their intrinsic ability to migrate, proliferate, and differentiate into astrocytes and their characteristic release of axon-growth inhibitory molecules around an injury lesion. Indeed, NG2 glia react to inserted probes by extending processes and migrating towards the device, similar to microglia, however, on the scale of hours post-insertion as opposed to minutes. Unique to glia cells is the ability for NG2 glia to form synapses with neurons and receive synaptic input. NG2 glia express both GABAergic receptors and glutamatergic receptors, such as α-amino-3-hydroxy-5-methyl-4-isoxazolepropionic acid (AMPA) and *N*-methyl-D-aspartic acid (NMDA). Activation of AMPA receptors by glutamatergic signaling modulates the proliferation and differentiation of

NG2 glia (ANDREA, DE LA ROCHA, & REBEKAH, 2016). The presence of these channels allows NG2 glia to sense and modulate neuronal activity. The selective ablation of NG2 glia results in reduced glutamatergic transmission and decreased neuronal viability in pyramidal neurons (ANDREA et al., 2016). This perturbation in glutamatergic signaling due to a loss of NG2 glia can trigger depressive-like behavior. NG2 glia also express dopaminergic and serotonergic receptors but their functional significance is currently unknown. While altered glutamate signaling and NG2 glia abnormalities are observed in neurodegenerative diseases such as multiple sclerosis (MS) and Alzheimer's disease (AD), the functional state of myelin and oligodendrocytes most directly dictate neuronal viability (ANDREA et al., 2016).

1.3.2 Oligodendrocytes and Myelin

Oligodendrocytes, a third glial component of the central nervous system, exist predominantly in white matter tracks alongside their myelin fibers but are also present at lower densities within the gray matter cortex (Giulio Srubek Tomassy et al., 2014). They provide trophic and mechanical support to neurons and promote signal propagation between neural circuits via myelin ensheathment (see review (S. M. Wellman, F. Cambi, & T. D. Y. Kozai, 2018)). Secretion of neuronal growth factors requires oligodendrocytes and their precursors to maintain constant contact with neurons within the parenchyma (Y. Du & Dreyfus, 2002). However, as energy-demanding cells, oligodendrocytes require high metabolic needs in order to produce and maintain the amount of myelin needed to support the central nervous system (Bradl & Lassmann, 2010; McTigue & Tripathi, 2008; Snaidero & Simons, 2017). As a result, oligodendrocytes and their precursors are highly susceptible to ischemic and hypoxic stress events (Dewar, Underhill, & Goldberg, 2003; McTigue & Tripathi, 2008). Since electrode insertion can induce stroke-like

events such as BBB disruption and loss of perfusion as well as glial cell activation, mechanical strain, and edema, oligodendrocytes and their precursors are vulnerable to the inflammation sustained from chronic microelectrode implantation (Z. J. Du et al., 2017; Steven M. Wellman et al., 2018; S. M. Wellman & T. D. Y. Kozai, 2017). The only characterization of oligodendrocytes or myelin during electrode-induced inflammation was conducted by Winslow et. al. where they presented evidence of chronic demyelination around an electrode array following 12 weeks of implantation (B. D. Winslow, Christensen, Yang, Solzbacher, & Tresco, 2010a; Brent D Winslow & Tresco, 2010). As of yet, oligodendrocyte and myelin pathology have not been thoroughly characterized around acute or chronically implanted devices.

Oligodendrocytes are critical for neuronal survival through the secretion of essential neurotrophic factors including brain-derived neurotrophic factor (BDNF), glial-derived neurotrophic factor (GDNF), and insulin-like growth factor 1 (IGF-1) as well as the supply of glucose from the extracellular space for ATP production (Alizadeh, Dyck, & Karimi-Abdolrezaee, 2015a). Likewise, the expression of glutamate transporters (GLUT1 and GLAST) in myelin are important in maintaining glutamate homeostasis (Alba, Du, Catt, Kozai, & Cui, 2015). However, the constant production and maintenance of myelin around axons exerts a strong metabolic dependence on oligodendrocytes, making them particularly vulnerable to incidences of ischemia and hypoxia which are defining features of stroke. Oligodendrocytes, as well as their precursors, store limited amounts of the antioxidant glutathione making them susceptible to oxidative stresses involving increased ROS production. Oligodendrocyte damage is also mediated by glutamate over-signaling via NMDA receptors in myelin, resulting in excitotoxicity via the accumulation of calcium and consequently the over-secretion of glutamate by neurons due to lack of metabolic clearance (ANDREA et al., 2016). Compromising oligodendrocyte viability during device

insertion could leave neurons demyelinated and without trophic support (Figure 1-2). In incidences of demyelination, NG2 glia will differentiate into myelinating oligodendrocytes. However, if NG2 glia are preferentially differentiated into astrocytes after injury and are participating in the formation of a glia scar, then they will be unable to supplement the loss of oligodendrocyte cells and neurons will remain demyelinated until pro-inflammatory forces overwhelm the cell leading to apoptosis and a reduction in neurochemical signaling.

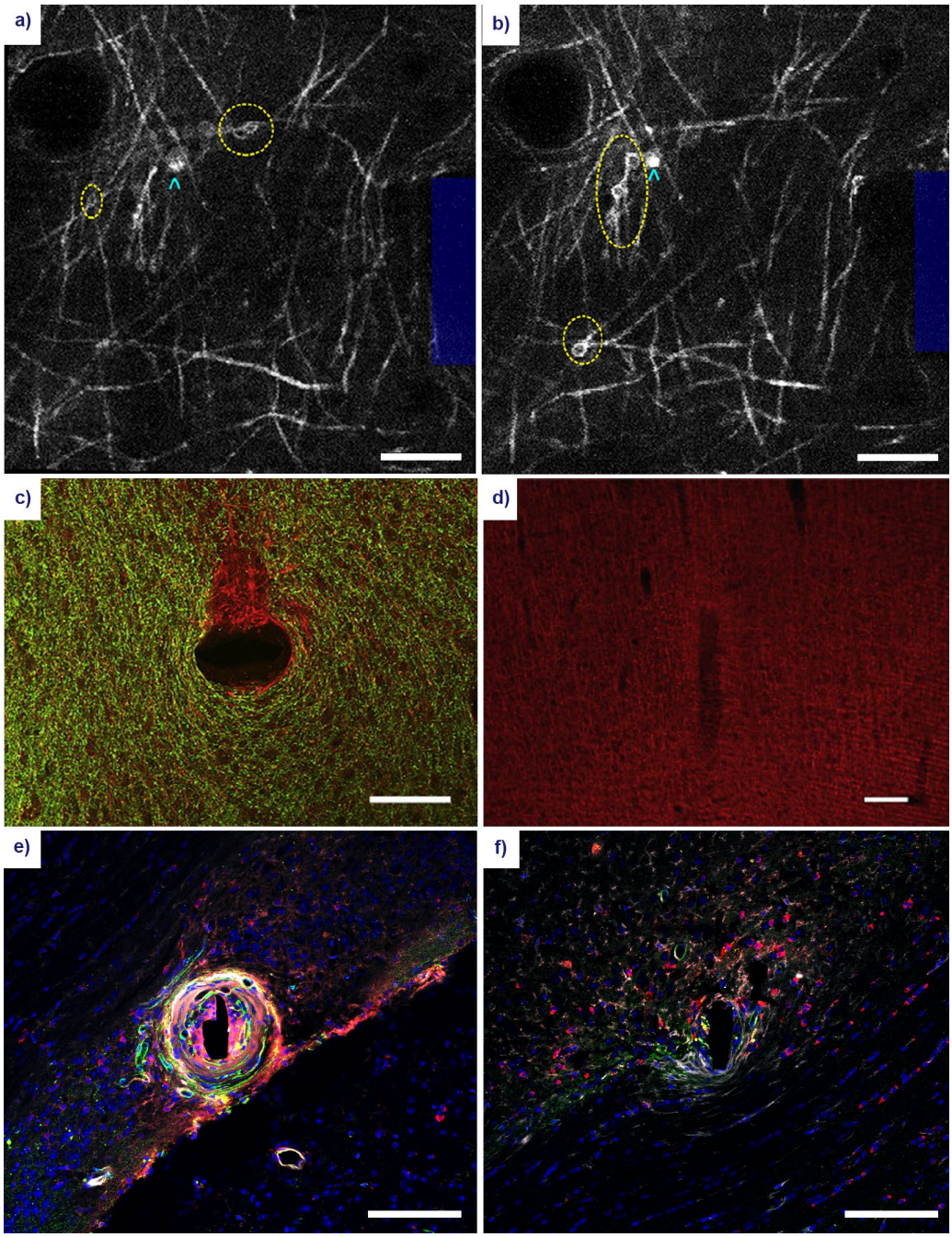

Figure 1-2 Gross morphological changes to oligodendrocyte and myelin structure following microelectrode implantation. Acute myelin damage in the form of myelinosomes (yellow ellipses) can be observed within the vicinity of the electrode (blue outline) at 1 hour (a) and 6 hours (b) post-insertion using in vivo two-photon microscopy of CNP-eGFP mice. Oligodendrocyte cell bodies can be identified as adjacent somas (cyan arrowheads). Reproduced with permission from IOP Publishing (N. J. Michelson et al., 2017). Scale bar = 100 µm. Large scale damage to the myelin architecture has been observed at 12 weeks post-insertion of an electrode in the rat cortex. (c) A stain for myelin basic protein (green) shows demyelination in a discrete area of unmyelinated axons (red) in a horizontal section. Reprinted from (B. D. Winslow et al., 2010b), with permission from Elsevier. Scale bar = 100 µm. (d) A coronal section of the implanted electrode shows a similar characteristic reduction in myelin around the insertion site. Reprinted from (Brent D Winslow & Tresco, 2010), with permission from Elsevier. Scale bar = 100 µm. (e) A stain for APC/CC1 oligodendrocytes (red), platelet-derived growth factor β pericytes (PDGFβ, green), immunoglobulin

IgG (white), and cell nuclei (blue) in white matter region CA1 of the adult mouse brain. Scale bar = 100 μm. (f) Similar stain, implant duration, and implant region as in (e) in an apoptosis-resistant Caspase-1 knockout mouse. Scale bar = 100 μm. Reprinted from (T. D. Y. Kozai et al., 2014), with permission from Elsevier.

1.3.3 Perivascular Pericytes

Pericytes are mural cells that interface directly between the blood-brain barrier and parenchyma, mediating cross-talk between the brain and the peripheral circulation (Armulik et al., 2010). Another NG2-expressing cell within the brain, pericytes possess a variety of vascular homeostatic functions such as BBB maintenance, BBB repair, blood flow regulation, angiogenesis, as well as mesenchymal stem cell properties (Melanie D Sweeney, Shiva Ayyadurai, & Berislav V Zlokovic, 2016). Pericytes also facilitate neuroinflammatory reactions following injury and have been implicated as targets of interest in a variety of neurodegenerative diseases such as stroke, Alzheimer's disease, multiple sclerosis, and more (Ethan A Winkler, Robert D Bell, & Berislav V Zlokovic, 2011). Many of these studies have correlated a reduction or loss in pericyte reactivity to occurrences of increased blood-brain barrier permeability (Lindahl, Johansson, Levéen, & Betsholtz, 1997). Blood-brain barrier disruption has recently been recognized as a significant factor of inflammation induced by intracortical electrodes and a potential perpetrator of reduced device performance (Figure 1-3) (T. Kozai et al., 2010; T. D. Y. Kozai, A. S. Jaquins-Gerstl, A. L. Vazquez, A. C. Michael, & X. T. Cui, 2015). Further investigation of pericyte behavior and reactivity to injury is required to understand how they fit into these sequences of inflammatory events.

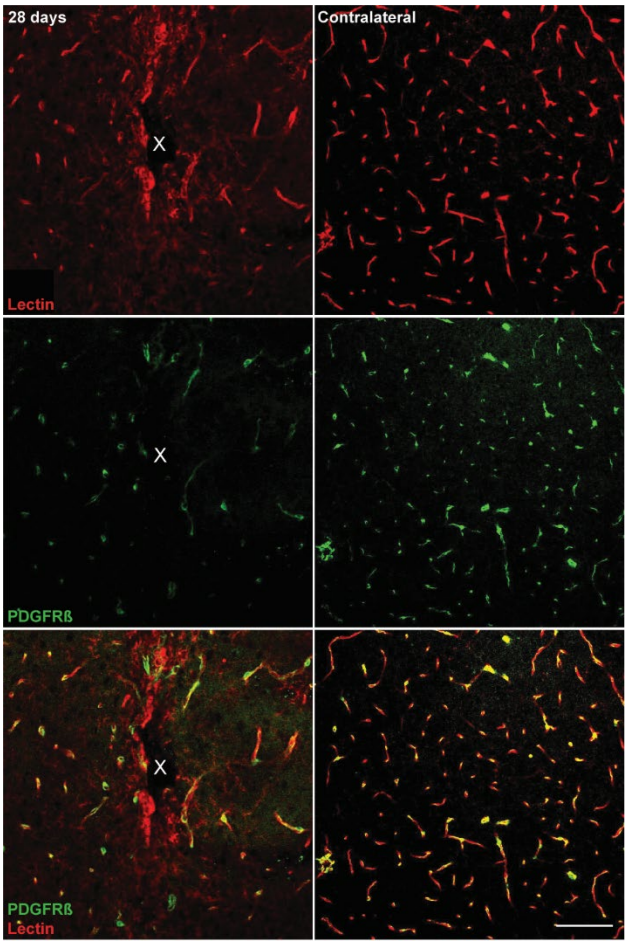

Figure 1-3 Reduced vascular structures around implanted microelectrode arrays at 28 days post-implantation. Chronic microelectrode implantation reveals specific insult to the endothelial component of the BBB, which may precede pericyte reactivity, vessel permeability, and leakage of plasma components. Blood vessels as well as vessel-bound pericytes are visualized by representative immunohistochemical stains for lectin (red) and PDGFR-β (green) at 28 days post-implantation compared to contralateral (non-implant) side. Center of the probe hole is denoted by a white 'x'. Scale bar = 100 μm.

Pericytes reside along the vascular membrane of the blood-brain barrier surrounding endothelial cells. Identified by their expression of PDGF-β receptors as well as the NG2 proteoglycan, pericytes are responsible for regulating blood flow, maintenance of the blood-brain barrier, as well as removal of toxic byproducts produced from cellular metabolism. Neurotransmitters dictate blood flow by altering the contractility and dilation of the vasculature through pericytes, activating downstream messengers. Glutamate, GABA, dopamine, and adenosine are vasodilatory while norepinephrine is vasoconstrictory (M. D. Sweeney, S. Ayyadurai, & B. V. Zlokovic, 2016). Pericytes help clear tissue debris, foreign pathogens, and

amyloid-β toxins present in AD (M. D. Sweeney et al., 2016). They are also involved in endothelial cell-mediated recruitment and adhesion of peripheral leukocytes, most common around areas lacking pericytes.(M. D. Sweeney et al., 2016) Their viability is dependent on PDGF-β secretion from endothelial cells and the inability for pericytes to perform normal physiological functions could compromise the integrity of the blood-brain barrier as well as clearance of toxic waste. In incidences of stroke or spinal cord injury, pericytes are known to detach from vascular membranes and migrate towards the site of injury where the BBB is compromised, possibly to initiate angiogenesis and neovascularization. Similar expression patterns have been observed around chronically implanted intracortical sensors (Alba et al., 2015). Pericyte morphology changes within 72 hours post-insertion with signs of angiogenesis occurring near the device shank. Also, pericytes are capable of phagocytosis owing to their ability to mediate waste clearance from the brain. Observed by the autofluorescence emitted from the oxidative breakdown of waste products, pericytes display phagocytotic behavior around inserted probes. Different from microglia and astrocytes, pericytes appear to be important for remodeling tissue after injury by re-establishing the BBB, the first step toward closing off the parenchyma from peripheral inflammatory cells and pathogens and returning to a normal neurochemical environment.

1.4 Dissertation Organization

In Chapters 2 and 3, we focus on the role of a 3rd and 4th group of glial cells, NG2 glia and oligodendrocytes, during the foreign body response of implanted microelectrodes within the brain. Chapter 2 explores the spatiotemporal reactivity of NG2 glia cells to neural probes via two-photon imaging. In this study, we characterize dynamic cellular responses of NG2 glia around inserted

microelectrodes over a 72-hour implantation period within the mouse cortex. We measure changes in process extension, soma migration, cellular morphology, and surface coverage of NG2 glia around chronically implanted microelectrodes in real time and compare our results to a previously characterized reactive microglia population. We reveal a time-dependent pattern of activation, polarization, and surface coverage of the NG2 glial population in response to implanted electrodes distinct from other activated glial populations. This is the first study of its kind to characterize the spatial and temporal behavior of NG2 glial cells around penetrating microelectrodes within the brain in real-time using intravital imaging, implicating a novel glial population in the brain tissue response to chronically implanted neural interfaces.

Chapter 3 explores how oligodendrocytes and myelin contribute to the recordability of neuronal signals from chronically implanted microelectrodes within the brain. A cuprizone mouse model of oligodendrocyte loss and demyelination is used to investigate neuronal circuit changes that occur following near-complete depletion of oligodendrocytes and myelin around recording microelectrodes over a 7-week implantation period. We use advanced electrophysiological analyses to assess changes in single- and multi-unit firing activity, stimulus-evoked latency, frequency-dependent neural oscillations, and laminar coherence between oligodendrocyte-depleted and demyelinated mice treated with cuprizone and a wild-type control group on a normal rodent diet. We determine that the presence of oligodendrocytes and myelin are essential for the detection of electrophysiological signals as well as maintaining neuronal firing rates, frequency-dependent cortical oscillations, and laminar communication within the brain. This study highlights a previously understudied glial population surrounding recording microelectrodes within the cortex as a potentially novel target for therapeutic intervention during the brain tissue response to chronically implanted neural interfaces.

Chapter 4 shifts gear and focuses on the biological response of brain mural cells to chronically implanted neural microelectrodes. This study utilizes a combination of two-photon imaging and post-mortem histology to characterize alterations in structure and function of pericytes around implanted microelectrodes up to a 28-day implantation period. We reveal here that pericyte calcium becomes activated immediately upon electrode insertion and that pericytes are the source of capillary deformations and stalled blood flow around implanted electrodes. Following the initial response to electrode insertion, pericytes demonstrate dynamic changes in angiogenic function and vascular coverage. The relationship between pericytes and microglia, both myeloid lineage cells, is also explored using a specialized dual-fluorescent mouse model where we reveal a distinct population of immune cells separate, from pericytes and microglia, that are actively involved in encapsulation of brain implants.

Chapter 5 takes a broader look at electrode implantation promotes different biomarkers of neurodegeneration within the brain by exploring the abnormal accumulation of age- and disease-related factors around chronically implanted microelectrodes within a rodent model of Alzheimer's disease. Similar to Chapter 4, this study uses a combination of intravital imaging and immunohistology to identify previously unknown tissue factors that are preferentially expressed at the electrode-tissue interface related to aging and disease, such as lipofuscin, amyloid, and tau, within a genetically susceptible Alzheimer's mouse model up to a 16-week electrode implantation period. We go on to reveal novel spatiotemporal relationships between these tissue markers with traditionally characterized neuronal, glial, and vascular cell populations around chronically implanted neural probes. Ultimately, this study provides new knowledge on potential neurodegenerative processes in action at the electrode-tissue interface and reveals novel therapeutic targets to combat the biological failure modes which degrade the longevity and fidelity

of chronically implanted neural interfaces.

2.0 In Vivo Spatiotemporal Dynamics of NG2 glia Activity Caused by Neural Electrode Implantation

This chapter is taken directly from a first authorship manuscript published in Biomaterials titled, "In vivo spatiotemporal dynamics of NG2 glia activity caused by neural electrode implantation" (S. M. Wellman & T. D. Kozai, 2018).

2.1 Overview

Neural interface technology provides direct sampling and analysis of electrical and chemical events in the brain in order to better understand neuronal function and treat neurodegenerative disease. However, intracortical electrodes experience inflammatory reactions that reduce long-term stability and functionality and are understood to be facilitated by activated microglia and astrocytes. Emerging studies have implicated another cell type in the formation of a high-impedance glial scar following brain injury; the oligodendrocyte precursor cell (OPC). These cells maintain functional synapses with neurons and are a crucial source of neurotrophic support. Following injury, OPCs migrate toward areas of tissue injury over the course of days, similar to activated microglia. The delayed time course implicates these OPCs as key components in the formation of the outer layers of the glial scar around the implant. *In vivo* two-photon laser scanning microscopy (TPLSM) was employed to observe fluorescently-labeled OPC and microglia reactivity up to 72 hours following probe insertion. OPCs initiated extension of cellular processes (2.5 ± 0.4 μm h^{-1}) and cell body migration (1.6 ± 0.3 μm $hour^{-1}$) toward the probe beginning 12

hours after insertion. By 72 hours, OPCs became activated at a radius of about 190.3 μm away from the probe surface. This study characterized the early spatiotemporal dynamics of OPCs involved in the inflammatory response induced by microelectrode insertion. OPCs are key mediators of tissue health and are understood to have multiple fate potentials. Detailed spatiotemporal characterization of glial behavior under pathological conditions may allow identification of alternative intervention targets for mitigating the formation of a glial scar and subsequent neurodegeneration that debilitates chronic neural interfaces.

2.2 Introduction

Communicating with the nervous system through bidirectional microelectrode arrays enhances our understanding of the brain and provides the possibility of improving the quality of life for patients who suffer from neurodegenerative disorders (Cogan, Ludwig, Welle, & Takmakov, 2016; Kipke et al., 2008; J. W. Salatino et al., 2017; Andrew B. Schwartz, X. Tracy Cui, Douglas J. Weber, & Daniel W. Moran, 2006). Arrays that record specific populations of neurons in the brain can provide information about neural coding that occurs during memory formation and learning in order to better understand the neural basis of cognition and physiological functions of the brain (Huber et al., 2012). Likewise, the high spatial resolution provided by these neural interfaces has the potential to enable tetraplegic patients to control functional neuroprosthetic limbs (J. L. Collinger et al., 2013; Andrew B. Schwartz et al., 2006). Applications involving microelectrode arrays are critically dependent on the device's ability to reliably deliver or record signals to and from electrically excitable cells over chronic periods of time. Ultimately,

the goal is to develop neural technology that seamlessly integrates with biological tissue and achieves high functionality as well as long-term stability.

Implantation of a microelectrode array triggers a series of events beginning with blood-brain barrier (BBB) disruption followed by an inflammatory tissue response that has been hypothesized to impair device performance over time (Goss-Varley et al., 2017; Saxena et al., 2013). Gliosis, described as the scar formed due to the activation of microglia and astrocytes, encapsulates the microelectrode surface and creates a mechanical and chemical barrier between the device interface and neural tissue. One role of microglia is to act as resident immune cells in response to brain injury, facilitating tissue breakdown and repair through the removal of debris and secretion of inflammatory factors. Normally, microglia maintain a ramified state through the extension and retraction of processes radially around their cell body constantly surveying their surroundings for disturbances in the extracellular environment. After probe insertion, microglia in the vicinity of the insertion site preferentially extend microglial processes in the direction of the implant within the first 45 minutes and maintain relatively little cell body movement within the first 6 hours (T. D. Kozai, A. L. Vazquez, C. L. Weaver, S. G. Kim, & X. T. Cui, 2012). At 6 hours post-insertion, microglia appear to be activated through the observation of distinct changes in cell morphology up to a radius of about 130 μm (T. D. Kozai, A. L. Vazquez, et al., 2012). When activated, microglia undergo an amoeboid morphology, becoming phagocytic and secreting various pro-inflammatory cytokines, chemokines, and reactive oxygen intermediates (T. D. Kozai, A. L. Vazquez, et al., 2012). Reactive astrocytes become hypertrophic in morphology, synthesizing cytoskeletal proteins to expand their plasma membrane and form a sheath of cells around the electrode (T. D. Kozai, Z. Gugel, et al., 2014; Szarowski et al., 2003). The development of a glial

scar progresses in the days and weeks following electrode insertion fostering a pro-inflammatory environment that contributes to neuronal loss, diminishing the quality of recordable activity.

NG2-expressing progenitor cells, also referred to as NG2 glia or oligodendrocyte precursor cells (OPCs), are glial cells that exist in both the developing and mature central nervous system (CNS) (Dawson, Polito, Levine, & Reynolds, 2003). They represent 5-8% of all cells in the adult CNS and are distributed in a grid-like orientation throughout gray and white matter with individual cells occupying non-overlapping regions of space (E. G. Hughes, S. H. Kang, M. Fukaya, & D. E. Bergles, 2013; Nishiyama, Komitova, Suzuki, & Zhu, 2009). They possess the unique glial ability to form functional synapses with neurons, allowing them to provide neurotrophic support and modulate neuronal activity (Sakry et al., 2014). These connections are bidirectional; neurons can influence NG2 glia by mediating their proliferation and differentiation via glutamatergic signaling of AMPA receptors (Gautier et al., 2015). It is hypothesized that neuronal health is dependent on the maintenance of these synaptic connections with NG2 glia. Previous studies have shown that induced ablation of NG2 glia compromises neuronal viability by inducing neuroinflammation and cell death (Birey et al., 2015; Nakano et al., 2017). Additionally, NG2 glia are an important reservoir of oligodendrocyte progenitors for oligodendrocyte repopulation after a demyelinating injury. Oligodendrocyte cell bodie and myelin are prevalent in the cortex, albeit at lower relative densities due to the presence of neuronal cell bodies (G. S. Tomassy et al., 2014). They are responsible for the mechanical and trophic support of neurons through myelin ensheathment, which is critical for the long-range propagation of action potentials (Fields, 2008). For example, in the demyelinating disease multiple sclerosis, a failure of remyelination in chronic lesions is hypothesized to be attributed to the insufficiency or depletion of oligodendrocyte precursors which would precede neurodegeneration (Xu, Zhao, & Li, 2011). While the scale of demyelination is

different, chronic implantation of intracortical microelectrodes have been shown to cause local demyelination around the implant, which could impact the local tissue microenvironment (B. D. Winslow et al., 2010b). Lastly, while NG2 glia are primarily known for their role in the oligodendrocyte lineage to differentiate into mature oligodendrocytes, they are also considered polydendrocytes due to their capacity for multipotent differentiation into neurons and astrocytes (Kondo & Raff, 2000; Nishiyama et al., 2009). As a result, their mutually dependent relationship with neurons coupled with their multi-differentiating potential prompts additional insight into NG2 glia behavior in both the healthy and diseased CNS.

Similar to microglia and astrocytes, NG2 glia display multi-processed, stellate shaped morphology. They are highly proliferative cells in the brain, maintaining cell density among neighboring cells by proliferating and migrating in the event of cell loss or differentiation (E. G. Hughes et al., 2013). During embryonic development, more then 1/3 of protoplasmic astrocytes from the ventral forebrain are derived from NG2 glia (Xiaoqin Zhu, Hill, & Nishiyama, 2008), whereas no astrocytes are derived from NG2 glia postnatally (Rivers et al., 2008). However, differentiation of NG2 glia into astrocytes have been shown during pathological conditions such as spinal cord injury and cortical stab wound injury (Amber R. Hackett et al., 2016; Komitova, Serwanski, Lu, & Nishiyama, 2011), implicating their participation in the immune response to CNS injury. NG2 glia share attributes with reactive glia in the brain that suggests a complementary role in the response to tissue injury. Like microglia, NG2 glia survey their local environment through the extension of processes in response to local changes in tissue homeostasis (Hill, Patel, Goncalves, Grutzendler, & Nishiyama, 2014; E. G. Hughes et al., 2013). Furthermore, NG2 glia alter their morphology towards a more hypertrophied state similar to astrocytes and secrete axon-growth inhibiting factors in cases of CNS injury, such as the chondroitin sulfate proteoglycan NG2

(neural-glia antigen 2) (J. M. Levine, 1994). Taken together, these recent findings have implicated NG2 glia in the formation of a glial scar and mediator of neuroinflammation following damage to the CNS. However, the dynamics of NG2 glia to intracortical microelectrode insertion has yet to be characterized.

The objective of the present study aims to uncover the spatiotemporal role of NG2 glia in the development of a barrier-forming scar, which impairs microelectrode performance by facilitating progressive neurodegeneration. Discovering biochemical pathways that trigger the activation of glia or loss of neurons have helped improve tissue health and recording capabilities of implanted neural devices in the past (T. D. Kozai, X. Li, et al., 2014; T. D. Y. Kozai, A. S. Jaquins-gerstl, A. L. Vazquez, A. C. Michael, & X. T. Cui, 2016). Traditional immunohistochemistry has been used previously to highlight patterns between different immune response biomarkers and chronically implanted electrodes. However, these methods limit the visualization of varying cellular dynamics that occur acutely during inflammation. Here, we account the use of two-photon microscopy to uncover the reactive dynamics of NG2 glia after electrode insertion *in vivo*. We observe microglia in parallel to determine temporal and spatial observations of the response between both cell types to inserted devices, possibly highlighting novel patterns in glial activity previously unknown. Identifying a temporal pattern of glial reactivity may allow targeted intervention at critical time points (Takashi D Y Kozai, Andrea S Jaquins-gerstl, et al., 2016). For example, mitigating this immune response induced by microelectrode insertion can help improve the stability and longevity of neural devices through enhanced integration with host tissue (T. D. Kozai, X. Li, et al., 2014).

2.3 Methods

2.3.1 Surgical Probe Implantation

Two-photon experiments were conducted using four-shank 16-channel Michigan style silicon probes (3 mm long, 15 μm thick, 55 μm wide, 125 μm center-to-center shank spacing) mounted on non-functional tabs (NeuroNexus Technologies, Ann Arbor, MI). Electrodes were implanted into the cerebral cortex of transgenic mice (male, 22-30g, Jackson Laboratories; Bar Harbor, ME) expressing either green fluorescent protein (GFP) in NG2-glia (*Cspg4-EGFP*, n=5) or GFP in microglia cells (*CX3cr1-EGFP*, n=5). Prior to surgery animals were administered an intraperitoneal (IP) injection of 75 mg/kg ketamine and 7 mg/kg xylazine and placed in a stereotaxic frame. After removing the skin and connective tissue from the skull, a thin layer of Vetbond (3M) was applied to dry the bone and improve adhesion between the bone and headcap. Two bone screws were inserted into bone screw holes made using a high-speed dental drill over both motor cortices and secured with dental cement. A 4 mm by 6 mm craniotomy was performed over the visual cortex centered at a point 1.5 mm rostral to lambda and 1 mm lateral from the midline. To prevent thermal damage from drilling, the skull was periodically bathed in saline. The dura and pia mater were kept intact prior to insertion. Probes were inserted in the rostral direction into the cortex at a 30º angle and parallel to the midline at 200 μm/s for a total distance of 600 μm (oil hydraulic Microdrive; MO-82, Narishige, Japan) and a final resting depth of 250-300 μm (layer II-III) beneath the surface of the brain. Effort was taken to avoid blood vessel penetration during insertion. To create a chronic imaging window, Kwik-Sil was used as a sealant inside the craniotomy before placing a glass coverslip and securing with dental cement(T. D. Y. Kozai, J. R. Eles, A. L. Vazquez, & X. T. Cui, 2016). A 2 mm tall well was formed around the imaging window

to hold the water for a water-immersive objective lens. Sulforhodamine 101 (SR101) was injected IP to visualize vascularization (red; 0.02-0.04 cc; 1 mg of drug per ml of sterile saline; taken from (James R Eles et al., 2017)). Updates of SR101 were administered approximately every hour to maintain vascular labeling. All procedures and experimental protocols were approved by the University of Pittsburgh, Division of Laboratory Animal Resources, and Institutional Animal Care and Use Committee in accordance with the standards for humane animal care as set by the Animal Welfare Act and the National Institutes of Health Guide for the Care and Use of Laboratory Animals.

2.3.2 Two-Photon Imaging

In vivo imaging was performed using a two-photon laser scanning microscope as previously published (James R Eles et al., 2017). The microscope consisted of a scan head (Bruker, Madison, WI), an OPO laser (Insight DS+; Spectra-Physics, Menlo Park, CA) tuned to a wavelength of 920 nm, non-descanned photomultiplier tubes (Hamamatsu Photonics KK, Hamamatsu, Shizuoka, Japan), and a 16X, 0.8 numerical aperture water immersion objective lens (Nikon Instruments, Melville, NY). During imaging, mice were anesthetized with isoflurane (1.0-1.5%, mixed with 0.9 L/min O_2) and, prior to every Z-stack, injected with sulforhodamine 101 for visualization of blood vessels. If animals experienced pial surface bleeding severe enough to impact imaging quality, the animal was removed from the study. An imaging window of 407.5 x 407.5 μm (1024 x 1024 pixels) was used to visualize electrode shanks and adjacent tissue for quantification. Regions of interest were chosen by judging either two of the outermost shanks for the least amount of vasculature within the adjacent tissue to maximize image clarity. Z-stack

images every 2 μm along the full depth of the implant were acquired at 2, 4, 6, 8, 10, 12, 24, 48 and 72 hours post-insertion with a scan rate of ~5 s/image.

2.3.3 Data Analysis

Image z-stacks were processed using ImageJ (National Institute of Health). In order to quantify differences in cell processes extension, soma migration, and morphology, z-stacks of consecutive time points were aligned with each other with respect to the probe. To do this, the offset position of one z-stack relative to another z-stack was determined using a "TurboReg" plugin for ImageJ. Next, the translate feature was used to align both z-stacks with each other. Cell processes and soma migration were quantified up until the point of destination at the surface of the implant. Both processes and cell body movements moving toward or away from the probe were tracked by determining XY coordinates and using the 'Measure' feature in ImageJ. Direction of cell processes extension and soma movement was noted by drawing a line through the center of the cell parallel to the surface of the probe. Processes extension was recorded as the distance between processes for consecutive time points while migration of cell bodies was recorded as the distance between soma for consecutive time points.

Surface coverage of NG2 glia and microglial processes along the face of the probe were measured as the percent of fluorescent signal measured over the total probe area. Each z-stack was rotated using ImageJ's built-in plugin "Interactive Stack Rotation" to reslice the total volume of tissue normal to the probe surface. A binary mask of the sum slice projection of a small volume of tissue directly above the probe surface was created by using a built-in ImageJ thresholding method utilizing an isodata algorithm ("Picture Thresholding Using an Iterative Selection Method," 1978). The outline of the probe was identified and the number of nonzero pixels were counted and taken

as a fraction of the total area measured. The outline defined around the probe was verified to ensure correct dimensions around the probe perimeter.

Since the NG2 protein is also expressed in pericytes and macrophages as well as NG2 glia (Jones, Yamaguchi, Stallcup, & Tuszynski, 2002), examination of each tracked cell for a multi-processed morphology, a characteristic unique to NG2+ oligodendrocyte precursor cells, were confirmed before analysis. Cell morphology was characterized using morphological metrics developed previously (James R Eles et al., 2017). Cells were classified as either ramified (1), with processes extending equally in every direction, or in a transitional (activated) stage (0), with processes orientated preferentially on one side of the soma. This morphological state was determined using the same hemispheric divide previously detailed for cell processes and soma velocity. Cells were binned based on the distance between the center of soma and the probe surface. A logistic regression was used to fit the data to show the Bernoulli Probability Distribution of cells in a ramified or transitional state (0 or 1) as a function of distance from the surface of the probe as previously published (James R Eles et al., 2017).

Two other metrics, the transitional index (T-index) and directionality index (D-index), were used to quantify and compare cell morphology. The T-index was calculated by measuring the length of the leading process (*n*), which is the longest process extending toward the probe, and the length of the longest lagging process (*f*), which is the process extended away from the probe at each time point. The D-index was calculated in a similar manner by counting the number of processes extending toward the probe (*n*) and the number of processes orientated away from the probe (*f*) using the hemispheric divide to distinguish between toward and away processes. The following formula was used to calculate index values for each time point:

$$\mathbf{Index} = \frac{(f-n)}{(f+n)} + \mathbf{1} \qquad (2\text{-}1)$$

For both T-index and D-index, a measured index of 1 indicates a ramified, or non-activated, morphology while an index of 0 indicates a fully transitional, or activated, morphology with processes extending toward the surface of the probe, similar to the ramification method detailed previously (James R Eles et al., 2017). After binning, cell morphology was reported as a distribution of index values as a function of distance from the probe surface. A dual sigmoidal function generated from a custom MATLAB script was used to fit this index distribution. The function required inputs of amplitude (a), shoulder location (d_1 and d_2 in μm), and shoulder width (w_1 and w_2 in μm), with the constraints maintained between 0 and 1:

$$\boldsymbol{y(d)} = \frac{\boldsymbol{a}}{\boldsymbol{1+e^{d-d_1/w_1}}} + \frac{\boldsymbol{1-a}}{\boldsymbol{1+e^{d-d_2/w_2}}} \quad (2\text{-}2)$$

Lastly, quantifiable changes in the vasculature over 72 hours were recorded by measuring blood vessel diameter. The percent change in blood vessel (b.v.) diameter was calculated as the difference between vessel diameter at the current time point and vessel diameter at 2 hours divided by the vessel diameter at 2 hours post-insertion.

2.3.4 Statistical Analysis

A Welch's *t*-test (unequal variance) was used to compare differences in processes extension, cell body migration, surface coverage, and morphological alterations between NG2 glia and microglia populations. To determine differences between time points within NG2 glia populations and blood vessel z-stacks, a repeated measures analysis of variance (ANOVA) was used. A $p < 0.05$ was chosen to demonstrate significant differences.

2.4 Results

Prior to insertion, the distribution of NG2 glia and microglia was uniform and no morphological changes were observed across the cortex due to the craniotomy. A probe was inserted at an angle into the cortex and sealed by a chronic imaging window that allows for two-photon visualization of fluorescently labeled glial cells (Figure 2-1a). Due to the physical constraints of two-photon microscopy, observations of the tissue response around electrodes traditionally inserted perpendicularly to the brain are difficult and the extent of these limitations have been addressed in a previous publication (T. D. Kozai, A. L. Vazquez, et al., 2012). Large surface vasculature was avoided during insertion to minimize bleeding and proper sealing methods were used to preserve the region of interest in the tissue during chronic imaging (Takashi D. Y. Kozai et al., 2016; Takashi D Y Kozai, Andrea S Jaquins-gerstl, et al., 2016; T. D. Y. Kozai et al., 2010). Laser and PMT settings were set to the lowest settings necessary to prevent thermal damage while imaging. A region of interest 300 μm adjacent to the probe shank was chosen for quantification (Figure 2-1b,c). Vascular bound pericytes also express the NG2 antigen and therefore were fluorescently labeled by the transgenic model. These pericytes maintain distinct morphological characteristics that are distinguishable from NG2+ oligodendrocyte progenitors and were not included in the analysis (Figure 2-1d). Additionally, the literature indicates that pericytes experience a rapid decrease in number following trauma to the brain, while pericyte migration or pericytosis around the lesion does not occur until 3-5 days post-injury (Francisco Fernández-Klett et al., 2013; Zehendner et al., 2015). Therefore, it is not expected to observe any migrating GFP-labeled pericytes given the timeframe of analysis. Furthermore, proliferating NG2 glia can be mistaken as activated cells that are morphologically distinct from the ramified state; however, they can be easily identified as a pair of two NG2 glia cells migrating in opposite directions and thus

were also excluded from quantification (Figure 2-1e). Fluorescently-labeled NG2 glia and microglia were observed every 2 hours for the first 12 hours and 24, 48, and 72 hours following electrode insertion. Sulforhodamine 101 was administered intraperitoneally to observe changes in the vasculature.

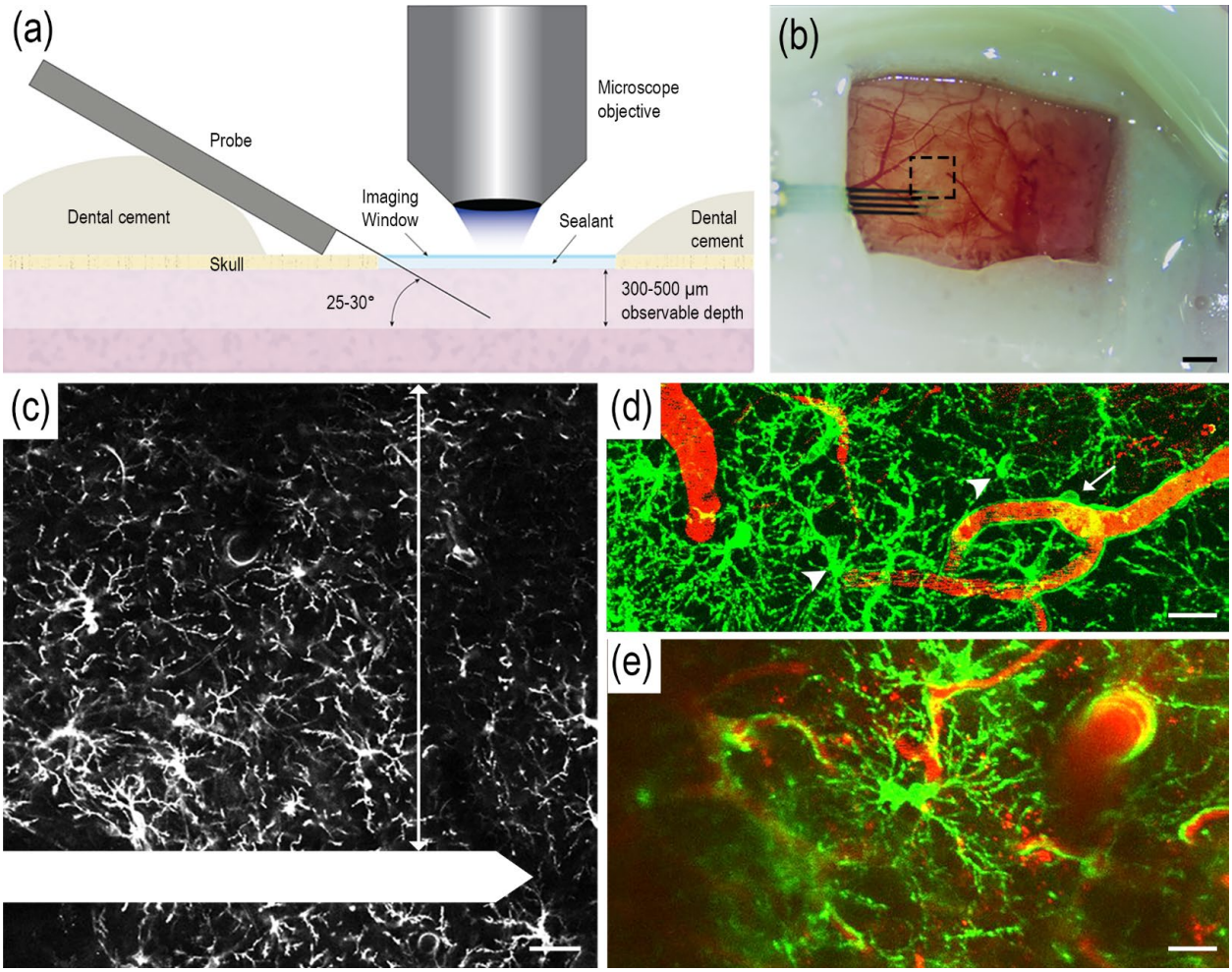

Figure 2-1 Experimental setup for in vivo tracking of NG2 glia and microglia cell dynamics. (a) Schematic of chronic imaging window preparation for two-photon microscopy. The electrode was implanted at a 25-30º angle over the mouse visual cortex, sealed with kwik-sil and a cover glass was applied over the top to preserve imaging clarity and maintain tissue health. Dental cement is used to secure the probe in place and seal the craniotomy. (b) The chronic imaging window. Black dotted box is the region of interest where z-stacks was acquired. Scale bar = 1 mm. (c) Inset of (b). NG2 glia was observed and quantified 300 µm adjacent to the electrode shank (arrow). The electrode shank is outlined in white. Scale bar = 50 µm. Both vascular bound NG2+ pericytes (d, arrow), which display distinct morphology compared to NG2 glia (d, arrowhead), and proliferating NG2 glia (e) were excluded from quantification. GFP fluorescence is labeled green and blood vessels are labeled red for (d) and (e). Scale bar = 25 µm.

2.4.1 NG2 glia Begin Cellular Processes Extension Between 12 to 24 Hours Following Electrode Insertion

NG2 glia react first through the extension of processes toward the surface of the probe (Figure 2-2a). Processes on the soma opposite to the probe surface are retracted and processes facing the implantation site are extended. As a result, the soma of NG2 glia appear elongated along this direction. There was no observable movement in NG2 glia cell processes for the first 12 hours following insertion (Figure 2-2b). After 12 hours, NG2 glia processes moved at a rate of about 2.5 $\pm$ 0.4 $\mu m\ h^{-1}$ toward the direction of the electrode before decreasing over the next 48 hours (Figure 2-2c). Velocities were no longer quantified once cell processes reached their destination (probe surface). In comparison, microglia extend cellular processes immediately following electrode insertion, with most extensions occurring within the first hour following injury. NG2 glia process velocities were significantly different than microglia processes at 12 hours post-insertion when NG2 glia begin initiate changes in cell polarity (Welch's T-test; $p < 0.05$). Interestingly, while microglia processes move at the rate of microns per minute, NG2 glia processes move at rate of microns per hour, considerably slower than microglia.

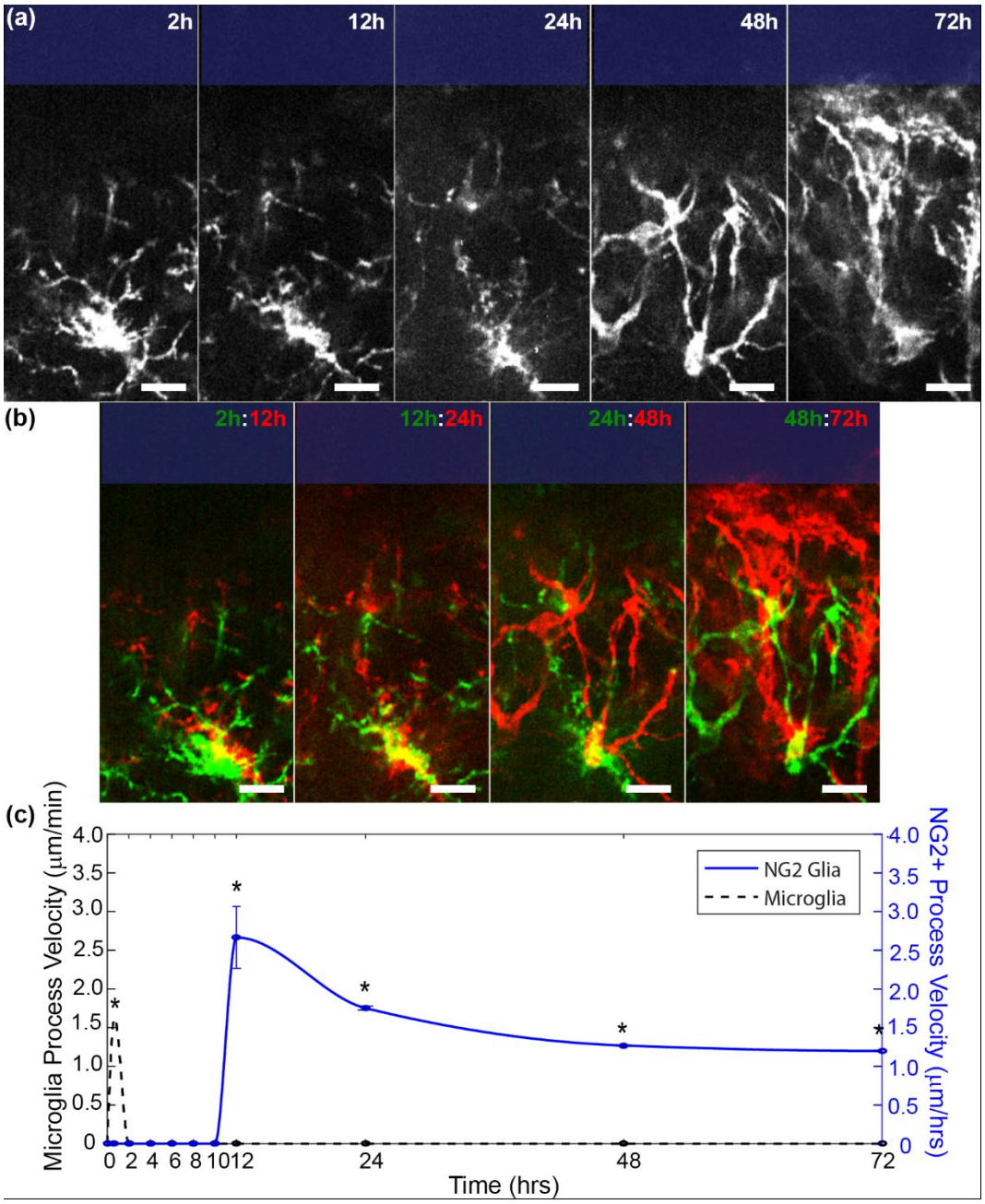

Figure 2-2 NG2 glia extend processes toward the probe beginning 12 hours post-insertion. (a) NG2 glia processes extend toward the probe surface (blue rectangle). Scale bar = 15 µm. (b) Merged images of NG2 glia cell. Yellow denotes where pixels before and after overlap. Red indicates extended features while green denotes retracted features. Scale bar = 15 µm. (c) NG2 glia (blue) and microglia (black dashed) process velocities were tracked over time. Velocity data for acute microglia process migration within the first hour of insertion was obtained from (James R Eles et al., 2017). * indicates $p<0.05$.

2.4.2 NG2 Glia Migrate Toward the Probe Surface Shortly After Extension of Processes

Cell body migration of NG2 glia toward the surface of the device begins 12 to 24 hours following insertion (Figure 2-3a). Likewise, microglia did not show any discernable locomotion in the first 10 hours once their processes contacted the probe surface within the first hour of insertion (Figure 2-3b). NG2 glia cell bodies migrate at a rate of 1.6 ± 0.3 μm hour^{-1} while microglia migrate at a rate of 2.1 ± 0.3 μm hour^{-1}. No significant differences were found for cell body migration velocities between NG2 glia and microglia (Welch's T-test; $p > 0.05$), indicating rate of migration is not inherent to either individual glia cell (Figure 2-3c). Similarly, when observed as a function of distance from the probe surface, there were no significant differences ($p > 0.05$) in cell migration velocities between different distances of the cell relative to the probe as well as between NG2 glia and microglia (Figure 2-3d). Since no NG2 glia were seen activated near 300 μm from the probe surface, quantification of cell body velocity of NG2 glia was not permitted within this region. Additionally, both NG2 glia and microglia increase in coverage over the surface of the probe from 2 to 72 hours post-insertion (Figure 2-4a,b). The percent of tissue labeled with GFP-fluorescence increased significantly for each cell type over time from $36.3 \pm 4.2\%$ to $72.6 \pm 8.9\%$ for NG2 glia (Welch's T-test; $p < 0.05$) and from $52.8 \pm 4.5\%$ to $91.4 \pm 3.3\%$ for microglia ($p < 0.05$). At 2 hours, microglia coverage was significantly increased compared to NG2 glia ($p < 0.05$). However, NG2 glial coverage did not differ significantly from microglia at 72 hours post-insertion ($p > 0.05$).

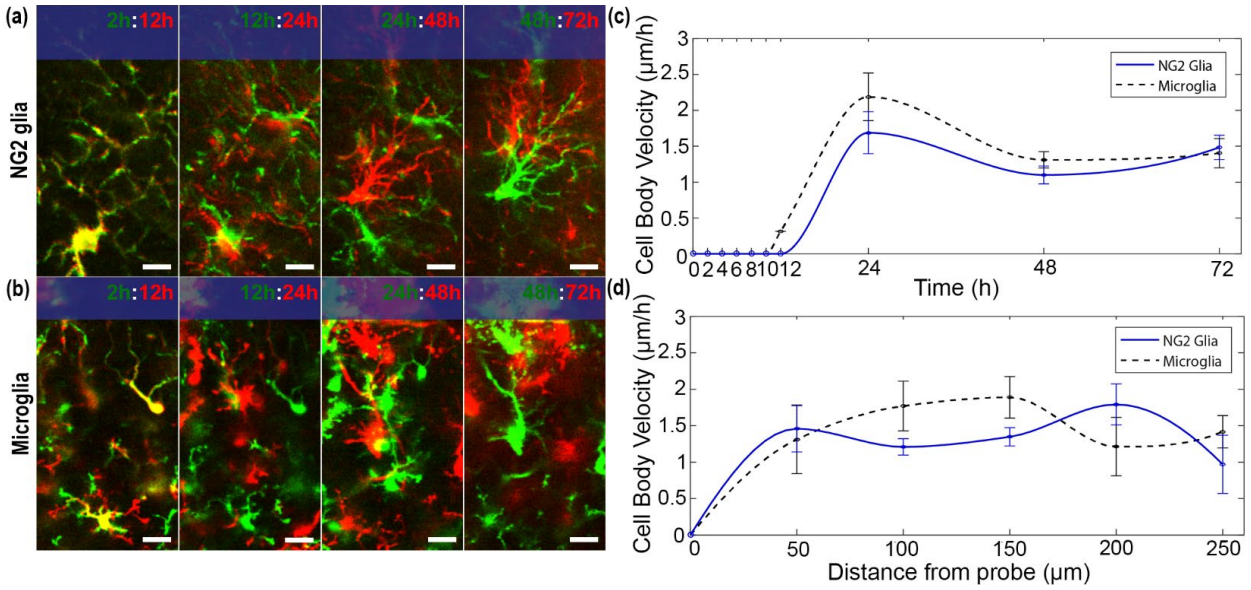

Figure 2-3 NG2 glia share similar kinematic patterns of cell body migration with microglia. (a) NG2 glia cells migrate toward the surface of the probe (blue rectangle) shortly after the extension of cellular processes. Green and red denotes before and after each time point, respectively. Yellow represents areas where pixels overlap, indicating no cellular movement. Scale bar = 15 µm. (b) Microglia cell body migration toward the surface of the probe (blue rectangle) over 72 hours. Scale bar = 15 µm. (c) Velocity of migrating cell bodies for NG2 glia (blue line) and microglia (black dashed) over 72 hours. (d) Cell body velocity plotted as a function of distance from the probe.

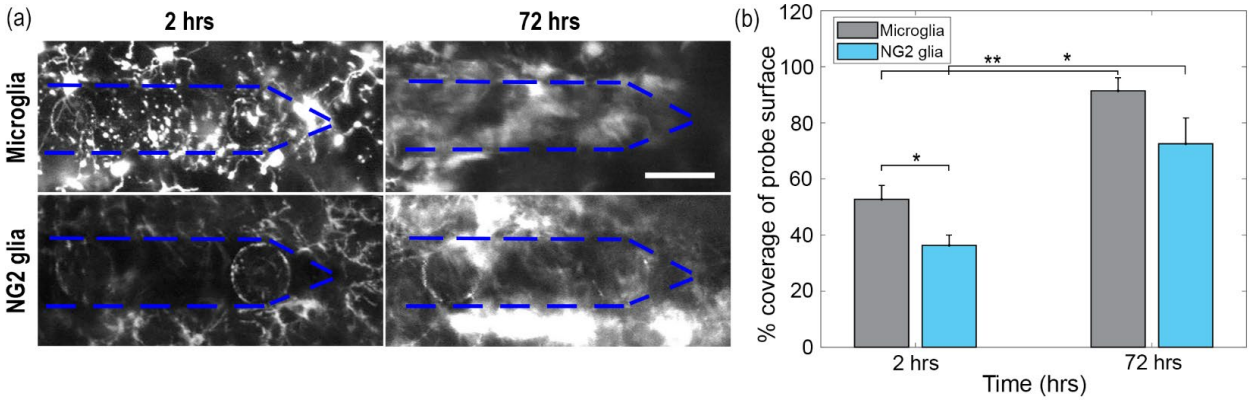

Figure 2-4 Coverage of cellular processes over the probe surface by NG2 glia increases following 72 hours of implantation. (a) Increases in GFP-labelled signal of NG2 glial and microglia processes over the surface of the probe from 2 hours to 72 hours post-insertion. The perimeter of the probe is outlined (blue dashed). Scale bar = 50 µm. (b) Percent of coverage over the probe surface from NG2 glia and microglia cells at 2 hours and 72 hours. * indicates $p<0.05$. ** indicates $p<0.001$.

2.4.3 Ramified NG2 Glia Become Activated Over Time with Distance from the Electrode

NG2 glia were classified as either ramified (R) or transitional (T) through visual observation of the orientation of their processes on either side of an imaginary line drawn through

their cell soma parallel to the surface of the implant (Figure 2-5a). NG2 glia transform from a ramified to activated morphology beginning 12 hours after insertion. At 72 hours, NG2 glia were activated at a radius of about 190.3 μm away from the probe surface. (Figure 2-5). Characterization of their leading and lagging processes relative to the injury showed that NG2 glia begin extending processes toward the probe surface while retracting processes which are orientated away from the opposite direction (Figure 2-5c). Gradually, the number of processes facing away from the probe begin to reduce as NG2 glia begin to alter cell polarity and extend processes toward the direction of the implant (Figure 2-5d). In comparison, microglia are activated up to a distance of 105.6 μm beginning 2 hours after insertion and by 72 hours they are activated at least 300 μm away from the probe surface, spanning the fully imaged region of interest (Figure 2-6a). Over time, lagging microglia processes begin to shorten and reduce as more leading processes lengthen in the direction of the probe which were quantified as T-index and D-index (Figure 2-6b,c).

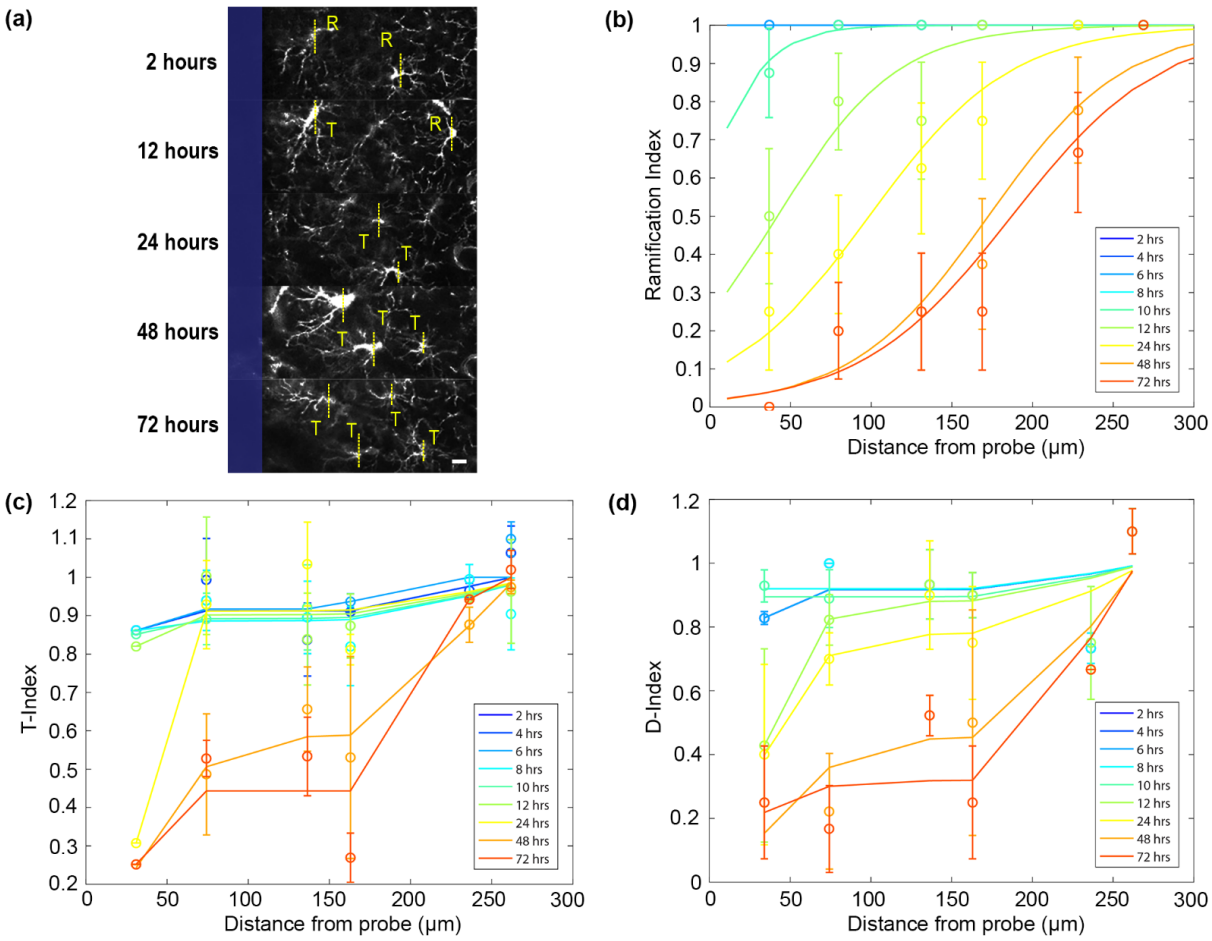

Figure 2-5 NG2 glia experience morphological changes 12 hours after probe insertion. (a) Classification of ramified (R) or transitional/activated (T) NG2 glia over 72 hours. The surface of the probe is outlined in blue. Scale bar = 10 μm. (b) NG2 glia ramification as a function of distance from the probe over 72 hours. NG2 glia become activated to a radius of 190.3 μm away from the surface of the probe at 72 hours. (c) Morphological index of the transitional state of NG2 glia with respect to distance from the probe (T-index). (d) Morphological index of the orientation of NG2 glia processes with respect to distance from the probe (D-index).

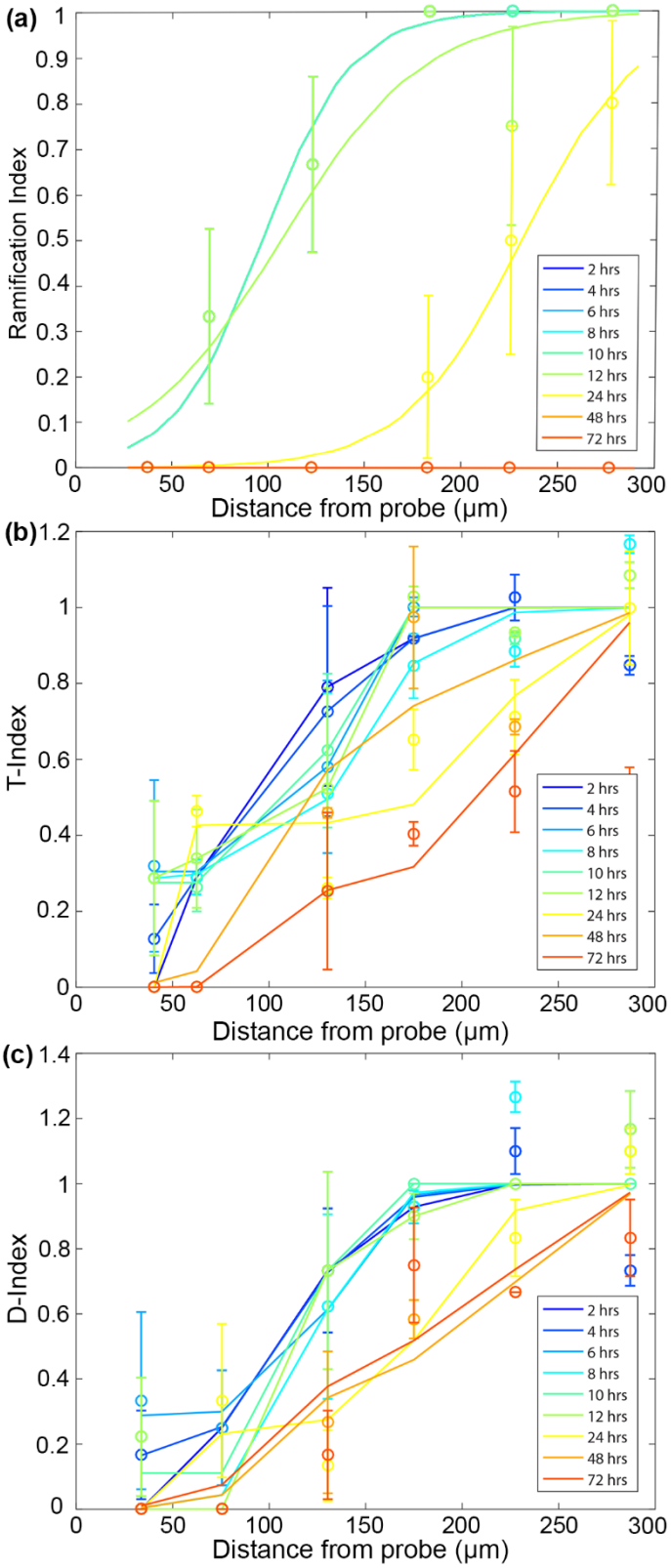

Figure 2-6 Distribution of microglia activation increases up to 72 hours after probe insertion. (a) Characterizing the ramification of microglia with distance from the probe surface. An index of 1 represents ramified morphology

while an index of 0 represents activated, or transitional, microglia. (b) Transitional index of activated microglia where 1 represents processes extending equally in all directions and 0 represents leading processes extended toward the probe surface. (c) Directionality index of microglia where an index of 1 indicates equal number of processes extending toward and away the surface of the probe and an index of 0 indicates all processes extending toward the surface of the probe.

2.4.4 Activation Radius of NG2 Glia 72 Hours Following Probe Insertion

NG2 glia and microglia share a number of morphological similarities and differences in ramified and activated states. Both glia processes extend radially about their somas while ramified; however, NG2 glia processes appear long and thin while microglia processes are short, more highly branched, and bulbous at the tips Figure 2-7a). When activated, each glia orientates processes in a preferred direction relative to their cell bodies. However, large temporal differences were observed between NG2 and microglia activation. Two hours post-insertion, all nearby NG2 glia remain ramified while microglia become activated up to a distance of 105.6 μm (Figure 2-7b). Within this radius, microglia were significantly more activated than NG2 glia (Welch's T-test; $p < 0.05$). No significant differences ($p > 0.05$) were noted in the activation patterns of NG2 glia and microglia 12 hours following insertion (Figure 2-7c). At 72 hours post-insertion, ramified NG2 glia can still be observed greater than 200 μmfrom the electrode while nearly all microglia within a 300 μm radius were observed to be in an activated state (Figure 2-7d). Microglia beyond 200 μm were significantly more activated than NG2 glia at 72 hours post-insertion ($p < 0.05$).

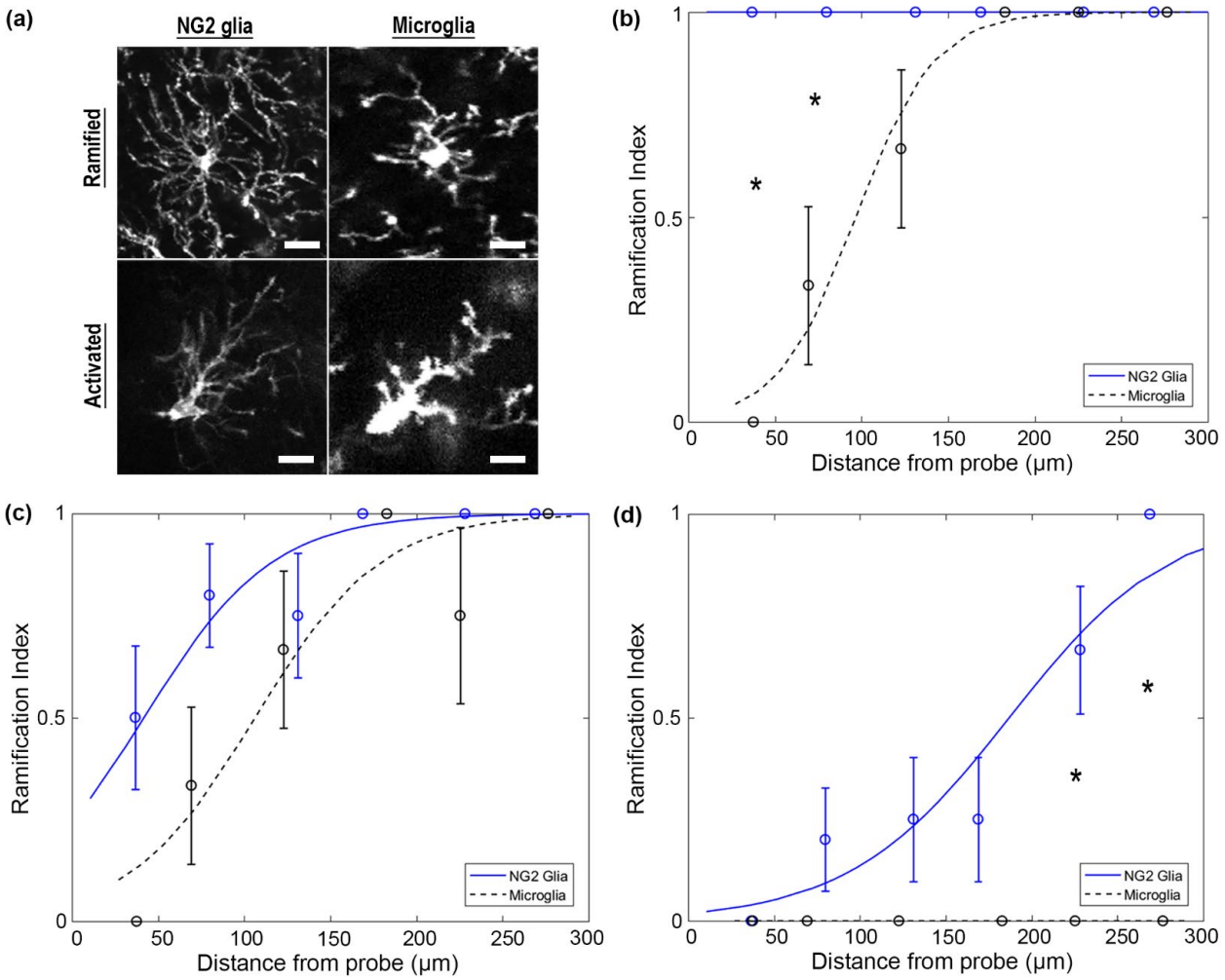

Figure 2-7 NG2 glia differ temporally in activation patterns compared to microglia up to 72 hours post-insertion. (a) NG2 glia express long and thin processes while microglia processes appear short and bulbous. Both cell types extend processes radially around their cell bodies when ramified and preferentially in a particular direction when activated. Scale bar = 15 μm. (b) NG2 glia and microglia have temporally different patterns of activation at 2 hours, (c) 12 hours, and (d) 72 hours post-insertion. * indicates $p<0.05$.

2.4.5 Dynamic Vasculature Changes after Insertion Injury

Venuoles within the vicinity of the probe experienced increases in vessel diameter over the course of 72 hours following insertion (Figure 2-8a). Venuoles can be easily identified from arterioles and capillaries due to the distinct lack of NG2+ smooth muscle cells and pericytes, respectively (Ampofo, Schmitt, Menger, & Laschke, 2017; Chan-Ling & Hughes, 2005).

Quantifying the change in blood vessel diameter over time (taken as the percentage of the change in vessel diameter from 2 hours post-insertion) showed a significant difference in vessel size between 12 and 24 hours post-insertion (repeated ANOVA; $p < 0.01$) and 24 and 48 hours post-insertion ($p < 0.001$). On average, venuoles increased by 50% of their original size around the probe (Figure 2-8b). Figure 7a shows an extreme scenario where one venuole nearly tripled in vessel diameter. Interestingly, arterioles did not show any noticeable differences in diameter over the 72 hour period. Furthermore, NG2 glia were observed to respond to vasculature events (Figure 2-8c).

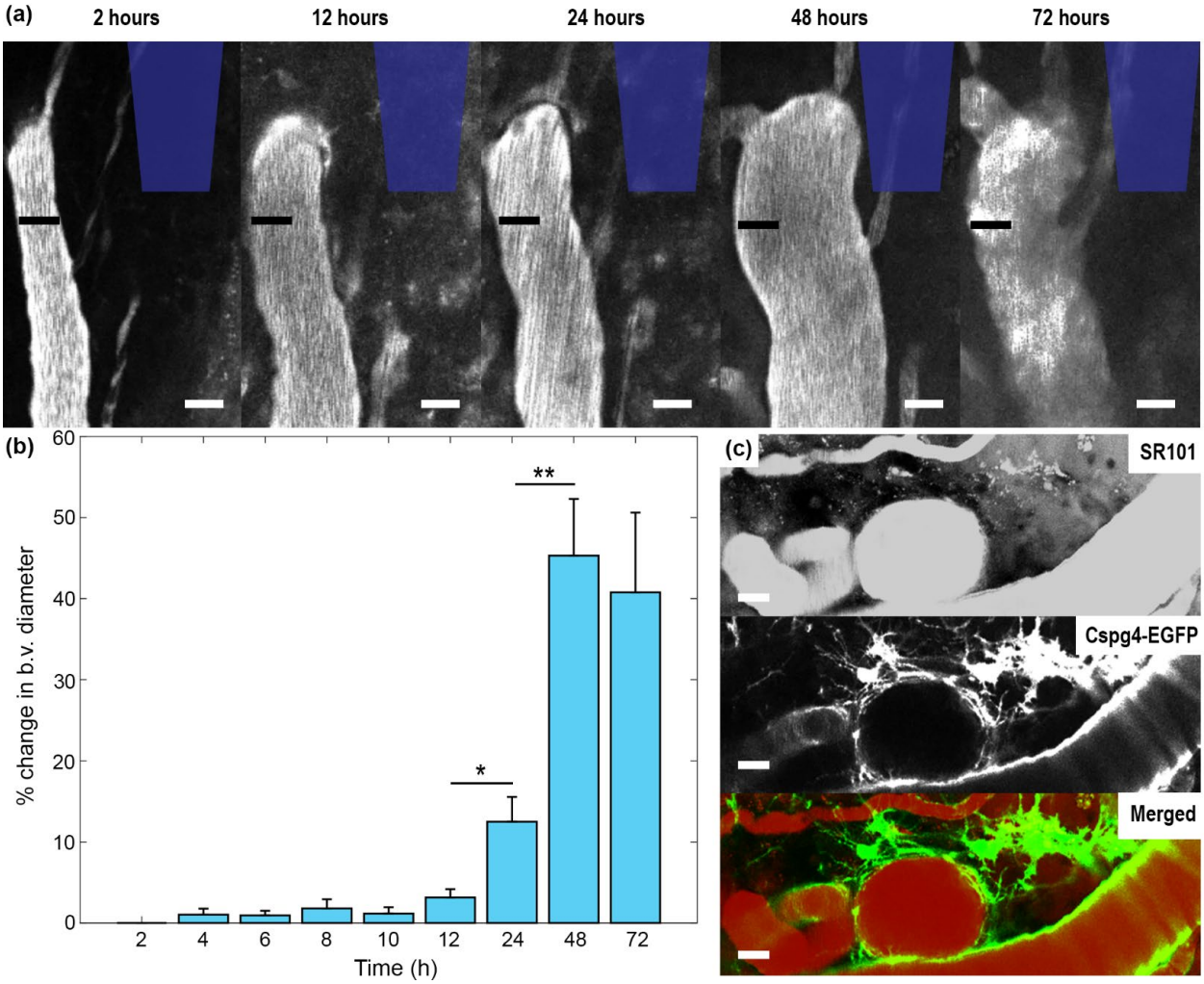

Figure 2-8 Vascular dynamics during inflammatory response after insertion. (a) Venuoles near the inserted probe increased in diameter over 72 hours following probe insertion. The black bar denotes the diameter of the blood vessel

at 2 hours post-insertion for all time points. The position of the probe is outlined in blue. Scale bar = 25 μm. (b) Percent change in blood vessel (b.v.) diameter over time compared to original blood vessel diameter at 2 hours post-insertion. (c) NG2 glia respond to vascular events at 72 hours post-insertion. Vasculature is visualized with SR-101. Scale bar = 20 μm. * indicates $p<0.01$. ** indicates $p<0.0001$.

2.5 Discussion

Under normal physiological conditions, NG2 glia exist as a distinct glial population in the brain, with numerous roles including acting as precursors to myelinating oligodendrocytes and providing neurotrophic support to neurons through synaptic connections. They extend and retract processes radially around their cell bodies constantly surveying their extracellular environment (E. G. Hughes et al., 2013). However, unlike microglia who display a few short processes with bulbous endings, NG2 glia maintain numerous long, thin processes around their cell soma. During injury, NG2 glia are highly proliferative and widely distributed across the brain, hold astrogliogenic potential, and can secrete axon-growth inhibitory factors (L. Dimou & V. Gallo, 2015). Electrode insertion in the brain induces a graded inflammatory response beginning with blood-brain barrier disruption, which leads to infiltration of blood-borne leukocytes/macrophages, complement system activation, edema, and plasma protein exposure to neuronal and glial cells (T. D. Kozai, A. S. Jaquins-Gerstl, A. L. Vazquez, A. C. Michael, & X. T. Cui, 2015). Activation of microglia (within minutes) and astrocytes (within days) elicits a change in their behavior and morphology as they initiate glial scar formation around the device and secrete cytokines and chemokines which affect other glial cells, neurons, and permeability of the BBB. NG2 glia have reportedly been implicated in glial scar formation following brain injury (A. R. Hackett & Lee, 2016; E. G. Hughes et al., 2013). Here we demonstrate a temporal and spatial sequence of NG2 glia activation around inserted probes using two-photon microscopy to track processes extension, cell body migration,

and quantifiable changes in cell morphology. NG2 glia responses to the presence of the probe are characteristically similar to the behavior previously reported for microglia cells. However, the reaction observed from NG2 glia occur hours following injury as opposed to microglia which react within minutes.

2.5.1 NG2 Glia do Not Respond to Insertion Injury Within the First 12 hours

NG2 glia have been shown previously to react to brain injury, both in response to the death of individual NG2 glia (E. G. Hughes et al., 2013) and large-scale lesions such as spinal cord injury and stroke (Buss et al., 2009; F. E. Song et al., 2017). Along with microglia, they are the first cells to proliferate within 24 hours following injury, whereas astrocytes proliferate days later (Simon, Gotz, & Dimou, 2011). Previously, it has been shown that microglia activate immediately upon insertion via the extension of cellular processes toward the probe surface (T. D. Kozai, A. L. Vazquez, et al., 2012). Here we observe that NG2 glia do not undergo changes in cell morphology within the first 12 hours following probe insertion. This is confirmed by the observation of equal length processes in all radial directions around their cell bodies as well as the lack of a hypertrophic cell shape that is a characteristic of activated glia. Following 12 hours after insertion, NG2 glia begin to preferentially extend their processes in the direction of the probe at a rate of 2.5 ± 0.4 μm h^{-1}, similar to what has been reported previously (2.7 ± 0.4 μm h^{-1}) (E. G. Hughes et al., 2013). In contrast, microglia processes extend at a rate of 1.6 ± 1.3 μm min^{-1} and terminate on the probe surface within the first hour following insertion (T. D. Kozai, A. L. Vazquez, et al., 2012). This results in spatially distinct layers of microglia processes surrounded by NG2 glia processes within the glia scar (E. G. Hughes et al., 2013).

2.5.2 NG2 Glia Migrate Cell Bodies Toward the Surface of the Device Shortly After Activation

Within 24 hours after CNS injury, a rapid increase in NG2+ expression is observed around the implant site (Fitch & Silver, 1997; Lemons, Howland, & Anderson, 1999). Here we show that NG2 glia migrate toward the surface of the probe shortly following processes extension at 12 hours post-insertion. NG2 glia migrate toward the probe at a rate of 1.6 ± 0.3 μm hour^{-1}, which did not differ significantly ($p = 0.3219$) from the rate of microglia migration (2.1 ± 0.3 μm hour^{-1}) indicating the velocity of cell body movement is not intrinsic to either individual glial cell. Currently, the circumstances surrounding NG2 activation, and thus migration and proliferation, during glial scar formation is relatively unknown. It is known that microglia become activated when exposed to inflammatory plasma proteins that are released following blood-brain barrier permeability, explaining their immediate reaction to the disruption of vasculature from inserted microelectrodes (Adams et al., 2007; Ralay Ranaivo & Wainwright, 2010). Cytokine gradients that are produced following injury may explain the graded increase in cell activation over time as a function of distance from the implant (Fan, Xie, & Chung, 2017). NG2 produced in NG2 glia is known to direct migration and orientation by regulating cell polarity via fibroblast growth factor (FGF)-dependent activation of the RhoA/ROCK pathway (Biname, Sakry, Dimou, Jolivel, & Trotter, 2013). FGF production is observed in CNS injuries such as multiple sclerosis (MS) and cortical stab wounds (Clemente, Ortega, Arenzana, & de Castro, 2011; do Carmo Cunha et al., 2007; Robel, Berninger, & Gotz, 2011) and it is important for wound healing and angiogenesis after blood vessel injury (Lin, Te, Lee, Sun, & Hsu, 1997). Thus, severity of blood-brain barrier disruption could lead to the upregulation of chemotactic FGF, recruiting NG2 glia and other immune cells to the implant injury site. Other factors which influence NG2 glia migration as well

as proliferation are platelet-derived growth factor (PDGF) and chemokines CXCL1, CXCR4, CXCL12, and CCL11 (Dziembowska et al., 2005; Maysami et al., 2006; Tsai et al., 2002).

Once NG2 glia and microglia cells extended processes and migrated cell bodies towards the probe, there was no indication of extension or migration away from the surface throughout the duration of study. At 2 hours post-insertion, microglia covered 52.8 ± 4.5% of the probe surface, similar to what was reported previously (47.7% ± 3.4%) (James R Eles et al., 2017). NG2 glia coverage differed significantly from microglia coverage at 2 hours following implantation, which is expected given that microglia extension of processes begins within the first hour following insertion while NG2 glia do not respond until after 12 hours post-insertion. Over the course of 72 hours, both microglia and NG2 glia significantly increased in coverage over the probe surface reflecting their parallel migration toward the device over this time period. However, it is not clear to what extent is this surface coverage the result of glial cell migration to the probe or proliferation at the lesion site, given that both NG2 glia and microglia significantly proliferate within the following days after acute injury to the brain (Susarla, Villapol, Yi, Geller, & Symes, 2014). Cell division is not easily measured using single channel fluorescence such as with two-photon microscopy; therefore, other methods of analyses are needed to determine the extent of cellular proliferation around an implanted device. At 72 hours post-insertion, NG2 glia doubled the amount of surface coverage within this period resulting in no significant difference from microglial coverage. Additional longitudinal studies are needed to determine whether or not NG2 glia coverage would continue to increase in surface coverage beyond 72 hours of implantation.

2.5.3 Activated NG2 Glia Undergo Morphological Changes Following Insertion Injury

After injury, NG2 glia cell bodies begin to hypertrophy as their cytoskeletal structure rearranges and prepares for movement, similar to microglia and astrocytes during the formation of a glial scar (Hansson, 2015). NG2 glia activate from normal ramified morphology 12 hours after probe insertion. A distribution of NG2 glia ramification as a function of distance from the surface of the probe was generated by assigning an index value of either 0 for transitional, or activated, morphology or 1 for a ramified morphology. NG2 glia became activated up to a distance of 190.3 μm from the probe surface after 72 hours. In other words, at 72 hours, the probability that 50% or more of NG2 glia will be polarized will occur within a radius of 190.3 μm from the surface of the probe. At this time, all microglia observed within a 300 μm radius of the probe were activated. While the ramification index provided an indication of the extent of activation of NG2 glia or microglia, it lacked information about the specific orientation of the cell. This information was given by the T-index (transitional state) and D-index (directionality). Over time, both NG2 glia and microglia began to extend leading processes further toward the implant while retracting lagging processes that were orientated away from the implant (T-index = 0). Likewise, NG2 glia and microglia began preferentially orientating most of their processes in the direction of the implant (D-index = 0). These metrics allowed characterization of the preference for glia to respond to the presence of the device as opposed to responding to other insults in the brain, such as neuronal or glial cell death or disruptions of distant vasculature, reflected by a T-index or D-index greater than 1.

2.5.4 Changes in the Vasculature Around Implanted Probes in the Brain

Electrode insertion inevitably impacts the integrity of the blood-brain barrier, either through direct disruption of vasculature or through the inflammation-induced upregulation of cellular pathways that influence its permeability (T. D. Kozai et al., 2015; T. D. Y. Kozai et al., 2010). Dynamic changes to the vasculature occurred 24-48 hours following injury, where venuoles increased in diameter around the probe site. The change in blood vessel diameter differed significantly with a 12.5 ± 3.1% increase in diameter at 24 hours and 45.3 ± 6.9% increase at 48 hours following insertion. It remains to be investigated if venuoles dilate in order to redirect blood flow from damaged capillary networks, accommodate additional traffic from glial cells clearing debris and waste products, or alleviate increases in drainage pressure. Interestingly, no appreciable differences were observed in arteriole size over the 72 hours in the animals in this study. NG2 glia were observed proximal to these vascular events near the inserted probe. However, it is unclear whether they were responding to the changes to the blood vessel or were merely being pushed away by the rapidly expanding vascular membrane. Regardless, functional analysis showed that NG2 glia play a role in maintaining BBB integrity through the release of TGF-β1, a factor that induces extracellular matrix production in pericytes (Seo et al., 2014). Pericytes express platelet-derived growth factor beta (PDGFR-β) as well as the NG2 antigen and therefore can be observed using the *Cspg4-EGFP* transgenic mouse model. However, they were excluded from this study as this study focused on NG2+ oligodendrocyte precursor cells. These pericytes are visually distinct from NG2 glia in morphology and position in the cortex, normally residing along capillary walls as opposed to freely roaming within the parenchyma (Attwell, Mishra, Hall, O'Farrell, & Dalkara, 2016). Besides regulation of blood flow, pericytes are also responsible for clearance of metabolic

waste products from the parenchyma and mediating angiogenesis (E. A. Winkler, R. D. Bell, & B. V. Zlokovic, 2011), and therefore are of great interest for future studies.

2.5.5 Future Directions

One of the roles of NG2 glia in the central nervous system is to act as a reservoir of precursor cells that differentiate into myelinating oligodendrocytes after a demyelinating insult (Tripathi, Rivers, Young, Jamen, & Richardson, 2010). Although the extent of oligodendrocyte cell death has not been investigated in the context of microelectrode implantation, demyelinated axons have been anecdotally observed around the insertion site (B. D. Winslow et al., 2010b). It is possible that NG2 glia who migrate toward the surface of the probe are responding to damaged myelin and oligodendrocytes within the area and compensate for the loss of myelinating cells by differentiating into mature oligodendrocytes. Likewise, NG2 glia are also known to have astrogliogenic potential. Similar to astrocytes, they are derived from radial glia during development, display stellate morphology, and express ion channels and receptors for neurotransmitters secreted by neurons (Bergles & Richardson, 2015; Nishiyama, Yang, & Butt, 2005a). Differentiation of NG2 glia into astrocytes has been shown under *in vitro* conditions; and have been implicated as differentiating into astrocytes at the lesion sites to form part of the glial scar (Komitova, Serwanski, Lu, et al., 2011; K. Tatsumi et al., 2005; Kouko Tatsumi et al., 2008). While NG2 glia differentiation into astrocytes has been observed during specific injury to the cerebral cortex such as during cryoinjury as well as focal cerebral ischemia, the extent of NG2 glia contribute to the increase in expression of glial fibrillary acidic protein (GFAP) observed around chronically implanted microelectrodes remains to be elucidated (Martin et al.). A longer timescale study is necessary to identify the spatiotemporal dynamics between astroglial scar formation and

differentiation of NG2 glia into astrocytes or myelinating oligodendrocytes (oligodendrogenesis). However, detailed studies tracking oligodendrocyte progenitor differentiation into astrocytes or oligodendrocytes *in vivo* have been difficult due to the fact that differentiating NG2 glia lose antigenic markers that are targeted using immunohistochemistry techniques, such as NG2+ and PDGFRα+, as well as during *in vivo* imaging. For example, Hughes et al. observed a decrease in GFP fluorescence when oligodendrocyte precursor cells began to differentiate into oligodendrocytes as the *Cspg4* promoter was down regulated (Ethan G. Hughes, Shin H. Kang, Masahiro Fukaya, & Dwight E. Bergles, 2013a). Tracking the differentiation of NG2 glia using fate-independent markers could help determine contribution of NG2 glia during injury. Ultimately, understanding the purpose for NG2 migration and proliferation around the inserted probe will provide insight as to whether the cell is participating in tissue degeneration or repair.

A unique characteristic that is not observed in other glial cells such as microglia and astrocyte is the ability for NG2 glia to provide metabolic support and neuronal modulation by establishing synaptic contacts with neurons (Sakry et al., 2014). However, additional studies are necessary to characterize the impact of NG2 glia on neuronal viability. Furthermore, it has been shown that oligodendrogenesis is regulated through neuronal signaling in which electrical depolarizations via AMPA receptors on NG2 glia induce oligodendrocyte differentiation (Gibson et al., 2014). In addition, chemical ablation of NG2 glia has been shown to lead to increased neuronal loss (Birey et al., 2015). It is possible these connections could be compromised during injury in which NG2 glia are preferentially activating and migrating in response to the presence of an implanted microelectrode. This activation may require NG2+ cells to abandon their supportive roles under their ramified state. As a result, an increase in NG2 glial cell loss around microelectrodes could impair neuronal health and ultimately the recording and stimulating

performance of neural devices. However, it has been shown that NG2 glia can be manipulated to produce new neurons following traumatic injury due to their inherent neurogenic potential (Heinrich et al., 2014). In fact, previous studies have demonstrated that it is possible to observe neural progenitor cells near chronically implanted microelectrodes (T. D. Kozai, Z. Gugel, et al., 2014). Guiding differentiation of these progenitors cells or chemically reprogramming glial cells into neurons may be one approach to repair brain injuries (L.-L. Wang & Zhang, 2018). Utilizing the cell's natural machinery to convert reactive glia into functionally integrated neurons could attenuate and potentially reverse the pro-inflammatory, tissue degrading microenvironment surrounding inserted devices leading to improved chronically implantable neural interfaces.

2.6 Conclusion

The current study is novel in that, for the first time, it characterized the spatiotemporal activity of NG2 OPC glia participation during the inflammatory response caused by implantation of microelectrode arrays in the cortex. Two-photon microscopy techniques allow for the observation and enhanced characterization of acute NG2 glia activation 72 hours after insertion. Beginning 12 hours following insertion, NG2 glia become activated by extending cellular processes and migrating toward the surface of the device. Using previously characterized microglia cells as comparison, NG2 glia activate in a similar, yet delayed, fashion. This work enhances our understanding of the cellular and subcelluar changes that occur following injury and provides a time course of dynamic behavior that can be targeted for future interventions seeking to attenuate the activation of glial cells around implanted devices. Understanding the impact NG2 glia have on

the functional performance of inserted microelectrodes could shift the focus on current efforts to improve the stability and functionality of chronically implanted neural interfaces.

3.0 Cuprizone-induced Oligodendrocyte Loss and Demyelination Impairs Recording Performance of Chronically Implanted Neural Interfaces

This chapter is taken directly from a first authorship manuscript published in Biomaterials titled, "Cuprizone-induced oligodendrocyte loss and demyelination impairs recording performance of chronically implanted neural interfaces" (S. M. Wellman et al., 2020).

3.1 Overview

Biological inflammation induced during penetrating cortical injury can disrupt functional neuronal and glial activity within the cortex, resulting in potential recording failure of chronically implanted neural interfaces. Oligodendrocytes provide critical support for neuronal health and function through direct contact with neuronal soma and axons within the cortex. Given their fundamental role to regulate neuronal activity via myelin, coupled with their heightened vulnerability to metabolic brain injury due to high energetic demands, oligodendrocytes are hypothesized as a possible source of biological failure in declining recording performances of intracortical microelectrode devices. To determine the extent of their contribution to neuronal activity and function, a cuprizone-inducible model of oligodendrocyte depletion and demyelination in mice was performed prior to microelectrode implantation. At 5 weeks of cuprizone exposure, mice demonstrated significantly reduced cortical oligodendrocyte density and myelin expression. Mice were then implanted with functional recording microelectrodes in primary visual cortex and neuronal activity was evaluated up to 7 weeks alongside continued

cuprizone administration. Cuprizone-induced oligodendrocyte loss and demyelination was associated with significantly reduced recording performance at the onset of implantation, which remained relatively stable yet decreased over time compared to mice on normal diet. Further, electrophysiological analysis revealed deficits in multi-unit firing rates, frequency-dependent disruptions in neuronal oscillations, and altered laminar communication within the cortex of cuprizone-treated mice. Post-mortem immunohistochemistry revealed robust depletion of oligodendrocytes around implanted microelectrode arrays alongside comparable neuronal densities to control mice, suggesting that oligodendrocyte loss was a possible contributor to chronically impaired device performances. This study highlights potentially significant contributions from the oligodendrocyte lineage population concerning the biological integration and long-term functional performance of neural interfacing technology.

3.2 Introduction

Investigative and clinical neuroscience have the potential to benefit from the use of penetrating cortical neural interfaces, which can be applied as tools to reveal unknown neuroscientific phenomenon or alleviate neurological deficiencies following central nervous system (CNS) injury or disease (Buzsáki et al., 2015; Jennifer L Collinger et al., 2013; J. R. Eles & Kozai, 2020; Hatsopoulos & Donoghue, 2009; L. R. Hochberg et al., 2006; Iordanova, Vazquez, Kozai, Fukuda, & Kim, 2018; Nicholas J. Michelson, Eles, Vazquez, Ludwig, & Kozai, 2018; Andrew B Schwartz, X Tracy Cui, Douglas J Weber, & Daniel W Moran, 2006; Stocking, Vazquez, & Kozai, 2019). Despite the wide versatility of implantable microelectrode arrays, overwhelming biological inflammation and large variability in recording performances debilitate

the long-term applications of neural interfacing technology (Alba et al., 2015; James C Barrese et al., 2013; Cynthia A Chestek et al., 2011; Cody, Eles, Lagenaur, Kozai, & Cui, 2018; Takashi D. Y. Kozai et al., 2016; T. D. Y. Kozai et al., 2010; Patrick J. Rousche & Richard A. Normann, 1998; J. W. Salatino et al., 2017; Justin C. Williams, Robert L. Rennaker, & Daryl R. Kipke, 1999). Investigations into proposed biological failure modes of microelectrode devices, such as chronic neurodegeneration or glial scar formation, have been unable to account for the characteristic degradation in device performances over time (T. D. Kozai, X. Li, et al., 2014; A. Prasad et al., 2011; Steven M. Wellman et al., 2018; Steven M Wellman, James R Eles, et al., 2018a). However, the brain parenchyma is not limited to neurons, microglia, and astrocytes, nor are these the only cells whose physiological activity can be compromised during CNS injury (Alba et al., 2015; J. Eles, A. Vazquez, T. Kozai, & X. Cui, 2018; Steven M. Wellman et al., 2018; S. M. Wellman & T. D. Kozai, 2017b). Cells of the oligodendrocyte lineage, which have gone largely uninvestigated in regards to chronic device implantation, are intimately associated with neurons and may have a more direct contribution to the chronic degradation in recordable neuronal signals around intracortical microelectrode interfaces (Steven M. Wellman et al., 2018; S. M. Wellman, L. Li, Y. Yaxiaer, I. N. McNamara, & T. D. J. F. i. N. Kozai, 2019b).

Oligodendrocytes, a third type of glia alongside microglia and astrocytes, possess the ability to directly regulate neuronal health and function through the deposition of myelin membranes around axons (N. Baumann & Pham-Dinh, 2001; Bradl & Lassmann, 2010; Dougherty, Dreyfus, & Black, 2000). Myelin sheaths support saltatory conduction of neuronal signals by providing electrical insulation of far-projecting axons within the white matter (Hartline, 2009). Both oligodendrocytes and myelin exist within gray matter structures, such as the cortex, although at relatively lower numbers compared to the white matter (Giulio Srubek Tomassy et al.,

2014; Valério-Gomes, Guimarães, Szczupak, & Lent, 2018). Furthermore, a fraction of oligodendrocytes existing in the gray matter, termed satellite oligodendrocytes, maintain close contact with neuronal soma and may have a more critical role in providing metabolic and neurotrophic support (Battefeld, Klooster, & Kole, 2016; S. M. LeVine & Torres, 1993; Takasaki et al., 2010). However, the presence of monocarboxylate transporters in myelin suggest that myelinating oligodendrocytes are also a sustainable source of support for neurons (Fünfschilling et al., 2012; Y. Lee et al., 2012). Oligodendrocyte densities are maintained by a self-renewing population of differentiating progenitor cells, called oligodendrocyte precursor cells, which replenish lost or damaged oligodendrocytes following demyelinating CNS injury (Ethan G. Hughes, Shin H. Kang, Masahiro Fukaya, & Dwight E. Bergles, 2013b; Joel M Levine & Reynolds, 1999; Tripathi et al., 2010). This precursor population can become exhausted in their capacity to form new oligodendrocytes following persistent demyelinating injury or from experiencing differentiation block (Kuhlmann et al., 2008). As a result, neurological symptoms can occur due to a loss of oligodendrocyte support or myelin encapsulation and are commonly observed during multiple sclerosis (MS) and other demyelinating diseases with the CNS (Ettle, Schlachetzki, & Winkler, 2016; Smith & McDonald, 1999).

Due to their need for continuous production of lipid-dense myelin membranes, oligodendrocytes are considered one of the most energy demanding glial cells within the brain, and therefore have an increased susceptibility to metabolically damaging CNS injury (Jana, Hogan, & Pahan, 2009; Rosko, Smith, Yamazaki, & Huang, 2018; Roth & Núñez, 2016). Low levels of the antioxidant glutathione in oligodendrocytes and their precursors render them increasingly vulnerable to oxidative stresses that can occur during ischemia, traumatic brain injury (TBI), or autoimmune-mediated inflammatory diseases such as MS (JUURLINK, 1997;

Thorburne & Juurlink, 1996). Oligodendrocyte degeneration and demyelination are commonly observed during focal cerebral ischemia and white matter stroke (Dewar et al., 2003). Similarly, traumatic brain injury has demonstrated oligodendrocyte cell death and myelin loss in gray and white matter regions of the CNS (Dent et al., 2015; Flygt, Djupsjö, Lenne, & Marklund, 2013; Lotocki et al., 2011). Penetrating cortical injuries, such as microelectrode device insertion, demonstrate inflammation cascades similar to stroke and TBI and induce similar damage on the oligodendrocyte lineage population (Steven M. Wellman et al., 2018). Winslow et al. demonstrated myelin loss as well as signs of blood-brain barrier leakage near chronically implanted single-shank electrodes (Brent D Winslow & Tresco, 2010). We have recently shown oligodendrocyte degeneration, myelin reorganization, and reactive oligodendrocyte precursor population preferentially around implanted electrode arrays (S. M. Wellman & T. D. Kozai, 2018; Steven M Wellman et al., 2019b). However, how oligodendrocyte loss or dysfunction affects the intrinsic electrophysiological properties of neuronal tissue and the functional performance of intracortical recording microelectrodes has yet to be investigated.

Cuprizone, a copper-chelating agent, can be administered as a highly reproducible model of oligodendrocyte depletion and demyelination within distinct brain regions, such as the corpus callosum and cortex (Skripuletz et al., 2008). It is often used as an alternative to experimental autoimmune encephalomyelitis (EAE), which induces activation of immunological and inflammatory processes to mimic biological symptoms of MS (Praet, Guglielmetti, Berneman, Van der Linden, & Ponsaerts, 2014). Cuprizone is most often administered via rodent chow, and acute exposure (<5-6 weeks) can effectively deplete a significant population of oligodendrocytes and myelin within the CNS (Gudi, Gingele, Skripuletz, & Stangel, 2014; Sen, Mahns, Coorssen, & Shortland, 2019). The effects of cuprizone administration can be reversed if mice are returned

to normal diet following this acute period (Gudi et al., 2009; Matsushima & Morell, 2001). A chronic state of oligodendrocyte depletion and demyelination can be achieved by administrating cuprizone continuously for up to 12 weeks, effectively exhausting the precursor population and incapacitating their ability to generate new oligodendrocytes and myelin (Skripuletz et al., 2008). Finally, cuprizone preferentially targets mature oligodendrocytes with no significant changes to neurons or axons within the brains of young mice, allowing for specific investigation of the effects of oligodendrocyte and myelin depletion on neuronal function (Benetti et al., 2010; Praet et al., 2014).

Since oligodendrocytes mediate neuronal health and activity via metabolic and trophic support as well as myelin ensheathment, we hypothesized that the presence of oligodendrocytes is critical for the neuronal signals acquired by intracortical microelectrode arrays. In this study, we used a cuprizone-induced oligodendrocyte depletion model to deplete oligodendrocytes and myelin within the cortex and evaluate the recording performance of chronically implanted intracortical devices. We demonstrate that cuprizone effectively depletes a majority of cortical oligodendrocytes resulting in myelin loss by 5 weeks of diet administration. We also show that the oligodendrocyte loss and demyelination due to cuprizone-treatment significantly reduces recording performance at the onset of device insertion and remains relatively steady over a 7-week implantation period compared to mice on control diets. Additional recording analyses revealed chronic alterations in multi-unit firing rate, neuronal oscillatory activity, and laminar coherence within the cortex of cuprizone-treated mice. Furthermore, histology at 7 weeks post-insertion and 12 weeks of cuprizone administration depicted robust loss of oligodendrocytes in cuprizone-treated mice coinciding with matched neuronal densities compared to controls. In summary, we establish that the presence of oligodendrocytes and myelin within the cortex is necessary to

maintain normal electrophysiological properties of neurons and that their loss or dysfunction could underlie possible biological failure modes of chronically implanted neural interfaces.

3.3 Methods

Neural recording performances were compared between C57BL/6J mice fed with cuprizone diet (depleted oligodendrocyte) and C57BL/6J mice on a normal diet (normal oligodendrocyte). Post-mortem immunohistochemical analysis was performed for end-point analyses of different cellular markers following device implantation with and without cuprizone administration. All animal care and procedures were performed under approval of the University of Pittsburgh Institutional Animal Care and Use Committee and in accordance with regulations specified by the Division of Laboratory Animal Resources.

3.3.1 Animals and Cuprizone Administration

Cortical oligodendrocyte depletion and demyelination was induced by feeding 6-8 week old, male C57BL/6J mice (22-30g, Jackson Laboratory, Bar Harbor, ME) rodent chow infused with 0.2% cuprizone (bis-cyclohexanone oxaldihydrazone; Evigo, Cambridgeshire, United Kingdom). Mice were fed cuprizone diet for 5 weeks prior to electrode insertion, following which diet was maintained for another 7 weeks during recording experimentation for a total of 12 weeks of cuprizone administration, which is the maximum length of cuprizone exposure before mice begin to experience epileptic seizures in response to environmental stress (Hoffmann, Lindner, Gröticke, Stangel, & Löscher, 2008). A separate cohort of cuprizone-treated mice (n = 3) along

with control mice (n = 3) were sacrificed after 5 weeks of cuprizone administration for immunohistological analysis in non-implanted brain tissue. Food and water were made available *ad libitum,* and since cuprizone is easily degraded due to environmental exposure (Gudi et al., 2014), feeds were replaced every other day with fresh pellets.

3.3.2 Surgical Electrode Implantation

Single shank Michigan-style electrodes (A16-3 mm-50-703-CM15) were inserted into the left primary monocular (V1m) visual cortex of cuprizone-fed (n = 5) and control (n = 5) mice. Procedures for surgical device implantation were performed as described previously (T. D. Kozai, X. Li, et al., 2014). Briefly, an anesthetic cocktail of xylazine (7 mg/kg) and ketamine (75 mg/kg) was injected intraperitoneally (I.P.) for surgery sedation prior to fixing the animal onto a stereotaxic frame. Hair, skin, and connective tissue were removed from the top of the skull to reveal the site of surgical implantation. Vetbond adhesive was used to dry the surface of the skull prior to drilling and provide a supportive grip for a dental cement head cap. Three bone screw holes were drilled (two over both motor cortices and one over the contralateral visual cortex) prior to insertion of 4 mm long, 0.86 mm diameter stainless steel bone screws (Fine Science Tools, British Columbia, Canada) for wrapping of ground and reference wires. The ground wire was wrapped around the bone screw over the ipsilateral motor cortex while the reference wire was wrapped over the bone screws located above the contralateral motor and visual cortex. A drill-sized craniotomy positioned at 1 mm anterior to Lambda and 1.5 mm lateral to midline was made using a high speed dental drill and 0.7 mm drill bit. Saline was periodically applied to prevent thermal damage due to drilling. A microelectrode device was perpendicularly inserted at a speed of 15 mm/s using a DC motor-controller (C-863, Physik Instructmente, Karlsruhe, Germany). The

electrode was inserted to a cortical depth of 800 μm, visually confirming that the last contact site disappeared beneath the pial surface. A silicone elastomer (Kwik-Sil) was used to fill the craniotomy around the electrode prior to sealing with a dental cement head cap. Body temperature was maintained and monitored using a rectangular heating pad (Deltaphase isothermal pad, Braintree Scientific Inc. Braintree, MA). Mice were given an I.P. injection of ketofen (5 mg/kg) on the day of surgery and up to two days after for post-operative recovery.

3.3.3 Electrophysiological Recording

Electrophysiological recordings were conducted inside a grounded Faraday cage to prevent electrical interference from environmental noise as described previously (Alba et al., 2015; Kolarcik et al., 2015; Takashi D Y Kozai, Kasey Catt, et al., 2016; E. Nicolai et al., 2018). Mice were situated on a rotating platform for awake, head-fixed recording. Trials to obtain spontaneous neural activity were recorded in a dark room. Visually-evoked neural activity was stimulated using the MATLAB-based Psychophysics toolbox on a 24" LCD (V243H, Acer. Xizhi, New Taipei City, Taiwan) monitor located 20 cm from the contralateral eye of the mouse covering a 60° wide by 60° high visual field. A drifting gradient of solid white and black bars were presented and synchronized with the neural recording system (RX7, Tucker-Davis Technologies, Alachua, FL) at a sample rate of 24,414 Hz. Each white and black grating was presented for 1 s (rotated in 135° increments), separated by 1 s of a dark screen, and repeated for a total of 64 trials per recording session.

3.3.4 Neural Signal Data Processing

3.3.4.1 Current Source Density

Current source density (CSD) was used to identify layer IV along the length of the electrode following evoked activity within the visual cortex. CSD plots were generated by computing the average evoked (stimulus-locked) LFP for each electrode site, smoothing the signal across all electrode sites, and then calculating the second spatial derivative. CSDs were averaged across 64 stimulus trials and layer IV was identified as an inversion in LFP polarity within the first 100 ms following stimulus onset. Cortical drift and the magnitude change in drift of implanted arrays over time was reported as the average change in layer IV depth relative to depth at day 0 (day of surgery). All electrophysiological evaluation between different cortical depths occurred following alignment of all animals in each group for each day to their corresponding layer IV depth.

3.3.4.2 Single-unit (SU) Sorting and Analysis

Processing of raw signal data occurred offline using a custom MATLAB script modified from previously published methods (Alba et al., 2015). Data was passed through a Butterworth filter with a passband from 2 to 0.3 kHz to produce data containing information on local field potentials (LFP) and 0.3 to 5 kHz to isolate spiking information. Common average referencing was applied to the data as previously described (Ludwig et al., 2009). A fixed threshold value of 3.5 standard deviations below the mean was used to identify potential neuronal single-unit (SU) and multi-unit (MU) activity. Only channels which exhibited a signal-to-noise ratio (SNR) >2 were considered for single-unit sorting. Signal-to-noise ratios (SNR) were calculated by dividing the peak-to-peak amplitude of each single unit by the noise and reported as average SNR and average SNR per active site (electrode channels reporting detection of SU) over time. Sortable single units

were confirmed by observing the quality and shape of neuronal waveforms, auto-correlograms, and peri-stimulus time histograms (PSTH) with 50 ms bins. SU yield was calculated as the percentage of electrode sites (out of 16) with at least one identifiable single unit. The noise floor for each electrode site was taken as two times the standard deviation (2*STD) of the entire recorded data stream after removing all threshold crossing events. Finally, the SNR of any channels without a sortable SU waveform were reported as zero for the purposes of calculating averages.

3.3.4.3 Multi-unit (MU) Analysis

Multi-unit activity was measured as any threshold crossing event that occurred within the 1 s period after each stimulus-locked trigger or pseudotrigger was recorded. Peri-stimulus time histograms (PSTHs) of 50 ms bin size were generated to gauge the dynamics of multi-unit activity. Multi-unit firing rate was measured as the average number of threshold crossing events within a 1-s period after each stimulus presentation or pseudotrigger. Evoked multi-unit activity was evaluated by calculating multi-unit yield and signal-to-noise firing rate ratio (SNFRR). Parameters for multi-unit spike counts involved varying the temporal bin size and latency after stimulus presentation from 0 to 1 seconds in length via 1 ms increments in order to evaluate multi-unit yield and SNFRR. Multi-unit yield was defined as the number of electrode sites that had a significantly different ($p < 0.05$) spike count for a given bin size and latency following stimulus presentation (stim ON) compared to spike counts within that same bin size immediately before stimulation (stim OFF). SNFRR measured the difference in the firing rate of multi-unit activity before and after stimulus relative to the average standard deviation between each stimulus condition:

$$\boldsymbol{SNFRR} = \frac{\mu_{ON} - \mu_{OFF}}{\frac{1}{2}(\sigma_{ON} + \sigma_{OFF})} \quad (3\text{-}1)$$

where μ_{ON} and μ_{OFF} are the average firing rates (across 64 trials) during stimulus ON and OFF conditions and σ_{ON} and σ_{ON} are the standard deviations of firing rates during ON and OFF conditions, respectively. Reported values were calculated as absolute SNFRR.

3.3.4.4 Local Field Potential Analysis

LFP power spectra were calculated using a multitaper method of 1 s duration, 1 Hz bandwidth, and a taper number of 1. Relative power was calculated as the ratio of power within a specific frequency band over the entire frequency range of LFP power (broadband power). LFP power was normalized by subtracting the spontaneous power spectrum from the evoked power spectrum.

$$\boldsymbol{R} = \frac{\sum_{a}^{b} \boldsymbol{S(f)}}{\sum \boldsymbol{S(f)}} \quad (3\text{-}2)$$

$$\boldsymbol{N(f)} = \mathbf{10}\,\mathbf{log_{10}}\left[\frac{\boldsymbol{S_E(f)}}{\boldsymbol{S_{RS}(f)}}\right] \quad (3\text{-}3)$$

where R is relative power, $S(f)$ is the LFP power spectrum, a and b are lower and upper values of the specific frequency range, $N(f)$ is the normalized power spectrum, and $S_E(f)$ and $S_{RS}(f)$ are evoked and resting-state power spectra, respectively.

3.3.4.5 Laminar Coherence Analysis

Electrophysiological activity within and between different laminar depths was evaluated by calculating the magnitude-squared coherence, described previously (Nicholas J. Michelson & Kozai, 2018). Coherence is a quantitative description of the similarity between two signals based on their frequency-dependent responses. Coherence was reported as a value between 0 and 1, with 0 indicating no relationship and 1 indicating a perfect linear relationship between two corresponding signals. Coherence was calculated as follows:

$$\boldsymbol{C_{xy}(f)} = \frac{\boldsymbol{S_{xy}(f)}}{\sqrt{\boldsymbol{S_{xx}(f)S_{yy}(f)}}} \quad (3\text{-}4)$$

$$\boldsymbol{\Delta C_{xy}(f)} = \boldsymbol{C^{E}_{xy}(f)} - \boldsymbol{C^{RS}_{xy}(f)} \quad (3\text{-}5)$$

where $C_{xy}(f)$ is the coherence, $S_{xy}(f)$ is the cross spectrum, and $S_{xx}(f)$ and $S_{yy}(f)$ are the autospectra of LFP activity between electrode sites *x* and *y*, respectively. Normalized coherence $\Delta C_{xy}(f)$ was calculated by taking the difference between evoked coherence $C^{E}_{xy}(f)$ and resting-state coherence $C^{RS}_{xy}(f)$. Coherence calculations were performed within 1 s intervals following each stimulus presentation or pseudotrigger, at a half-bandwidth of 3 Hz and a taper number of 5, and then averaged across all trials. Coherence between different cortical regions was assessed by comparing the average coherence of all electrode sites located within each respective layer. Coherence values for a specific frequency band were reported as the average coherence within that frequency range across all animals within each group.

3.3.5 Electrochemical Impedance Spectroscopy

Electrochemical impedances were measured prior to each recording session. Mice were awake and head-fixed on a rotating platform while the implanted device was connected to an Autolab potentiostat along with a 16 channel multiplexer. Impedances were measured from each channel using a 10 mV RMS sine wave ranging from 10 Hz to 32 kHz. Impedances were reported as the average impedance at 1 kHz over all animals for each day unless otherwise noted.

3.3.6 Post-mortem Immunohistochemistry

Mice were intracardially perfused with 4% paraformaldehyde (PFA), post-fixed in 4% PFA for 18 hours and equilibrated in 30% sucrose at 4°C. Brains were frozen while embedding with optimum cutting temperature (OCT) media directly on the headpiece of the cryostat (Leica) and sectioned horizontally at 14 μm thickness starting from the convexity of the brain down to 800 μm below the cortex. Sections adhered to positively charged slides were permeabilized and blocked using 0.1% Triton-X with 10% normal goat serum in PBS at room temperature for 1 hour and incubated with primary antibodies to CC1 (1:100, Millipore, Burlington, Massachusetts USA, #OP80), Olig2 (1:200 Millipore, Burlington, Massachusetts USA, #Mabn50), NG2 (1:100, Millipore, Burlington, Massachusetts USA, #Ab5320), GFAP (1:1000 Abcam, Cambridge, Massachusetts USA, #Ab4674), Iba-1 (1:1000 Wako, Richmond, Virginia USA, #019–19741), MBP (1:500 Abcam, Cambridge, Massachusetts USA, #Ab40390), NeuN (1:200 Millipore, Burlington, Massachusetts USA, #MAB377), Neurofilament (NF-200) (1:200, Sigma-Aldrich, St. Louis, Missouri USA # N4142-.2ML), and phosphorylated NF-200 (SMI-31, Stenberger Monoclonals) overnight at 4°C. Alexa Fluor 488/594 conjugated secondary Ab (1:300 Jackson ImmunoResearch, West Grove, Pennsylvania USA # 115-585-003, # 111-605-003, #111-545-003), IgG2b isotope specific (1:300 anti-mouse 488 Jackson ImmunoResearch, West Grove, Pennsylvania USA #115-545-207) and 633 anti-chicken (1:300 Thermo Fisher Scientific, Waltham, Massachusetts #a21103) were reacted for 1 hr at RT. Sections were washed and allowed to dry overnight in the dark before mounting with Fluoromount-G and DAPI (SouthernBiotech, Birmingham, Alabama USA, #0100-20).

3.3.7 Imaging and Data Analysis

For cellular markers, 20x TIFF images were captured over the probe site and at an equivalent area in the contralateral hemisphere or baseline tissue with an Olympus (Center Valley, Pennsylvania USA) BX-51 epifluorescent microscope with MicroSuite software. Grey scale, individual layer images were cropped to square and loaded into using a previously published I.N.T.E.N.S.I.T.Y. MATLAB script where the binning was applied around the probe site (Z. J. Du et al., 2017; T. D. Kozai, Z. Gugel, et al., 2014). Three bins were applied 0-50 μm, 50-100 μm and 100-150 μm extending from the center of the probe site or image of non-implanted tissue. Labeled cells were counted per bin at 400-800 μm through the cortical depth per brain. For intensity analysis, images were acquired by collecting 20x z-stack fields with 9 steps (1 μm step size) using Nikon A1R Confocal microscope (Melville, NY USA) with NIS Elements software. The sum intensity projections (SUMIP) were processed through MATLAB by applying 10 μm bins up to 15 bins concentrically around the site of probe insertion, contralateral tissue, or baseline tissue in non-implanted mice. Data were expressed as the fold intensity change at the probe site over the intensity in the corresponding area in the contralateral hemisphere (T. D. Kozai, Z. Gugel, et al., 2014).

3.3.8 Statistics

Changes in recording metrics with respect to time were modeled using a linear mixed effects model, described previously (James R Eles et al., 2017). To fit the model to nonlinear relationships, a restricted cubic spline was implemented by placing 4 knots at the 5^{th}, 35^{th}, 65^{th}, and 95^{th} percentiles of the data. Group (cuprizone versus control) and group-by-time interactions

were included as fixed effects. A likelihood ratio test was performed on the estimated model. Confidence intervals were determined using a bootstrapping method with 1000 iterations. A 95% confidence interval was taken as 1.96 times the standard error of the model output. For histological analysis, a two-way ANOVA ($p < 0.05$) was used to determine significant differences in tissue stains between cuprizone-treated and control mice. Pairwise significances were determined using a *post hoc t-test followed by a* Bonferroni correction, to reduce the probability of type I error when performing multiple comparisons.

3.4 Results

3.4.1 Cuprizone Administration Induces Oligodendrocyte Loss and Demyelination Within the Mouse Cortex

For safety reasons, cuprizone could only be administered consecutively for 12 weeks (Hoffmann et al., 2008). Therefore, C57BL/6J mice (n = 8) were pre-treated with cuprizone for 5 weeks to deplete oligodendrocytes and myelin within the visual cortex prior to electrode insertion while longitudinal electrophysiological recordings were carried out during the last 7 weeks of cuprizone administration- (Figure 3-1a). To determine the extent of oligodendrocyte loss and demyelination at the time of implantation, cortical tissue was examined in experimental mice following 5 weeks of cuprizone treatment (n = 3) as well as age-matched mice on control diet (n = 3) without electrode implantation to confirm success of the cuprizone depletion model. The CC1 marker was used to measure the survival of mature oligodendrocytes after cuprizone administration. At five weeks following cuprizone exposure, mice demonstrated significant

reductions in CC1+ oligodendrocyte density (~85-90%) within the visual cortex (Figure 3-1b). Similarly, MBP, a marker used to stain myelin fibers, showed significant decreases in MBP+ fluorescence intensity (~65-70%) compared to control mice (Figure 3-1c). Staining for the NG2+ oligodendrocyte precursor population demonstrated a slight, yet not significantly different, elevation in NG2 glial densities (Figure 3-1d). This reported increase in NG2+ glial density following cuprizone administration is expected after five weeks of treatment alongside a reduced oligodendrocyte population, since NG2 glia proliferate in an attempt to repopulate lost oligodendrocyte densities. Since glial cell activation is associated with cuprizone-induced oligodendrocyte and myelin loss (Gudi et al., 2014; Xing et al., 2018b), mice were also examined for microglia and astrocyte density within the cortex following 5 weeks of cuprizone administration. Cuprizone-treated mice demonstrated comparable Iba-1+ fluorescence intensities relative to control animals, indicating no activation of microglia cells following cuprizone treatment (Figure 3-1e). However, cuprizone-treated mice did exhibit a slight increase in GFAP+ staining intensity, indicating partial activation of astrocyte cells following cuprizone toxicity, although there were no significantly reported differences in the GFAP+ fluorescence intensities between cuprizone-treated and control groups (Figure 3-1f). Overall, cuprizone demonstrated effective depletion of oligodendrocytes and myelin with little influence on glial activation within the cortex by 5 weeks of diet administration.

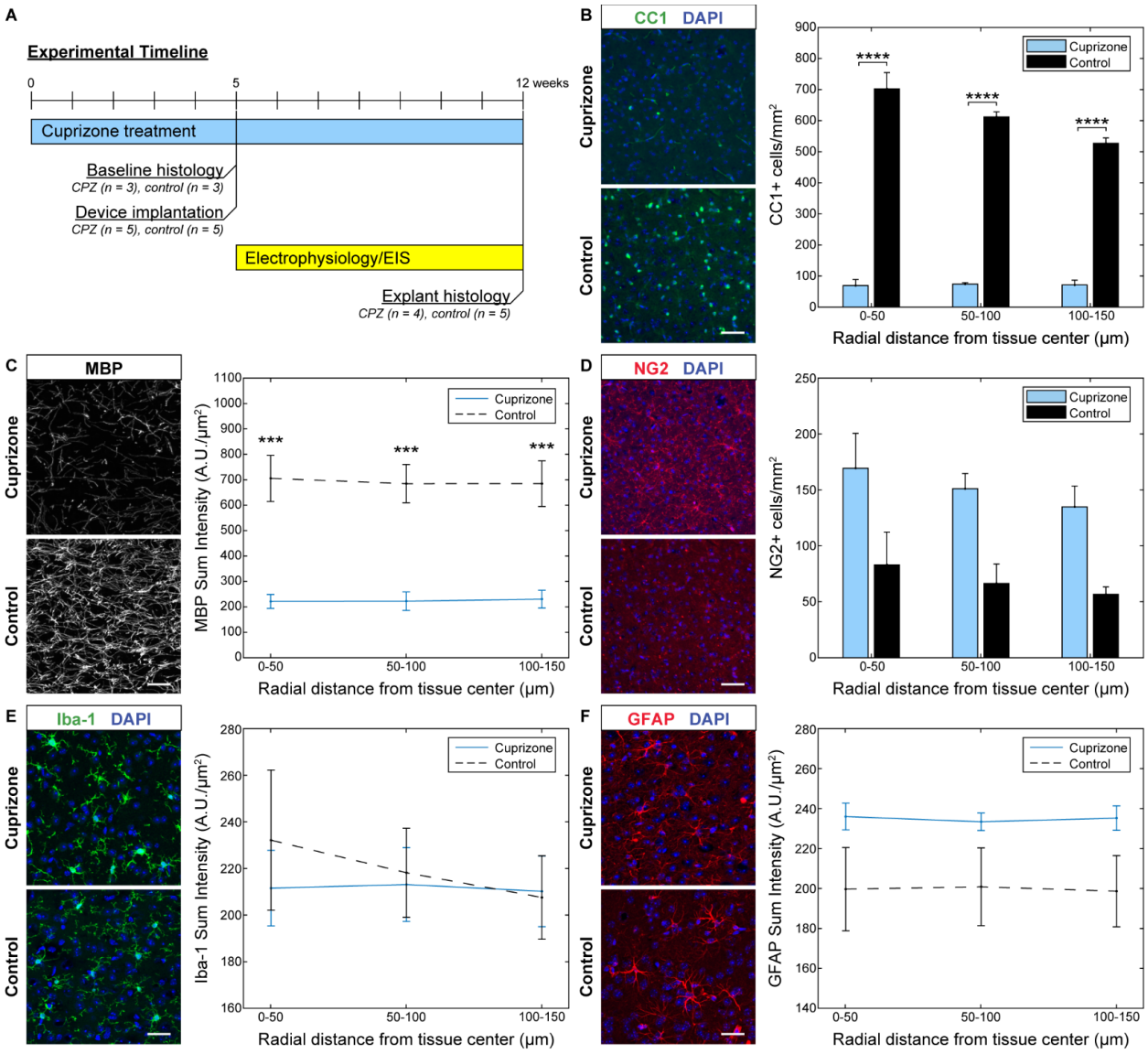

Figure 3-1 Depletion of oligodendrocytes and demyelination in the visual cortex at 5 weeks following cuprizone administration without electrode implantation. (a) Experimental timeline of cuprizone administration, device implantation, electrophysiological and impedance recording, and pre- and post-implant histology. (b) CC1+ staining reveals marked reduction in oligodendrocyte density in the visual cortex following 5 weeks of cuprizone administration. (c) MBP+ stain demonstrates reduced myelin fluorescence intensity in the visual cortex following 5 weeks of cuprizone treatment. (d) Staining for NG2+ cells shows elevated oligodendrocyte precursor cell density following 5 weeks of cuprizone administration. (e) Iba-1+ staining demonstrates relatively comparable microglia fluorescence intensities between cuprizone-treated and control mice. (f) GFAP+ astrocyte staining similarly shows comparable fluorescence intensities between cuprizone-treated and control mice. Scale bars = 50 μm. *** indicates $p < 0.001$. **** indicates $p < 0.0001$.

3.4.2 Electrode Implantation and Neural Recording Setup

Five weeks of continuous cuprizone administration can induce near-complete depletion of oligodendrocytes and myelin within the visual cortex. To test whether oligodendrocyte and myelin depletion impairs neuronal electrophysiology, cuprizone-treated mice (n =5) and mice on normal rodent diet (n = 5) were implanted with a 16 channel single-shank Michigan-style microelectrode array (50 μm site spacing) to a depth of 800 μm below the visual cortex. For electrophysiological data acquisition, mice were head-fixed on a rotating platform inside a grounded, electrically-isolated Faraday cage for awake recording (Figure 3-2a,b). The cage was enclosed in a blackout curtain to record spontaneous visual activity in a dark environment. To record visually-evoked activity, mice were positioned in front of an LED screen displaying a drifting bar gradient. Electrophysiological signals were passed through a biological amplifier before being collected by an external recording system for further signal processing. Raw data streams were passed through a high-frequency filter to isolate neuronal spiking events, which were aligned to the onset of visual stimulation (Figure 3-2c). Spike sorting was performed using principal component analysis to isolate distinct recorded signals and assign them to individual clusters (Figure 3-2d). For each recording session, waveforms on each channel were aligned to the onset of visual stimulation or to pseudotriggers assigned to spontaneously recorded data for single-unit and multi-unit classification (Figure 3-2e,f). Authentic neuronal units were confirmed based on average waveform shape and stimulus-evoked firing properties (Figure 3-2g,h).

Current source density (CSD) plots were generated to identify the position of cortical layer IV along the depth of the implanted microelectrode shank following visual stimulus presentation (Figure 3-2i). Electrical activity was evoked at the onset of visual stimulation (‘stim on’), causing neurons to depolarize (current sink) within the input layer (layer IV) of the visual cortex. This

appears as a negative deflection in LFP polarity within CSD plots. Layer IV depth can also be confirmed by the temporally delayed activity in cortical layer II/III above and layer V below. For drift analysis, the depth of layer IV on the day of surgery was defined as the starting point (0 μm) to compare subsequent changes in electrode drift between groups. Cuprizone-treated mice experienced a gradual decrease in layer IV depth along the microelectrode array for the first two weeks post-insertion before remaining stable throughout the remainder of device implantation (Figure 3-2j). In contrast, mice on control diet demonstrated an upward shift in layer IV position along the microelectrode array for the first two weeks before stabilizing until experimental end-point. Analysis of the magnitude change in depth demonstrated that most of the drift in layer IV position occurred within the first two weeks post-insertion (Figure 3-2k). These patterns in layer IV drift are similarly supported by previously published results (T. D. Kozai, X. Li, et al., 2014). An electrode site spacing of 50 μm and an average change in layer IV depth of only ~30-50 μm beyond the first two weeks of implantation indicates the implanted microelectrode experienced minimal drift within the range of 1 electrode site throughout the duration of implantation. As a result, we employed a robust and reproducible model of oligodendrocyte and myelin depletion around chronically implanted microelectrode arrays to study the electrophysiological properties of neurons within the demyelinated cortex.

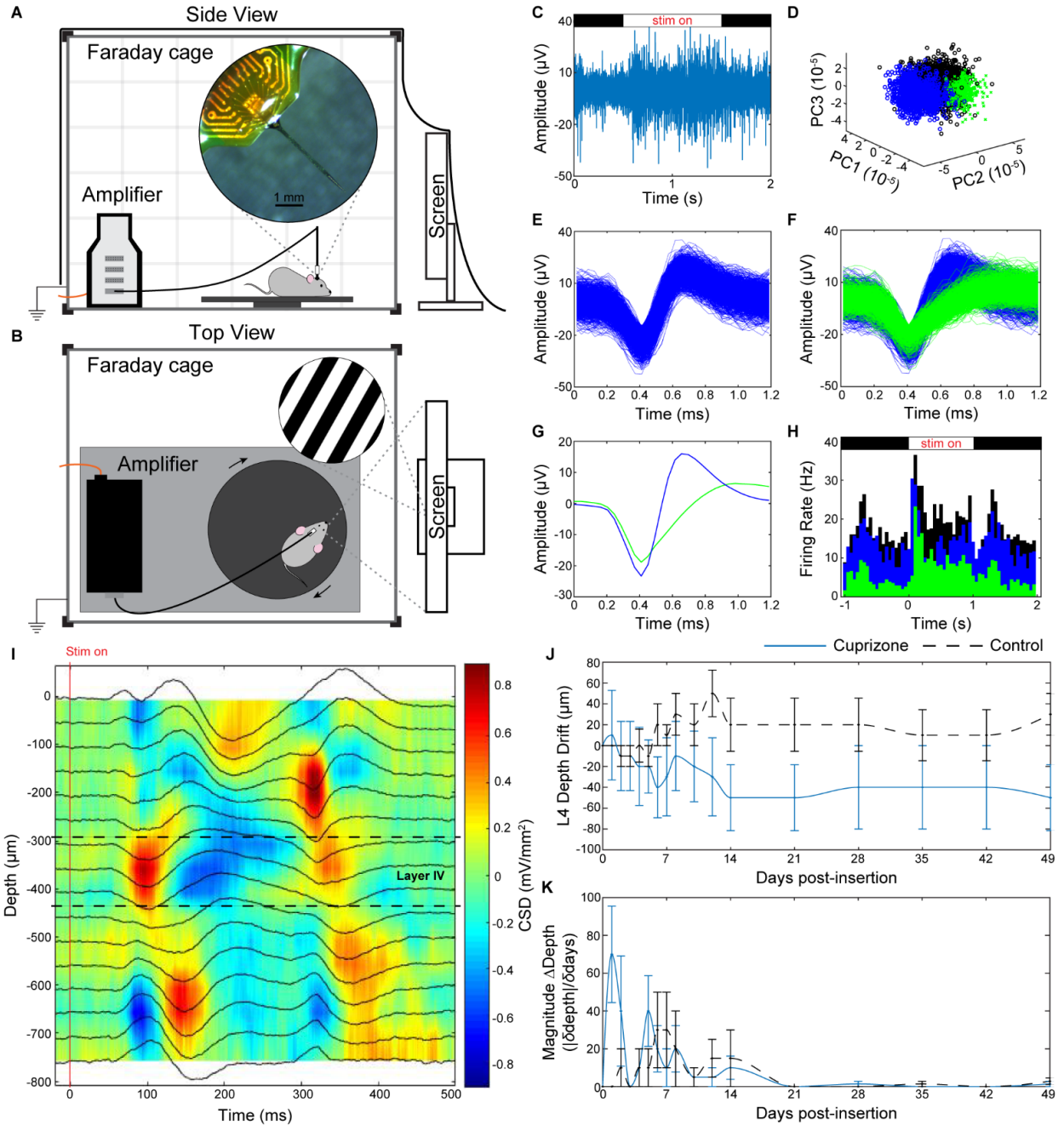

Figure 3-2 Device implantation and electrophysiological recording setup. (a) Side view and (b) top view of electrophysiological recording setup in an electrically-isolated Faraday cage. Implanted mice were head-fixed using a stand (*not shown)* magnetically attached to a base plate on a movable platform for awake recording. An LED monitor displaying drifting bar gradients was used for visual stimulation. Recorded signals were filtered through a biological amplifier before transmission to an external recording system via a non-conductive fiber optic cable (*orange wire).* (c-h) Representative examples of one electrode channel in control mice demonstrating (c) stimulus-evoked raw spiking data, (d) unit sorting using principal component analysis, pile plot of (e) single-unit and (f) multi-unit activity, (g) average waveforms, and (h) evoked firing rate activity. (i) Representative current source density plot demonstrating 500 ms of electrical current activity versus electrode implant depth following visual stimulus presentation ('stim on') in the visual cortex used to identify layer IV depth (sink = red, source = blue). (j) Average drift of layer IV depth along

implanted microelectrode shank compared to day 0 of device insertion between cuprizone (blue solid) and control (black dashed) mice. (k) Magnitude change in depth over change in time demonstrating most fluctuations in layer IV depth occur with the first two weeks before stabilizing.

3.4.3 Cuprizone-induced Oligodendrocyte Loss and Demyelination Impairs Neuronal Single-unit Activity at the Onset of Device Implantation

The use of microscale recording arrays with high spatial and temporal resolution allowed observation of how oligodendrocyte loss and demyelination influences the electrophysiological characteristics of individual neurons. Due to the dense distribution of oligodendrocytes and myelin fibers, particularly within cortical input (layer IV) and output layers (layer V) (Rowley et al., 2015), cuprizone-induced oligodendrocyte depletion and demyelination was expected to significantly alter the health and strength of detectable neural signals within the visual cortex. To demonstrate the impact of oligodendrocyte loss and demyelination on electrophysiological recording quality, comparison of recording metrics was first examined independent of cortical depth by averaging across all 16 microelectrode channels. Due to the residual effects of anesthesia, specifically the influence of ketamine/xylazine on evoked activity within the visual cortex on the day of surgery (Nicholas J. Michelson & Kozai, 2018), acute recording metrics were evaluated with respect to data collected on day 1 post-implantation. One day after electrode insertion following 5 weeks of cuprizone administration, oligodendrocyte-depleted mice demonstrated a significant reduction of nearly 36% in electrode yield compared to mice on normal diets (cuprizone: 40 ± 5%, control: 62.5 ± 8.6%, Figure 3-3a). By 7 weeks post-insertion, SU yield of cuprizone mice was reduced to 30 ± 9.1%. Control mice, however, experienced a greater and more pronounced decline in yield over time, reducing to 42.5 ± 4.1% and demonstrating no significant differences in yield compared to cuprizone-treated animals by 7 weeks post-insertion. Similar

patterns of significant difference between cuprizone-treated and control mice were reported for SNR (Figure 3-3b). Average SNR on day 1 following implantation was significantly reduced by nearly 52% in cuprizone-treated animals compared to control mice (cuprizone: 1.3 ± 0.62, control: 2.7 ± 0.44). Over time, SNR in control mice gradually declined to the level of cuprizone-treated animals (cuprizone: 1.75 ± 0.6, control: 1.75 ± 0.29). Evaluation of only active electrode sites (channels which detected SU activity) revealed no significant differences in SNR between cuprizone-treated and control mice over time, although cuprizone-treated animals demonstrated overall reduced values of SNR (Figure 3-3c). The average amplitude of cuprizone-treated mice on day 1 post-insertion was 7.5 ± 1.1 μV compared to 14.3 ± 1.4 μV in control mice (Figure 3-3d). Over the course of the subsequent 4 weeks, signal amplitude in control mice remained elevated before declining to the level of cuprizone-treated mice by 7 weeks post-insertion (cuprizone: 8.8 ± 2.8 μV, control: 10.6 ± 2.0 μV). Similarly, cuprizone-treated mice demonstrated reduced amplitudes of the noise floor compared to control mice on day 1 post-insertion (Figure 3-3e, cuprizone: 1.69 ± 2.1 μV, control: 3.4 ± 4.6 μV). Control mice maintained elevated noise amplitudes until declining to the level of cuprizone-treated animals by 7 weeks post-insertion (cuprizone: 1.93 ± 5.8 μV, control: 2.5 ± 5.3 μV). Device impedances in cuprizone-treated animals were reduced significantly compared to control mice for the first week post-insertion, slightly fluctuating until 14 days post-insertion, and then stabilized after 3 weeks (Figure 3-3f).

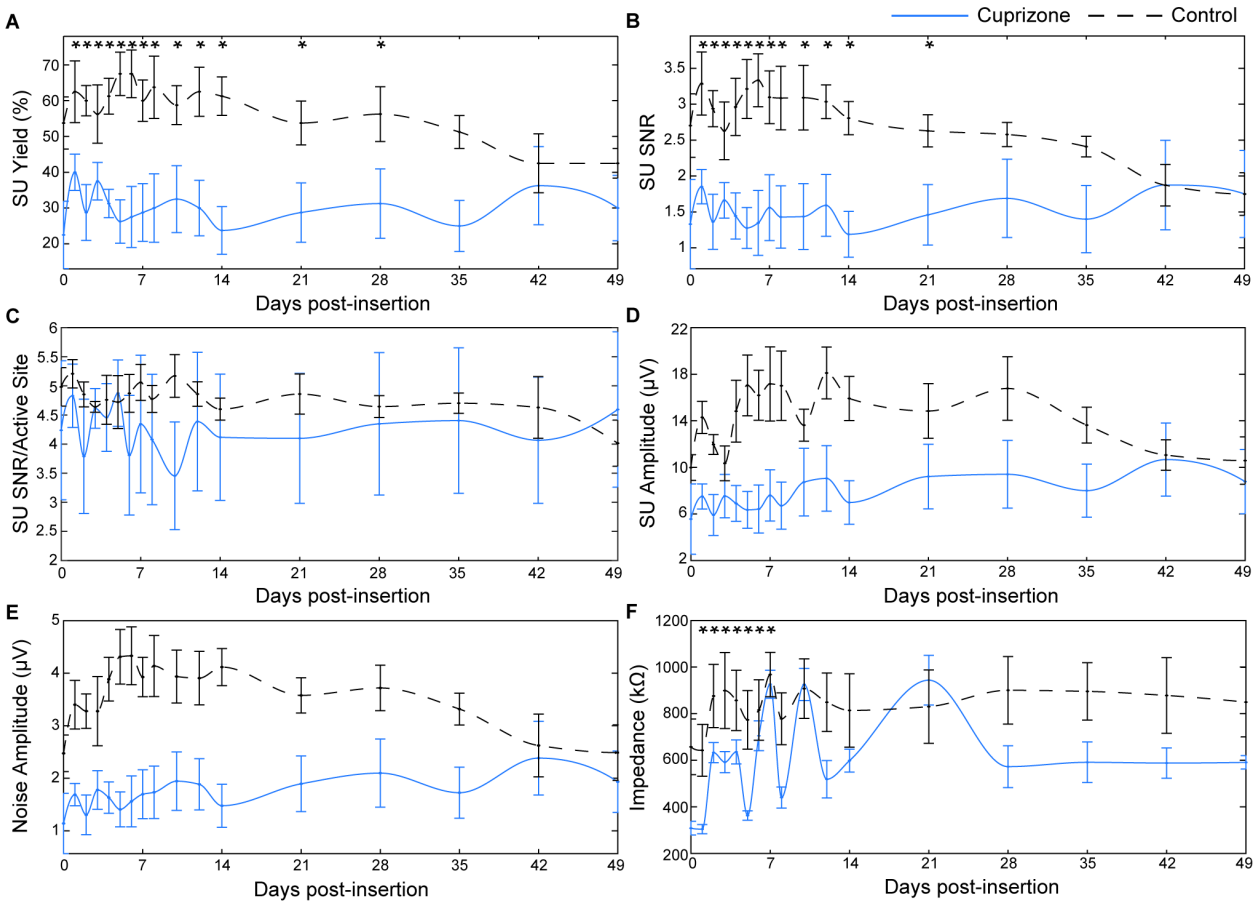

Figure 3-3 Cuprizone-induced oligodendrocyte loss and demyelination reduces electrode recording performance over time. Chronic electrophysiological metrics over time between cuprizone-treated (blue solid) and control mice (black dashed). a) Single-unit yield over time. b) Single-unit SNR (mean peak-peak amplitude over 2*STD of noise floor). c) SNR per electrode channel detecting a single unit (active site). d) Single-unit amplitude over time. e) Amplitude of noise floor over time. f) Average impedance reported at 1 kHz over time. * indicates non-overlapping 95% confidence intervals at each time point as determined by likelihood ratio test applied to a linear mixed effects model for cuprizone-treated and control mice.

Reduction of single-unit recording metrics in cuprizone-treated mice compared to mice on control diets was also observed in a depth-dependent manner (Figure 3-4a,b,c,d). Animals at each time point were aligned to their average layer IV depth, determined from their CSD analysis. Recording performance within different cortical depths along the electrode shank as well as over time post-insertion were demonstrated in the form of averaged heat maps. Smoothing was applied to easily visualize gradual changes in recorded metrics over time and depth. Cuprizone-treated animals demonstrated visually apparent reductions in electrode recording yield compared to control mice specifically in cortical layers II/III, IV, and V (Figure 3-4a). Control mice

demonstrated a reduction in yield over time, most notably decreasing in cortical layer II/III by 6 and 7 weeks post-insertion. Average SNR was reduced in cuprizone-treated mice vs. control mice within layer II/III, IV, and V, demonstrating the most loss in SNR values within layer II/III and IV (Figure 3-4b). Furthermore, amplitudes were most visibly reduced in layer II/III and IV following cuprizone-administration compared to control mice (Figure 3-4c). Single-unit amplitudes in control mice were particularly reduced in cortical layer IV after 4 weeks post-insertion. Finally, cuprizone-treated mice demonstrated reduced noise amplitudes within each cortical layer (II/III, IV, and V) compared to control mice (Figure 3-4d). Control mice demonstrated a decline in noise amplitude in all cortical layers after 5-6 weeks post-insertion. Collectively, the results indicate that a deficiency in oligodendrocyte function and myelination within the cortex can alter the detectability and recording strength of individual neurons around implanted microelectrode arrays.

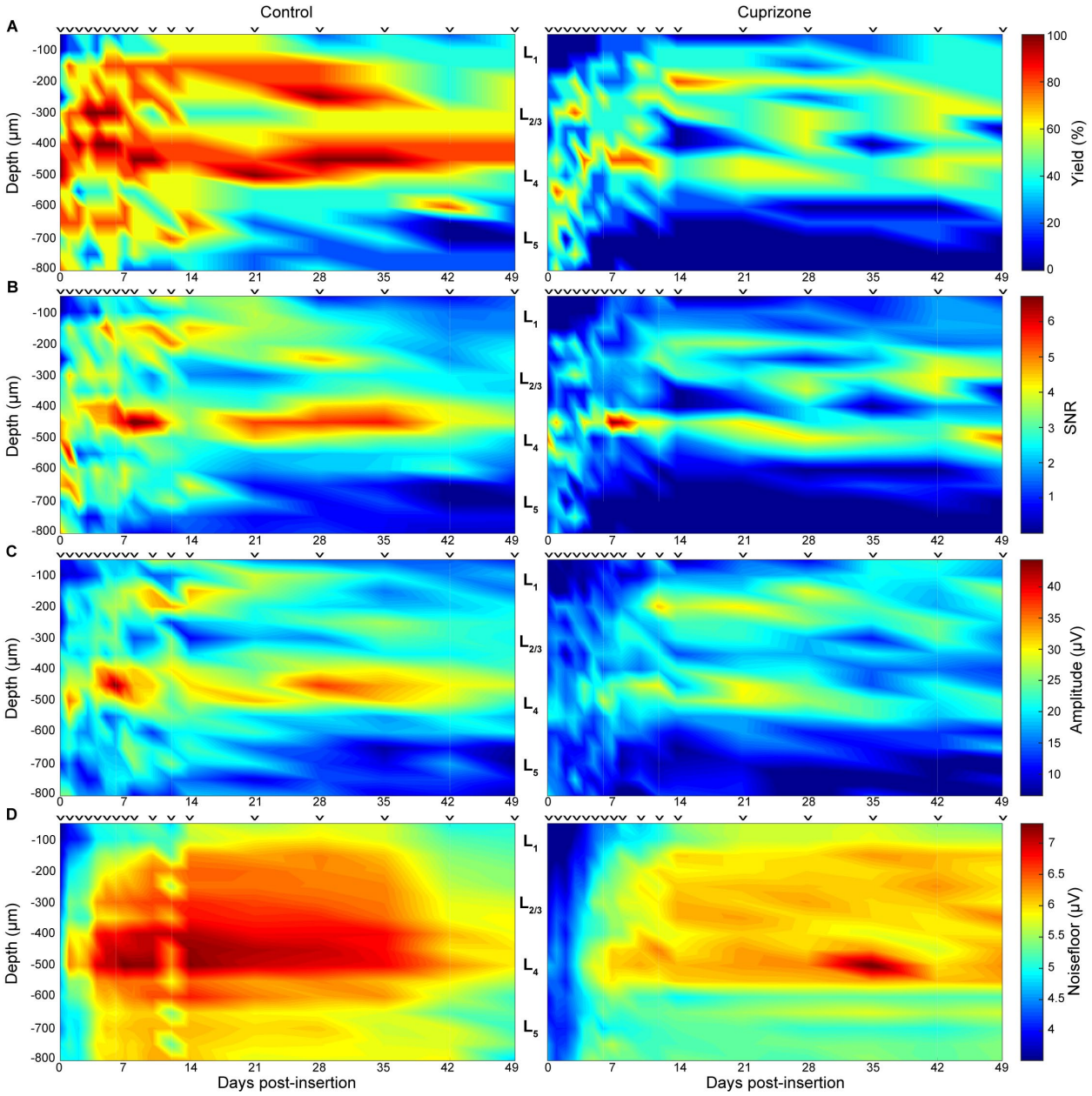

Figure 3-4 Cuprizone administration reduces recording performance metrics in a depth-dependent manner. Recording performance metrics between cuprizone-treated and control mice demonstrated as a function of depth and time. ▼ indicate discrete sampling time points. a) Recording yield. b) SNR. c) Peak-to-peak amplitude. d) Noise amplitude.

3.4.4 Cuprizone Administration Reduces Spontaneous and Evoked Neuronal Firing Rate

After demonstrating that oligodendrocyte and myelin depletion impairs single-unit recordings, we asked whether cuprizone administration would affect the functional multiunit firing

properties of local neuronal populations within the visual cortex. Given the dual purpose of myelin as electrical insulation for fast propagation of action potentials as well as being a conduit for metabolic and neurotrophic support to satisfy energetic demands of neurons, cuprizone-induced demyelination was expected to reduce overall neuronal firing rates within the vicinity of microelectrode arrays. Multi-unit activity was compared between cuprizone-treated and control mice by evaluating all threshold-crossing events (non-sorted spiking activity) that occurred during resting-state and evoked recording sessions. Average firing rate was defined as the number of threshold-crossing events that occurred within a 1 second period after each visual stimulus trial (or 1 second after each pseudotrigger assigned to spontaneous activity). As expected, neuronal firing rate was increased following visually evoked stimulation compared to spontaneous (resting-state) activity in both cuprizone-treated and control mice (Figure 3-5a,b). However, cuprizone administration effectively reduced firing rate compared to control mice under both spontaneous and visually-evoked recording conditions, albeit not significantly. Neuronal firing rate during resting-state activity was highest on day 1 post-insertion for both cuprizone (12.1 ± 0.6 spikes/s) and control mice (13.9 ± 0.7). By 7 weeks post-insertion, spontaneous firing rate decreased in both groups (cuprizone: 9.5 ± 0.9 spikes/s, control: 9.81 0.8 spikes/s). Similarly, firing rate was highest during visually-evoked stimulation on day 1 post-insertion for cuprizone-treated mice (17.4 ± 1.6 spikes/s) and control mice (18.5 ± 1.0 spikes/s) before firing rate in both groups gradually declined by 7 weeks post-insertion (cuprizone: 12.9 ± 1.3 spikes/s, control: 13.9 ± 1.4 spikes/s). Changes in neuronal firing rate for cuprizone-treated and control mice were also observed in a depth-dependent manner (Figure 3-5c,d). Reductions in firing rate over time during resting-state and visually-evoked activity for both cohorts occurred predominantly in cortical layer II/III, matching depth-dependent patterns of single-unit recording. Interestingly, evoked firing rate for both groups

increased within layer II/III following 2 weeks post-insertion. Together, these findings establish that oligodendrocytes and myelin modulate the firing properties of neuronal networks during resting-state and evoked cortical activity.

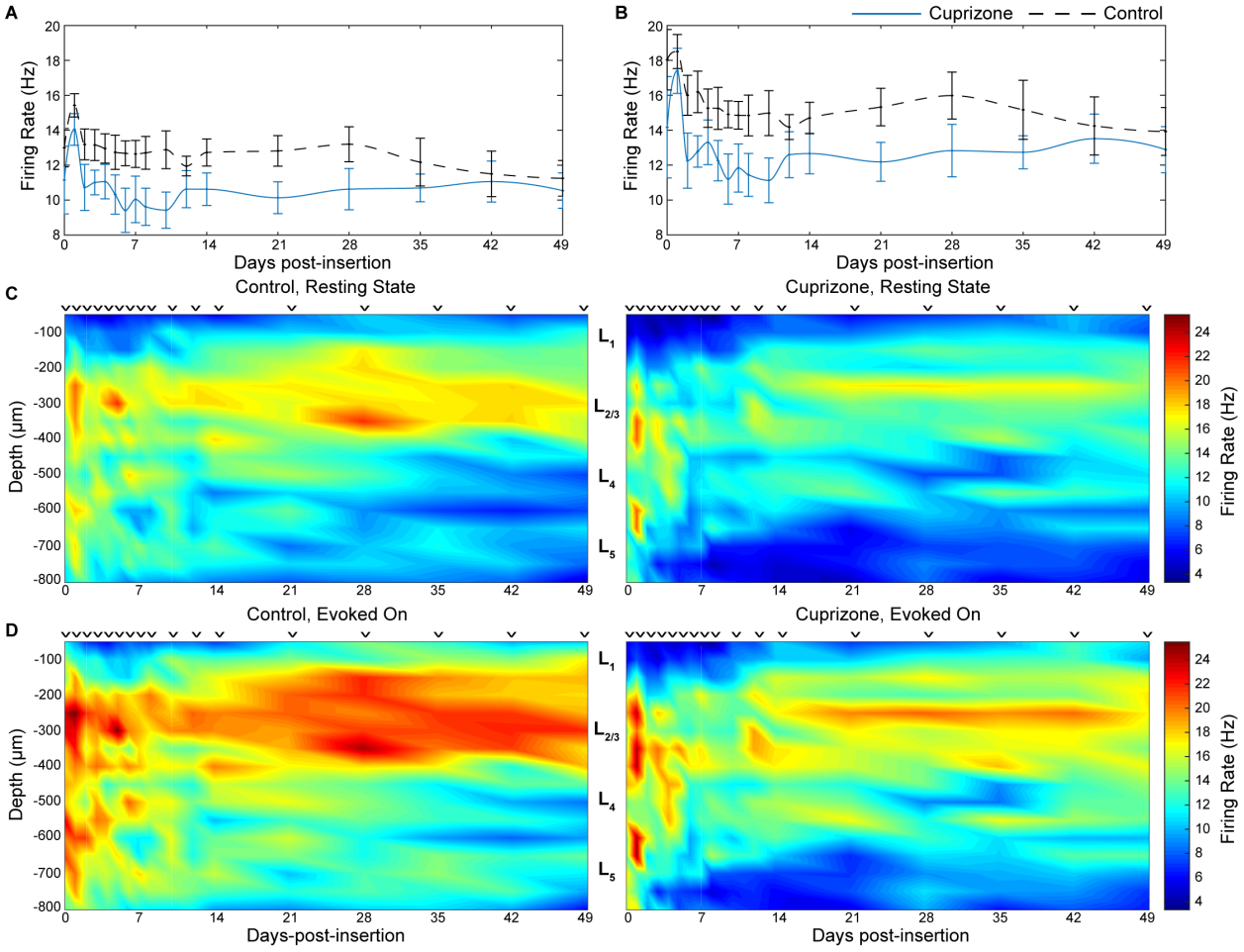

Figure 3-5 Oligodendrocyte loss reduces neuronal firing rate over time and depth around chronically implanted microelectrode arrays. Average neuronal firing rate during resting-state (a) and visually-evoked (b) activity between cuprizone-treated and control mice over time. Firing rate between cuprizone-treated and control mice demonstrated as a function of depth and time during resting-state (c) and visually evoked (d) activity. ᵛ indicate discrete sampling time points.

3.4.5 Cuprizone-induced Oligodendrocyte Loss and Demyelination Reduces Multi-unit Activity in a Latency-dependent Manner

Multi-unit activity was evaluated further to determine how oligodendrocytes and myelin, whose function is to regulate conduction velocities of neuronal signals, affect electrophysiological latency following evoked visual stimulation within the cortex. Contribution of oligodendrocytes and myelin on evoked neuronal population responses were further evaluated by observing dynamic changes in multi-unit activity (MUA) following implantation. Multi-unit yield and SNFRR were metrics generated by comparing spike counts before and after visual stimulation, whose responses can differ based on parameters such as bin duration and temporal latency from stimulation onset (Nicholas J. Michelson & Kozai, 2018). Therefore, a range of bin sizes and latencies post-stimulation were evaluated to observe patterns in MUA responses between cuprizone-treated and control mice over time (Figure 3-6a). Bin sizes and latencies varied from 1 ms to 1000 ms with a temporal bin resolution of 1 ms, generating heat maps that highlight hotspots of MU yield and SNFRR for certain durations of bin size and latency (Figure 3-6b). Naturally, bin sizes and latencies less than 50 ms produced low or virtually no evoked responses in MUA due to the time required for evoked responses to be recognized by the recording electrode within the visual cortex (Figure 3-2i). Most dynamic changes occurred within a bin size duration up to 200 ms and latencies up to 800 ms, which were further observed as the difference in MU yield and SNFRR between cuprizone-treated and control mice over time (Figure 3-6c,d). On the day of surgery, control mice demonstrated greater MU yield and SNFRR compared to cuprizone-treated mice for all bin durations and latencies. Interestingly, cuprizone-treated mice exhibited higher MU yield and SNFRR compared to control mice on day 1 post-implantation. Beyond this first day after device insertion, MU yield and SNFRR were elevated in mice on control diets for latencies greater than

200 ms. Note that most significant differences in MU yield and SNFRR were observed only when values were higher in control mice and when latencies were greater than ~400 ms. Significant differences that did occur in cuprizone-treated animals generally occurred less than ~400 ms after stimulus presentation. In line with aforementioned trends in single-unit activity and firing rate, control mice demonstrated virtually no significant differences in MU yield or SNFRR compared to cuprizone-treated mice at 6 and 7 weeks post-insertion, indicating a reduction in evoked MUA of control mice over time. To summarize, loss of cortical oligodendrocytes and myelin following cuprizone administration impaired evoked multi-unit activity with increasing latency post-stimulation, a difference which deteriorated in mice fed on control diets over time.

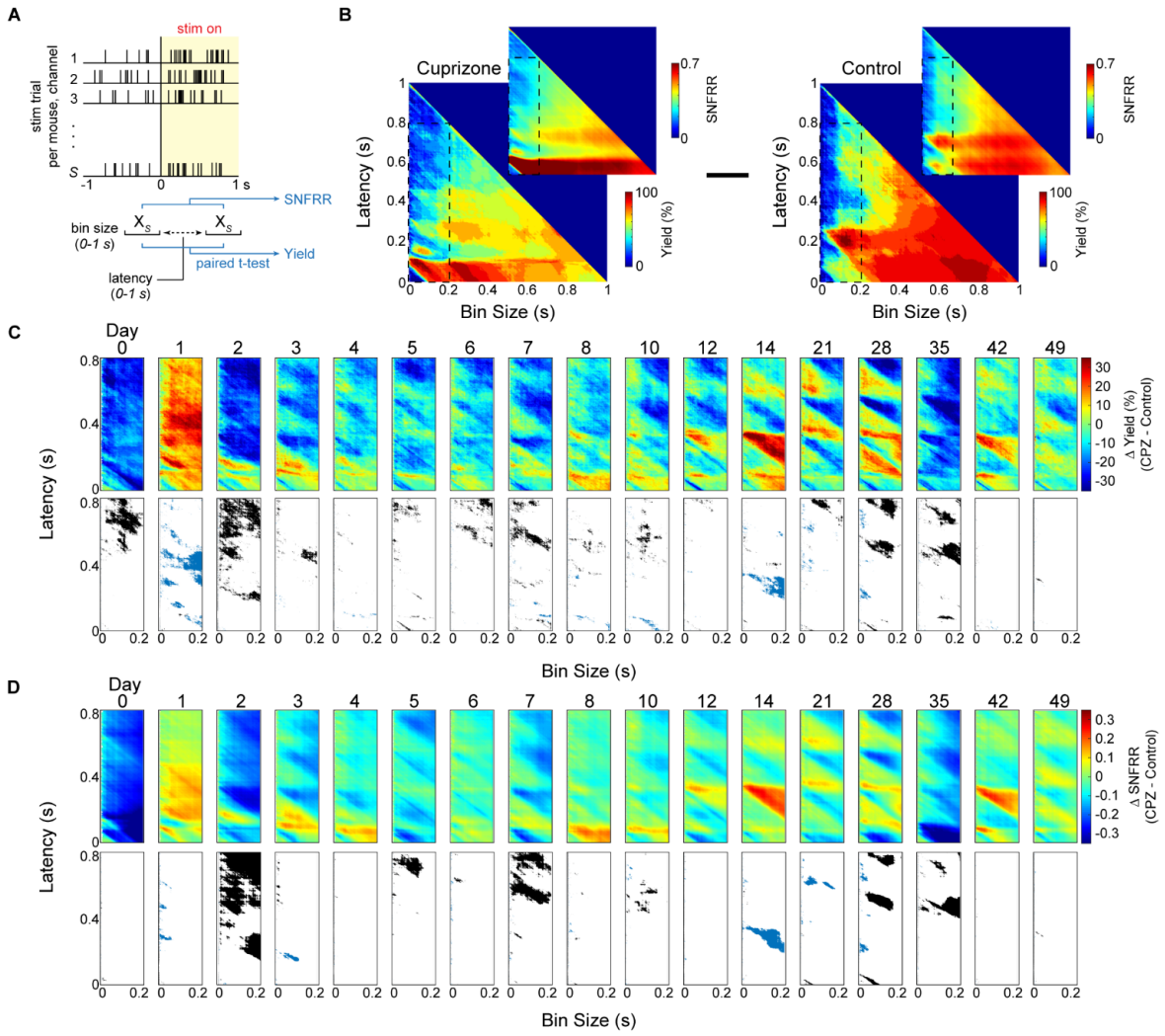

Figure 3-6 Oligodendrocyte depletion and demyelination following cuprizone administration impairs multi-unit recording activity. (a) Diagram demonstrating how dynamic changes in multi-unit yield and SNFRR during evoked electrophysiological recordings were measured. Spike counts, XS, were collected within a temporal bin size and latency ranging from 0 to 1 s following stimulus presentation and compared to counts within the same bin size before stimulus presentation using a paired t-test. MU yield was calculated as the percentage of electrode channels (out of 16 sites) that had a significantly different spike count for a given bin size and latency after stimulus presentation compared with the same bin size before stimulus presentation. MU SNFRR was calculated as the difference in average spike counts relative to the standard deviation in spike counts before and after stimulus presentation. (b) Representative plots of MU yield and SNFRR taken at varying bin sizes and latency between 0 and 1 s at 1 ms increments in cuprizone-treated and control mice. MU yield and SNFRR plots within a window of 200 ms bin size and 800 ms latency (inset) were averaged within each group and control data was subtracted from cuprizone mice to produce (c) and (d). (c-d) Difference in MU yield or SNFRR between cuprizone-treated and control mice over time (top panel). A paired t-test ($p < 0.05$) was performed at each bin size and latency between cuprizone-treated and control mice. Significant differences where yield or SNFRR was greater in control mice are reported in black, where yield or SNFRR was greater in cuprizone mice are reported in blue, and no significant difference between the two groups are reported in white (bottom panel).

3.4.6 Cuprizone-induced Oligodendrocyte Loss and Demyelination Alters Evoked Oscillatory Activity Within the Visual Cortex

The previous findings demonstrated that oligodendrocyte and myelin depletion alters electrophysiological properties within local neuronal populations. Knowing that oligodendrocytes and myelin regulate neuronal activity in a time-dependent manner, we then asked how the frequency-dependent oscillations in neuronal signaling are influenced by cuprizone administration. The contribution of oligodendrocytes and myelin on evoked oscillatory neuronal activity within the cortex was evaluated by performing power spectral analysis. Power was calculated by taking the base 10 logarithm of recorded local field potentials. Evoked power was normalized by subtracting spontaneous power across a frequency range of 0.5 to 125 Hz (Figure 3-7a,b). While both cuprizone-treated and control mice experienced similar evoked power across frequencies, cuprizone-treated mice demonstrated greater fluctuations in power within the first two weeks post-insertion across the entire frequency spectrum (Figure 3-7c). Furthermore, while power did not change in a depth-dependent manner between cuprizone-treated and control mice over time, similar fluctuations in evoked power over the first two weeks were observed in cuprizone-treated mice. Conversely, evoked power in control mice remained relatively stable except for slight increases in power at 1 and 6 weeks post-insertion (Figure 3-7d). These fluctuations in LFP activity were further reflected by averaging evoked power over the entire frequency range between cuprizone-treated and control mice (Figure 3-7e). Additionally, cuprizone-treated mice demonstrated a reduced peak in evoked power within the first week of insertion compared to control mice before gradually increasing and stabilizing over time (Figure 3-7f). Finally, evoked power was evaluated at distinct frequency ranges between cuprizone-treated and control mice over time (Figure 3-7g). Cuprizone-treated mice demonstrated reduced power within delta (2-4 Hz),

theta (5-7 Hz), and alpha (8-14 Hz) frequency bands compared to control animals. Alternatively, cuprizone-treated mice exhibited an increase in power in gamma (30-90 Hz) and high frequency bands (>90 Hz). At all frequency bands, cuprizone-treated mice demonstrated high fluctuations in evoked power compared to control mice, which remained relatively stable over time. Together, these results indicate that cuprizone-induced oligodendrocyte loss and demyelination alters evoked oscillatory activity in a frequency-dependent manner within the mouse visual cortex.

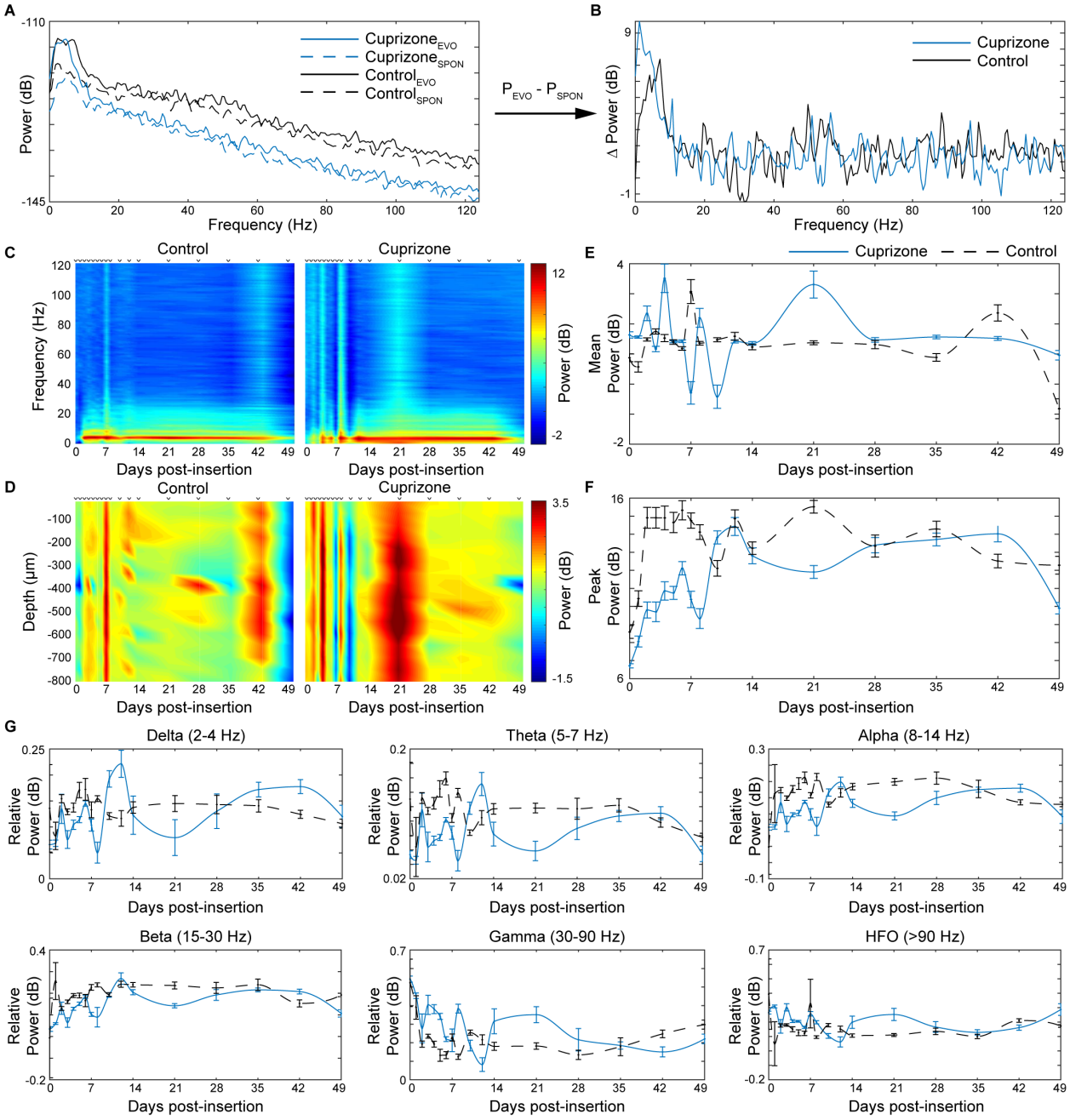

Figure 3-7 Cuprizone-induced oligodendrocyte loss and demyelination reduces evoked power in a frequency-dependent manner. (a) Representative power spectra of one mouse from each group (cuprizone-treated, blue; control, black) taken at the same electrode site in layer IV demonstrating evoked (solid) and spontaneous (dashed) power over frequency. (b) Normalized power spectrum taken by subtracting the spontaneous power from evoked power. (c) Heat maps of average evoked power as a function of frequency and time between cuprizone-treated and control animals. (d) Heat maps of average evoked power as a function of depth along microelectrode array and time between cuprizone-treated and control animals. (e) Cuprizone-administration induces oscillations in mean power over entire frequency spectrum for first two weeks compared to control mice. (f) Cuprizone-administration reduces peaks power compared to control mice acutely during insertion. (g) Relative power within different frequency bands demonstrate differential outcomes following cuprizone administration. P_{EVO}: evoked power; P_{SPON}, spontaneous power.

3.4.7 Cuprizone-induced Oligodendrocyte Loss and Demyelination Alters Evoked Laminar Communication Within the Visual Cortex

Since the evoked oscillatory activity differed between wildtype and oligodendrocyte depleted mice, we next investigated the influence of oligodendrocytes and myelin on functional communication within and between cortical laminar circuits through coherence analysis. It is expected that the loss of myelin, a critical substance considered to facilitate information transmission of far-reaching projections, would have significant impacts on interlaminar, if not intralaminar, communication following cuprizone administration. Coherence, reported as a value between 0 and 1, was first normalized by subtracting spontaneous coherence from evoked coherence and then calculated for all 16 pairs of electrode channels, resulting in heat maps of evoked coherence values in a 16 x 16 site diagram (Figure 3-8a,b). The greatest difference in coherence between cuprizone-treated and control mice was observed at 8 days post-insertion. Therefore, this time point was compared alongside the experimental endpoint of 49 days post-insertion, which has demonstrated comparable performance between cuprizone-treated and control mice for all electrophysiological metrics observed so far. At 8 days post-insertion, cuprizone-treated mice demonstrated increases in evoked coherence within superficial (layer II/III) and deep layers (layer V/VI) as well as between granular-supragranular (G-SG: layer IV to layer II/III), granular-infragranular (G-IG: layer IV to layer V/VI), and supragranular-infragranular (SG-IG: layer II/III to layer V/VI) regions (Figure 3-8a). These responses in cuprizone-treated mice differed from control mice most within higher frequency beta (7-30 Hz) and gamma (30-90 Hz) bands. By day 49 post-insertion, previously coherent regions in cuprizone-treated mice were reduced,

demonstrating similar or reduced coherence heat maps compared to control mice (Figure 3-8b). These temporal trends in evoked coherence between cuprizone-treated and control mice are further reflected by observing interlaminar connectivity as a function of frequency. Cuprizone-treated mice demonstrated the greatest difference in coherence compared to control mice in G-IG and G-SG regions at 8 days post-insertion (Figure 3-8c). Due to a decrease in evoked coherence in cuprizone-treated mice by 49 days post-insertion, coherence between cuprizone-treated and control mice were virtually the same (Figure 3-8d). Finally, evaluating the coherence averaged between 7 and 90 Hz between laminar regions demonstrated a significant increase in coherence within G-SG regions over the first 4 weeks post-insertion between cuprizone-treated and control mice (Figure 3-8e). Furthermore, synchronicity between neuronal populations is an important property of functional resting-state activity. Therefore, we measured coherence between and within different cortical layers and demonstrated similar trends in coherence during resting-state in cuprizone-treated mice (Figure 3-9). This analysis indicates that the loss in function of oligodendrocyte and myelin compromises functional communication during resting-state and evoked activity within and between laminar structures of the visual cortex.

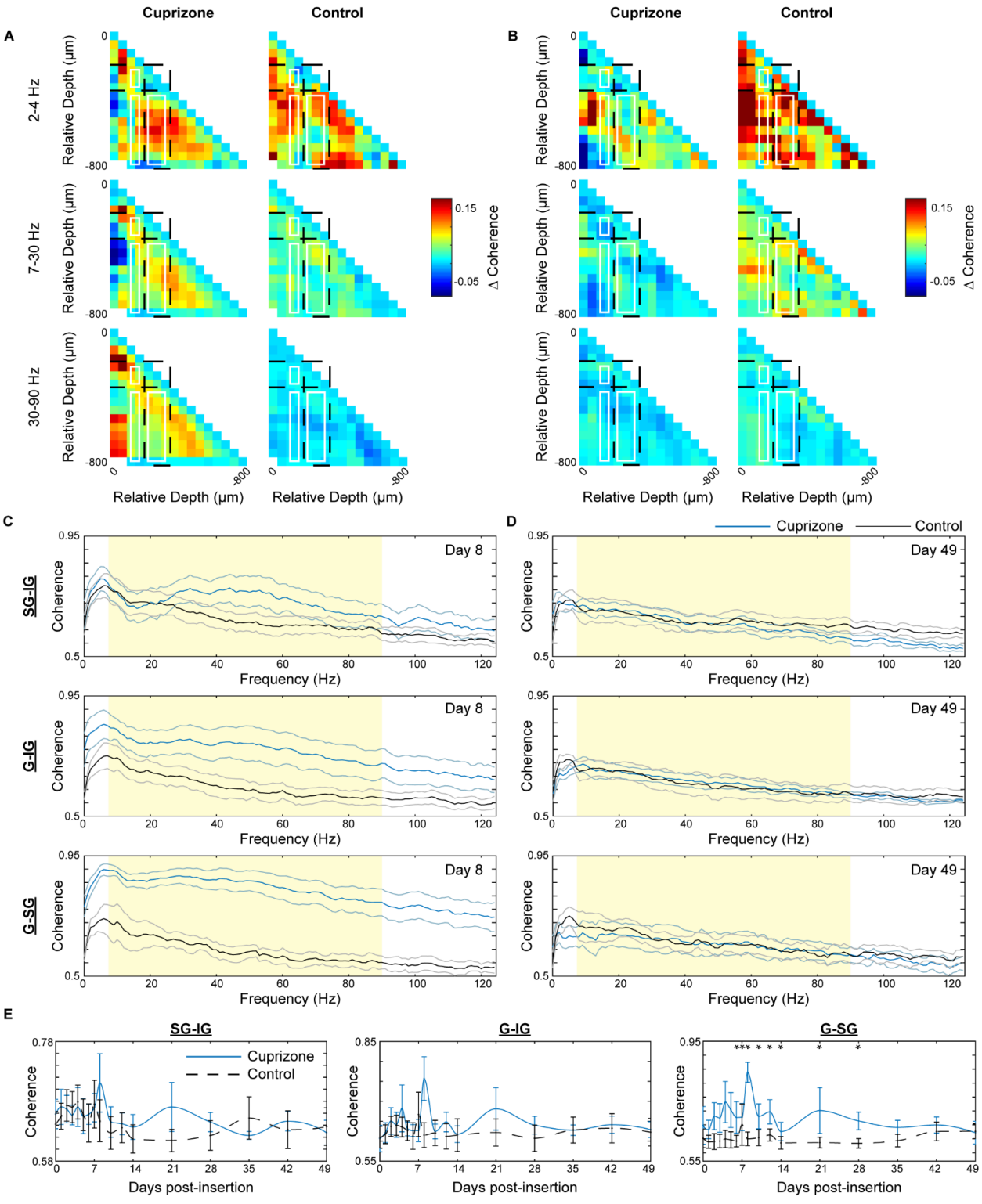

Figure 3-8 Oligodendrocyte depletion and demyelination increases visually-evoked coherence within and between different cortical layers. Normalized pairwise coherence, taken as the difference in coherence during visually-evoked and spontaneous activity, between cuprizone-treated and control animals at day 8 (a) and day 49 (b) post-insertion. Missing coherence values in (a) are an indication of lost information following electrode depth adjustment to layer IV. Evoked coherence between supragranular-infragranular (SG-IG), granular-infragranular (G-

IG), and granular-supragranular (G-SG) regions over frequency between cuprizone-treated and control mice at day 8 (c) and day 49 (d) post-insertion. (e) Mean coherence between 7 and 90 Hz (shaded region of c and d), averaged across animals in each group. * indicates non-overlapping 95% confidence intervals at each time point as determined by likelihood ratio test applied to a linear mixed effects model for cuprizone-treated and control mice. Data presented as mean ± SEM.

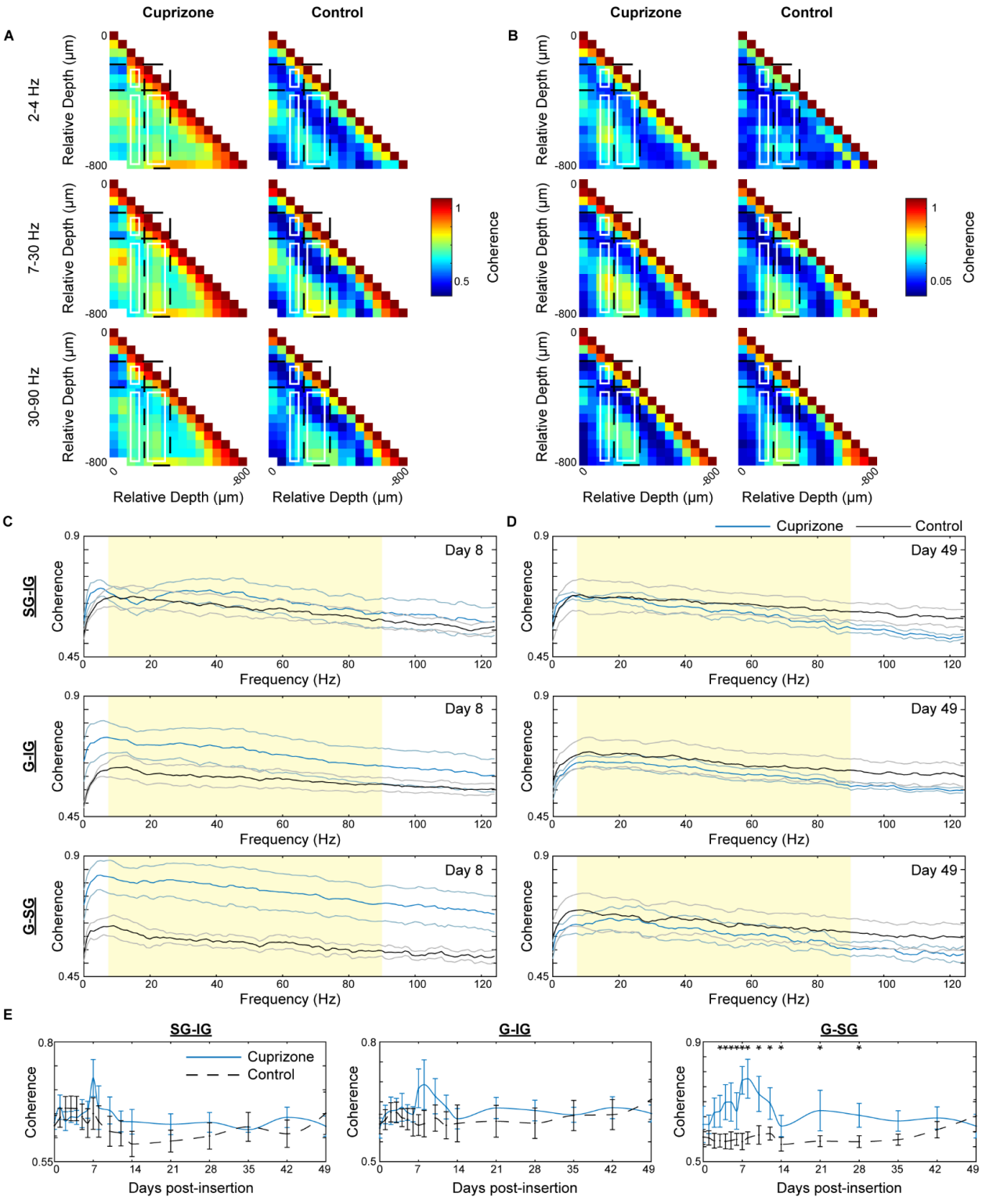

Figure 3-9 Oligodendrocyte depletion and demyelination increases resting-state coherence within and between different cortical layers. Resting-state coherence between cuprizone-treated and control animals at day 8 (a) and day 49 (b) post-insertion. Missing coherence values in (a) are an indication of lost information following electrode depth adjustment to layer IV. Resting-state coherence between supragranular-infragranular (SG-IG), granular-infragranular (G-IG), and granular-supragranular (G-SG) regions over frequency between cuprizone-treated and control mice at day

8 (c) and day 49 (d) post-insertion. (e) Mean coherence between 7 and 90 Hz (shaded region of c and d), averaged across animals in each group. * indicates non-overlapping 95% confidence intervals at each time point as determined by likelihood ratio test applied to a linear mixed effects model for cuprizone-treated and control mice. Data presented as mean ± SEM.

3.4.8 Histological Analysis of Microelectrode Explants Reveals Sustained Oligodendrocyte Loss Around Chronically Implanted Microelectrode Arrays

Following 7 weeks of implantation in control and 12 weeks of cuprizone administration, cortical tissue around microelectrode explants were analyzed for changes in cellular and subcellular dynamics resulting from device-induced inflammation and cuprizone-mediated toxicity. A chronic loss of oligodendrocytes and myelin coupled with damage incurred during chronic device implantation was expected to impair neurons around the device-tissue interface and account for the late-stage decline in recording performance of mice fed control diet. Surprisingly, staining for NeuN+ neurons showed no device-dependent changes in neuronal density between cuprizone-treated or control mice (Figure 3-10a,b). However, staining for NF-200+ axons demonstrated increased, yet not significant, levels in neurofilament immunoreactivity in cuprizone-treated mice around the microelectrode implant, suggesting a cuprizone-induced impact on axonal pathology following injury (Figure 3-11). Further staining for SMI-31+ phosphorylated NF200 axons demonstrated increased immunoreactivity as well as increased neurofilament accumulations in cuprizone-treated mice around an implanted microelectrode array (Figure 3-11 and Figure 3-12). Additionally, cuprizone-treated mice maintained low oligodendrocyte density following 7 weeks post-implantation (Figure 3-10c,d), consistent with previous cuprizone studies reporting a chronic depletion of oligodendrocytes by 12 weeks of cuprizone administration. Cuprizone-treated mice demonstrated markedly reduced oligodendrocyte density compared to control animals. However, there was no significant differences in oligodendrocyte density between

cuprizone-treated animals and controls, on account of high variability in CC1+ cell counts in control mice. This variability may be explained by the heterogeneous presence of oligodendrocytes throughout the cortex, which may be differentially susceptible to device insertion injury (Steven M. Wellman et al., 2018). Staining for MBP+ myelin revealed comparable fluorescence intensities in control mice at 7 weeks post-insertion (Figure 3-10e,f) relative to pre-insertion results (Figure 3-1c). Analysis of contralateral tissue demonstrated significantly reduced MBP+ fluorescence intensities in cuprizone-treated mice compared to controls, confirming that 12 weeks of cuprizone administration induced a chronic state of demyelination within the visual cortex (Figure 3-14). Interestingly, cuprizone-treated mice demonstrated an increase in myelin intensity around the site of microelectrode implantation relative to baseline (Figure 3-10e,f). As a result, no significant differences in MBP+ myelin intensity compared to control mice were reported at 7 weeks post-insertion, similar to observed oligodendrocyte density. Together, the results suggest that impaired recording performances over time could be explained by the chronic depletion of oligodendrocytes and myelin following long-term cuprizone administration.

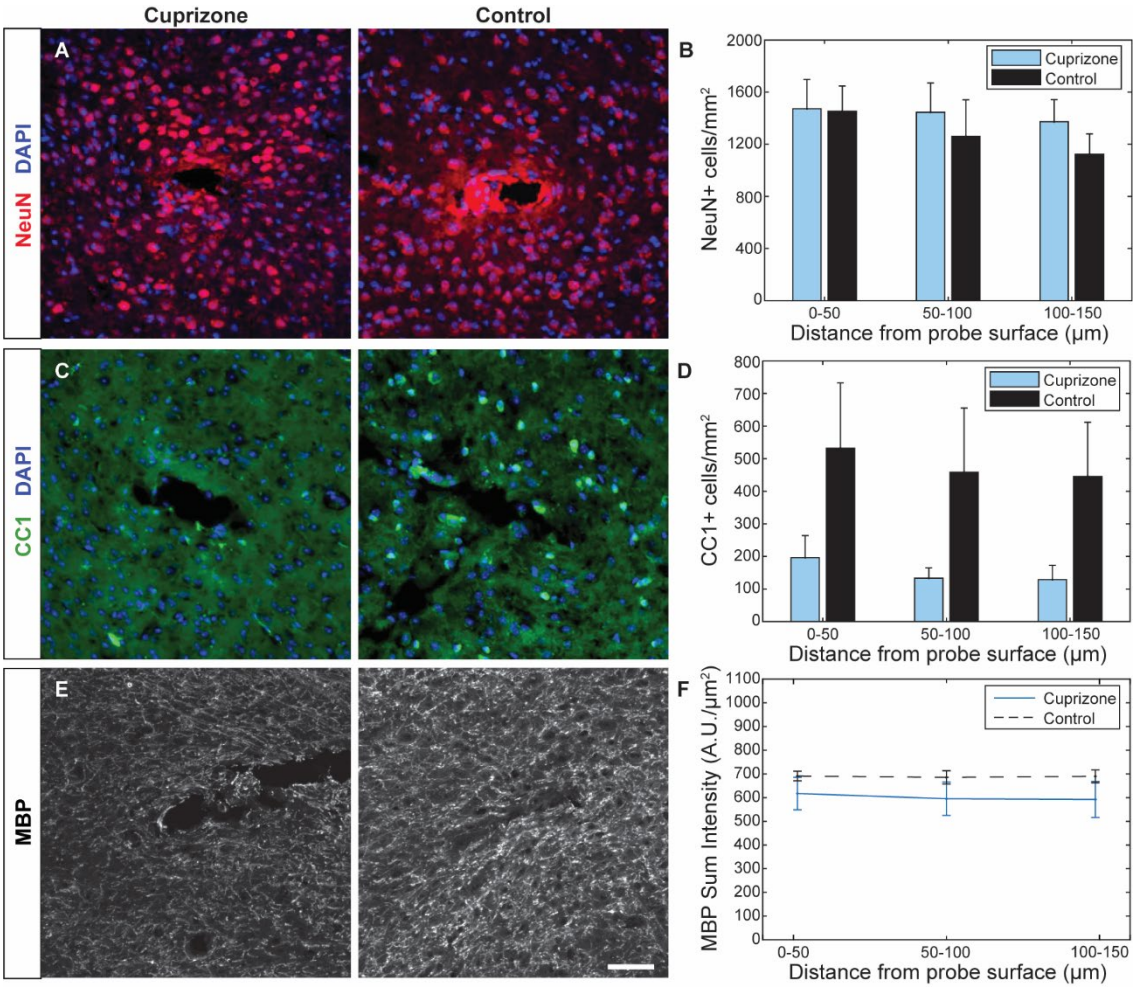

Figure 3-10 Explant histology 7 weeks post-insertion reveals sustained depletion of cortical oligodendrocytes alongside comparable neuronal densities. (a) Representative histological stain for NeuN+ neurons around a microelectrode probe hole in cuprizone-treated and control animals. (b) Cell counts demonstrate comparable neuronal populations between the two groups within 150 μm from the probe surface. (c) Representative stain for CC1+ oligodendrocytes around a microelectrode probe hole in cuprizone-treated and control animals. (d) Cell counts demonstrate reduced oligodendrocyte density within 150 μm from the probe surface in cuprizone-treated mice. (e) Representative stain for MBP+ myelin around a microelectrode probe hole in cuprizone-treated and control animals. (f) Sum fluorescence intensity demonstrates a slight reduction in MBP intensity in cuprizone-treated animals compared to controls. Scale bar = 50 μm.

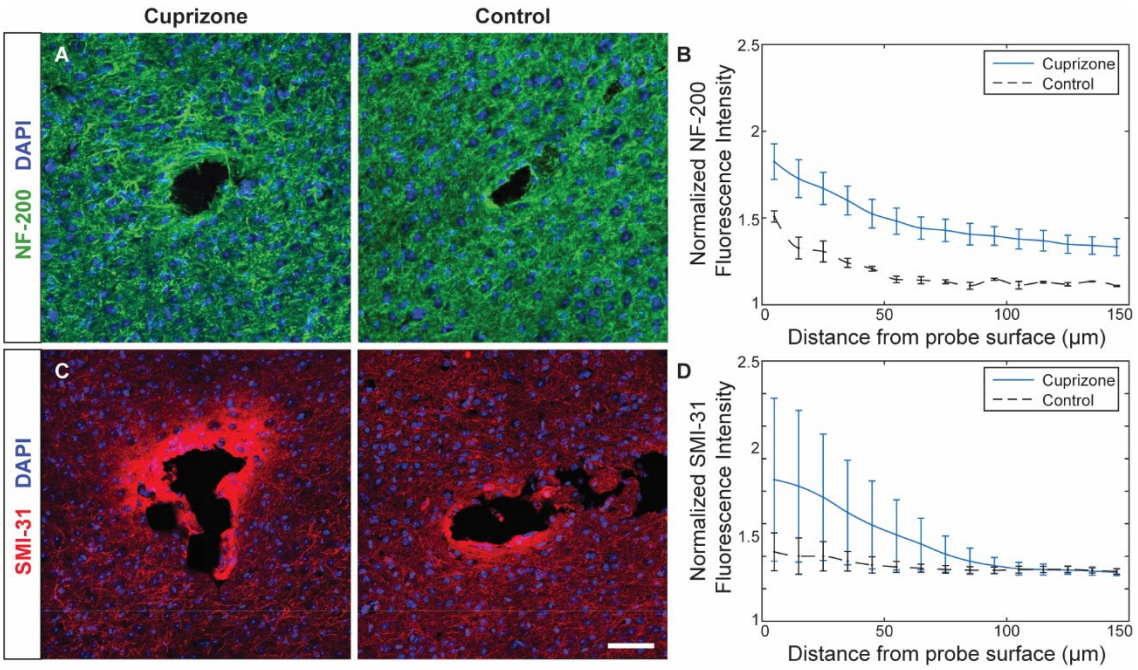

Figure 3-11 Cuprizone administration induces axonal immunoreactivity around chronically implanted microelectrode arrays. (a) Representative stain for NF-200+ axons in cuprizone-treated and control animals around a microelectrode probe hole (n = 3). (b) Normalized intensity demonstrated increased NF-200+ intensity in cuprizone-treated mice compared to controls. (c) Representative stain for SMI-31+ phosphorylated axons in cuprizone-treated and control animals around a microelectrode probe hole. (d) Normalized intensity demonstrated increased SMI-31+ intensity in cuprizone-treated mice compared to controls. Scale bar = 50 μm.

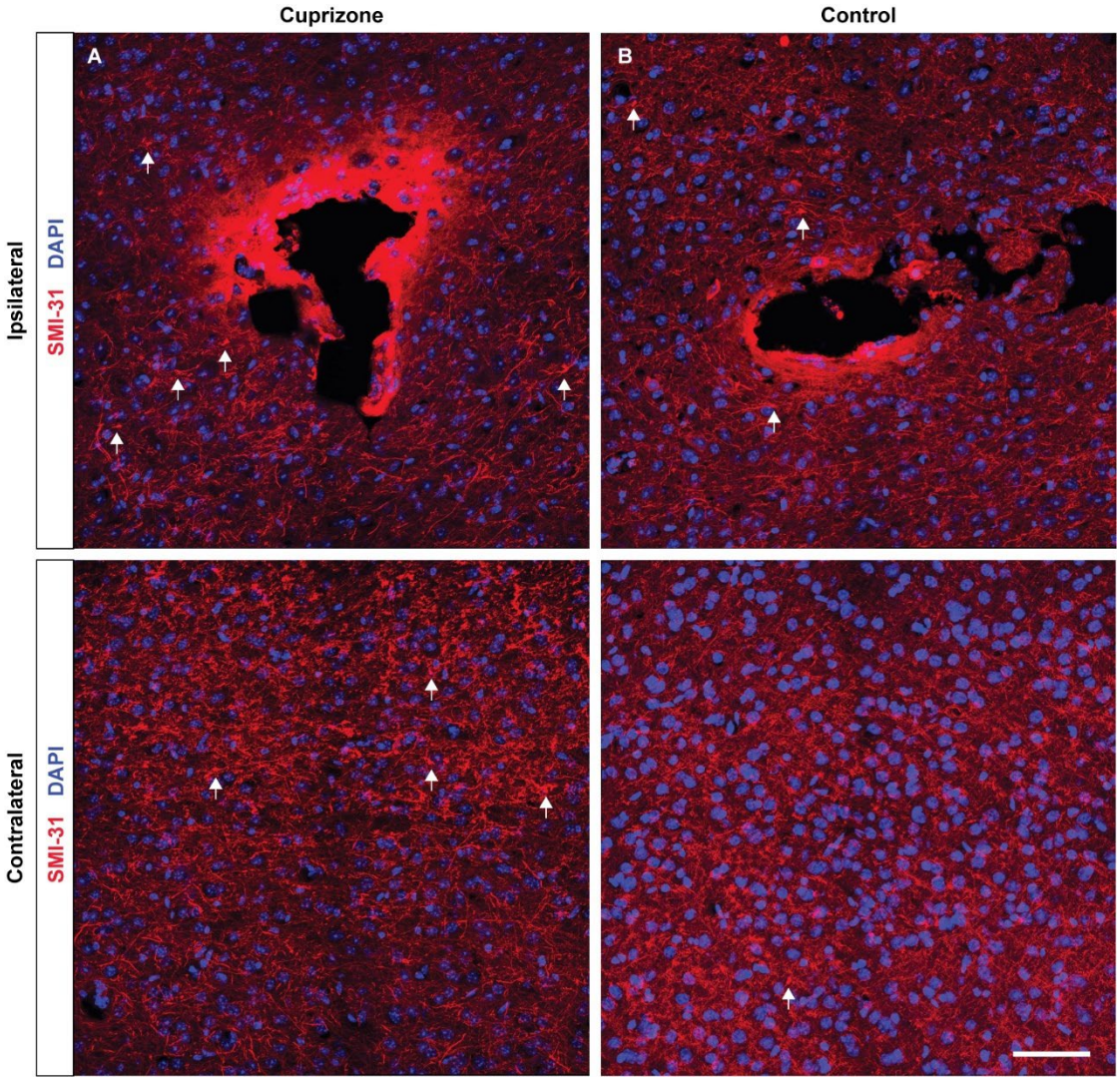

Figure 3-12 Increased accumulations of phosphorylated neurofilaments following cuprizone administration around chronically implanted microelectrode arrays. Representative images of SMI-31+ phosphorylated axons on ipsilateral and contralateral hemispheres in (a) cuprizone-treated and (b) control mice (n = 3). White arrows indicate instances of SMI-31+ axonal accumulation, which is more prevalent around the microelectrode insertion site in cuprizone-treated mice compared to controls. Scale bar = 50 μm.

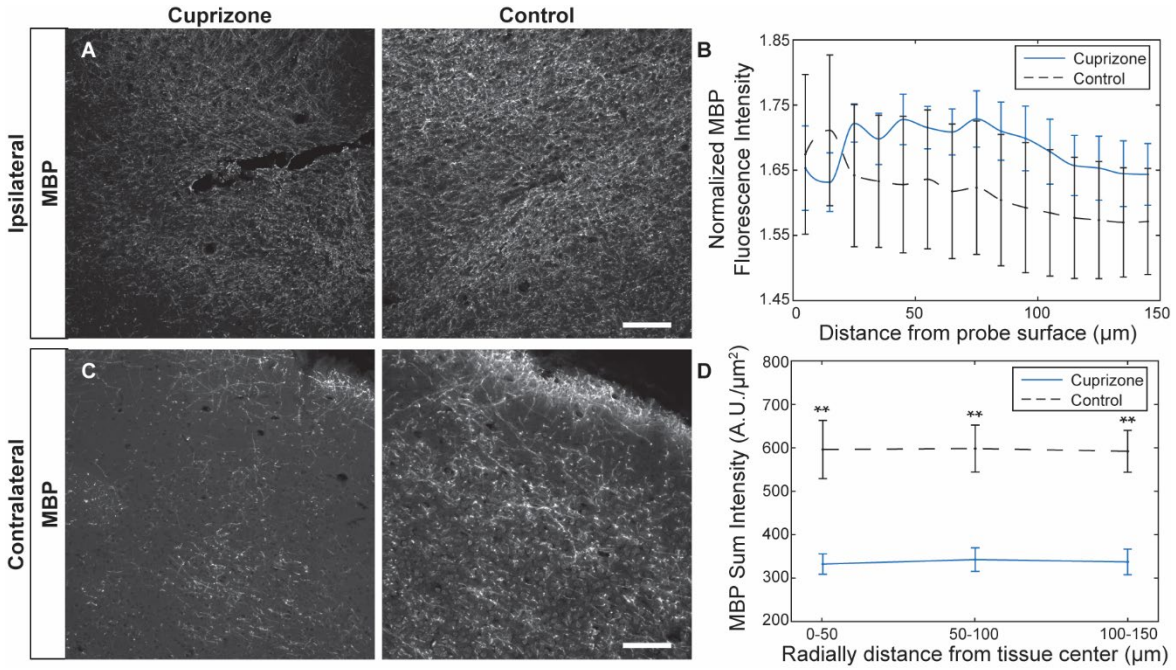

Figure 3-13 Microelectrode implantation increases myelin expression proximal to site of injury despite chronic administration of cuprizone. (a) Representative images of MBP+ myelin around the microelectrode insertion site 7 weeks after insertion in cuprizone-treated and control mice. (b) Normalized MBP fluorescence intensity demonstrates increased MBP staining with increased proximity to microelectrode device. (c) Representative image of MBP+ myelin in contralateral hemisphere of cuprizone-treated and control mice. Scale bar = 100 μm. (d) Sum fluorescence intensity of MBP+ myelin on contralateral hemispheres demonstrate reduced myelin expression in cuprizone-treated mice compared to controls. ** indicates $p < 0.01$.

Since glial cell activation is commonly reported in both models of cuprizone administration and intracortical electrode implantation, we wanted to determine the extent of glial activation by experimental endpoint. Chronic implantation of a microelectrode array induced glial reactivity with spatial preference around the device interface (Figure 3-14). However, only certain glial cells responded to chronic cuprizone administration. The number of NG2+ oligodendrocyte precursor cells within 150 μm radius from site of device insertion was lower in cuprizone-treated mice compared to mice on control diet, demonstrating significant reduction within 50 μm from the site of insertion (Figure 3-14a,b). While oligodendrocyte precursor cells in cuprizone-treated mice maintained similar densities within each bin, control mice demonstrated greater NG2+ cell density with increasing proximity to the site of probe implantation and compared to pre-implantation cell counts, indicating specific glial reactivity in response to device implantation injury. Chronic

implantation of a microelectrode array induced similar distance-dependent activation of Iba-1+ microglia and GFAP+ astrocytes (Figure 3-14c,d,e,f). However, the average Iba-1+ fluorescence intensity was virtually the same between cuprizone-treated and control mice indicating no cuprizone-specific influences on microglia activation post-injury (Figure 3-14c,d). On the other hand, cuprizone demonstrated specific astrocyte reactivity, with increased, and more highly varied, GFAP+ signal intensity in cuprizone-treated animals compared to controls (Figure 3-14e,f). These results indicate that long-term cuprizone toxicity induces a reduction in oligodendrocyte precursor density as well as mild activation of astrocyte populations around chronically implanted microelectrode arrays.

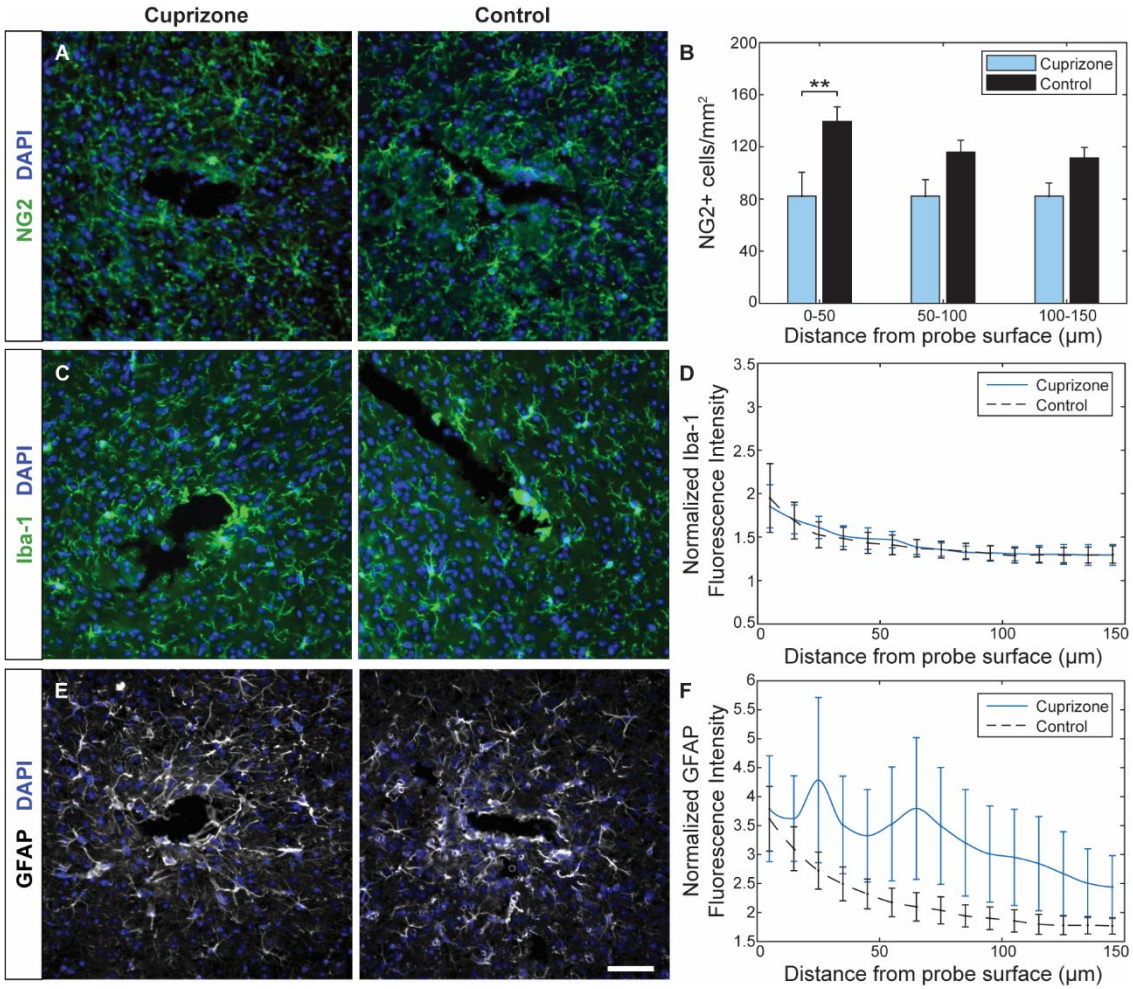

Figure 3-14 Cuprizone-induced glial reactivity around implanted microelectrode arrays at 7 weeks post-insertion. (a) Representative histological stain for NG2+ glial cells around a microelectrode probe hole in cuprizone-treated and control animals. (b) Cell counts demonstrated reduced NG2+ precursor population within 150 μm from the probe surface in cuprizone-treated mice. (c) Representative stain for Iba-1+ microglia in cuprizone-treated and control animals around a microelectrode probe hole. (d) Normalized intensity demonstrated comparable Iba-1+ intensity between control and cuprizone-treated mice. (e) Representative stain for GFAP+ astrocytes in cuprizone-treated and control animals around a microelectrode probe hole. (f) Normalized intensity demonstrated elevated GFAP+ intensity within 150 μm from the probe surface in cuprizone-treated mice. Fluorescence intensities were normalized to contralateral hemisphere. Scale bar = 50 μm. ** indicates $p < 0.01$.

3.5 Discussion

The contribution of oligodendrocytes and myelin on electrophysiological activity within the mouse visual cortex was observed in a cuprizone-inducible model of demyelination. Sixteen

channel, single-shank microelectrode arrays were used to record neuronal data over a 7 week period following 5 weeks of cuprizone administration in oligodendrocyte- and myelin-depleted mice compared to control mice fed with normal diets. Changes in single- and multi-unit activity as well as changes in local field potentials were analyzed to reveal the influence of oligodendrocyte loss and demyelination on the electrophysiological properties of individual neurons, activity of local neuronal populations, neuronal oscillatory activity, and laminar connectivity of cortical circuits. Overall, cuprizone administration induced significant reductions in the evoked firing properties of recordable neurons, decreased firing rates of resting-state and evoked neuronal activity, decreased multi-unit activity in a latency-dependent manner, disrupted the evoked frequency of neuronal oscillations, and altered interlaminar communication within the cortex. Furthermore, post-mortem histology revealed chronic depletion of oligodendrocytes alongside quantitatively matched neuronal densities near the site of microelectrode insertion in cuprizone-treated mice compared to control mice, promoting the idea that loss or dysfunction of oligodendrocytes is a possible source of recording performance failure around intracortical neural interfaces.

3.5.1 Targeted Depletion of Cortical Oligodendrocytes Following 5 weeks of Cuprizone Administration

After 5 weeks of cuprizone exposure, oligodendrocytes and myelin were significantly (p<0.001) depleted within the visual cortex (Figure 3-1). It is important to note that cuprizone depletion does not lead to complete elimination of oligodendrocytes, since a complete loss of oligodendrocyte would likely be fatal. Even though cuprizone does not target myelin directly, loss of oligodendrocytes and inability for oligodendrocytes to regenerate and re-myelinate during

cuprizone administration results in demyelinating injury (Torkildsen, Brunborg, Myhr, & Bø, 2008). *In vitro* analysis determined that cuprizone exposure does not affect the viability of cultured neurons, microglia, or astrocytes, nor does it affect the proliferation or survival of oligodendrocyte progenitor cells (Bénardais et al., 2013). Furthermore, cuprizone treatment does not induce a copper deficiency or toxicity in cultured neurons, demonstrating that cuprizone does not readily pass through neuronal cell membranes (Benetti et al., 2010). Thus, cuprizone acts with high specificity on oligodendrocyte cells through cellular dysfunctions in a copper-dependent and independent manner (Taraboletti et al., 2017).While the underlying mechanisms of cuprizone-induced oligodendrocyte toxicity are unclear, the most common theories are disturbances in mitochondrial function important for energy metabolism (Praet et al., 2014; Taraboletti et al., 2017; Werner et al., 2010). Oligodendrocytes require high amounts of generated ATP to sustain their metabolic output due to continuous synthesis of lipid myelin membranes, which heightens their vulnerability to mitochondrial injury above other metabolically active cells within the CNS (Rosko et al., 2018). Cuprizone treatment reportedly alters mitochondrial enzymes dependent on copper as a co-factor and can disrupt electron transport function of complexes I-III within the respiratory chain (Acs, Selak, Komoly, & Kalman, 2013; Faizi et al., 2016; Pasquini et al., 2007). As a result, reductions in intracellular energy, accumulation of reactive oxidative species, and inherently low antioxidant levels in oligodendrocytes can lead to cellular apoptosis following cuprizone administration (Bradl & Lassmann, 2010; Praet et al., 2014). Alternatively, cuprizone-induced copper deficiency has the potential to directly affect the production or deposition of myelin within oligodendrocytes, which requires the translation, transcription, and translocation of myelin-related proteins within endosomes that fuse with an expanding myelin membrane (Krämer, Schardt, & Nave, 2001). Endosome fusion to the oligodendrocyte cellular membrane is the

principle method for depositing myelin proteins and lipids necessary to generate and maintain myelination. Copper has been implicated in the regulation of intrinsic cellular mechanisms which control fatty acid synthesis within the brain as well as mRNA gene expression of myelin-related proteins during cuprizone-induced toxicity (Franco-Pons et al., 2009; Gybina & Prohaska, 2008; Morell et al., 1998). Furthermore, as a transitional metal ion whose abundance can lead to cellular toxicity, copper can induce vesicular fusion with the plasma membrane (exocytosis) in order to maintain homeostatic levels, and in the process promotes the repair or replacement of damaged cellular membranes (Peña, Coblenz, & Kiselyov, 2015). As a result, a lack of copper due to cuprizone administration could possibly inhibit this myelin forming process within oligodendrocytes, resulting in CNS demyelination.

In response to oligodendrocyte loss, oligodendrocyte precursor cells migrate, proliferate, and differentiate into myelinating oligodendrocytes in order to restore homeostatic density (Ethan G. Hughes et al., 2013b). As a result, an increase in oligodendrocyte precursors within the cortex is expected following acute cuprizone toxicity (Figure 3-1d). Existing myelin is degraded following cuprizone-induced oligodendrocyte cell death and the remaining debris is cleared away by microglia (Figure 3-1c). Additionally, protection of mature oligodendrocytes during cuprizone administration results in attenuation of myelin loss and reduced microglia or astrocyte reactivity in white matter tracts, suggesting that debris left from oligodendrocyte and myelin degeneration induces glial cell activation (Xing et al., 2018b). Therefore, glial cell activation is commonly reported in white matter tracts of the cuprizone model (Kotter, Li, Zhao, & Franklin, 2006; Napoli & Neumann, 2010). However, we report no significant differences in activation of microglia or astrocytic markers in cortex by 5 weeks of cuprizone administration (Figure 3-1e,f). This could be accounted for by a different temporal course of cortical glial activation and extent of glial response

due to lower amount of myelin and, consequently, accumulation of myelin debris in the cortex compared to the heavily myelinated white matter tracts. Furthermore, this phenomenon is known to be strain-dependent, which would explain why we demonstrate little to no activation of microglia or astrocytes within the cortex of C57BL/6J mice following 5 weeks of cuprizone toxicity (Skripuletz et al., 2008).

3.5.2 Loss of Cortical Oligodendrocytes and Myelin on Electrophysiological Recording Properties of Individual Neurons

Neural electrophysiology was evaluated in the mouse visual cortex due to the fact that visual stimulation can elicit robust neural responses and is a more reliable and reproducible method of stimulation compared to somatosensory or motor cortex stimulation. Single-shank Michigan-style microelectrode arrays were implanted to a depth of 800 μm within the cortex (layer V/VI) in order to avoid insertion into white matter areas beneath the cortex which consist of a different distribution of oligodendrocyte cells and myelin fibers. Mice were recorded while head-fixed on a movable platform for linear ambulation and while awake to avoid unwanted influences in neural responses seen with anesthetized recording (Nicholas J. Michelson & Kozai, 2018). Motion artifacts that appeared during recording were minimized by repeating trials as needed to collect continuous, undisrupted data (E. N. Nicolai et al., 2018). Current source density analysis showed that the electrode did not drift more than the distance occupied by one electrode site in either direction (<50 μm) within the first two weeks of insertion before stabilizing, indicating electrode position was relatively stable throughout the course of implantation (Figure 3-2). Control mice demonstrated a slight increase in layer IV position along the implanted microelectrode array, which is a result of tissue swelling that can occur following brain injury (Donkin & Vink, 2010).

Interestingly, cuprizone mice experienced, on average, a decrease in layer IV position along the implanted microelectrode array indicative of tissue shrinkage, which may be a result of a bulk loss and clearance of oligodendrocyte and myelin following cuprizone administration (Figure 3-2j). The insulating properties of myelin decrease the capacitance of axonal membranes (Hartline, 2009). Therefore, the reduction of myelin via cuprizone toxicity would effectively increase axonal membrane capacitance and may reduce impedances around an implanted microelectrode. Here, we show that electrode impedances were significantly reduced in cuprizone-treated animals for the first week after insertion (Figure 3-3f). Abnormally high or low impedances, which would be indicative of mechanical or material failure, were not reported in either cuprizone-treated or control mice, demonstrating electrode stability and functionality throughout the course of implantation (Steven M. Wellman et al., 2018; Justin C Williams, Joseph A Hippensteel, John Dilgen, William Shain, & Daryl R Kipke, 2007). This may be due to revised fabrication methods or subtle design differences compared to previously reported work using 100 μm site spacing probes (T.D.Y. Kozai et al., 2015). Regardless, hardware issues should equally affect both experimental group and control, which should not diminish the significant differences of the electrophysiological recording properties reported here.

Recording yield, which is a measure of device recording efficacy, was significantly impaired at the onset of implantation in cuprizone-treated mice (Figure 3-3a). Given that other established modes of recording performance failure, such as glial scar formation and neurodegeneration, are identified as late-stage events that occur following chronic device implantation (>2-4 weeks post-implantation), this decrease in yield can likely be attributed to the absence of cortical oligodendrocytes and myelin membranes following the cuprizone pretreatment (Streit et al., 2012). Reduced single-unit yields can suggest a failure in signal transduction of

demyelinated axons, resulting in decreased signal amplitudes of more distal neurons, which would not be threshold detected by the recording device. Indeed, the amplitude of evoked neuronal responses in cuprizone-treated mice were decreased compared to controls (Figure 3-3d). This is consistent with an observed decrease in signal-to-noise ratios (SNRs), a metric that measures the strength of detected signals against the recorded noise (Figure 3-3b). SNRs are dependent on the amplitude or strength of neuronal action potentials as well as electrophysiological noise (i.e. neuronal noise, glial reactivity) for each contact site, which also appeared reduced in cuprizone-treated mice. Furthermore, oligodendrocytes and myelin populate the gray matter cortex in a layer-specific manner, with oligodendrocyte and myelin densities the highest in deeper laminar structures (Giulio Srubek Tomassy et al., 2014). This spatial distribution is consistent with a recorded loss in yield, SNR, and amplitudes in layer IV and V of cuprizone-treated mice, indicating that recording performance is altered as a function of depth along the implanted microelectrode array due to spatial specificity of oligodendrocytes and myelin within the cortex (Figure 3-4). This may also explain the plateau in recording yield between 20-40% in cuprizone-treated animals (Figure 3-3a), which equates to ~3-6 recording sites (~150-300 μm of cortical depth). Considering that cuprizone toxicity significantly depletes most oligodendrocytes (Figure 3-1b), but not all oligodendrocytes within the CNS, as well as the fact that not all neurons within the gray matter cortex are myelinated (and therefore unaffected from cuprizone demyelination) suggests that this is the maximum possible deficiency in recording performance we can observe given the limitations of the model and the myeloarchitecture of the brain.

Trends in single-unit activity were relatively stable throughout the 7 week implantation period in cuprizone-treated mice (Figure 3-3). Recording performance in the oligodendrocyte-depleted group began at a low performance state on day 1 and remained plateaued at that low

performance state over time. In contrast, recordings in control mice, which began with healthy oligodendrocytes were significantly higher ($p<0.05$) relative to cuprizone-treated mice before experiencing a gradual decline over time, which is consistent with previously published data (Golabchi et al., 2018b; Takashi DY Kozai, Zhanhong Du, et al., 2015; T. D. Kozai, X. Li, et al., 2014). By 7 weeks post-insertion, electrophysiological performance in control mice was indistinguishable from that of cuprizone-treated mice. These results were contradictory to our initial hypothesis, that recording performance in cuprizone-treated mice would decline more rapidly than control animals given a lack of oligodendrocyte- and myelin-mediated support for neurons and axons. In fact, by 7 weeks post-insertion, neuron density was similar between the two groups (Figure 3-9b). However, it is important to note that previous studies have demonstrated that the presence of NeuN staining does not necessarily indicate that the neuron is functional as opposed to being silenced or otherwise dysfunctional (Nicholas J. Michelson, Alberto L. Vazquez, et al., 2018). Indeed, previous evaluation of cortical neurogenesis following injury or via induced differentiation has demonstrated the inability for new neurons to integrate functionally due to an unfavorable microenvironment (Arvidsson, Collin, Kirik, Kokaia, & Lindvall, 2002; Berninger et al., 2007). Instead, an alternative hypothesis is that the initial pre-insertion depletion of oligodendrocytes (Figure 3-1) leads to an environment where neurons are more susceptible to becoming dysfunctional even without (or following) a microelectrode implantation. This could explain why recording performance starts low and remains plateaued over the course of cuprizone treatment (Figures 3-8). Taken together, significant decreases in oligodendrocytes and myelin with cuprizone-treatment prior to array implantation (Figure 3-1b,c) leads to significantly lower initial recording performance (Figures 3-8) without significantly impacting neuronal density (Figure 3-9b) compared to controls. However, over the course of 7 weeks, there are complex cell dynamics

and the significant differences between the two groups are lost for oligodendrocyte density (Figure 3-9d; cuprizone 0-50 μm: 168.6 ± 55.5 cells/mm^2, control 0-50 μm: 449.3 ± 124.2 cells/mm^2), which is accounted for in large part by the drop in CC1+ cells in control mice and a small increase of CC1 in the cuprizone group (compare Figure 3-1 with Figure 3-9), myelin intensity (Figure 3-9f; cuprizone 0-50 μm: 617.3 ± 137.1 A.U./μm^2, control 0-50 μm: 690.9 ± 45.6 A.U./μm^2), which is largely accounted for by the increase in MBP staining in the cuprizone group (compare control in Figure 3-1 and Figure 3-9), and recording performances (Figures 3-8). Interestingly, the number of NG2 cells in control mice is unchanged at 7 weeks versus the time of implantation while it is reduced to half in the cuprizone group. The latter could represent a depletion of NG2 cells that have differentiated into oligodendrocytes, possibly explaining the increase in CC1+ cells in the cuprizone group and leading to increase in myelin density. This supports the notion that over time in wildtype controls (that recapitulates normal implantation injury), the microenvironment around the electrode within the recording radius becomes depleted of oligodendrocytes and myelin, which contribute to recording performance degradation. While the current study does not establish causation, this work motivates future mechanistic studies that link oligodendrocyte health and their metabolic and/or neurotrophic function to recording performance.

While recording performances trend slightly higher in the cuprizone treated group at later time points, these changes are non-significant (Figure 3-3). In contrast to NeuN, neurofilament expression was increased in cuprizone-treated mice (Figure 3-11 and Figure 3-12). However, SMI-31 labeling was also substantially elevated around the implant, which is associated with dystrophic neurite formation and abnormal axonal transport (Vickers et al., 1996). Therefore, it is important to keep in mind that the presence of antibody labeling (NF-200) does not necessarily indicate that those cells or cellular elements are functional as previously shown with NeuN staining (Nicholas

J. Michelson, Alberto L. Vazquez, et al., 2018). Given the limitation in endpoint analyses with the cuprizone model, it is uncertain whether recording performance in control mice would have plateaued at this level by 7 weeks post-insertion or would have continued declining over time. However, these findings suggest that the microenvironment around chronically implanted electrodes in healthy mice gradually becomes increasingly similar to cuprizone-treated cortical tissue. Furthermore, the observed decrease in electrophysiological properties of control mice to a level that is comparable to recordings in cuprizone-treated mice suggest that loss or dysfunction in oligodendrocytes and myelin could potentially act as a source of biological failure for chronically implanted intracortical devices. These findings support the premise that preserving the function of oligodendrocytes and myelin can help improve neural recording performances following injury induced by chronically implanted microelectrode devices.

3.5.3 Cuprizone-induced Oligodendrocyte Loss and Demyelination Impairs Multi-unit Activity Within the Cortex

Analysis of multi-unit recordings provided insight on how oligodendrocytes and myelin modulate the functional activity of local neuronal populations within the visual cortical circuit. Cuprizone-induced oligodendrocyte loss and demyelination reduced neuronal firing rates compared to control mice at the onset of device insertion and remained reduced throughout the course of implantation (Figure 3-5). This was observed in a depth-dependent manner, with cuprizone-treated mice experiencing the most reduction in multi-unit firing rate within layers II/III. Beyond two weeks post-insertion, firing rate appeared to non-significantly increase in cuprizone-treated mice, which may be due to the unexpected increase in oligodendrocyte density and myelination observed during explant histology. Myelin sheaths cluster voltage-gated Na^+ sodium

channels into nodes along axons, providing saltatory propagation of neuronal signals (Hartline, 2009). The loss or addition of myelin can result in a re-distribution of those sodium channels, weakening or strengthening the propagative effect of action potentials down the axon (Hamada & Kole, 2015). Therefore, weakened axonal conduction velocities due to cuprizone-induced demyelination could diminish signals before they are detected by the microelectrode, reducing recorded firing rates. One study investigating the effects of increases in myelin sheath thicknesses of ERK1/2-mutant mice demonstrated a decrease in latency-to-peak of evoked amplitudes within the auditory cortex compared to wild-type mice, suggesting that myelin provides direct functional consequences of neuronal activity by regulating conduction velocity (Jeffries et al., 2016). However, significant differences were not detected during the 1st action potential peak, which would be indicative of a conduction velocity issue during myelin sheathing, but during the 2nd, 3rd, and 5th peak after stimulus presentation, suggesting perhaps a deficiency in metabolic or trophic support from damaged or dysfunctional oligodendrocytes, which would be necessary for repetitive neuronal firing (Philips & Rothstein, 2017). Demyelinated axons require more energy to support repolarization of active neurons as well as match the levels of metabolic transport within previously myelinated axons (Alizadeh, Dyck, & Karimi-Abdolrezaee, 2015b). Indeed, we show comparable recording outcomes within the first 100 ms after stimulation onset in multi-unit yield and SNFRR between cuprizone-treated and control mice, which is within the range of normal physiological latencies reported for visual information to reach the cortex (Figure 3-6). Furthermore, we report that significant differences in multi-unit dynamics, where recording of multi-unit activity was increased (i.e. repetitive neuronal firing) in control mice over cuprizone-treated mice (Figure 3-6), were more apparent following sustained evoked visual stimulation. These results are more indicative of a loss in energetic support from oligodendrocytes impairing

recurrent neuronal firing activity than a reduction in myelin-mediated conduction velocities. In either case, these results establish that loss of oligodendrocytes and myelin can reduce the firing properties of local neuronal populations.

3.5.4 Oligodendrocyte Depletion and Demyelination Alters Oscillatory Activity and Functional Laminar Connectivity Within the Cortex

Cognition and other brain functions are highly dependent on synchronized neural circuits to achieve highly coordinated levels of rhythmic activity. Alterations in myelin are known to have direct influences on neuronal oscillatory dynamics given their regulation on axonal conduction velocities important for fast information transmission over far-reaching brain regions (Almeida & Lyons, 2017; Filley & Fields, 2016; Pajevic, Basser, & Fields, 2014). Here, we demonstrated that peak LFP power was visibly reduced in cuprizone-treated mice compared to control mice and that cuprizone administration induced large fluctuations in average power within the first two weeks post-insertion (Figure 3-7). Changes in power were not reflected in a depth-dependent manner, which is expected given that neuronal oscillations occur between large neuronal networks in the brain. However, relative changes in power (evoked power in relation to spontaneous power) were observed to be altered within distinct frequency bands following cuprizone administration. At lower frequency ranges, such as the theta (2-4 Hz), delta (5-7 Hz), and alpha (8-15 Hz) frequency range, relative power was reduced in cuprizone-treated mice compared to controls. Oscillations in neuronal activity over larger distances are often governed by these lower frequency ranges given that small changes in neuronal conduction velocities can have profound impacts on network synchronization (Pajevic et al., 2014). This would explain the reduced power observed within lower frequency bands, given demyelination of far-reaching neuronal projections following

cuprizone administration. Alternatively, power at higher frequency bands, such as gamma (30-90 Hz) bands and beyond (high-frequency oscillations, >90 Hz), were increased in cuprizone-treated mice relative to controls. Satellite oligodendrocytes have been shown to be entrained to high-frequency activity of pyramidal neurons (Battefeld et al., 2016), which could influence the high-frequency oscillations within these local circuits depending on the cuprizone-induced depletion of satellite versus non-satellite oligodendrocyte cells. One study reported higher survivability in satellite oligodendrocytes above other oligodendrocytes following cuprizone administration (Ludwin, 1979). Perineuronal oligodendrocytes also demonstrated active re-myelination following demyelinating injury and could explain the observed increase in power within higher frequency bands observed in cuprizone-treated mice. In all, these alterations in spectral power demonstrate that cuprizone-induced oligodendrocyte loss and demyelination alter the synchronicity of neuronal circuits within the cortex.

Brain connectivity can also be evaluated in terms of coherence, which is a statistical metric measuring how populations of neurons within different regions are activated in a similar fashion (Bowyer, 2016; Maier, Adams, Aura, & Leopold, 2010). Changes in resting-state coherence between brain regions have been observed to occur naturally throughout development and adulthood (Fleck et al., 2017). During development, increases in coherence between hemispheric brain regions are hypothesized due to increased myelination by enhancing neural transmission and reducing phase lag (Barry et al., 2004). However, we report that coherence actually increases following cuprizone-induced oligodendrocyte depletion and demyelination (Figure 3-8). We demonstrate that cuprizone-treated mice exhibit the greatest difference in resting-state and evoked G-SG coherence and G-IG coherence, with relatively little change between SG-IG regions. This disruption in layer IV communication is reflected by reductions in evoked single- and multi-unit

activity of cuprizone-treated mice compared to controls. Furthermore, cuprizone administration altered communication within cortical layers, particularly superficial and deeper layers of the cortex. Despite the fact that myelin is traditionally viewed as insulating far-projecting axons, mainly the excitatory pyramidal neurons that connect both cortical hemispheres and other distal brain regions, recent advances in electron microscopy (EM) techniques have revealed that a significant portion of cortical interneurons, which are important for local circuit function, are also myelinated (Micheva et al., 2016). Specifically, EM revealed that parvalbumin-positive (PV+) interneurons possess about half of all myelinated axons in layer II/III and a quarter of myelinated axons in layer IV. Since inhibitory interneurons are important for regulating the excitability of different regions of the cortex, it is possible that a significant demyelinating insult to cortical interneurons following cuprizone administration can reduce the inhibitory influence of local circuits, altering the intricate balance in neuronal excitation/inhibition and, by extension, the functional coherence within and between different cortical layers. Indeed, vulnerability of inhibitory interneurons has been observed previously in experimental demyelinating models of MS (Falco, Pennucci, Brambilla, & de Curtis, 2014; Rossi et al., 2012). Furthermore, abnormal increases in cortical coherence are commonly observed in different brain disorders. For example, EEG studies track increases in coherence between different brain regions to predict areas of seizure onset in epilepsy patients (J. Song et al., 2013; G. Wang et al., 2016). Fluctuations in coherence are also observed in ADHD patients in an age-dependent manner (Clarke et al., 2008). The sensitive balance in neuronal excitation and inhibition is necessary for different brain regions to function coherently. In all, we show that myelinating oligodendrocytes are important regulators of communication between different cortical circuits and that cuprizone-induced depletion of oligodendrocytes and myelin alters normal intra- and interlaminar coherence within the cortex.

3.5.5 Histological State of Explanted Cortical Tissue Following Chronic Cuprizone Administration

Explant histology provided insight into cellular and subcellular tissue changes following 7 weeks of device implantation and 12 weeks of cuprizone administration that led to functional neural activity (Figures 9-10). Labeling for neurons showed that 12 weeks of cuprizone administration did not have an effect on neuronal distribution around chronically implanted microelectrode arrays (Figure 3-9a,b), which is consistent with previously reported findings that cuprizone itself does not induce neuronal damage or cell death within young mice (Praet et al., 2014). However, NF-200 fluorescence demonstrated increased immunoreactivity of axonal neurofilaments in cuprizone-treated mice compared to controls (Sup. Fig. 2). Indeed, histological labeling demonstrated altered neurofilament distribution around the implanted probe hole for cuprizone-treated mice, indicating axonal re-organization in response to combined influence of implantation injury and cuprizone administration. This result stands contrary to our hypothesis that a lack of trophic support from oligodendrocytes and myelin due to cuprizone administration would reduce the number of neurons and axons during device implantation injury, particularly given the limited capacity for the CNS to regenerate. One possible explanation is the lack of inhibitory chondroitin sulfate proteoglycans (CSPGs) secreted by astrocytes and NG2 glia in cuprizone-treated animals, which can prevent axons from extending through the lesion to re-establish functional neural circuits following injury (Dou & Levine, 1994; Friedlander et al., 1994; Zhong & Bellamkonda, 2007). Furthermore, the presence of NG2 glial cells themselves, which can form specialized synapses with neurons, are hypothesized to be axon inhibitory by acting as regulators of neurite outgrowth (Filous et al., 2014). Of note is that the elevation of NG2 cells reverses between cuprizone-treated and control groups before device implantation (Figure 3-1d, cuprizone

0-50 μm: 169.4 ± 31.2 cells/mm^2, control 0-50 μm: 83.1 ± 29.2 cells/mm^2) and 7 weeks after implantation (Figure 3-10b; cuprizone 0-50 μm: 82.2 ± 18.3 cells/mm^2, control 0-50 μm: 139.5 ± 11.2 cells/mm^2). These observations, together with changes in MBP, NF200, and SMI31 may provide an avenue for future investigations. This hinderance to axonal regeneration coupled with an exhausted population of oligodendrocyte precursor cells (and therefore fewer deposited CSPGs) following chronic cuprizone administration may explain the increase in neurofilament staining observed around the site of injury. However, it is again important to note that the presence of antibody labeling does not necessarily indicate functionality (Nicholas J. Michelson, Alberto L. Vazquez, et al., 2018).

By 7 weeks post-insertion and 12 weeks of cuprizone exposure, cuprizone-treated mice demonstrated reduced oligodendrocyte densities around chronically implanted microelectrode arrays compared to control mice. (Figure 3-9c,d) This level of oligodendrocyte loss is consistent with previous studies employing long-term administration of the cuprizone toxin, which can induce chronic depletion of oligodendrocytes in white and gray matter tissue. However, cuprizone-treated mice remarkably demonstrated an increase in oligodendrocyte density following 7 weeks of insertion and 12 weeks of cuprizone administration (Figure 3-9d; cuprizone 0-50 μm: 168.6 ± 55.5 cells/mm^2) compared to pre-insertion at 5 weeks of cuprizone treatment (Figure 3-1b; cuprizone 0-50 μm: 69.5 ± 33.9 cells/mm^2). Furthermore, while myelin staining demonstrated reduced fluorescence intensity in cuprizone-treated mice compared to control mice at the experimental endpoint, there were no significant differences in myelin fluorescence between the two groups, and myelin intensity of cuprizone-treated mice was in fact upregulated compared to pre-insertion baseline (Figure 3-9e,f). Furthermore, myelin expression was upregulated near the site of insertion in both cuprizone-treated and control animals compared to myelin intensity on

contralateral hemispheres (Sup Fig. 4). Despite this increase in myelination near the electrode, deficits in recording performance persisted, suggesting a lack of functional connectivity with newly generated myelin or newly myelinated axons with the local neuronal circuit. This may be explained by an inability for the MBP+ antibody to differentiate intact versus degenerated myelin in cuprizone-treated (and control) animals, obfuscating the possibility of accumulated or unresolved myelin debris around the microelectrode array. The dual insult of cuprizone toxicity with injury from penetrating cortical insertion and implantation has not been observed before and may indicate that oligodendrocyte and myelin loss experienced during chronic cuprizone exposure is counteracted by tissue healing events that occur following CNS injury. Unlike previous cuprizone studies without a second insult of brain injury (Gudi et al., 2014; Skripuletz et al., 2008), these results indicate a potential increased activation of oligodendrocyte regeneration and re-myelination pathways with simultaneous chronic cuprizone exposure and probe implantation injury. Additionally, an important aspect of device implantation injury is the upregulation of oxidative stress events, which can occur from blood-brain barrier disruption, impairment of waste clearance pathways, and activation of inflammatory glial cells (Takashi DY Kozai, Andrea S Jaquins-Gerstl, Alberto L Vazquez, Adrian C Michael, & X Tracy Cui, 2015). Generation of reactive oxidative species and free radicals can impact tissue health by reducing neuron viability as well as the material properties of the electrode by inducing corrosion and delamination (Kelsey A Potter et al., 2013; Abhishek Prasad et al., 2012; Takmakov et al., 2015). This is relevant due to the fact that cuprizone, a chelator of copper ions important for metabolic redox reactions, can exert its own oxidative stress on CNS tissue. However, as mentioned previously, cuprizone toxicity and copper chelation is a phenomenon specific to the oligodendrocyte population and would not be expected to influence the redox reactions occurring within neurons and other CNS cells.

Oligodendrocytes are particularly susceptible to oxidative damage given their intrinsically low supply of antioxidant enzymes, which may contribute to their vulnerability during cuprizone exposure. Previous studies have applied pharmacological or biomaterial approaches to alleviate the build-up of oxidative damage that can occur around implanted devices, such as application of the anti-oxidant resveratrol or surface modification with superoxide dismutase, a free radical scavenger (Nguyen et al., 2016; Potter-Baker et al., 2014; Kelsey A Potter et al., 2013; Zheng et al., 2019), which can potentially protect oligodendrocytes and other CNS cells sensitive to harmful oxidative species. These intrinsic mechanisms that can lead to oligodendrocyte dysfunction induced during device implantation and inflammation could provide further insight into the inflammatory biological microenvironment and deteriorating electrophysiological signals detected by microelectrode arrays.

As expected, the number of NG2 glia around the site of device insertion was significantly reduced in cuprizone-treated mice compared to controls following chronic cuprizone toxicity (Figure 3-10a,b). Oligodendrocyte regeneration and re-myelination typically occurs when mice return to a normal diet after 5-6 weeks of cuprizone treatment due to local progenitor cells proliferating and differentiating to restore depleted cells (Baxi et al., 2017). During chronic cuprizone administration, however, oligodendrocytes are unable to repopulate and re-myelinate the affected tissue due to an exhausted precursor population that cannot support the continual renewal and immediate loss of oligodendrocyte cells. Interestingly, the number of NG2 glia in control mice was increased compared to baseline data, indicating a proliferative response to the insertion of a microelectrode device at 7 weeks post-insertion (Figures 1,10). This data is in line with previously reported reactivity of the NG2 precursor population following acute electrode implantation as well as increased proliferation up to 4 weeks post-insertion of a microelectrode

array (S. M. Wellman & T. D. Kozai, 2018; Steven M Wellman et al., 2019b). Both cuprizone-treated and control mice demonstrated similar fold changes in microglia fluorescence intensity compared to contralateral control tissue as well as a device-dependent increase in intensity with proximity to the site of insertion, suggesting no cuprizone-specific activation of microglia cells following injury (Figure 3-10c,d). Interestingly, astrocyte intensities were increased in cuprizone-treated animals compared to control mice 7 weeks post-insertion (Figure 3-10e,f). The dual incidence of decreased NG2 glia alongside increased astrocytic intensities could be indicative of previously reported phenomenon describing the conversion of oligodendrocyte precursors into reactive astrocytes following CNS injury (L Dimou & Vittorio Gallo, 2015; Amber R. Hackett et al., 2016). These results may suggest that damage and inflammation during device insertion coupled with oligodendrocyte precursor depletion/exhaustion from cuprizone administration preferentially directs differentiation of NG2 glia toward a more astrocytic cell fate. Alternatively, intercellular communication between oligodendrocytes and astrocytes is facilitated via membrane gap junctions linking the cytosol of both cells (Nualart-Marti, Solsona, & Fields, 2013). This connection is critical for the diffusion of potassium ions and other neurotransmitters released from depolarizing neurons to prevent axonal swelling and is suggested to support myelin integrity following demyelinating injury (Kıray, Lindsay, Hosseinzadeh, & Barnett, 2016; Rash, 2010). A reduction in connexin proteins involved in oligodendrocyte-astrocyte gap junctions reportedly occurs alongside increased astrogliosis within gray matter lesions of MS patients (Markoullis et al., 2014). Furthermore, cuprizone administration and subsequent recovery can alter the distribution of these same connexins within myelinating oligodendrocytes and astrocytes (Parenti et al., 2010). As a result, loss or dysfunction in intercellular communication between

oligodendrocytes and astrocytes due to cuprizone toxicity may explain elevated astrocyte reactivity observed in cuprizone-treated animals.

3.5.6 Holistic Summary of Combined Electrophysiology and Histological Outcomes

Summarizing the immunohistochemical results between cuprizone-treated and control mice at 7 weeks post-implantation with respect to their pre-implant histology is necessary to understand how it relates to the measured electrophysiology. Prior to implantation following 5 weeks of cuprizone administration, oligodendrocytes and myelin were significantly reduced (~85% and ~65%, respectively) within the cortex compared to control animals. Due to cuprizone toxicity, the number of oligodendrocyte precursor cells were elevated while astrocyte activation was slightly, yet not significantly, increased in cuprizone-treated mice. At the time of implantation, cuprizone-treated mice, experiencing an oligodendrocyte- and myelin- depleted state, demonstrated significantly reduced recording metrics compared to control animals, which persisted between the two experimental groups until ~1-2 weeks after implantation. Beyond the first two weeks, recording performance in control animals began to decline steadily over time while cuprizone-treated animals remained relatively stable until week 6 and 7 after implantation at which point cuprizone-treated animals experienced a slight increase in recording metrics such that both groups demonstrated similar levels of performance by experimental endpoint. Histological analysis around the microelectrode array at 7 weeks post-implantation determined that neuronal densities between cuprizone-treated and control mice were matched. However, cuprizone-treated animals demonstrated a slight increase in oligodendrocyte density and a relatively large increase in axonal and myelin intensity around the implant compared to baseline. Control animals on the other hand experienced a slight decrease in oligodendrocyte density

compared to pre-insertion values. While microglia activation was matched between the two groups, cuprizone-treated mice experienced a large reduction in the number of oligodendrocyte precursor cells around the implant as well as greater and more variable astrocyte activation.

3.5.7 Limitations of Study and Future Directions

There were a few limitations inherent to the experimental design of the study that should be considered. First is the constraint of chronic cuprizone treatment. Most studies traditionally observe the effects of cuprizone administration acutely at 5-6 weeks or chronically at 12 weeks (Kipp, Clarner, Dang, Copray, & Beyer, 2009). Mice treated with cuprizone within 13-16 weeks reportedly experienced clonic-tonic seizures, systemic symptoms, and death, particularly male C57BL/6J mice (Hoffmann et al., 2008; Matsushima & Morell, 2001). This restricted the experimental window of device insertion to 7 weeks of implantation following 5 weeks of cuprizone-induced oligodendrocyte depletion and demyelination. While 7 weeks was enough to observe electrophysiological metrics of control mice gradually decline down to the level of cuprizone-treated mice, recording performances could potentially continue to decline up to 12 weeks post-insertion before plateauing (T. D. Kozai, X. Li, et al., 2014). This suggests that further discrepancies in recording quality beyond 7 weeks of insertion may be observed but would necessitate an alternative method of oligodendrocyte and myelin depletion. One study, however, reported the use of cuprizone for up to 34 weeks in female C57BL/6J mice, which may be explained by sex specificity of the cuprizone model, and would be worth considering in the future (Nomura, Bando, Nakazawa, Kanemoto, & Yoshida, 2019). Furthermore, cuprizone administration and neural recording performed in parallel with *in vivo* imaging would provide insight into the loss or regeneration of oligodendrocytes around the microelectrode implant over

time, allowing for spatial and temporal correlations between tissue responses and device performance. The second limitation is the unknown contribution of non-myelinating satellite oligodendrocyte cells, which maintain close contact with neuronal soma instead of only extending cellular projections for myelin ensheathment, to neuronal health and function (Ludwin, 1979; Taniike et al., 2002). It is known that these satellite cells are electrically-coupled within a glial syncytium and can modulate the excitability and oscillations of local circuits (Battefeld et al., 2016). However, to what extent cuprizone exposure impacts the function of these perineuronal oligodendrocytes is unknown and was not specifically examined in this study. The third limitation considers the fact that cuprizone-induced oligodendrocyte cell death and demyelination induces activation of phagocytic glial cells within the brain, such as reactive microglia and astrocytes (Gudi et al., 2014). Still, more recent work has suggested that this glia activation (microglia and astrocytes) is in response to rapid oligodendrocyte loss and myelin debris accumulation as opposed to direct activation of glia by cuprizone (Xing et al., 2018a).

While we did not observe increased activation of glial cells at 5 weeks post-cuprizone administration, GFAP+ fluorescence intensities were elevated in cuprizone-treated animals compared to controls at 7 weeks post-implantation of a microelectrode array, suggesting a long-term effect of cuprizone-induced astrogliosis. It is worth noting that neurons cannot store glucose as glycogen and do not generally engage glycogenolysis for energy production (Howarth, Gleeson, & Attwell, 2012; Kasischke, Vishwasrao, Fisher, Zipfel, & Webb, 2004). However, over short periods, hypoxic neurons are able to rely on lactate from nearby astrocytes and oligodendrocytes (that are connected to astrocytes via gap junctions) to support neuronal oxidative metabolism (Howarth et al., 2012; Kasischke et al., 2004). Therefore, one future direction may be elucidating if metabolic support mechanisms of nearby astrocytes play a crucial role in neuronal dysfunction

and silencing around chronically implanted microelectrode arrays (Nicholas J. Michelson, Alberto L. Vazquez, et al., 2018). Since glial activation and scar formation can alter device impedances and attenuate recorded neural signals, an alternative method of oligodendrocyte and myelin knockout without a glial-activating component should be considered to delineate the effects of oligodendrocyte and myelin loss on neuronal electrophysiology and electrode performance in the absence of cuprizone-induced glial cell reactivity. In addition, further investigation of whether NG2 glia proliferation, oligodendrocyte differentiation and regeneration, or remyelination events have greater influences in maintaining or improving long-term neural interface performance would facilitate focused development of biomaterial design and intervention strategies.

3.6 Conclusion

Oligodendrocyte depletion and demyelination via cuprizone administration resulted in deficits in neuronal activity and recording performance around chronically implanted microelectrode arrays. Electrophysiological analysis revealed reduced single-unit and multi-unit recording metrics at the onset of device insertion in oligodendrocyte-depleted cortical tissue compared to control animals and remained reduced throughout the duration of device implantation. Furthermore, cuprizone changed global connectivity of neural circuits within the cortex, altering oscillatory activity and laminar communication. Recordings in control mice gradually declined to the level of performance seen in cuprizone-treated animals over time, suggesting oligodendrocyte loss as a critical regulator of neuronal physiology and a potential biological failure mode of neural electrode arrays. This study highlights the importance of preserving oligodendrocyte and myelin function to improve the electrophysiological properties of neurons around chronic intracortical

microelectrode devices and reveals a potentially novel target for therapeutic intervention to enhance functional tissue recovery following CNS injury and increase the longevity and stability of neural interfacing technology.

4.0 Elucidating Dynamic Changes in the Structure and Function of Brain Mural Cells Around Chronically Implanted Neural Microelectrodes

This chapter is taken directly from a first authorship manuscript currently in preparation for journal submission titled, "Elucidating dynamic changes in the structure and function of brain mural cells around chronically implanted neural microelectrodes."

4.1 Overview

Integration of neural interfaces with minimal tissue disruption in the brain is ideal to develop robust tools that can address essential neuroscience questions and combat neurological disorder. However, implantation of intracortical devices provokes severe tissue inflammation within the brain, which requires a high metabolic demand to support a complex series of cellular events mediating tissue degeneration and wound healing. Pericytes, peri-vascular cells involved in blood-brain barrier maintenance, vascular permeability, waste clearance, and angiogenesis, have recently been implicated as potential perpetuators of neurodegeneration in brain injury and disease. While the intimate relationship between pericytes and the cortical microvasculature have been explored in other disease states, their behavior following microelectrode implantation, which is responsible for direct blood vessel disruption and dysfunction, is currently unknown. Using two-photon microscopy, we observed dynamic changes in the structure and function of pericytes during implantation of a microelectrode array over a 4-week implantation period. Pericytes respond to electrode insertion through transient increases in intracellular calcium and underlying constriction

of capillary vessels. Then, in days following the initial insertion, we revealed an influx of new, proliferating pericytes which contribute to new blood vessel formation. Additionally, in pursuit of the different brain cell factors responsible for fibrotic scar formation around implanted electrodes, we discovered a potentially novel population of reactive immune cells in close proximity to the electrode-tissue interface actively engaging in encapsulation of the microelectrode array. Ultimately, this study provides a new perspective on the complex biological sequelae occurring the electrode-tissue interface and will foster new avenues of potential research consideration and lead to development of more advanced therapeutic interventions towards improving the biocompatibility of neural electrode technology.

4.2 Introduction

Advances in implantable microelectrode technology are evolving at a rapid rate, with recent electrode designs offering the capability to interface with hundreds or thousands of neurons at a time (Steinmetz et al., 2021). Recording or manipulating brain activity with high spatial and temporal resolution has revolutionized medical treatment for individuals who suffer from neurological disabilities or debilitating brain disease (Flesher et al., 2016; C. L. Hughes, Flesher, Weiss, Boninger, et al., 2021). Despite this progress, use of neural microelectrodes for long-term clinical applications is currently unfeasible due to severe and unresolvable immune responses to an indwelling foreign body (Takashi DY Kozai, Andrea S Jaquins-Gerstl, et al., 2015; Szymanski et al., 2021; Urdaneta et al., 2022; Steven M Wellman, Franca Cambi, et al., 2018; S. M. Wellman & T. D. Kozai, 2017a; Steven M Wellman et al., 2019a). Investigators have spent the last three decades attempting to discern the biological origins of a gradual neurodegenerative fate

surrounding chronic microelectrodes, yet efforts to identify different aspects of the brain response to device implantation have been confounded by unexplained variability in research findings (Nicholas J Michelson et al., 2018; Patrick J. Rousche & Richard A. Normann, 1998; Justin C. Williams et al., 1999). Realizing the potential of a fully integrated, long-lasting neural electrode interface necessitates a more in-depth understanding of this experimental variability in the foreign body response to neural microelectrode implants.

One theory of biological variability to neural microelectrodes involves the presently unknown consequence of neurovascular damage to device implantation (Takashi DY Kozai, Andrea S Jaquins-Gerstl, et al., 2015). Insertion into a dense vascular landscape using current FDA-approved devices, which are characterized by their large three-dimensional geometric profiles and mechanically non-compliant substrates, renders the onset and spread of neurovascular injury unavoidable. Sharp, penetrating electrodes can produce variable amounts of bleeding within the brain both near and far from the site of device implantation depending on insertion conditions (Takashi Daniel Yoshida Kozai et al., 2010). The sudden influx of harmful plasma proteins into the parenchyma, previously kept isolated from the brain due to an intact blood-brain barrier, initiates a cascade of cellular and tissue processes involving neuroinflammation, glial activation, and neurodegeneration around chronically inserted microelectrodes (Takashi Daniel Yoshida Kozai et al., 2010; Steven M Wellman et al., 2019a). Pericytes are mural cells which exist on the abluminal side of the blood-brain barrier and are responsible for various regulatory, homeostatic, and neuroimmune functions within the brain (Melanie D Sweeney et al., 2016). Situated between neuronal synapses and astrocytic endfeet on one side and the endothelial barrier on the other, pericytes are uniquely positioned to communicate signals between neurons and blood vessels to drive neurovascular coupling within the brain (Kozberg & Hillman, 2016). Despite their

significance in supporting the metabolic and waste clearance demands of neurons within the brain, pericytes are currently severely underacknowledged in the study of neural electrode biocompatibility (T. D. Kozai, X. Li, et al., 2014; S. M. Wellman & T. D. Kozai, 2017a).

Immediately following a major insult to the brain, pericytes constrict capillary vessels, reduce blood flow, and subsequently perish (Dalkara, Alarcon-Martinez, & Yemisci, 2019; Di, Wu, Xie, & Lin, 2021; F. Fernández-Klett et al., 2013). This loss in pericyte number is followed by a resurgence of new cells which initiate angiogenesis and re-vascularize damaged tissue (Hess et al., 2004; Ozerdem & Stallcup, 2003). Coverage of cortical blood vessels is an important pericyte function for regulating blood-brain barrier permeability and has been linked to the neuropathology of degenerative brain diseases, such as stroke and Alzheimer's disease (Halliday et al., 2016). Due to the ability to regulate vascular permeability, pericytes also contribute to the recruitment of peripheral immune cells following injury (Rika Sakuma et al., 2016). Finally, pericytes reportedly possess mesenchymal stem cell like activity, such as differentiating into microglia-like cells during pathological conditions such as stroke (Ilknur Özen et al., 2014; Rika Sakuma et al., 2016). Nevertheless, pericytes are increasingly emerging as significant perpetuators of the neurodegenerative outcomes in brain injury and disease.

Previously, we demonstrated that pericyte densities fluctuate spatiotemporally around chronically implanted microelectrodes (Steven M Wellman et al., 2019a). Until now, the pericyte contribution to the foreign body response following neural probe implantation has been examined solely through observation of post-mortem tissue sections (T. D. Kozai, X. Li, et al., 2014; Steven M Wellman et al., 2019a), which provides only a snapshot of the tissue response outcomes at the endpoint of the experiment. Two-photon microscopy is an emerging imaging technique to longitudinally visualize the morphology and activity of different cellular populations within the

brain in real-time and offers a more detailed characterization of the dynamic tissue response to chronic brain implants (Chen, Wellman, Yaxiaer, Eles, & Kozai, 2021; J. R. Eles, A. L. Vazquez, T. D. Kozai, & X. T. Cui, 2018; T. D. Y. Kozai, A. L. Vazquez, C. L. Weaver, et al., 2012; Savya et al., 2022; S. M. Wellman & T. D. Kozai, 2018). Here, we report the use of two-photon microscopy to observe dynamic changes of brain pericytes longitudinally around chronically implanted microelectrodes *in vivo*. Specifically, we employ multiple transgenic animal models to understand the alterations, if any, in the structure and function of mural cells, as well as their relationship with neurons and glia around chronically implanted microelectrodes within the brain.

4.3 Methods

4.3.1 Experimental Animal Models

Tg(Cspg4-DsRed.T1)1Akik mice (male, 22-30 g, 8-12 weeks old) expressing fluorescent DsRed protein in vascular smooth muscle cells (vSMCs) and pericytes were obtained from Jackson Laboratories (Stock #008241, Bar Harbor, ME). Dual-fluorescent pericyte and microglia models were generated by crossing male Tg(Cspg4-DsRed.T1)1Akik mice (Cspg4-DsRed Stock #008241, Jackson Laboratories, Bar Harbor, ME) and female B6.129P-CX3cr1/J mice (CX3cr1-GFP, Stock #005582, Jackson Laboratories, Bar Harbor, ME). To visualize GCaMP expression within pericytes, male B6.Cg-Tg(Pdgfrb-CreERT2)6096Rha/J mice (Pdgfrb-CreERT2, Stock #029684, Jackson Laboratories, Bar Harbor, ME) were crossed with female B6J.Cg-Gt(ROSA)26Sortm96(CAG-GCaMP6s)Hze/MwarJ mice (Ai96(RCL-GCaMP6s), Stock

#028866, Jackson Laboratories, Bar Harbor, ME). Both male and female pups (6-8 weeks old) were used. To induce GCaMP6s expression, PDGFRβ-GCaMP6s mice were injected intraperitoneally with tamoxifen (10 mg/mL in corn oil) at a dose of 100 mg/kg on five consecutive days six weeks prior to surgery. All procedures and experimental protocols were approved by the University of Pittsburgh, Division of Laboratory Animal Resources, and Institutional Animal Care and Use Committee in accordance with the standards for humane animal care as set by the Animal Welfare Act and the National Institutes of Health Guide for the Care and Use of Laboratory Animals.

4.3.2 Surgical Probe Implantation

Probe implantation surgeries were performed as described previously (Chen, Wellman, et al., 2021; J. R. Eles et al., 2018; T. D. Kozai, J. R. Eles, A. L. Vazquez, & X. T. Cui, 2016; T. D. Y. Kozai, A. L. Vazquez, C. L. Weaver, et al., 2012; Savya et al., 2022; S. M. Wellman & T. D. Kozai, 2018). Prior to surgery, animals were sedated using an anesthetic cocktail mixture of xylazine (7 mg/kg) and ketamine (75 mg/kg). The top of the mouse head was shaved and sterilized with alternating betadine and ethanol scrubs. A single incision was made over the mouse skull followed by removal of excess hair and connective tissue. Adhesive Vetbond was applied to the skull prior to drilling. Two bone screw holes centered over each motor cortex were drilled and fitted with bone screws. A 4x4 mm sized craniotomy was created over both hemispheres. A 4-shank Michigan style microelectrode array was inserted at a 30° angle to a depth of 300 μm below the surface within the right visual cortex (1.5 mm anterior, 1 mm lateral from lambda). The contralateral cortex was left un-implanted as an un-injured control region for comparison. A silicone elastomer (Kwik-sil) was used to fill the space within the craniotomy above the brain prior

to covering with a glass coverslip and sealing the edges of the glass with dental cement for optical imaging. A separate cohort of C57BL/6J mice were implanted for post-mortem histological analysis as described previously (Steven M Wellman et al., 2019a). Similar implantation procedures were repeated in these mice with the exception of the formation of a drill-sized craniotomy over the visual cortex (1.5 mm anterior, 1 mm lateral from lambda) in which a single shank Michigan style microelectrode array was lowered to a 1.6 mm depth into the cortex at a 90° angle. Kwik-sil was applied to fill the space within the craniotomy and around the electrode prior to sealing within a dental cement headcap. Ketofen (5 mg/kg, Covetrus, Inc., Portland, ME) was provided post-operatively on the day of surgery and up to 2 days post-surgery to all implanted animals.

4.3.3 Two-photon Laser-scanning Microscopy

Two-photon microscopy was used to track the dynamic pericyte response to chronically implanted microelectrodes. The microscope was equipped with a scan head (Bruker, Madison, WI), a OPO laser (Insight DS+; Spectra-Physics, Menlo Park, CA), non-descanned photomultiplier tubes (Hamamatsu Photonics KK, Hamamatsy, Shizuoka, Japan), and a 16X, 0.8 numerical aperture water-immersive objective lens (Nikon Instruments, Melville, NY). A 920 nm & 980 nm two-photon laser wavelength were used for fluorescence excitation in PDGFRβ-GCaMP6s or Cspg4-DsRed mice, respectively. Blood vessels were visualized using either sulforhodamine 101 (intraperitoneal injection, 1 mg/mL) or a FITC-dextran dye (retro-orbital injection, 2 MDa, 10 mg/mL). Volumetric Z-stack ROIs were acquired from both the ipsilateral and contralateral hemisphere for each imaging session (0, 2, 4, 7, 14, 21, and 28 d post-implantation). Images were collected at ~5 s frame scan rate (1024x1024 pixels, ~5.0 µs dwell

time, ~1.5-2x optical zoom) and 2-3 μm step size beginning at the pial surface all the way along the full depth of the electrode implant.

4.3.4 Post-mortem Immunohistochemistry

C57BL/6J mice with perpendicularly implanted probes were sacrificed at 1-, 7-, and 28-days (n = 5) following insertion for immunohistochemical analysis. Briefly, mice were anesthetized with a xylazine/ketamine cocktail and transcardially perfused with 1X PBS followed by 4% paraformaldehyde (PFA). Probes were left intact attached the skull and within the brain and post-fixed in 4% PFA at 4°C overnight. Then, brains were extracted and allowed to equilibrate in 15% and then 30% sucrose at 4°C for 12-24 hours each. Samples were embedded and frozen in a 2:1 PBS:optimal cutting temperature (OCT) media prior to cryosectioning. Tissue sections of 25 μm thickness were collected horizontally along the entire depth of the implant. Prior to staining, sections were re-hydrated in 1X PBS for 5 min. For antigen retrieval, slides were incubated in 0.01 M sodium citrate buffer for 30 min at 60C and then in peroxidase blocking solution (10% v/v/ methanol and 3% v/v/ hydrogen peroxide) for 20 min on a table shaker at room temperature. Prior to antibody staining, sections were permeabilized with a solution of 1% triton X-100 and 10% donkey serum in PBS for 30 min at RT. To eliminate non-specific binding, sections were then blocked with donkey anti-mouse IgG fragment (fab) or 647 conjugated anti-mouse IgG fragment (Fab) for 2 h at 1:13 or 1:16 dilution at RT. Sections were then washed 8 x 4 min in 1X PBS prior to incubating in a primary antibody solution for 12-18 hr at 4°C. Primary antibodies used were rabbit anti-NG2 (1:200, ab5320, Sigma Aldrich, St. Louis, MO), goat anti-PDGFRβ (1:100, AF1042, R&D Systems, Minneapolis, MN), mouse anti-Ki67 (1:100, 550609, BD Biosciences), anti-Tomato lectin (1:250, B-1175, Vector Labs, Newark, CA).

The following day, sections were rinsed with 1X PBS three times for 5 minutes each prior to incubation with the following secondary antibodies at 1:500 in 1X PBS for 2 hr at RT: 405 donkey anti-rabbit, 488 donkey anti-goat, and 568 donkey anti-mouse (Sigma Aldrich, St. Louis, MO). After secondary antibody incubation, sections were then rinsed again with 1X PBS 3x5 min. Slides were mounted with Fluoromount-G, coverslipped, and allowed to dry overnight at RT before being stored in 4°C.

4.3.5 Data Analyses

4.3.5.1 Pericyte GCaMP Fluorescence Intensity Analysis

For acute insertion trials, PDGFRβ-GCaMP6s mice were imaged for up to 20 min post-insertion. ROIs of pericyte soma and processes were manually defined using the ROI manager in ImageJ. Fluorescence intensities were calculated as $\Delta F/F_0$, where F_0 is the average baseline fluorescence intensity averaged over 1 min pre-insertion. Activated pericytes were defined as cells whose $\Delta F/F_0$ was greater than F_0 plus three times standard deviation (3*STD) of baseline recordings. Fluorescence intensities were normalized to pre-insertion recording of calcium activity.

4.3.5.2 Pericyte Coverage Analysis

Pericyte vascular coverage following chronic electrode implantation was assessed via immune-stained sections for PDGFRβ+ pericytes and lectin+ blood vessels. Both PDGFRβ- and lectin-stained images were binarized by setting a threshold fluorescence intensity value of 2.5 times the standard deviation above the mean. Binarized images were then binned every 50 μm up to 300 μm away from the center of probe implantation. Vascular coverage was measured as the

number of overlapping PDGFRβ- and lectin-stained pixels divide by the total number of lectin-stained pixels within each bin. Pericyte coverage was then normalized to the contralateral hemisphere. Data was reported as the mean ± standard error, average across 5 mice per timepoint.

4.3.5.3 Quantification of Cspg4+/Cx3cr1+ Cell Distribution and Surface Encapsulation

The geometric distribution of the Cspg4+/Cx3cr1+ cell population was determined by generating a three-dimensional distance map of the electrode surface, as described previously (J. R. Eles et al., 2018). Briefly, the orientation angle of the electrode within the imaged volume was determined using the 'Interactive Stack Rotation' plugin in ImageJ (National Institute of Health) and used to rotate the electrode into a single horizontal plane. Then, a binary mask was created by manually defining an outline of the probe. This binary mask was then rotated back into the original electrode orientation and a distance transformation was applied to the resultant 3D mask using the 'bwdist' function in Matlab (MathWorks, Boston, MA) to form a distance map. The spatial coordinates of identified cell counts were then referenced using this distance map for each mouse and each time point quantified.

Cspg4+ and CX3cr1+ cellular encapsulation was determined as a percentage of fluorescent signal covering the surface of the implanted probe, as previously described (T. D. Y. Kozai, A. L. Vazquez, C. L. Weaver, et al., 2012; Savya et al., 2022; S. M. Wellman & T. D. Kozai, 2018). Briefly, each image volume was rotated and resliced using the ImageJ plugin "Interactive Stack Rotation" to orient the entire length of the angled probe within a single 2D plane. Then, a small volume of tissue above the probe was sum slice projected into a single image and a binary mask was created using an "IsoData" thresholding algorithm within ImageJ. The percentage of fluorescent signal was taken as the number of non-zero pixels within a manually-defined outline

of the probe over the total area measured. The final dimensions of the outlined probe area were verified prior to thresholding for accuracy.

4.3.6 Statistics

A one-way or two-way ANOVA ($p<0.05$) was used to assess for differences cell counts and cell motility over time and distance away from the electrode. Significant pairwise differences were then assessed post-hoc using a Student's t-test.

4.4 Results

In order to reveal potential alterations in the structure and function of brain pericytes following neural electrode implantation, we utilized two-photon microscopy to longitudinally assess dynamic changes in pericyte fate and morphology around chronically implanted microelectrode arrays. The Cspg4-DsRed model was chosen to identify and characterize brain pericytes based on differences in their structure, morphology, and anatomical position within the brain (Figure 4-1). Cspg4-DsRed mice were implanted with a four-shank Michigan style microelectrode under an optical window for longitudinal imaging over a 28-day implantation period.

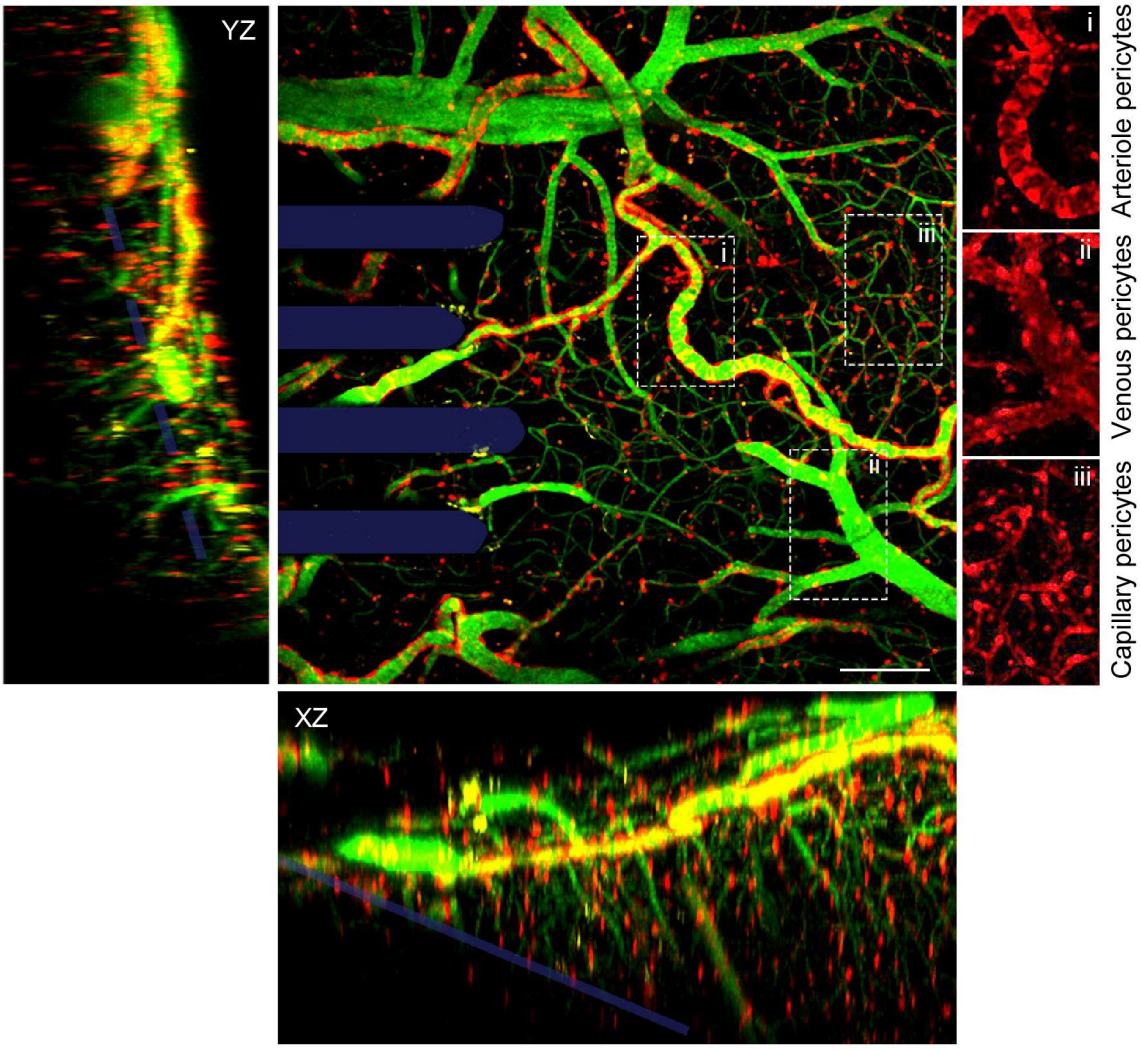

Figure 4-1 Orthogonal view of brain pericytes around an implanted multi-shank microelectrode array within Cspg4-DsRed mouse model. The Cspg4-DsRed mouse model allows us to visualize alterations in the structure and morphology of different distinct classes of brain mural cells, such as arteriole pericytes (i), venous pericytes (ii), and capillary pericytes (iii). Scale bar = 100 μm.

4.4.1 Pericytes Constrict Capillaries and Increase Intracellular Ca^{2+} Following Electrode Insertion

Pericytes possess contractile proteins that allow them to regulate cerebral blood flow by exerting mechanical forces on blood vessels (David A Hartmann et al., 2021; Nelson et al., 2020). Perturbations to the brain can produce contractions of pericyte somata and constriction of

microvessels, often time to a pathological extent (Costa et al., 2018; Yemisci et al., 2009). To determine whether pericytes respond in a similar manner to electrode insertion, we used intravital imaging to capture changes in pericytes in real-time around an implanted microelectrode (Figure 4-2a). We demonstrate that pericytes are present at positions along the capillary network where occlusions in blood flow and constriction of microvessels are apparent (Figure 4-2b). For capillary constriction, we show that vessels are constricted beyond baseline diameter at the position of pericyte soma (Figure 4-2c). We further confirm pericyte-mediated constriction of microvessels by staining explanted brain tissue using PDGFRβ for pericytes and tomato lectin for the vasculature at 7 days post-implantation in wild-type mice (Figure 4-2d). Intracellular calcium ($[Ca^{2+}]$) levels regulate the contractile machinery necessary for pericytes to mechanically constrict around blood vessels (David A Hartmann et al., 2021; Nelson et al., 2020). To determine whether electrode implantation alters pericyte Ca^{2+} activity, we implanted an electrode into the brains of PDGFRβ-GCaMP6s mice express GCaMP within PDGFRβ+ pericyte cells (Figure 4-2e). There was a transient increase in pericyte Ca^{2+} within the initial minutes following insertion followed by a decrease back to baseline levels after 20 min of implantation. While the temporal pattern of Ca^{2+} changes were similar over the course of electrode insertion, we discovered that pericyte soma demonstrate larger changes in Ca^{2+} from baseline compared to pericyte processes (Figure 4-2g). Overall, we demonstrate that pericytes produce deformations on cortical microvessels around implanted microelectrodes and respond to electrode insertion through transient increases intracellular calcium.

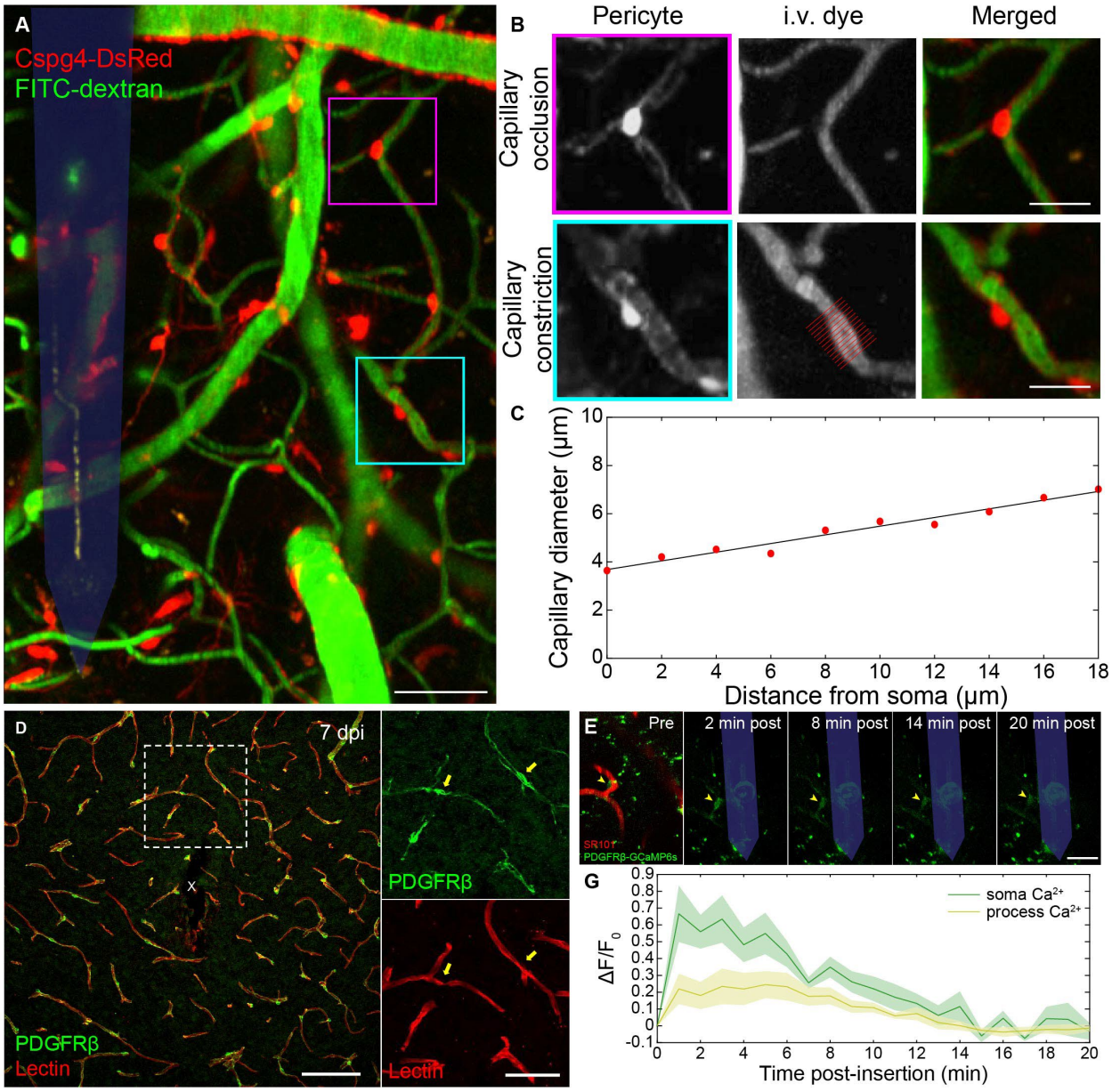

Figure 4-2 Pericytes constrict capillary vessels and transiently increase in intracellular Ca2+ following electrode insertion. (a) Two-photon image of pericytes (Cspg4-DsRed, *red*) and blood vessels (FITC-dextran, *green*) around an implanted microelectrode (*shaded blue)*. Scale bar = 50 μm. (b) Inset of (a) demonstrating regions of capillary occlusion and constriction overlap with position of pericyte soma. Scale bar = 20 μm. (c) Quantification of change in capillary diameter of with respect to distance from center of cell soma. (d) Histological image demonstrating pericytes (PDGFRβ, *green*) located on regions of deformed capillary (Lectin, *red*) structures at 7 days post-implantation of a microelectrode array (*white 'x')*. Scale bar = 50 μm, 25 μm (inset). (e) Time course of a transient increase in intracellular pericyte Ca^{2+} (PDGFRβ-GCaMP6s, *green*) near an inserted microelectrode over a 20 min implantation period. Scale bar = 50 μm. (g) Normalized fluorescence intensity profile of soma and process compartments of pericyte cell in (e) over 20-minute post-insertion period (n = 4 soma and 4 processes). All data is reported as mean ± SEM.

4.4.2 Microelectrode Implantation Promotes Pericyte Proliferation and Angiogenesis.

The acute pericyte response to severe brain injury is followed by a resurgence of proliferating, angiogenic pericytes into the damaged tissues regions. To understand whether pericytes respond similarly to electrode implantation injury, we implanted microelectrode arrays into the brains of Cspg4-DsRed mice and monitored the chronic response of pericytes over a 28-day implantation period. Previously, we demonstrated that reactive glial populations proliferate around chronically implanted microelectrodes due to their elevated expression of the proliferative marker, Ki67. Using immunohistochemistry, we show that pericytes within the microenvironment of implanted electrodes during this period of dynamic tissue remodeling, identified by co-expression of NG2 and PDGFRβ markers, also express Ki67 at 7 and 28 days post-implantation (Figure 4-3a,b). Ki67+ pericytes were not observed at 1-day post-implantation nor were they observed on the contralateral hemisphere (*data not shown*), supporting our findings that pericytes respond and proliferate specifically in response electrode implantation injury. Additionally, through our two-photon imaging experiments, we observed an influx of new pericytes accumulating at the electrode-tissue interface starting within the first week up until 28 days post-implantation (Figure 4-3c). These cells exhibited dynamic cell motility, migrating preferentially toward the surface of the electrode in order to facilitate angiogenesis. The vessels previously occupied by these cells were then devoid of pericyte coverage. Coincidentally, the diameters of these vessels which lack pericyte coverage appear markedly increase, most likely due to the loss of pericyte contact. Overall, these results support the idea that chronic electrode implantation promotes dynamic remodeling and angiogenesis with the local tissue microenvironment through a population of proliferating pericyte cells.

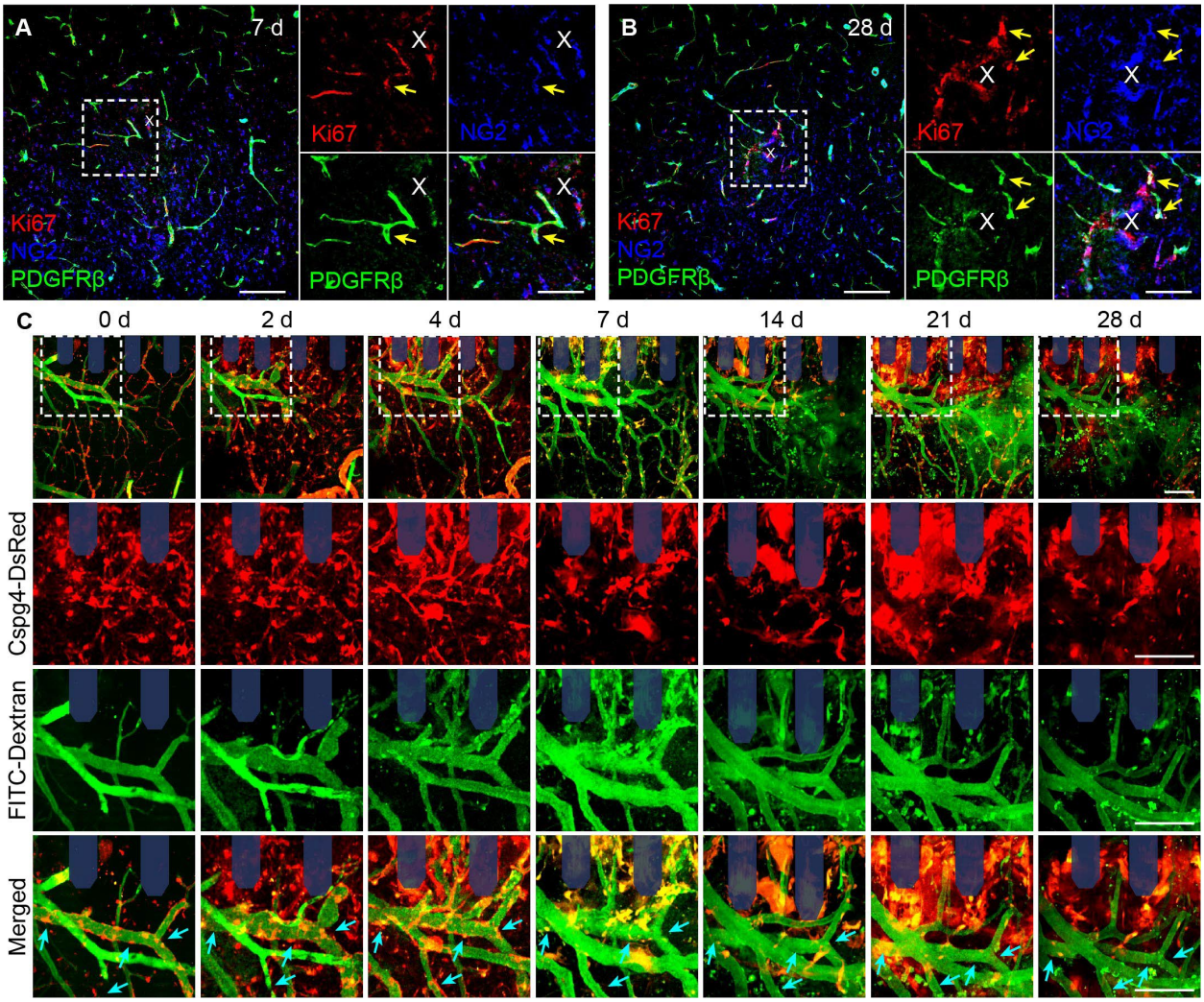

Figure 4-3 Influx of proliferating pericytes facilitate angiogenesis around implanted microelectrodes. (a-b) Histological stain of NG2+ (*blue*) and PDGFRβ+ (*green*) pericytes co-expressing proliferative marker Ki67 (*red)* around implanted microelectrodes (*white 'x'*) at 7 and 28 days post-insertion. Scale bar = 100 µm, 50 µm (inset). (c) Two-photon representation of time course of dynamic pericyte activity around chronically implanted microelectrodes (*shaded blue*). Cyan arrows indicate areas of in which blood vessels lose pericyte coverage over time. Scale bars = 100 µm.

4.4.3 Pericyte Coverage of Blood Vessels is Not Significantly Impacted by Chronic Electrode Implantation

Spatial cell coverage over microvessels within the brain is an important regulatory function unique to pericytes which allow them to maintain microvascular tone as well as modulate the level of blood-brain barrier permeability (Berthiaume, Grant, et al., 2018; Berthiaume, Hartmann,

Majesky, Bhat, & Shih, 2018). To determine whether pericyte coverage is affected by chronic electrode implantation, we visualized the amount of cellular overlap between PDGFRβ+ pericytes and lectin+ blood vessels at 1-, 7-, and 28-days post-implantation in post-mortem histological brain sections (Figure 4-4a). Quantification of the spatial coverage of pericytes with blood vessels around implanted microelectrodes revealed a slight reduction in normalized pericyte coverage compared to distal tissue within 0-50 μm distance from the probe surface at 7 days post-implantation, which returned to baseline levels by 28 days (Figure 4-4b). However, this effect of reduced pericyte vessel coverage due to microelectrode implantation was determined to not be statistically significant ($p > 0.05$, two-way ANOVA). Nevertheless, these results are in line with our two-photon findings in the previous figure and suggest that pericyte coverage of blood vessels may become impacted by implanted microelectrodes, although not significantly.

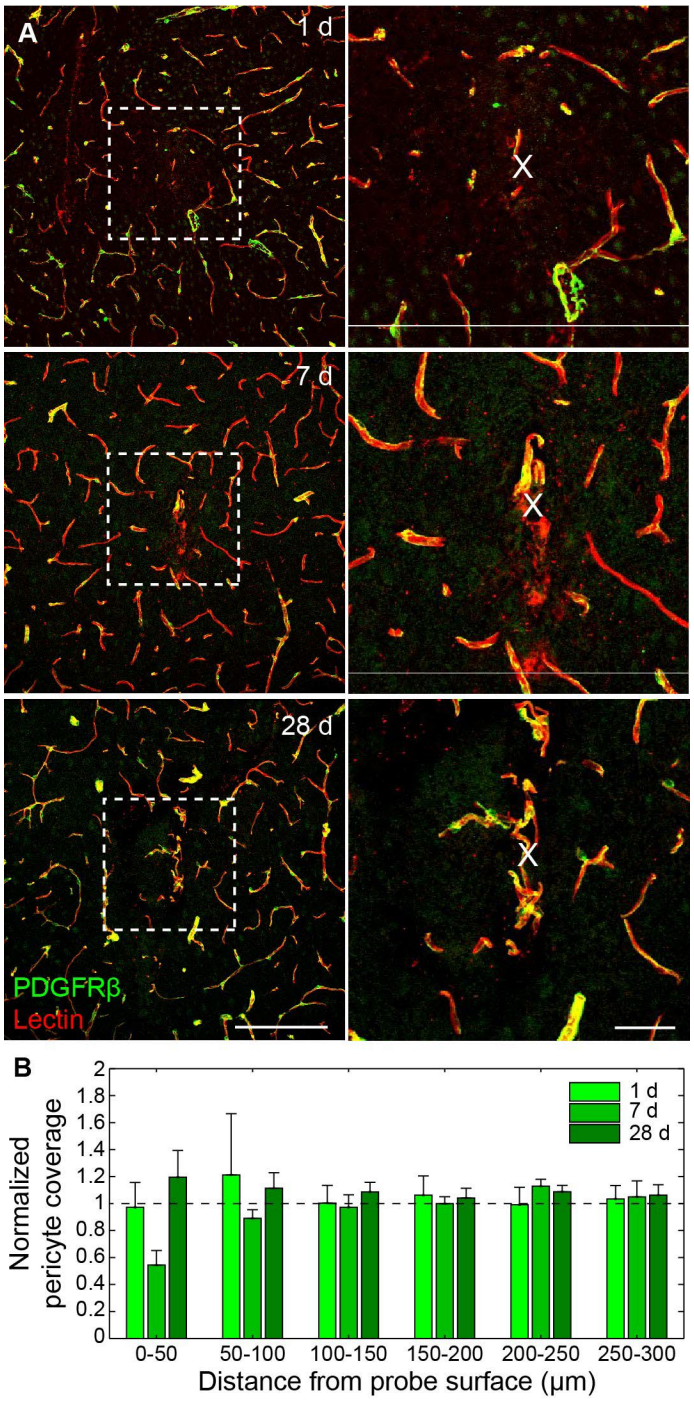

Figure 4-4 Microelectrode implantation does not have a significant impact on pericyte coverage of blood vessels. (a) Histological representation of pericyte (PDGFRβ, *green*) coverage of blood vessels (Lectin, *red*) around chronically implanted microelectrodes. Scale bar = 100 μm, 25 μm (inset). (b) Normalized pericyte coverage of blood vessels is not statistically impacted with distance from surface of implanted microelectrodes.

4.4.4 Involvement of Cspg4+ and CX3cr1+ Cells in Encapsulation of Chronically Implanted Microelectrodes

Pericytes have been previously implicated in the formation of a fibrotic scar. We previously reported on a temporally distinct pattern of device encapsulation by NG2 glia and microglia cells. To determine whether Cspg4+ expressing pericytes participated in the encapsulation of implanted microelectrodes, we generated a dual-fluorescent Cspg4-DsRed::CX3cr1-GFP mouse model to visualize electrode encapsulation of both brain cell populations within the same animal (Figure 4-5a). In the healthy, intact brain, both pericytes and microglia occupy spatially distinct tissue regions (Figure 4-5b). With chronic electrode implantation, we observe both Cspg4+ and CX3cr1+ cells gradually encapsulate the electrode surface over a 28-day implantation period (Figure 4-5c). Interestingly, we observed distinct regions on the electrode surface in which Cspg4+ and CX3cr1+ cells overlap. Upon quantitative measurement, we determined that the encapsulation region of these dual-labeled CX3cr1+/Cspg4+ cell was temporally distinct from that of Cspg4+ and CX3cr1+ areas alone (Figure 4-5d). Surface coverage peaks initially at 2 days post-implantation within CX3cr1+ only, then at 4 days post-implantation within dual-labeled CX3cr1+/Cspg4+, and then more gradually at 1-week post-implantation in Cspg4+ cells. Whereas surface coverage of individual CX3cr1+ or Cspg4+ cells have been previously recognized, here we report a spatially and temporally distinct pattern of surface encapsulation by dual-labeled CX3cr1+/Cspg4+ cells, suggesting the emergence of a novel reactive brain cell population around chronically implanted microelectrodes.

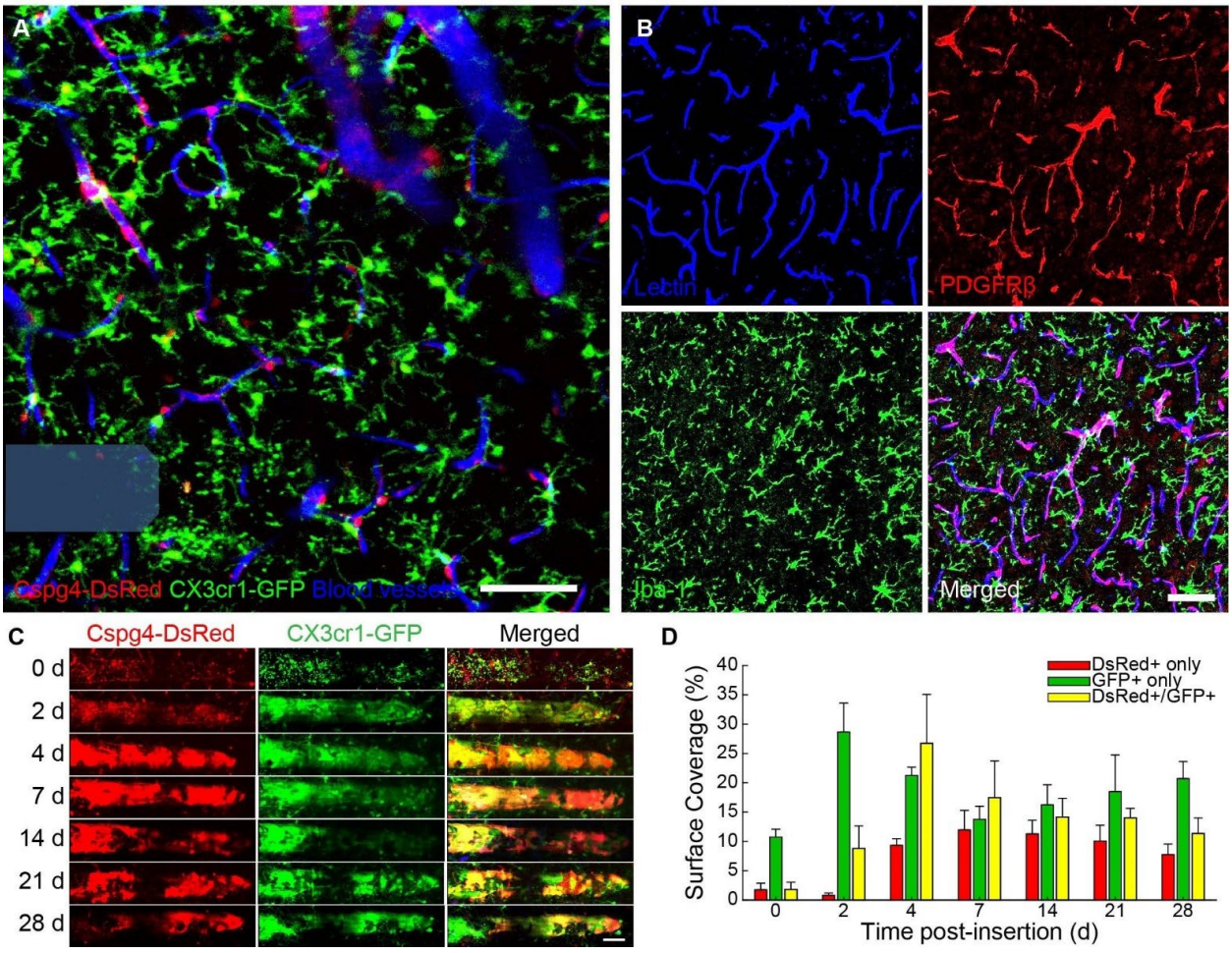

Figure 4-5 Temporal pattern of microelectrode encapsulation by spatially distinct Cspg4+ and CX3cr1+ cell populations. (a) Two-photon representative image of a microelectrode (*shaded blue*) inserted in a Cspg4-DsRed::CX3cr1-GFP. Blood vessels (*blue*) are visualized using an intravascular fluorescent dye. Scale bar = 50 µm. (b) Histological image of stained blood vessels, pericytes, and microglia in healthy, uninjured brain tissue. Scale bar = 100 µm. (c) Two-photon representative images of surface encapsulation of chronically implanted microelectrodes of Cspg4+ (*red*) and CX3cr1+ (*green*) brain populations. Yellow here denotes overlapping DsRed and GFP fluorescent signals. Scale bar = 50 µm. (d) Percent coverage of DsRed+ only, GFP+ only, and overlapping DsRed+/GFP+ signal over 28-day implantation period (n = 4 mice). All data is reported as mean ± SEM.

4.4.5 Novel CX3cr1+/Cspg4+ Population of Reactive Glial Cells Accumulate at the Site of Neural Electrode Implantation

In our pursuit of understanding the spatial relationship between activated microglia and pericyte cells following surface coverage of chronically implanted microelectrodes, we discovered the appearance of a unique population of immune cells at the electrode-tissue interface which

simultaneously express GFP+ and DsRed+ fluorophores denoting constitutive expression of both *CX3cr1* and *Cspg4* promoters (Figure 4-6a). Dual-labeled CX3cr1+/Cspg4+ cells were distinct from individual CX3cr1+ and Cspg4+ cells in morphology and positioning around chronic microelectrodes. Furthermore, these cells were not observed within contralateral (unimplanted) brain regions, suggesting an injury-specific emergence to chronically implanted devices. The appearance of CX3cr1+/Cspg4+ cells began 2-4 days, significantly increased around the first 7 days, and stabilizing toward the end of a 28-day implantation period (Figure 4-6b, $p < 0.01$, one-way ANOVA). During this time, CX3cr1+/Cspg4+ cells were observed significantly increased in very close spatial proximity (<50 μm) to the implanted electrode (Figure 4-6c**,** $p < 0.05$, one-way ANOVA). Investigation of the cortical depth in which these cells were observed revealed their positioning within 0-200 μm below the surface of the brain (layer I-II). CX3cr1+/Cspg4+ cells demonstrated active extension and retraction of processes toward the surface of the electrode over imaging short durations (<30 min) at any given time point (Figure 4-6e). Finally, CX3cr1+/Cspg4+ cells were most motile within the first week of electrode implantation, before stabilizing over the electrode surface between 2-4 weeks post-implantation (Figure 4-6f). Patterns of motility seen in our visual findings were similarly demonstrated in quantification of the motility of different cellular compartments of CX3cr1+/Cspg4+ cells, revealing high soma movement within the first week before decreasing over the following 2-3 weeks post-implantation (Figure 4-6g). Our results reveal for the first time a specialized population of reactive immune cells to the chronic implantation of a microelectrode array.

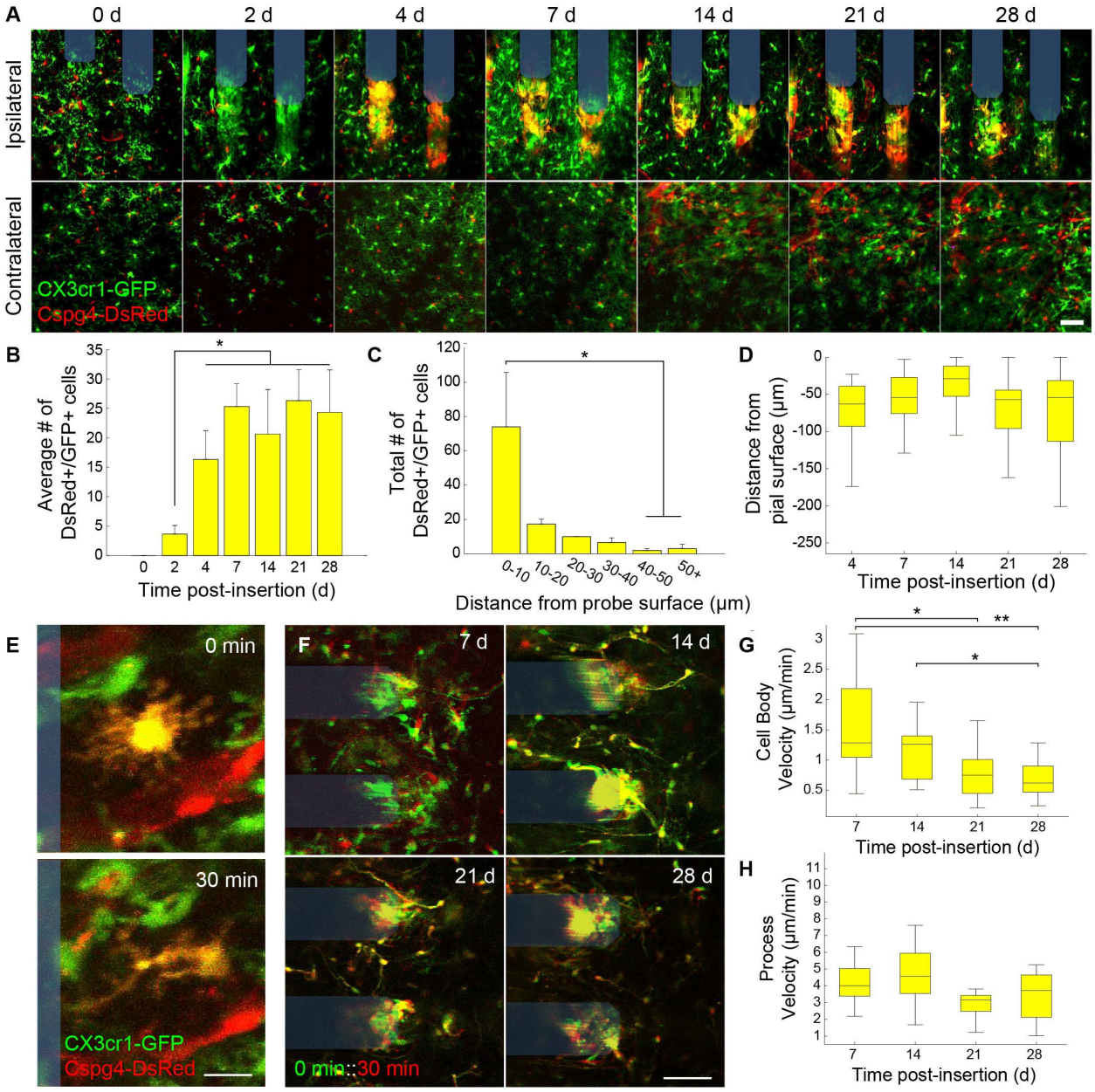

Figure 4-6 Emergence of reactive dual-labeled CX3cr1+/Cspg4+ cell population around chronically implanted microelectrodes. (a) Two-photon representative images of implanted microelectrodes (shaded blue) and contralateral control region over 28 day implantation period in a Cspg4-DsRed::CX3cr1-GFP mouse. Scale bar = 50 µm. (b) Average number of DsRed+/GFP+ cells counted over time post-insertion around chronically implanted microelectrode arrays. (c) Total number of DsRed+/GFP+ cells counted with respect to spatially binned distance away from the microelectrode surface. (d) Average distance of DsRed+/GFP+ with respect to pial surface over a 28 day implantation period. (e) Representative two-photon image demonstrating transition of DsRed+/GFP+ cell from a ramified to activated state over a 30 minute period. Scale bar = 10 µm (f) Superimposition of two time intervals 30 min apart demonstrating the change in motility of DsRed+/GFP+ cells over a 28 day implantation period. Note: Red vs. green labeling distinguishes between earlier (0 min, *green*) vs. later (30 min, *red*) timepoints, highlighting stationary features in yellow. Scale bar = 50 µm. (g) Average cell body velocity of DsRed+/GFP+ cells over a 28 day implantation period. (h) Average process velocity of DsRed+/GFP+ cells over a 28 day implantation period. * $p<0.05$, ** $p<0.01$. All data is reported as mean ± SEM.

4.5 Discussion

Penetrating microelectrodes allow researchers to interface directly with the brain and manipulate discrete brain cell populations in order to understand the function and dysfunction of our nervous system. While the long-term application of recording or stimulating electrodes can be used to diagnose and treat neurological brain dysfunction, their performance longevity and fidelity are limited by a severe foreign body response to an indwelling object within the brain. Efforts to identify the biological culprits responsible for a gradual decline in electrode performance have been obstructed by variable outcomes in the brain's response to implanted probes. One potential source of that variability may be due to a yet poorly understood impact of chronic electrode implantation on perivascular cells within the brain. Pericytes are brain mural cells responsible for governing a variety of neuroimmune, homeostatic, and regulatory functions related to neuronal network activity and neurovascular coupling. Pericyte pathology has been emerging more as a key hallmark in the neurodegenerative sequence of events of a variety of brain injury conditions as well as disease. Here, we use intravital imaging to assess the impact of chronic microelectrode implantation on the structure and function pericytes within the mouse cortex. We reveal phases of both acute and chronic responses of pericytes to chronic electrode implantation. We also report here for this first time the discovery of a novel subset of reactive immune cells around implanted electrodes encountered during our *in vivo* investigations.

4.5.1 Acute Pericyte Dysfunction in Response to Microelectrode Implantation

We revealed that insertion of a microelectrode within the brain immediately increases the intracellular Ca^{2+} levels of nearby pericytes. Neurons have also shown to transiently increase their

intracellular Ca^{2+} activity following microelectrode implantation (J. R. Eles et al., 2018). One possibility for the sequence of events observed here is that these activated pericytes are responding to electrical or chemical signals emitted from activated neurons following electrode insertion and thereby elevating their own intracellular Ca^{2+} levels. Intracellular Ca2+ activity within pericytes is invariably tied to their contractile function. However, due to the limitations in laser scan settings and image resolution, we were unable to discern whether activated pericytes during electrode insertion induced constriction of underlying capillary vessels. Nevertheless, the strength of Ca^{2+} responses was observed to be more pronounced in pericyte soma compared to their processes. This is not surprising considering the circumferential processes responsible for wrapping around capillaries and mechanically contracting the endothelial lumen are positioned closest to pericyte soma. In agreement with this idea, we demonstrate that pericytes produce maximal constriction of capillary vessels at the position of their cell soma. Similar results have been demonstrated in the presence of amyloid β oligomers within a rodent model of Alzheimer's disease, which act on pericytes by inducing pericyte constriction of microvessels (Nortley et al., 2019). We also similarly observed obstructions in capillary flow at the site of pericyte soma positioned nearby an implanted microelectrode, suggesting their contractility to electrode insertion can contribute to reductions in cerebral blood flow. While the concept of constricted microvessels and stalled blood flow around indwelling electrodes has been proposed previously, this is the first report to our knowledge implicating pericytes in the neurovascular dysfunction incurred during electrode implantation.

4.5.2 Pericytes Proliferate and Facilitate New Vessel Formation During the Chronic Response to Electrode Implantation

We previously revealed a spatiotemporal pattern of glial proliferation around chronically implanted microelectrodes (Steven M Wellman et al., 2019a). In this same study, we also reported on an increased number of PDGFRβ+ and NG2+ pericytes at 7 days post-implantation of a microelectrode array. Here, we show that this increase in number of pericytes is due to cellular proliferation within the first 7- and 28-days post-implantation. Similar time courses of pericyte proliferation and influx into damaged tissue regions following stroke have been reported (F. Fernández-Klett et al., 2013). During this time of elevated cellular proliferation, we observe pericytes facilitate angiogenesis around chronically implanted microelectrodes. Angiogenesis is a function unique to pericytes and is triggered by the binding of platelet-derived growth factor BB (PDGF-BB) secreted from sprouting endothelial tip cells onto platelet-derived growth factor receptor β (PDGFR-β) expressed on pericyte membranes (Ribatti, Nico, & Crivellato, 2011). This endothelial cell signaling recruits pericytes to areas required for re-vascularization and allows pericytes to establish contact with sprouting vessels, directing and stabilizing the endothelial growth. Angiogenesis is a regenerative tissue response following conditions of tissue hypoxia, such as in stroke, or in the case of high cellular metabolic demands, such as within the tumor microenvironment. The potential for of ischemic injury following microelectrode implantation has been reported before through hemodynamic imaging of intrinsic signals around a chronically implanted microelectrode (Nicholas J Michelson et al., 2018). Pericytes are also known to facilitate leukocyte infiltration following severe brain injury. The generation of new blood vessels around chronically implanted electrodes could be a means to recruit peripheral immune cells to the electrode implant. Indeed, infiltration macrophages has previously been shown to consist of a

significant population of immune cells around an implanted microelectrode array (Ravikumar et al., 2014). However, whether this presents a detriment to the survival of neural tissue around chronically implanted microelectrodes remains to be seen.

4.5.3 Appearance of a Distinct Subset of Reactive Immune Cells Around Chronically Implanted Microelectrodes

To our surprise, we witnessed the emergence of a phenotypically distinct population of reactive cells within the electrode-tissue interface through the generation of a dual-fluorescent transgenic mouse model. These cells seemingly expressed both *Cspg4* and *Cx3cr1* promoters given their simultaneous 1:1 expression of DsRed and GFP fluorophores, respectively. No dual labeled Cspg4+/CX3cr1+ cells were observed within the contralateral hemisphere or anywhere else within the brain, suggesting they appear specifically in response to the injury incurred from electrode implantation. Cspg4+/CX3cr1+ cells first appeared 2-4 days after electrode implantation and their numbers peaked by the end of the first week. The distribution of these cells was spatially confined to tissue areas immediately adjacent to the electrode surface (<50 μm). To our knowledge, this is the first report of its kind characterizing the appearance and behavior of a novel population of reactive cells within the electrode-tissue interface. One theory is that these cells are a reactive subset of pericytes (i.e. red cells upregulating expression of green fluorophores) operating within the fibrotic scar region of chronically implanted microelectrodes. Previous studies have reported that pericytes can develop microglia-like phenotypes in conditions of severe brain injury, such as stroke (I. Özen et al., 2014; R. Sakuma et al., 2016). In contrast, others have reported no evidence of pericyte expression of microglial markers in other pathological conditions, such as acute brain injury, which may be explained by a difference in conditions of pathology (Wenhui Huang,

Xianshu Bai, Erika Meyer, & Anja Scheller, 2020). Alternatively, these cells could constitute a subset of microglia (i.e. green cells upregulating expression of red fluorophores) who express the *Cspg4* promoter in response to electrode implantation injury. This theory is more likely given that microglia have demonstrated previously to upregulate the NG2 proteoglycan acutely in response to transient brain injury (Wenhui Huang et al., 2020). It is not clear from the data acquired in our study whether these reactive cells are fundamentally neuroprotective or neurotoxic to the tissue microenvironment around chronic electrodes. Their transitional morphologies and patterns of cell motility and behavior are reminiscent of other tissue scavengers commonly observed near the electrode surface, such as activated microglia and macrophages. Future work should be performed to characterize the functional role of these small, but reactive population of immune cells.

4.5.4 Limitations of Study & Future Directions

Despite being identified over a century ago, it is only within the last couple of decades that the physiology and pathology of pericytes were beginning to be understood (Attwell, Mishra, Hall, O'Farrell, & Dalkara, 2016; Rouget, 1873). This could be partly because pericytes are increasingly emerging as a heterogeneous group of vascular cells within the brain with a wide spectrum of genetic, structural, morphological, anatomical, physiological, and neuropathological profiles (Dias Moura Prazeres et al., 2017; David A. Hartmann, Coelho-Santos, & Shih, 2022). In the past, an inability for researchers to agree on how to robustly categorize these cells properly across different experimental studies has limited the translational application of new knowledge (Attwell, Mishra, Hall, O'Farrell, et al., 2016). For example, unlike neurons, microglia, and astrocytes, there is not one biomarker currently known that identifies only perivascular pericytes. Common pericyte markers such as NG2 or PDGFRβ are shared in some capacity by other structurally and

functionally distinct cell populations within the brain. Therefore, accurate identification and characterization of pericyte cells depends on the co-localization of two or more markers to rule out other cell populations. Furthermore, a severe lack of appropriate investigative tools and experiments models has added to the difficulty in effective study of brain pericytes in the past.

The recent development of more neuroscientific techniques and advanced animal models have shown promise on revealing the distinct role of pericytes in brain function and dysfunction (Nielson & Shih, 2022). Some in vivo dyes were found to only be taken up by certain cell populations within the brain, such as NeuroTrace 500/525 in pericytes (Damisah, Hill, Tong, Murray, & Grutzendler, 2017), and have demonstrated some success in the specific investigation of capillary pericytes. However, this dye requires topical application onto the brain and is therefore only applicable in studies which utilize an open skull preparation. In our study, we use an Cspg4-DsRed mouse model which constitutively expresses a red fluorescent protein within pericyte cells in the brain (X. Zhu, Bergles, & Nishiyama, 2008). This has been commonly used to assess pericyte physiology and pathology within the brain in the past, which can be accurately performed by identifying and characterizing cells which demonstrate the same anatomical, morphological, and structural properties as classically identified brain pericytes (i.e. anatomical position along blood vessels with "bump on a log" morphology) (Hall et al., 2014; Mishra et al., 2014; Zambach et al., 2021). However, in certain pathological conditions which promote mural cell reactivity and pericytosis, such as detachment from blood vessels and migration into the scarred region following brain injury, the assessment of pericyte fate and function becomes a bit more difficult. The Cspg4 gene encodes for the NG2 proteoglycan, which is not only expressed in pericytes but also known to be commonly expressed within oligodendrocyte precursor cells (NG2 glia), as well as microglia and astrocytes in certain pathological conditions (W. Huang, X. Bai, E. Meyer, & A. Scheller,

2020). We previously characterized the spatiotemporal reactivity of NG2 glia around implanted microelectrodes. Given the limitation in the model used, it is difficult to say whether the DsRed+ cells we observed encapsulating the electrode surface are partly from DsRed+ pericyte cells or if they consist of other glial cells which upregulate expression of NG2 following implantation injury. One way to discern whether the cells we observe within this scarred region are pericytes or not would be to employ advance transgenic mouse lines which express fluorophores under multiple pericyte promoters, such as the NG2 and PDGFRβ promoters in the recently developed pericyte-CreER line (Nikolakopoulou et al., 2019).

4.6 Conclusion

Development of advanced neural electrode technology is accelerating our understanding of nervous system health and disease at a rapid pace. Yet, despite their potential as tools for neuroscience discovery and clinical rehabilitation, intracortical electrodes regularly suffer from depreciations in detecting and modulating brain activity as a result of severe biological responses to a foreign body. Due to the inherent complexity of the brain's immune response to device injury, the mechanisms which govern biological failure modes of neural implants remain unknown. Efforts to pinpoint exact biological correlates of device performance are confounded by a poorly understood heterogeneity of immune cells (i.e. myeloid cells) within the brain which are known regulate tissue homeostasis, inflammation, and wound repair following injury. Brain pericytes are one such myeloid population whose contribution to the bodily tissue reactions to implanted electrodes is currently unknown. Here, we employed two-photon imaging of multiple transgenic mouse models over a 28-day implantation period to elucidate dynamic changes in the fate and

behavior of pericyte cells during the course of microelectrode implantation. We discovered that pericytes are dynamic in the presence of chronically implanted electrodes, initially constricting around capillary microvessels in response to electrode insertion before actively engaging in tissue remodeling at the electrode-tissue interface. During our investigation we also reveal distinct population reactive immune cells present within the scar region of chronically implanted microelectrodes. Future work further characterizing the heterogeneity in brain tissue responses of the pericyte population and their pathological roles within the brain will facilitate the development of more biologically adaptive implants and innovative therapeutic strategies to combat the body's inherent immune response to brain injury and disease.

5.0 Aberrant Accumulation of Age- and Disease-associated Factors Following Neural Probe Implantation in a Mouse Model of Alzheimer's Disease

This chapter is taken directly from a first authorship manuscript currently in preparation for journal submission titled, "Aberrant accumulation of age- and disease-associated factors following neural probe implantation in a mouse model of Alzheimer's disease."

5.1 Overview

Electrical stimulation has had a profound impact on our current understanding of nervous system physiology and provided viable clinical options for addressing neurological dysfunction within the brain. Unfortunately, the brain's immune suppression of indwelling microelectrodes currently presents a major roadblock in the long-term application of neural recording and stimulating devices. In some ways, brain trauma induced by penetrating microelectrodes produces similar neuropathology as debilitating brain diseases, such as Alzheimer's disease (AD), while also suffering from end-stage neuron loss and tissue failure. To understand whether there may be any parallel mechanisms at play between brains suffering from chronic microelectrode implantation and those of neurodegenerative disorder, we used two-photon microscopy to visualize the accumulation, if any, of age- and disease-associated factors around chronically implanted electrodes in mouse models of AD. With this approach, we determined that electrode injury leads to aberrant accumulation of lipofuscin, an age-related pigment, in wild-type and AD mice alike. Furthermore, we reveal that chronic microelectrode implantation reduces the growth

of pre-existing amyloid plaques while simultaneously elevating amyloid burden at the electrode-tissue interface. Lastly, we uncover novel spatial and temporal patterns of glial reactivity, axonal and myelin pathology, and neurodegeneration related to neurodegenerative disease around chronically implanted microelectrodes. This study offers multiple novel perspectives on the possible neurodegenerative mechanisms afflicting chronic brain implants, spurring new potential avenues of neuroscience investigation and design of more targeted therapies for improving neural device biocompatibility and treatment of degenerative brain disease.

5.2 Introduction

Penetrating microelectrodes offer investigators and clinicians a multi-modal approach for recording discrete signals from the brain and exogenously manipulating neuronal activity with high spatial and temporal resolution (Andrew B. Schwartz et al., 2006). Intracortical microstimulation in particular is an emerging clinical technique for restoring lost or impaired brain function and treating neurological disorders (Flesher et al., 2016; C. L. Hughes, Flesher, Weiss, Boninger, et al., 2021). Yet, significant unknowns in how artificially generated electrical current affects the sensitive biological milieu of the brain or even how the presence of an indwelling foreign object alters the structure and physiology of various brain cells limit the long-term clinical applications of the technology (Takashi DY Kozai, Andrea S Jaquins-Gerstl, et al., 2015; Nicholas J Michelson et al., 2018; S. M. Wellman & T. D. Kozai, 2017a; Steven M Wellman et al., 2019a). Furthermore, current standard operating procedures do not presently screen clinical users of implantable neural interfaces for potential history of genetic predisposition to neurodegenerative

or neurological disease, presenting a significant confound toward current efforts in understanding the brain's immune response to neural electrode implants.

Implantation of intracortical microelectrodes can have devastating and long-lasting effects on neuronal health and brain function. Insertion of a stiff, sharp object immediately severs neurons, axons, and blood vessels within the parenchyma, generating mechanical strain, neuroinflammation, and cerebral bleeding (Chen, Wellman, et al., 2021; J. R. Eles et al., 2018; Takashi Daniel Yoshida Kozai et al., 2010; Nicholas J Michelson et al., 2018). This acute insult leads to the activation of local glial and immune cells and release of factors which promote pro-inflammation, excitotoxicity, and oxidative stress, compromising local metabolic support (Takashi DY Kozai, Andrea S Jaquins-Gerstl, et al., 2015). The long-term presence of an indwelling electrode eventually results in the development of an encapsulating glial scar that is impermeable to the diffusion of ions and metabolites required to detect neuronal activity, physically displacing neurons farther from the device surface and promoting a neurotoxic microenvironment (Nicholas J Michelson et al., 2018; Savya et al., 2022). The gradual decline in performance and fidelity of recording and stimulating electrodes is ultimately attributed to this seemingly unavoidable progression in gliosis and neurodegeneration (C. L. Hughes, Flesher, Weiss, Downey, et al., 2021). However, attempts at identifying biological correlates of signal degradation, such as glial activation and neuronal viability, have proven unsuccessful, suggesting other biological mechanisms may be responsible for brain tissue response outcomes and long-term device performance (Nicholas J Michelson et al., 2018).

Age-related degenerative brain diseases, such as Alzheimer's disease (AD), culminate in late-stage neuron loss and tissue failure on account of presently unknown neurodegenerative mechanisms which gradually worsen over time (Vickers et al., 2000; Zlokovic, 2011). AD is

characterized by the appearance of extra-synaptic amyloid beta (Aβ) plaques and intra-neuronal neurofibrillary tau tangles and is clinically diagnosed by functional impairments in cognition and behavior. Despite several clinical trials demonstrating promising therapeutic potential at reducing Aβ and tau pathology or ameliorating clinical symptoms (Salloway et al., 2014; Zlokovic, 2011), there is currently no known cure or effective treatment for AD. The inherent biological cause(s) of AD remain elusive but several genetic (e.g. *APOE*, *APP*, *TREM2*) (Guerreiro et al., 2013; Neu et al., 2017; Sims et al., 2017) and non-genetic (Cations et al., 2018) (e.g. diet, exercise, cardiovascular health, and brain injury) risk factors for developing AD have been proposed. Particularly, trauma suffered to the brain has been linked to an increased risk of AD, years after the initial insult, and is most likely due to the nature in which brain injury and dementia share similar patterns of neurodegeneration(Gardner et al., 2014). The progression of AD as it is currently known shares many similarities with that of focal injury from a penetrating electrode array such as neuroinflammation, glial activation, and vascular injury. Hyperphosphorylated tau, a precursor for development of pathological tau tangles observed in AD, is reportedly elevated near chronically implanted microelectrodes within both wild-type rats and human Parkinsonian patients (George C McConnell et al., 2009). It is currently unknown, however, whether the neurotrauma suffered by intracortical microelectrodes in healthy control subjects is in any way similar to that observed in AD progression.

Characterizing Aβ deposition and tau accumulation in Alzheimer's and other neurodegenerative diseases often require the use of genetically specialized and aged mouse models, a cost- and time-expensive process. Furthermore, it is often difficult to pinpoint the biological processes responsible for the onset and progression of neurodegeneration. In contrast, focal tissue injury due to insertion of a penetrating microelectrode at a known time and location

within the brain allows for neurodegenerative processes to be spatiotemporally characterized from the onset. In this study, we investigated the appearance, if any, of age- and disease-associated factors following chronic implantation (12-16 weeks) in healthy, wild-type mice as well as a genetically susceptible mouse model of Alzheimer's disease (APP/PS1). We hypothesized that the foreign body response to intracortical electrodes promotes the onset and progression of brain pathology typically observed within aging and degenerative brain disease, resulting in long-term neuron loss. Using *in vivo* imaging and immunohistology, we determined that microelectrode implants exacerbate the accumulation of aberrant proteins such as lipofuscin and amyloid and promote the expression of other pathological factors associated with degenerative brain disease. Future work improving our understanding of neurodegenerative processes occurring at the intersection of brain injury and disease will have a profound impact on development of future intervention strategies for both implantable neural interfaces and neurological disorders within the brain.

5.3 Methods

5.3.1 Experimental Animal Models

C57BL/6J (2 months old and 18 months old, male, 22-30g, strain# 664, Jackson Laboratories; Bar Harbor, ME), B6.Cg-Apoe$^{tm1.1(APOE*4)Adiuj}$App^{em1Adiuj}Trem2^{em1Adiuj}/J (18 months old, male, 22-30g, strain# 30670, Jackson Laboratories; Bar Harbor, ME), and APP/PS1 (2 months old and 6 months old, male, 22-30g, strain# 34829, Jackson Laboratories; Bar Harbor, ME) were used in this study. All animal care and procedures were performed under approval of the University

of Pittsburgh Institutional Animal Care and Use Committee and in accordance with regulations specified by the Division of Laboratory Animal Resources.

5.3.2 Probe Implantation Surgery

Mice were implanted with a four-shank Michigan style microelectrode array for awake, head-fixed imaging, as described previously (Chen, Wellman, et al., 2021; J. R. Eles et al., 2018; Takashi DY Kozai, James R Eles, et al., 2016; T. D. Y. Kozai, A. L. Vazquez, C. L. Weaver, et al., 2012; Savya et al., 2022; S. M. Wellman & T. D. Kozai, 2018). Briefly, mice were sedated with an anesthetic cocktail (7 mg/kg xylazine and 75 mg/kg ketamine). The surgical site was shaved and sterilized 2-3 times with alternate scrubs of an aseptic wash and 70% ethanol. Mice were then fixed to a stereotaxic frame and a small incision was made over the skull. Care was given to remove all skin, hair, and connective tissue from the surface of the skull before a thin layer of Vetbond (3M) was applied to the surface. A rectangular head bar was fixed to the skull for awake, head-fixed imaging. Four bone screw holes were drilled and bone screws inserted over both ipsilateral and contralateral motor cortices and lateral visual cortices to secure the head bar. A 4 mm by 4 mm bilateral craniotomy was performed prior to probe insertion. The skull was periodically bathed in sterile saline to prevent the skull from overheating during drilling. Probes were inserted through an intact dura into the cortex at a 30° angle at 400 μm/s for a total linear distance of ~600 μm (oil hydraulic Microdrive; MO-82, Narishige, Japan) and final z-depth of ~250-300 μm beneath the pial surface. The craniotomy was filled with sealant (Kwik-Sil) before sealing with a glass coverslip and dental cement. Anesthesia was maintained throughout the surgery with ketamine (40 mg/kg), as needed. For immunohistochemistry, a separate cohort of C57BL/6J and APP/PS1 mice were implanted as described above with the exception of a single-

shank Michigan-style array implanted at a 90° angle, as described previously(Steven M Wellman et al., 2019a). Ketofen (5 mg/kg) was provided post-operatively up to two days post-surgery or as needed.

5.3.3 Two-photon Imaging and Aβ Labeling

Two-photon microscopy was used to track the rate of amyloid deposition or clearance around implanted microelectrodes over a 16-week implantation period (0, 2, 4, 7, 14, 21, 28, 56, 84, and 112 days post-implantation), as described previously (Chen, Wellman, et al., 2021; T. D. Y. Kozai, A. L. Vazquez, C. L. Weaver, et al., 2012; Savya et al., 2022; S. M. Wellman & T. D. Kozai, 2018). The microscope was equipped with a scan head (Bruker, Madison, WI), a OPO laser (Insight DS+; Spectra-Physics, Menlo Park, CA), non-descanned photomultiplier tubes (Hamamatsu Photonics KK, Hamamatsy, Shizuoka, Japan), and a 16X, 0.8 numerical aperture water-immersive objective lens (Nikon Instruments, Melville, NY). To visualize amyloid, mice were injected intraperitoneally with methoxy-X04 (2 mg/kg, Abcam, #ab142818) 24 hours prior to imaging[20]. Mice were retro-orbitally injected with FITC-dextran (2 MDa, 0.03 mL at 10 mg/mL) immediately prior to imaging to visualize surrounding blood vessels. The vasculature was used as a landmark to ensure similar ROI fields were captured between subsequent imaging sessions. Methoxy-X04 was excited at a 740 nm laser excitation wavelength and care was given not to exceed >20-30 mW of power during chronic imaging. Z-stacks were collected along the full depth of the implant at a step size of 2-3 μm, ~5 s frame rate, and zoom factor of ~1.5-2x.

5.3.4 Immunohistochemical Staining

C57BL/6J and APP/PS1 mice were sacrificed and perfused according to University of Pittsburgh IACUC approved methods at 1 week (n = 6 per group) or 16 weeks (n = 7 per group) post-implantation, as described previously (Steven M Wellman et al., 2019a). Briefly, mice were sedated using a cocktail mixture of xylazine (7 mg/kg) and ketamine (75 mg/kg). A toe-pinch test was performed to ensure proper level of anesthesia prior to beginning the procedure. For each mouse, 100 mL of warm phosphate buffered saline (PBS) was perfused transcardially (pump pressure between 80-100 mm Hg) followed by 100 mL of 4% paraformaldehyde (PFA). Mice were then decapitated with both skull and implant left intact for 24 h post-fixation at 4°C in 4% PFA. Brains were then carefully detached from both the skull and implant and sequentially soaked in 15% and 30% sucrose in PBS at 4°C for 24 h each. Once the brain samples had reached sucrose equilibration, they were frozen in a 2:1 ratio of 20% sucrose:optimal cutting temperature compound (Tissue Tek, Miles Inc., Elkhart, IN, United States). Frozen brain samples were then sectioned horizontally using a cryostat (Leica Biosystems, Wetzlar, Germany) at a 25 μm thickness throughout the entire depth of the implant (~1600 μm).

Before staining, frozen tissue sections were re-hydrated with two washes of 1x PBS for 5 min each. For antigen retrieval, slides were incubated in 0.01 M sodium citrate buffer for 30 min at 60°C. Slides were then incubated in in a peroxidase blocking solution (10% v/v methanol and 3% v/v hydrogen peroxide in 1x PBS) for 20 min on a table shaker (60 r.p.m.) at room temperature (RT) to block for active aldehydes and reduce the chance of non-specific binding. Sections were then pre-treated with a solution of 1% triton X-100 and 10% donkey serum in 1x PBS for 1 hr at RT followed by blocking endogenous mouse immunoglobulin G (IgG) with donkey anti-mouse IgG fragment (Fab) for 2 h at 1:10 dilution at RT. Then, sections were rinsed with alternating

washes of 1x PBS and 1x PBS-T (1% v/v of Tween-20 in 1x PBS) for 4 times 4 min each. Primary antibodies were diluted in solution of 1% triton X-100 and 10% donkey serum and applied to slides for 12-18 hr at 4°C. All primary antibodies used in this study are listed in Table 5-1. Sections were rinsed in 3x5 min washes of 1x PBS the following day. Secondary antibodies were diluted 1:500 in 1x PBS and applied to slides for 2 hr at RT. Secondary antibodies used were: 488 donkey anti-goat, 488 donkey anti-mouse, 568 donkey anti-rat, 568 donkey anti-sheep, 647 donkey anti-mouse, 647 donkey anti-chicken, 647 donkey anti-rabbit, 647 streptavidin (Sigma Aldrich, St. Louis, MO). Then, slides were rinsed once more with 3x5 min washes of 1x PBS. To stain for cell nuclei, slides were incubated in Hoechst 33342 (Invitrogen) at 1:1000 in 1x PBS for 10 min at RT followed by another rinse 3x5 min with 1x PBS. Finally, slides were cover slipped using Fluoromount-G (Southern Biotech, Birmingham, AL, United States) and sealed prior to imaging.

Table 5-1 List of primary antibodies used for immunohistochemical staining.

Primary antibody	Target	Supplier	Host	Dilution
Anti-6E10	Amyloid beta	Enzo Life Sciences (ABS612)	Rb	1:200
Anti-APP	Amyloid precursor protein	Abcam (ab2084)	Gt	1:400
Anti-AT8	Phospho-tau	Thermo Fisher (MN1020B)	Biotin	1:250
Anti-GFAP	Astrocytes	Abcam (ab4674)	Ck	1:500
Anti-Iba1	Microglia	Sigma (MABN92)	Ms	1:400
Anti-Myelin Basic Protein	Myelin	Abcam (ab7349)	Rt	1:100
Anti-NeuN	Neurons	Thermo Fisher (MA5-33103)	Ms	1:500
Anti-NF200	Neurofilament	Sigma (N5389)	Ms	1:250
Anti-Trem2	Triggering receptor expressed on myeloid cells 2	R&D Systems (AF1729)	Sh	1:100

Samples were imaged using a confocal microscope (FluoView 1000, Olympus, Inc. Tokyo, Japan) using a 20x oil-immersive objective lens (Nikon Instruments, Melville, NY). For each section, an ipsilateral and contralateral image was captured using same laser intensity and image settings for data normalization. For each image, a z-stack was collected consisting of 6 image

planes each spaced 5 μm apart (635.9 x 635.9 μm, 1024 x 1024 pixels on FV10-ASW Viewer V4.2). Raw images were saved as 16-bit grayscale TIFFs.

5.3.5 Data Analysis

For two-photon quantification, the distance between lipofuscin granules or amyloid plaques and the implant were determined by referencing to a 3D distance map of the electrode surface, as described previously (J. R. Eles et al., 2018). First, a 2D mask of the electrode footprint was manually outlined within ImageJ (National Institute of Health). Considering the original electrode implantation angle of 30-35°C, this 2D electrode mask was digitally rotated using ImageJ's built-in 'Interactive Stack Rotation' tool. A distance map was then generated by applying a distance transform to this 3D mask using the 'bwdist' function in Matlab (MathWorks, Boston, MA). The spatial coordinates of segmented lipofuscin granules or amyloid plaques were cross-referenced with this 3D distance map to determine the nearest Euclidean distance to the electrode surface for each timepoint.

For lipofuscin quantification, lipofuscin granules were identified by their natural autofluorescence signal detected across multiple emission filters (595nm for green and 525nm for red, 50nm bandpass). First, multi-channel z-stack images were spectrally unmixed using the ImageJ plugin, 'LUMoS Spectral Unmixing'. Then, background noise was subtracted by applying a Gaussian filter (sigma = 20) to the unmixed image containing the lipofuscin signal and subtracting the filtered image from the original. Background was further reduced by applying a bandpass filter, followed by a median filter, then finally using ImageJ's 'Despeckle' function. The resultant image was binarized by applying a fluorescence intensity threshold (mean + 2.5 standard deviation) before running the '3D Objects Counter' plugin to determine the size and spatial

coordinates of segmented lipofuscin granules. For amyloid quantification, images with methoxy-X04 signal and 6E10 signal were processed similarly as described above. The spatial coordinates of both amyloid clusters and plaques were referenced to respective 3D electrode distance map for each timepoint. The rate of change in size of individual amyloid plaques were tracked longitudinally by referencing with the vasculature as a landmark.

For fluorescence intensity analyses of stained tissue, images were processed using an automated intensity-based custom Matlab script (INTENSITY Analyzer), as described previously (T. D. Kozai, Z. Gugel, et al., 2014; Steven M Wellman et al., 2019a). Briefly, images were binned concentrically every 10 μm up to 300 μm away from the probe center. The average grayscale intensity was calculated for every pixel above a threshold determined from the intensity of the background noise for each bin. Fluorescence intensities were then normalized using average intensity values collected from the contralateral hemisphere of the section (i.e., intact hemisphere). For cell counting of stained tissue, images were binned concentrically every 50 μm up to 300 μm away from the probe center. Cells were identified and counted based on the presence of DAPI-stained nuclei and data was similarly normalized using cell counts from the contralateral hemisphere. Normalized intensity and cell counts were average over all animals per timepoint per group and presented as mean ± standard error.

5.3.6 Statistics

A two-way repeated measures ANOVA ($p < 0.05$) was used to determine significant differences in changes in plaque volume, staining fluorescence intensities, and histological cell counts between WT and APP/PS1 mice followed by a post-hoc t-test to determine pairwise

significances between groups. A Student's t-test ($p < 0.05$) was used to determine significant differences in 6E10 staining plaque area.

5.4 Results

Unlike humans, rodents do not develop Alzheimer's pathology naturally with aging. Therefore, specially developed transgenic mouse models are required to study the development of neuropathology within Alzheimer's disease. Here, we use the APP/PS1 mouse model expressing a humanized form of the *APP* gene, which promotes overexpression of the amyloid precursor protein, as well as the *PSEN1* gene, which controls for expression of the enzyme presenilin 1 required for proteolytic cleavage of amyloid (Figure 5-1a). These mice have been extensively characterized for study of Alzheimer's disease and therefore their temporal onset and progression of amyloid pathology is well known (Yan et al., 2009). To determine whether chronic electrode implantation leads to accumulation of age- or disease-associated factors, we used two-photon microscopy to longitudinally quantify aberrant protein aggregation around a multi-shank Michigan style microelectrode array within the WT and AD mouse cortex (Figure 5-1b). To assess lipofuscin accumulation, mice were aged to 18 months prior to electrode implantation surgery. To assess for amyloid deposition, 2-month-old and 6-month-old APP/PS1 mice were intraperitoneally administered methoxy-X04 (MX04), a Congo-red derivative which binds to amyloid and tau, 24 hrs prior to each imaging session (Figure 5-1c).

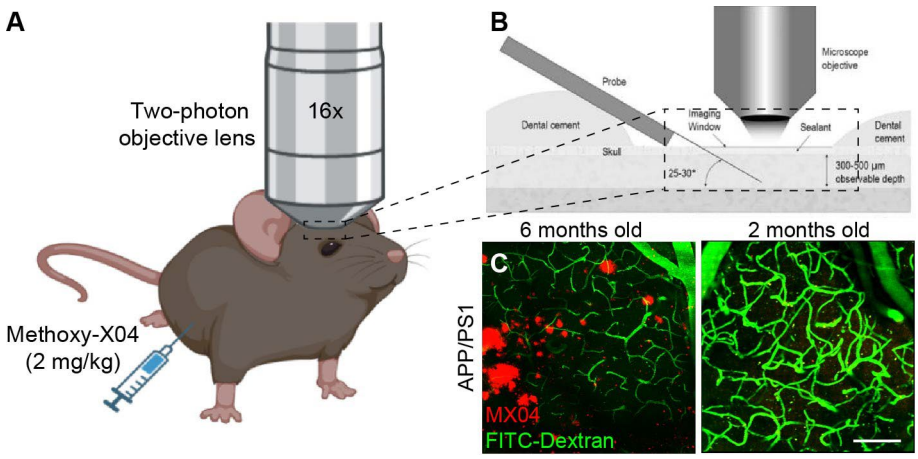

Figure 5-1 Two-photon visualization of age- and disease-related factors in a mouse model of Alzheimer's disease. (a) Methoxy-X04 (2 mg/kg) was administered to APP/PS1 mice in order to visualize amyloid deposition within the mouse brain using two-photon microscopy. (b) Schematic of microelectrode implantation within the mouse cortex underneath an optical window for longitudinal imaging of chronic tissue response. (c) Representative two-photon image demonstrating age-dependency of plaque visualization (MX04, red) in APP/PS1 mice. Vasculature is labeled with FITC-dextran (green). Scale bar = 100 µm.

5.4.1 Aberrant Accumulation of Lipofuscin Around Chronically Implanted Electrodes in Aged WT and AD mice

To assess whether chronic microelectrode implantation leads to aberrant protein aggregation with aging or in neurodegenerative disease, lipofuscin was assessed over a 12-week implantation period in an 18-month-old AD mouse model (hAbeta/APOE4/Trem2*R47H). The hAbeta/APOE4/Trem2*R47H mouse is a triple mutant strain carrying a humanized *ApoE* knock-in mutation, a humanized *App* allele, and a *Trem2* mutation. Lipofuscin, an aging pigment with natural auto-fluorescent properties that can be imaged without the need for transgenic models or additional fluorophore labeling, was identified by 1:1 fluorescent signal detected across multiple wavelength emission filters using two-photon microscopy (Figure 5-2a). Accumulation of lipofuscin was readily observed over time around an implanted microelectrode array in both the hAbeta/APOE4/Trem2*R47H model and an age-matched wild-type mouse (Figure 5-2b). Lipofuscin granules increased in volume and accumulated in larger densities with closer proximity

to the implant surface (Figure 5-2c,d). These results demonstrate that chronic microelectrode arrays suffer from aberrant protein aggregation near the site of implantation.

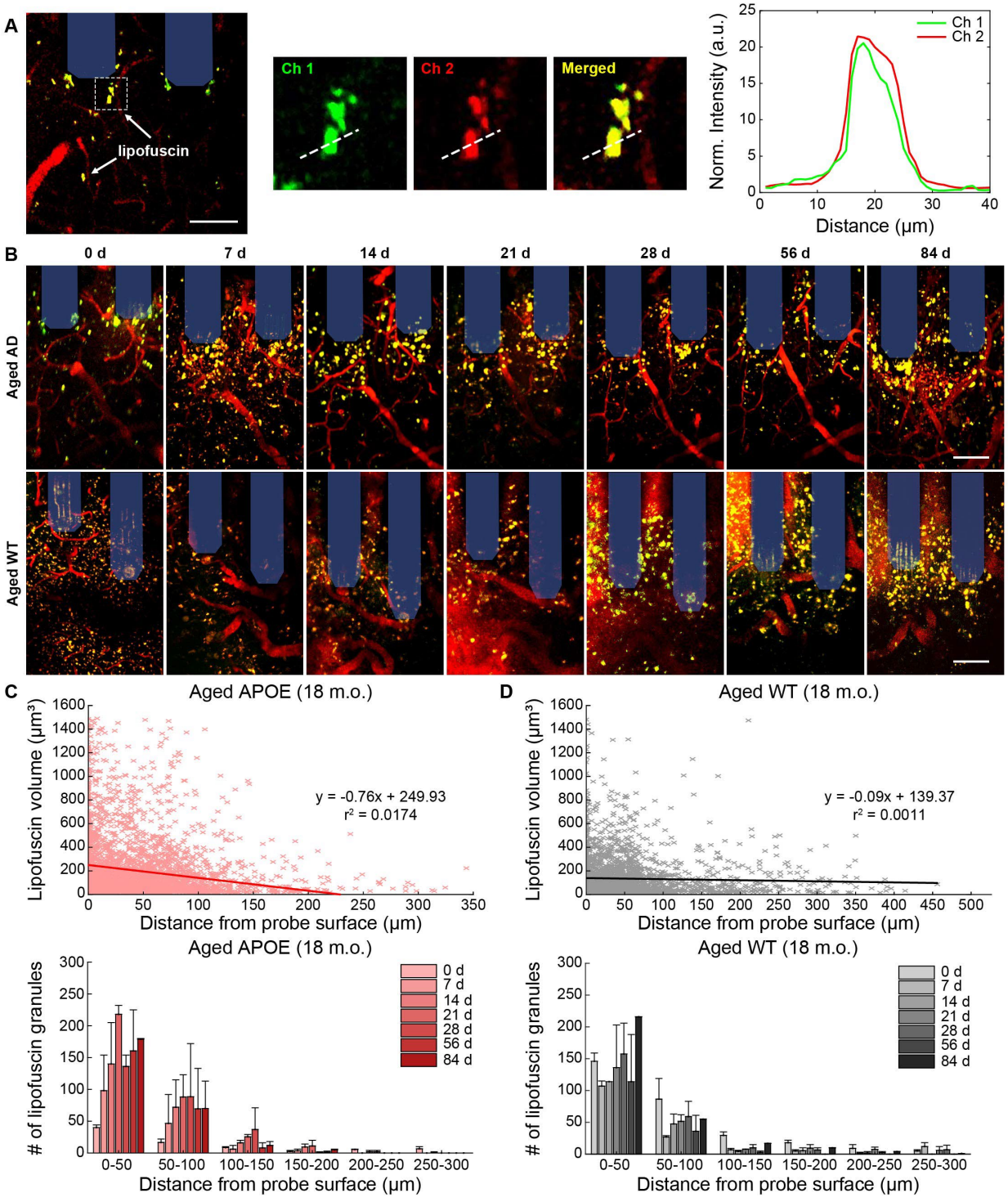

Figure 5-2 Lipofuscin accumulation around chronically implanted microelectrodes in aged WT and AD mice. (a) Example two-photon image of lipofuscin signal detected across multiple wavelength emission filters. Lipofuscin

can be detected by a 1:1 fluorescence intensity overlap in both red and green filtered channels. (b) Representative two-photon images of accumulated lipofuscin granules (*yellow*) around multi-shank microelectrode array (*shaded blue*) over 12-week post-implantation in aged (18 m.o.) WT and AD mice. Scale bars = 50 μm. (c-d) Scatter plots demonstrating trend in volume of lipofuscin granules with respect to distance from probe surface (aged APOE: 3,173 lipofuscin granules across 7 timepoints; aged WT: 2,757 lipofuscin granules across 7 timepoints). (e-f) Average number of lipofuscin granules with binned distance from the probe in aged AD and WT mice (n = 2 mice per group). All data is reported as mean ± SEM.

5.4.2 Chronic Electrode Implantation Halts the Growth of Pre-existing Aβ Plaques While Promoting Local Accumulation of New Amyloid Clusters

Amyloid beta (Aβ) is another protein whose aggregation and insufficient clearance from the brain is implicated in aging and neurodegenerative disease. To understand whether device implantation injury impacts the morphology of pre-existing Aβ plaques within the brain, we inserted microelectrodes within 6-month-old APP/PS1 mice and longitudinally assessed the growth of nearby Aβ plaques using intravenously administered MX04 over a 12-week implantation period. At this age, APP/PS1 mice readily present Aβ plaques throughout the cortex and therefore provide the opportunity assess changes in volume of pre-existing plaques around chronically implanted microelectrodes (Figure 5-3a). In the uninjured cortex of APP/PS1 mice, Aβ plaques begin to manifest around 5 months of age and continually increase in size until around 10-12 months. Surprisingly, we reveal that the Aβ plaques located on the ipsilateral hemisphere around chronically implanted microelectrodes do not change in size with chronic implantation compared to plaques on the contralateral hemisphere, whose volumes were significantly increased (Figure 5-3b, $p<0.05$, two-way ANOVA). We also show that the plaques quantified on the ipsilateral hemisphere near implanted microelectrodes decrease in size over a 12-week implantation period whereas plaques distal from the electrode demonstrate a significant increase in percent change in volume during the implantation period (Figure 5-3c, $p<0.05$, two-way ANOVA). In support of our *in vivo* imaging results, we demonstrate via immunohistochemical

staining of post-mortem tissue for 6E10, a common AD marker used to label amyloid beta, that amyloid plaques on the ipsilateral hemisphere are significantly smaller than plaques found on the contralateral hemisphere following 16-weeks post-implantation in APP/PS1 mice (Figure 5-3d). Quantifying the stained 6E10 area of individual Aβ plaques, we determine that plaques near the site of electrode implantation are, on average, significantly smaller than those located further away (Figure 5-3e, $p<0.001$, Student's t-test). Altogether, these findings suggest that device implantation injury effectively inhibits the growth of Aβ plaques located around chronically implanted microelectrodes.

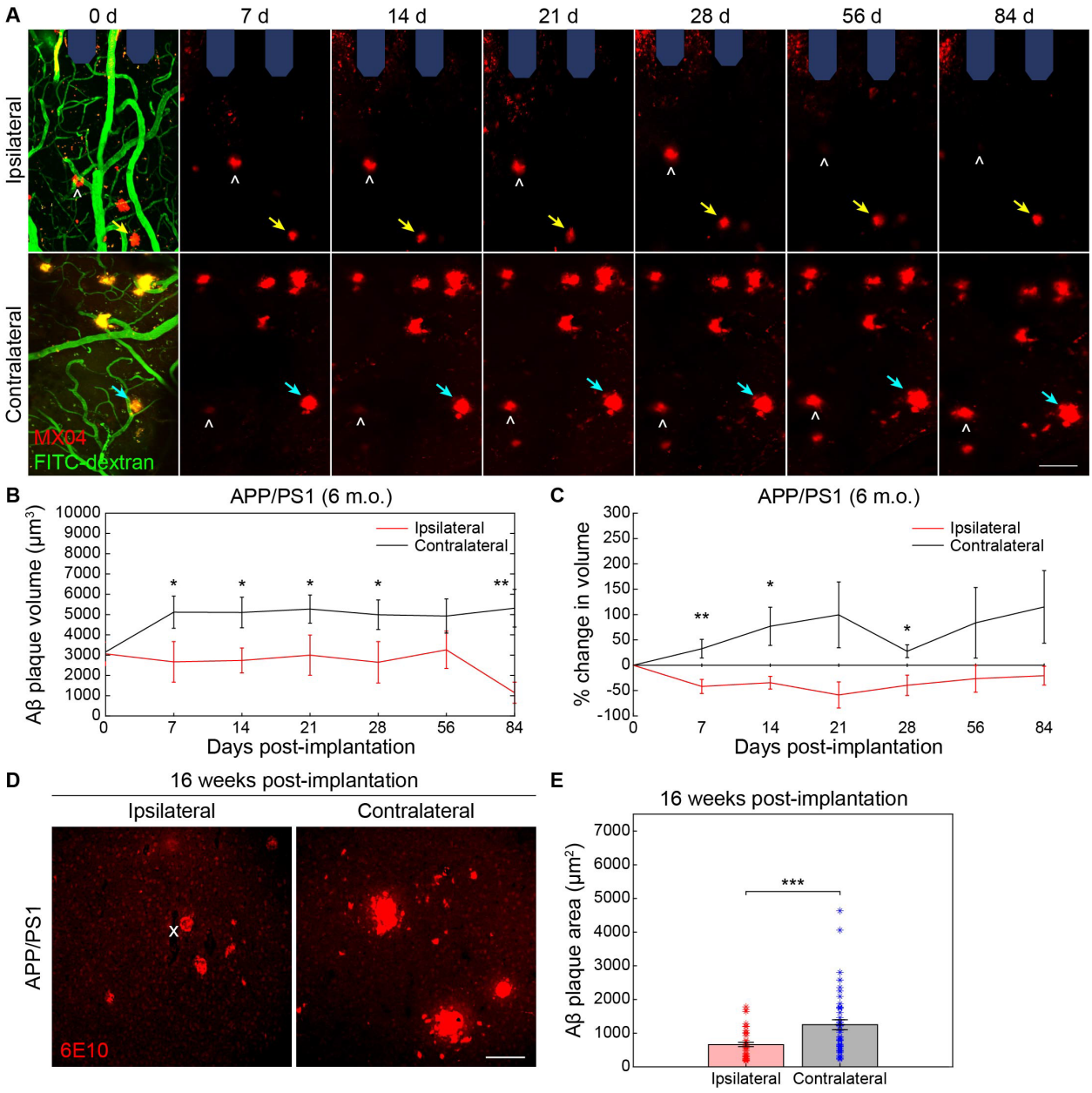

Figure 5-3 Chronic microelectrode implantation reduces the growth of local amyloid plaques in adult APP/PS1 mice. (a) Representative two-photon images of Aβ plaques labeled with methoxy-X04 (MX04, red) and blood vessels (FITC-dextran, green) in ipsilateral hemisphere around multi-shank microelectrode array (shaded blue) over 12 weeks post-implantation in adult (6 m.o.) APP/PS1 mice compared to contralateral (uninjured) hemisphere. Ipsilateral hemisphere demonstrates Aβ plaques which do not visually change in size with chronic implantation (yellow arrow) whereas Aβ plaques on the contralateral hemisphere appear to increase in size over time (cyan arrow). NOTE: some plaques move into and out of frame over time (white hat) due to tissue drift between subsequent chronic imaging sessions. Scale bar = 50 μm. (b) Change in Aβ plaque volume over a 12 week implantation period between ipsilateral and contralateral hemispheres in adult APP/PS1 mice (25 Aβ plaques on ipsilateral hemisphere and 27 Aβ plaques on contralateral hemisphere tracked longitudinally over 7 time points across n = 3 mice). (c) Percent change in Aβ plaque volume with respect to plaque size on day 0 of electrode insertion over a 12-week implantation period between ipsilateral and contralateral hemispheres in adult APP/PS1 mice. (d) Representative immunohistology stain for 6E10, an Aβ marker, following 16 weeks post-implantation in adult (6 m.o.) APP/PS1 mice demonstrating visually reduced Aβ plaque sizes in ipsilateral hemisphere around the site of probe insertion (denoted by white 'x') compared to

contralateral side. Scale bar = 100 μm. (e) Average Aβ plaque area measured by 6E10 stain between ipsilateral and contralateral hemispheres (n = 42 Aβ plaques on ipsilateral hemisphere over 13 histological tissue sections and n = 45 Aβ plaques on contralateral hemisphere over 17 histological sections across 6 mice total). * $p < 0.05$, ** $p < 0.01$, *** $p < 0.001$. All data is reported as mean ± SEM.

To determine whether microelectrode implantation preferentially favors the accumulation of amyloid, we first inserted microelectrode arrays within 2-month-old APP/PS1 mice. APP/PS1 mice at this age have yet to present stereotypical amyloid pathology within the brain and therefore provide an opportunity to assess whether device injury triggers the aggregation of amyloid protein prior to the temporally defined onset of neuropathology within the AD model. It is also important to note that these mice do not yet present lipofuscin pigments within the brain at this age as well. Surprisingly, we observed the appearance of MX04-labeled amyloid deposits, in which we term here as "amyloid clusters", within just the first 7 days following microelectrode implantation in young APP/PS1 mice (Figure 5-4a). From our analyses, we reveal a slight negative association between the size of Aβ clusters and their individual distances from the surface of an implanted microelectrode array (Figure 5-4b, $R^2 = 0.0123$). Additionally, we determined that the number of quantified Aβ clusters increases preferentially with distance near the implant and over time following chronic microelectrode implantation (Figure 5-4c). These results suggest that the tissue injury sustained from chronic electrode insertion within the brain accelerates the accumulation of amyloid pathology weeks to months before the expected onset of neuropathology within a mouse model of Alzheimer's disease.

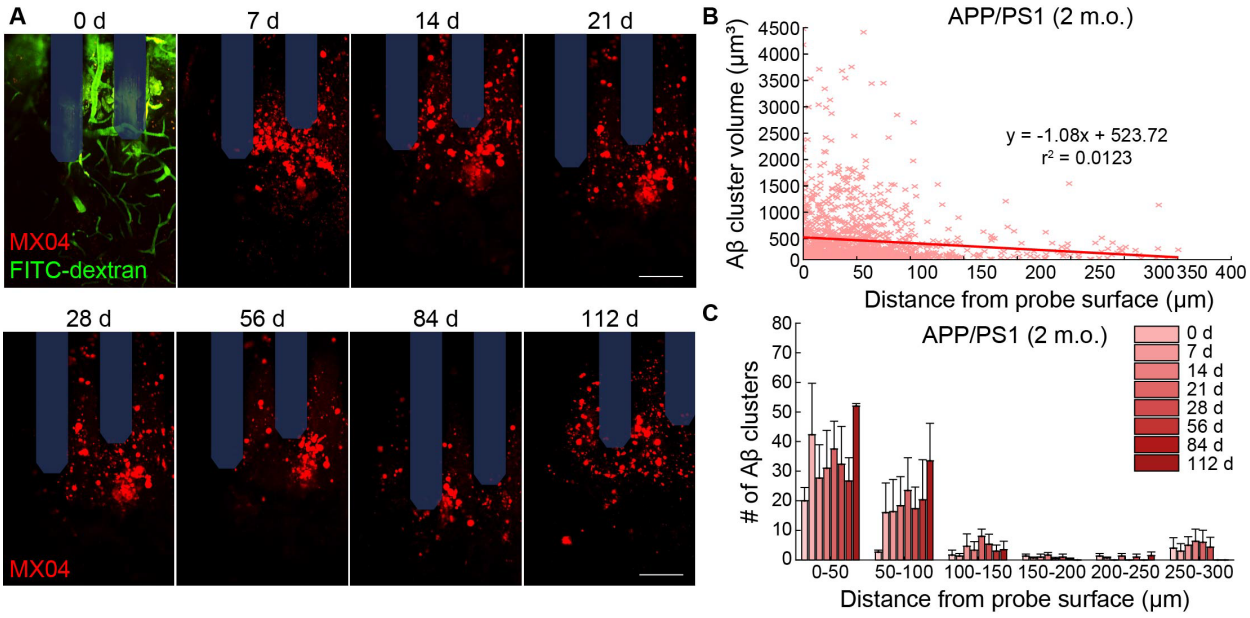

Figure 5-4 Accumulation of amyloid clusters around chronically implanted microelectrodes in young APP/PS1 mice. (a) Representative two-photon images of Aβ clusters labeled with methoxy-X04 (MX04, red) and blood vessels (FITC-dextran, green) around multi-shank microelectrode array (shaded blue) over 16 weeks post-implantation in young (2 m.o.) APP/PS1 mice. Scale bars = 50 μm. (b) Scatter plot demonstrating a trend in increased volume of Aβ clusters with respect to distance from probe surface (1,407 Aβ clusters across 7 timepoints). (c) Average number of Aβ clusters with binned distance from the probe in young APP/PS1 mice (n = 3). All data is reported as mean ± SEM.

5.4.3 Elevated Phagocytosis in Activated Microglia and Amyloid Precursor Protein in Reactive Astrocytes Around Chronically Implanted Electrodes

Microglia assume a critical role in phagocytosing cellular and tissue debris following brain injury or amyloid protein in Alzheimer's disease and their dysfunction has been linked to the progression of neurodegenerative disease. To determine whether phagocytosis within microglia due to device injury is elevated around implanted microelectrodes or within AD, explanted WT and APP/PS1 brain tissue were stained for Iba-1, a microglial marker, and triggering receptor expressed on myeloid cells 2 (TREM2), an innate immune receptor predominantly expressed by microglia within the brain during conditions of metabolic stress[25]. Interestingly, we found that microglia near the site of electrode implantation strongly co-localize with the expression of

TREM2 (Figure 5-5a). As expected, Iba-1 fluorescence intensities were visually elevated near the site of probe implantation at 1- and 16-weeks post-implantation in WT and APP/PS1 mice (Figure 5-5b). While normalized Iba-1 fluorescence intensities were increased with proximity to the site of electrode implantation, we did not reveal any significant differences in Iba-1 fluorescence intensities between WT and APP/PS1 at either 1-week or 16-week post-implantation (Figure 5-5c,d). Interestingly, we also observed a visual increase in TREM2 fluorescence intensities near the site of probe implantation at 1- and 16-weeks post-implantation in WT and APP/PS1 mice (Figure 5-5d). While normalized TREM2 fluorescence intensities were increased closer to the site of implantation, we did not reveal any significant differences in TREM2 fluorescence intensities between WT and APP/PS1 at either 1-week or 16-week post-implantation (Figure 5-5e,f). Nevertheless, these findings demonstrate that activated microglia increase expression of cellular immune receptors reportedly involved in phagocytosis of cellular debris and Aβ around chronically implanted microelectrodes.

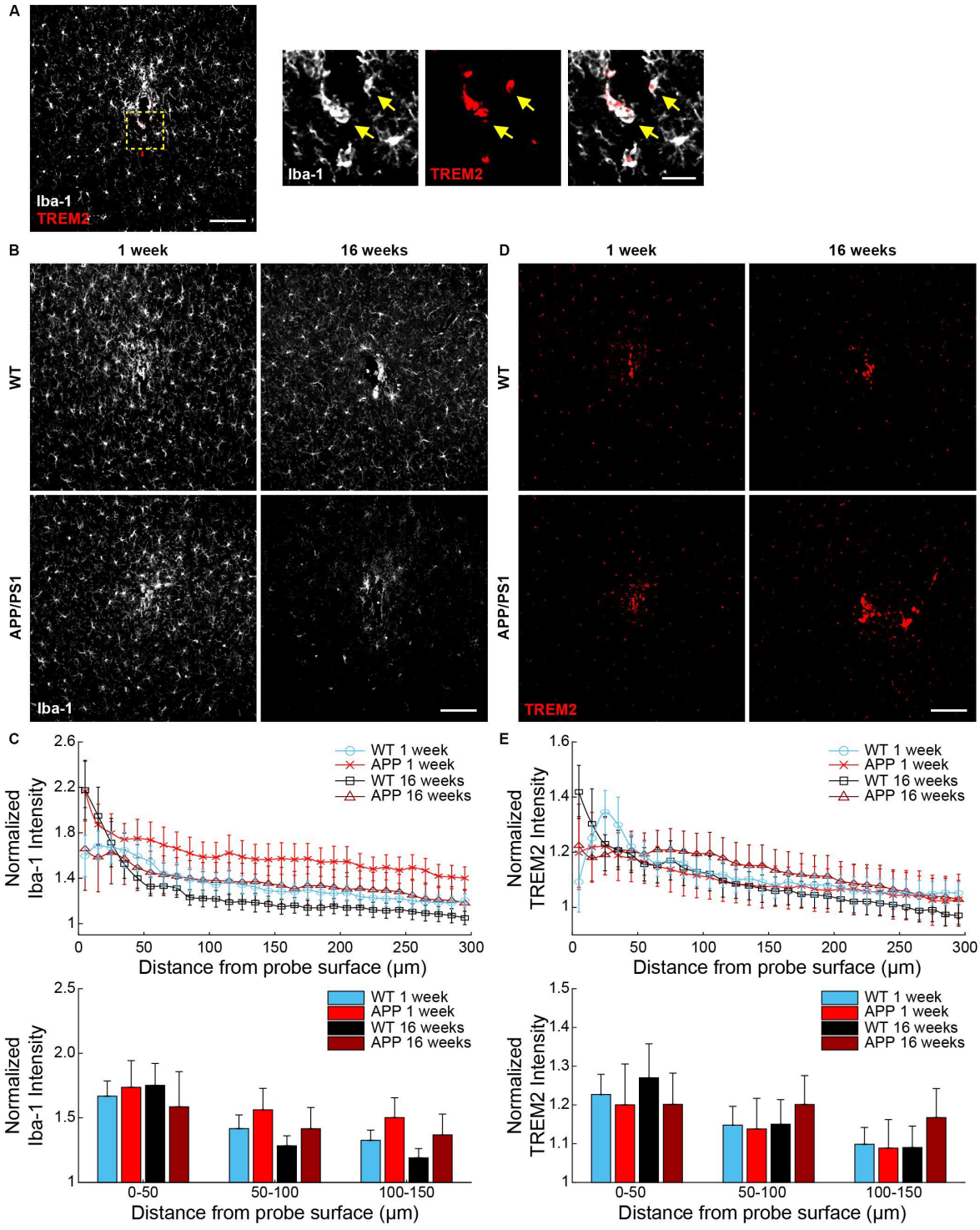

Figure 5-5 Microglial expression of phagocytic receptors around chronically implanted microelectrodes. (a) Immunohistological representation demonstrating co-localization of Iba-1+ microglia (*white*) with triggering receptor expressed on myeloid cells 2 (TREM2, *red*) around the site of electrode implantation (*yellow arrows*). Scale bar = 100 µm, 10 µm (inset). (b) Representative images of Iba-1 fluorescence staining around implanted microelectrodes at 1- and 16-weeks post-implantation in WT and APP/PS1 mice. Scale bar = 100 µm. (c) Normalized Iba-1 fluorescence intensity with respect to distance around chronically implanted microelectrodes at 1- and 16-weeks post-implantation in WT and APP/PS1 mice. (d) Average Iba-1 fluorescence intensity within 50 µm bins up to 150 µm around

chronically implanted microelectrodes at 1- and 16-weeks post-implantation in WT and APP/PS1 mice. (e) Representative images of TREM2 fluorescence staining around implanted microelectrodes at 1- and 16-weeks post-implantation in WT and APP/PS1 mice. Scale bar = 100 μm. (f) Normalized TREM2 fluorescence intensity with respect to distance around chronically implanted microelectrodes at 1- and 16-weeks post-implantation in WT and APP/PS1 mice. (g) Average TREM2 fluorescence intensity within 50 μm bins up to 150 μm around chronically implanted microelectrodes at 1- and 16-weeks post-implantation in WT and APP/PS1 mice (n = 6 mice per group at 1 week, n = 7 mice per group at 16 weeks). All data is reported as mean ± SEM.

Reactive astrocytes are the main culprits in formation of an astrocytic scar around intracortical electrodes and their dysfunction is commonly reported in neurological disorders[18,26]. To assess whether astrocyte reactivity due to chronic microelectrode implantation is exacerbated in a mouse model of AD, explanted WT and APP/PS1 brain tissue were stained for GFAP, a marker for reactive astrocytes. As expected, GFAP+ astrocyte staining was markedly increased near the site of device implantation in both WT and APP/PS1 mice at 1- and 16-weeks post-insertion (Figure 5-6a). GFAP fluorescence intensities were significantly elevated at 16-weeks post-implantation in both WT and APP/PS1 compared to 1-week post-implantation up to 150 μm from the site of electrode implantation (Figure 5-6b,c). Astrocytes reportedly can contribute to Aβ deposition due to their own production of amyloid precursor protein (APP)[27,28]. APP is a transmembrane protein whose pathological cleavage into aggregate forms of Aβ lead to the formation of senile plaques within AD and other dementia[29]. Interestingly, we report that GFAP+ astrocytes notably express APP near the site of probe implantation (Figure 5-6d). This co-expression of APP was specific to astrocytes and not microglia, since APP only co-labeled with GFAP+ astrocyte cells but not with Iba-1+ microglia cells. These results suggest that device implantation injury can induce the expression of potential precursors for Aβ production within reactive astrocytes around chronically implanted microelectrodes.

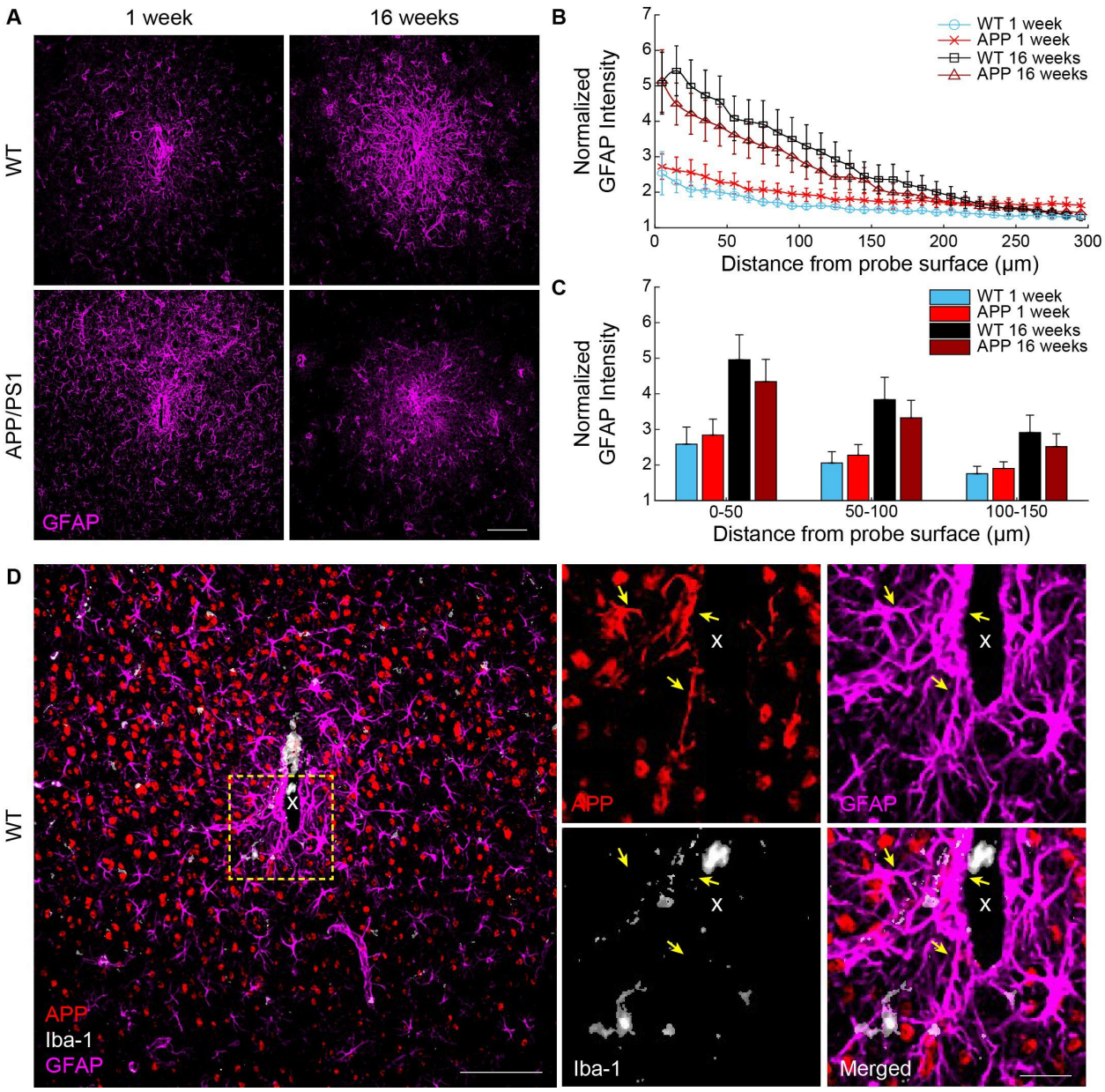

Figure 5-6 Reactive astrocytes express amyloid precursor protein around chronically implanted microelectrode arrays. (a) Representative images of GFAP+ reactive astrocyte staining (magenta) around implanted microelectrodes at 1- and 16-weeks post-implantation in WT and APP/PS1 mice. Scale bar = 100 μm. (b) Normalized GFAP fluorescence intensity with respect to distance around chronically implanted microelectrodes at 1- and 16-weeks post-implantation in WT and APP/PS1 mice. (c) Average GFAP fluorescence intensity within 50 μm bins up to 150 μm around chronically implanted microelectrodes at 1- and 16-weeks post-implantation in WT and APP/PS1 mice (n = 6 mice per group at 1 week, n = 7 mice per group at 16 weeks). (d) Immunohistological example demonstrating expression of amyloid precursor protein (APP, red) in GFAP+ astrocytes (magenta) but not Iba-1+ microglia (white) near the site of a chronically implanted microelectrode in a WT mouse. Scale bar = 100 μm, 25 μm (inset). All data is reported as mean ± SEM.

5.4.4 Neuronal Densities are Reduced Near Chronically Implanted Microelectrodes

We previously reported that neuronal densities are affected around chronically implanted microelectrodes up to 4 weeks post-implantation(Steven M Wellman et al., 2019a). Here, we stain for NeuN to visualize the distribution of neurons around microelectrode arrays in WT and APP/PS1 mice at 1- and 16-weeks post-implantation (Figure 5-7a). Quantification of neuronal densities normalized to contralateral hemispheres revealed a decrease in neurons within the 0-50 μm region near the site of implantation in both WT and APP/PS1 mice (Figure 5-7). Specifically, we determined that neuronal densities were significantly reduced in tissue regions between 0-50 μm and 100-150 μm at 1-week post-implantation and between 0-50 μm and 50-100 μm at 16-weeks post-implantation in WT mice but not APP/PS1 mice ($p<0.05$, two-way ANOVA). However, we did not detect any significant differences in neuronal density between WT and APP/PS1 mice at either 1- or 16-week post-implantation ($p>0.05$, two-way ANOVA). Nevertheless, these results reveal that chronic microelectrodes result in the loss of neurons local to the site of implantation.

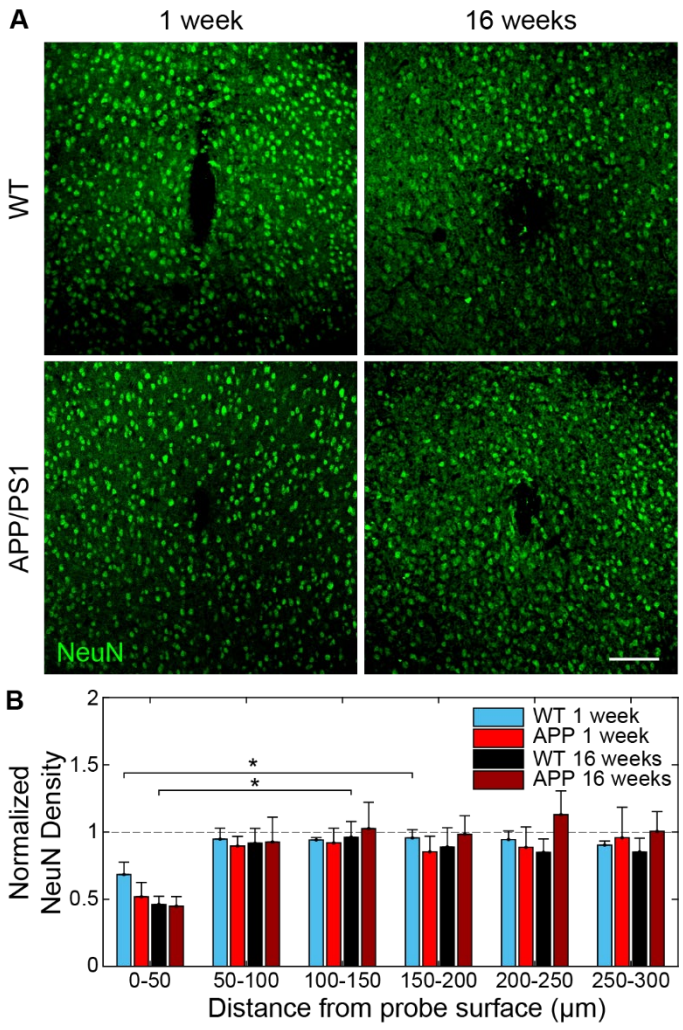

Figure 5-7 Reduced neuronal densities near chronically implanted microelectrodes. (a) Histological representation of neurons (NeuN, *green*) around chronically implanted microelectrodes in WT and APP/PS1 mice at 1- and 16- weeks post-implantation. Scale bar = 100 μm. (b) Average NeuN density within 50 μm bins up to 300 μm around chronically implanted microelectrodes at 1- and 16-weeks post-implantation in WT and APP/PS1 mice (n = 6 mice per group at 1 week, n = 7 mice per group at 16 weeks).

5.4.5 Abnormally Phosphorylated Tau Marks Regions of Axonal and Myelin Loss Around Chronically Implanted Electrodes

Previously, we demonstrated that chronic electrode implantation leads to the re-organization of axonal and myelin fibers near the site of probe implantation[18,30]. In this study, we aimed to better understand the pathology governing axonal and myelin loss during device

implantation injury and whether there is an impact following microelectrode implantation in a mouse model of AD. Staining explanted brain tissue with NF200, an axonal protein, and MBP, for myelin basic protein, we reveal unevenly distributed areas of axonal and myelin loss with close proximity to the site of microelectrode implantation (Figure 5-8a). Interestingly, when we co-stain for AT8, a marker commonly used to study hyperphosphorylated tau in neurodegenerative disease[31], we reveal that these areas of axon and myelin loss (i.e. NF200- and MBP- signal) correspond with abnormally high levels of AT8+ phosphorylated tau. AT8 staining intensity is visually increased near the site of probe implantation (Figure 5-8a). Normalized fluorescence intensities of AT8 are also increased above baseline levels near the site of electrode implantation in APP/PS1 mice, but not WT mice, at 1- and 16-weeks post-implantation (Figure 5-8b). The average normalized AT8 fluorescence intensity was significantly increased in APP/PS1 mice at 1-week post-implantation compared to WT mice, but not at 16 weeks post-implantation (Figure 5-8c). These results suggest that axonal and myelin pathology following device implantation injury is associated with abnormal phosphorylation of tau.

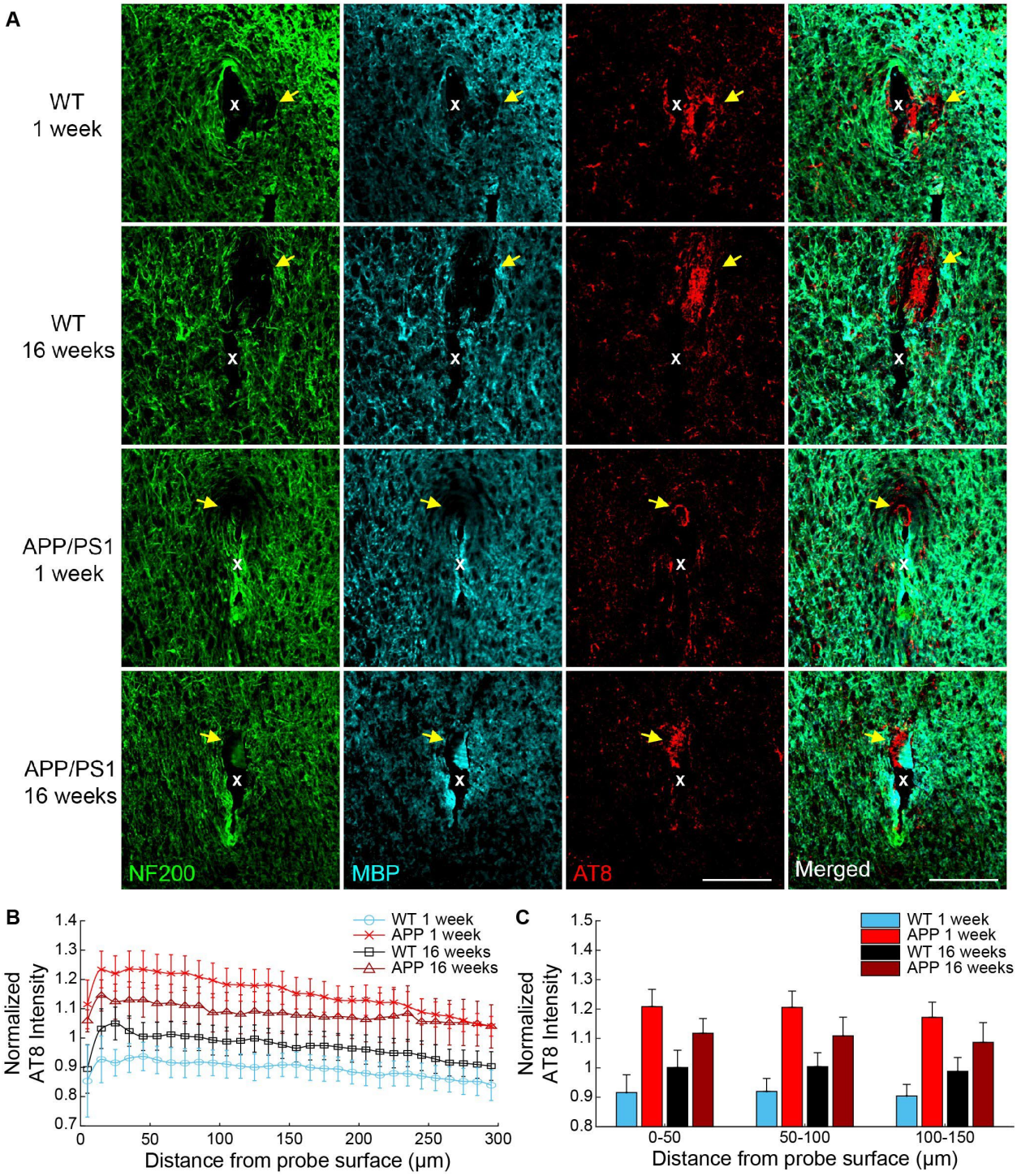

Figure 5-8 Axon and myelin pathology is associated with abnormal tau phosphorylation around chronically implanted microelectrodes. (a) Immunostaining for axons (NF200, green), myelin (MBP, cyan), and phospho-tau (AT8, red) reveals abnormal tau phosphorylation in areas of axon and myelin loss (yellow arrows) around 1- and 16-week implanted probes (white 'x') in WT and APP/PS1 mice. Scaler bar = 100 μm. (c) Normalized AT8 fluorescence intensity with respect to distance around chronically implanted microelectrodes at 1- and 16-weeks post-implantation in WT and APP/PS1 mice. (d) Average AT8 fluorescence intensity within 50 μm bins up to 150 μm around chronically

implanted microelectrodes at 1- and 16-weeks post-implantation in WT and APP/PS1 mice (n = 6 mice per group at 1 week, n = 7 mice per group at 16 weeks). All data is reported as mean ± SEM.

5.5 Discussion

The aim of this study was to understand whether the brain's immune response to neural electrode technology mimics neuropathology typically observed with neurodegenerative disease. Neuroinflammation, glial activation, and vascular dysfunction are all characteristic tissue events shared between both chronic implants and degenerative brain diseases, such as Alzheimer's disease. The neuropathology of Alzheimer's disease has been studied for more than a century, much longer than that of the foreign body response to neural microelectrodes. As a result, common biomarkers classically observed in disease, such as amyloid beta and neurofibrillary tau tangles, have been identified and implicated in the development of neurodegeneration and chronic tissue failure within diseased brains. Therefore, it would be of interest to determine whether any of the identified hallmarks of neurodegeneration in Alzheimer's disease are also involved in the biological failure mode of chronically implanted microelectrodes within the brain. Identifying predominant cellular and tissue mechanisms compromising neural health and neurotransmission around recording and stimulating brain implants will aide in the discovery and innovation of therapeutic approaches to improve the fidelity and longevity of neural electrode interfaces.

5.5.1 Accumulation of Age-related Lipofuscin Granules Following Chronic Electrode Implantation

With aging and cellular senescence comes a natural decline in cellular metabolism, leading to the buildup of harmful metabolic waste. Lipofuscin, an auto-fluorescent composite of proteins, lipids, and sugars, accumulates naturally within the brain with age(Gray & Woulfe, 2005). Lipofuscin granules are primarily found within lysosomes of post-mitotic and senescent cells, suggesting they are unable to be degraded normally through cellular metabolism("Oxidative Stress, Accumulation of Biological 'Garbage', and Aging," 2006; PORTA, 2002). We report here that chronically implanted microelectrodes promote lipofuscin aggregation within the aged brain. Lipofuscin accumulation around microelectrodes occurred in both WT and AD mice alike, although there was an increased trend for AD mice to produce lipofuscin deposits that were greater in both number and size within the electrode microenvironment. An impairment in the clearance and removal of pathological proteins is a commonly proposed theory of neurodegeneration within both natural aging and brain disease. The functional role of lipofuscin deposits within the brain and whether they are neurotoxic are currently unknown. However, lipofuscin accumulation has been previously associated with cellular oxidative stress as well as impairments in memory function, suggesting they have some impact on the health of neuronal tissue and regulation of brain activity. Nevertheless, elevated accumulation of lipofuscin granules observed here around chronically implanted microelectrodes suggests that electrode implantation injury induces a backstop in the clearance mechanisms regulating removal of cellular debris and metabolic waste from the brain.

5.5.2 Patterns of Amyloid Deposition Following Chronic Electrode Implantation

Our initial hypothesis was that chronic microelectrode implantation would exacerbate the growth of pre-existing amyloid plaques either due to elevated deposition of neuronal or glial Aβ or due to an impairment in glial clearance of amyloid. Contrary to this hypothesis, we observed that Aβ plaques existing prior to the start of electrode implantation were, on average, smaller in volume over a 12-week implantation period compared to plaques located further away in distal brain regions. This was the consequence of an overall negative change in size of plaques around microelectrodes. This finding contrasts with plaques on the contralateral, uninjured hemisphere, which gradually increased in size due to the natural progression of neuropathology within this mouse model. One possible explanation is that an increase in plaque size on the ipsilateral hemisphere was impaired due to a degradation in chronic imaging quality through an optical window around implanted microelectrodes over time, which would present a confound in our findings. However, in support of our two-photon findings, we observed a similar decrease in the overall area of plaques via post-mortem immunohistochemical staining confirming that the microenvironment around chronically implanted microelectrodes halts the rate of plaque growth. It is well understood that glial cells are responsible for the degradation and clearance of amyloid from the brain and that their physiological dysfunction in Alzheimer's disease could lead to the aberrant accumulation of amyloid, eventually forming senile plaques(Lai & McLaurin, 2012; C. Lee & Landreth, 2010). One possible interpretation of findings could be that an enhanced glial response results in the reduction in growth of nearby plaques. We show here that both microglia and astrocyte activity is upregulated with respect to chronically implanted microelectrodes in both WT and APP/PS1 mice alike.

Despite our results demonstrating that microelectrodes stall the growth of Aβ plaques locally, we also report novel amyloid deposition proximal to the electrode-tissue interface. The amyloid clusters we observed were smaller in size compared to traditionally measured Aβ plaques yet accumulated in greater numbers throughout the course of implantation. The morphology of these clusters also appeared rounder, denser, and more symmetrical in shape, different than that of plaques which are commonly asymmetrical and consist of a dense plaque core surrounded by diffuse amyloid fibrils. Microglia are known to form a neuroprotective barrier around amyloid plaques, and denser, more compact plaques are generally found to have more microglia contact(Condello, Yuan, Schain, & Grutzendler, 2015). One interpretation is that these amyloid clusters appear more compacted near the electrode where there is also an elevated microglial immune response and therefore more microglia association with amyloid. Alternatively, brain injury is known to increase the rate of APP processing, production of amyloid, and aggregation of Aβ plaques(Johnson, Stewart, & Smith, 2010; Washington, Morffy, Parsadanian, Zapple, & Burns, 2014) and microglia naturally phagocytose and sequester amyloid for proper degradation and removal from the brain(Lai & McLaurin, 2012). Therefore, another possible explanation could be that these amyloid clusters do not represent typical extracellular Aβ plaque deposits but represent accumulation intracellularly within neurons and glial cells following implantation injury from chronic microelectrodes. Future studies discerning the origin of these pathological amyloid by-products could reveal additional insight on the ongoing neurodegenerative processes around neural microelectrodes.

5.5.3 Glial Basis for Phagocytosis and Generation of Amyloid Precursor Protein Following Electrode Implantation

Microglia are the main potentiators of neuroinflammation both around chronic brain implants and with neurodegenerative disease. We report here that microglia activation is increased around chronically implanted microelectrodes in both WT and AD mice. We also demonstrate that microglia close to the site of electrode implantation exhibit increased expression of Triggering receptor expressed on myeloid cells 2 (TREM2). TREM2 is an important metabolic receptor expressed predominantly within microglia and assists with critical microglial functions such as phagocytosis and removal of pathological waste. TREM2 has been identified as a significant risk factor in the development of Alzheimer's disease. It is suggested that dysfunction in this critical immune cell receptor is what impairs the ability for microglia to remove amyloid and tau from Alzheimer's brains(Yuan et al., 2016). We demonstrate here that lipofuscin waste accumulates around chronically implanted microelectrodes in both WT and AD mice, but that AD mice trend more negatively (i.e. lipofuscin appears larger nearer to the electrode). Indeed, the hAbeta/APOE4/Trem2*R47H mouse model used in this study presents a mutation in the *Trem2* gene, potentially suggesting that increased lipofuscin accumulation around chronic microelectrodes within these mice is the result of impaired TREM2 function. Furthermore, impairment in TREM2 function interferes with the ability for microglia to form a protective barrier around amyloid plaques leading to increases in amyloid deposition and an increase in neuronal and axonal dystrophy(Yuan et al., 2016). It is unclear from the results reported here whether TREM2 function is compromised around chronically implanted microelectrodes or within AD brains. Future studies would benefit from examining the functional purpose of TREM2 within

microglia at the electrode-tissue interface and how their upregulation of this phagocytic receptor contributes to the foreign body response to chronically implanted microelectrodes.

Astrocytes mediate the formation of a neurochemically impermeable and neurotoxic glial scar as part of the foreign body response to chronic brain implants. Previously, we presented a dynamic spatiotemporal pattern of astrocyte reactivity within the first few weeks during implantation using two-photon imaging around implanted microelectrodes(Savya et al., 2022). We demonstrate here that astrocyte reactivity significantly increases from 1- to 16-weeks post-implantation in both WT and AD mice. Additionally, we report astrocyte-specific upregulation of APP in proximity to chronically implanted microelectrodes within WT mice. Based on these results, it is possible that the Increase in amyloid deposition observed around microelectrode implants could be partially due Aβ generation from reactive astrocytes. Amyloid precursor protein is a transmembrane protein expressed on cellular members and cleaved by secretases. With proper cleavage, the amyloid derived from APP does not aggregate into Aβ plaques and can be easily removed from the brain. Improper cleavage of APP, such as with –secretases, produces an aggregated form of Aβ resulting in the pathological formation of senile plaques. Future research should be performed assessing the function role of APP expression within reactive astrocytes around chronically implanted microelectrodes.

5.5.4 Neuronal and Axonal Pathology Following Chronic Electrode Implantation

The presence of nearby healthy neurons is critical to the long-term performance of neural microelectrode arrays. Neural densities are characteristically reduced both acute and chronically with close spatial proximity to implanted microelectrodes(Douglas McCreery, Stuart Cogan, Sheryl Kane, & Victor Pikov, 2016; Potter-Baker et al., 2014; Shoffstall et al., 2018). In this study,

we confirm that microelectrodes impact the number of neurons located adjacent to the site of implantation. Despite a visible difference in the density of neurons within the 0-50 μm tissue region around chronically implanted microelectrodes at 1- and 16-weeks post-implantation, we did not detect any significant differences between WT and APP/PS1 mice. It is important to keep in mind that at 16-weeks post-implantation APP/PS1 mice are at 6 months of age and neuronal numbers are not expected to be naturally altered within the AD model at this age(L. Liu et al., 2020; Szögi et al., 2022; J. Zhang et al., 2018). Furthermore, our analyses are only limited to understanding whether NeuN+ neurons are present or not around the electrode compared to intact control regions but does not discern whether the neurons that remain are viable or whether they may be otherwise functionally impaired around chronically implanted devices. In support of this, there have been reports of explanted tissue populated by many neurons yet still demonstrating poor electrophysiological recording performance(T. D. Kozai, X. Li, et al., 2014; Nicholas J Michelson et al., 2018). One possible explanation is that the neurons which were not directly impacted by implantation injury are quiescent or their activity is somehow suppressed(Nicholas J Michelson et al., 2018). Further *in vivo* evaluation is needed to understand the physiological consequences imparted on neurons around chronically implanted microelectrodes and in neurodegenerative disease.

Maintaining axonal and myelin integrity around chronically implanted electrodes is essential for effective transmission of neuronal information and excitability of neurons in brain regions both near and far from intracortical recording and stimulating electrodes. We have previously demonstrated re-organization and potential sprouting of axons as well as spatiotemporal patterns of axonal and myelin blebbing around intracortical electrodes(Chen, Wellman, et al., 2021; Nicholas J Michelson et al., 2018; Steven M Wellman et al., 2019a). Here, we demonstrate

that electrode implantation can induce regions of axonal and myelin loss with proximity to the site of electrode insertion. A previous study investigating local markers of tissue inflammation around chronically implanted microelectrodes noted the appearance of hyperphosphorylated tau at the lesion border within explanted brain tissue following 16-weeks of electrode implantation in rats(George C McConnell et al., 2009). This same study also noted similar neuropathology around the site of device insertion following 5 months of implantation in a human Parkinsonian patient, suggesting this phenomenon can occur in both rodents and humans. In line with this study, we observe elevated expression of phosphorylated tau near chronically implanted microelectrodes at 1- and 16-weeks post-implantation in both WT and AD mice. To our surprise, these areas of increased tau phosphorylation overlap with identified tissue regions lacking axons and myelin, suggesting that abnormal tau phosphorylation is an indicator of axonal and myelin pathology around chronically implanted microelectrodes. Phosphorylation of tau is a naturally occurring phenomenon important for microtubule assembly, axonal transport, and neuronal plasticity(Barbier et al., 2019; Dixit, Ross, Goldman, & Holzbaur, 2008; Noble, Hanger, Miller, & Lovestone, 2013). Hyperphosphorylated tau, however, is a pathological hallmark of Alzheimer's disease in which misfolded tau proteins aggregate and form neurofibrillary tau tangles within axons, interfering with neuronal information transmission(Noble et al., 2013). It is unclear from these findings whether hyperphosphorylated tau is the symptom or cause of axonal and myelin pathology around chronically implanted microelectrodes or whether abnormal tau phosphorylation would have a significant impact on the recording or excitability of neurons at the electrode-tissue interface. Understanding if tau phosphorylation precedes axonal and myelin loss (or vice versa) and if tau phosphorylation contributes to functional electrode performances could point towards novel biological targets to address neurodegeneration around chronic brain implants.

5.5.5 Future Directions

We determined that the levels of lipofuscin, APP, and Aβ are all upregulated around chronically implanted microelectrodes. While the pathological consequence of lipofuscin remains a mystery, it demonstrates no useful physiological purpose to-date. Previous work has demonstrated that chronic treatment with the antioxidant melatonin can reduce lipofuscin content within the rat hippocampus(Abd El Mohsen et al., 2005). Melatonin has previously shown to improve both microglia activation and recording performance of chronically implanted electrodes(Golabchi et al., 2018a; Krahe, Woeppel, Yang, Kushwah, & Cui, 2022)n , suggesting targeting glial function in general could be an effective way to address lipofuscin aggregation indirectly. APP itself is important for neural stem cell proliferation and axon outgrowth following injury and therefore may be neuroprotective in certain pathological conditions(Caillé et al., 2004; X. Wang, Huang, Bu, & Xu, 2014). However, impaired cleavage of APP by β-secretases generates precursors for Aβ. It is currently unclear how the levels of β-secretase, as well as α- and γ-secretase, are impacted around chronically implanted microelectrodes. Finally, previous and current FDA-approved clinical trials have focused on improving cognitive and behavioral outcomes in Alzheimer's disease by using monoclonal antibodies to target and promote clearance of Aβ plaques from the brain, yet the results have either been mixed or unsuccessful thus far(Honig et al., 2018; Salloway et al., 2014). There is current debate on whether the presence of amyloid is even a cause or just a symptom of neurodegeneration within Alzheimer's disease (i.e. "amyloidogenic" vs. "non-amyloidogenic" hypothesis). In any case, the abnormal accumulation of lipofuscin, APP, and amyloid around chronically implanted electrodes suggests a critical failure in tissue clearance mechanisms and may hint towards the accumulation of other potentially harmful factors, such as reactive oxidative species and misfolded tau proteins, whose improper

removal from the brain can be detrimental to neural health and function. Future studies should determine what other potential tissue factors accumulating at the electrode-tissue interface to develop a more holistic understanding of the potentially detrimental biochemical processes in effect around chronically implanted electrodes.

Tau phosphorylation is mediated by a number of different kinases, such as cyclin-dependent kinase 5 (cdk5) and glycogen synthase kinase-3 (GSK-3)(K. Baumann, Mandelkow, Biernat, Piwnica-Worms, & Mandelkow, 1993; Hanger, Hughes, Woodgett, Brion, & Anderton, 1992), and phosphatases, such as protein phosphatase PP1, PP2A, and PP5(F. Liu, Grundke-Iqbal, Iqbal, & Gong, 2005). Accounting for the changes in expression levels of these critical regulators of tau phosphorylation around microelectrodes could point toward novel targets during neurodegeneration surrounding chronic electrode implantation. There is also evidence that the presence of amyloid can alter tau phosphorylation(Busciglio, Lorenzo, Yeh, & Yankner, 1995; Pigino, Pelsman, Mori, & Busciglio, 2001). It is important to note that the methoxy-X04 label used in this study binds to both amyloid and tau within the brain(Klunk et al., 2002; Kuchibhotla et al., 2014). Therefore, is unclear whether the methoxy-X04 labeling around implanted microelectrodes is completely representative of amyloid protein or if there is also partial labeling of tau as well. Phosphorylated tau was also reported here as being increased in unusual densities around chronically implanted microelectrodes. Future research should use more targeted investigative methods, such as using P130S mouse models more directed at studying tau pathology in AD, to disentangle the potential relationship between amyloid and tau at the electrode-tissue interface.

Overall, we did not report much significance in the difference between WT and AD mice for some of the patterns of neuropathology commonly shared between the two models. For two-photon imaging experiments, mice were aged to 6 months prior to electrode implantation to

understand the impact of electrode implantation injury on the rate of growth of nearby pre-existing Aβ plaques. For histology experiments, APP/PS1 were implanted at 2 months of age and, by 16-weeks of implantation, mice were only 6 months old. At this age, APP/PS1 mice are just beginning to present amyloid deposition and therefore it is still relatively early in the progression of AD pathology typical for this mouse model. It could be, when comparing AD mice of a year or more in age to similarly age-matched controls, that we may observe a much greater difference in brain tissue responses following chronic microelectrode implantation. Despite this, we were still able to show that microelectrode implantation accelerates the onset of amyloid pathology even within 2 month-old APP/PS1 mice. Additionally, we reported novel findings on the expression of various cell and tissue factors related to aging and neurodegenerative disease around implanted microelectrodes which will aide future investigators in narrowing their research focuses and develop more informed intervention strategies for addressing the foreign body reaction to chronic brain implants.

5.6 Conclusion

The power of neural interface technology to aide in the discovery of previously unknown neuroscientific phenomenon and provide means for effective clinical therapy of neurological dysfunction is limited due to yet unresolved tissue responses to implanted recording and stimulating electrodes within the brain. These presently elusive biological mechanisms impairing the long-term application of neural microelectrodes could potentially be revealed by referencing the study of other brain disorders similarly plagued by neuronal, glial, and vascular dysfunction, such as Alzheimer's disease. In this study, we employed mouse models of Alzheimer's disease to

reveal the presence of various tissue factors that offer new insights on neurodegeneration surrounding chronic brain implants. We determined that microelectrode implantation preferentially favors the accumulation of pathological proteins related to aging and neurological disease at the electrode-tissue interface. We also highlighted novel spatiotemporal patterns of glial-specific expression of different factors related to deposition and clearance of amyloid within the brain as well as new information on potential neurodegenerative mechanisms governing axonal pathology around chronic microelectrodes. In summary, these research findings provide a new perspective regarding the progression of neurodegenerative injury surrounding neural interface technology and will aide in more rigorous study of electrode-tissue biocompatibility as well as expedited development of advanced therapies for both brain injury and disease.

6.0 Conclusion

6.1 Summary of Results

Chapters 2 and 3 of this dissertation fulfill a critical lack in understanding concerning the role oligodendrocyte lineage cells around chronically implanted microelectrodes. Chapter 2 focused on the spatiotemporal reactivity of NG2 glial cells following microelectrode implantation. Using two-photon microscopy, we demonstrated that NG2 glia extend processes and migrate toward the electrode surface beginning at 12 h post-implantation. Like microglia, NG2 glia become polarized, transforming from ramified to activated morphologies within 12-24 h post-implantation. Similarly, NG2 glia were revealed to participate in the encapsulation of the device surface over a 72 hr implantation period. Lastly, we revealed an association between NG2 glial activation and neurovascular dysfunction around chronically implanted microelectrodes. Ultimately, these results identified a novel glial contributor to the foreign body reaction of chronically implanted microelectrodes.

Chapter 3 investigated the functional relationship between myelinating oligodendrocytes and electrophysiological recordings detected by an implanted microelectrode. Using a cuprizone model of oligodendrocyte depletion and demyelination, oligodendrocytes and myelin were effectively removed from the cortex prior to the implantation of a recording microelectrode. Electrophysiological recordings over a 7-week implantation period determined that the detection and strength of neuronal signals were significantly impaired in oligodendrocyte-depleted and demyelinated animals compared to healthy controls. Furthermore, we revealed significant impacts to recording device latency, neuronal oscillations, and laminar coherence following cuprizone-

induced oligodendrocyte loss and demyelination around chronically implanted microelectrodes. The histological state of the tissue surrounding explanted electrodes was similar between oligodendrocyte-depleted and demyelinated animals and healthy controls implicating the loss of oligodendrocyte and myelin function in the chronic degradation of device recording performance.

Chapter 4 took a look at the dynamic changes in structure and function of perivascular pericytes around chronically implanted microelectrodes. Using a combination of two-photon microscopy and post-mortem histology, we demonstrated that electrode insertion promotes pericyte constriction and deformation of underlying capillaries and transient elevations in intracellular pericyte calcium activity. This acute response was followed by an influx of proliferating pericytes which dynamically remodeled blood vessels around the electrode microenvironment. Using a dual-fluorescent mouse model, we reveal distinct spatial and temporal patterns of immune cell encapsulation of electrode arrays over chronic implantation periods. Additionally, we unveil a potentially novel reactive population within the electrode-tissue interface which only emerge in response to chronic microelectrode implantation. This study provides fundamental insight on a relatively understudied brain population as a novel intervention target for improving the brain tissue response and device performance outcomes of chronically implanted microelectrodes.

Chapter 5 reveals the aberrant accumulation of factors related to aging and disease around chronically implanted microelectrodes in a mouse model of Alzheimer's disease (AD). Using two-photon microscopy, we reveal the aggregation of lipofuscin and amyloid beta (Aβ) near implanted microelectrodes in the aged AD brain. We also show that implantation injury slows or halts the growth of pre-existing amyloid plaques compared to plaques observed further from chronically implanted microelectrodes. Following post-mortem histology, we reveal the elevated expression

of phagocytic immune receptors within microglia and amyloid precursor protein within astrocytes, demonstrating a complex interplay between Aβ clearance and production around chronically implanted microelectrodes. Furthermore, we show that regions of abnormally phosphorylated tau within the tissue microenvironment around chronically implanted microelectrodes is associated with axonal and myelin pathology at the electrode-tissue interface. In sum, we highlight multiple novel tissue factors related to aging and neurodegenerative disease which can act as potential candidates for therapeutic intervention to improve the integration and longevity of neural electrode interfaces within the brain.

6.2 Future Directions

Understanding the full breadth of adverse tissue events which occur following chronic electrode implantation within the brain will now allow investigators to make more informed decisions regarding intelligent device design and development of strategic biomaterial interventions. Additionally, using advance *in vivo* methods to characterize the extent and time course over which these pathological processes occur will enable strategic delivery of pharmacological agents with spatial and temporal accuracy within the tissue microenvironment of chronic microelectrodes. In general, therapeutic drugs to mitigate the generation of metabolites related to oxidative stress or excitotoxicity will prevent the cell death and degeneration of metabolically sensitive glial and vascular populations, such as oligodendrocytes, their precursors, and pericytes (J. Y. Lee, Kang, & Yune, 2015; Price, Eranki, Banks, Ercal, & Shah, 2012; Shah et al., 2013; Spaas et al., 2021; M.-R. Wang et al., 2019). Anti-inflammatory drugs have been used successfully in the past to modulate glial responses around implanted microelectrodes, leading to

improve electrode integration and performance (Golabchi et al., 2018a; Takashi DY Kozai, Andrea S Jaquins-Gerstl, Alberto L Vazquez, Adrian C Michael, & X Tracy Cui, 2016; Krahe et al., 2022; Rennaker, Miller, Tang, & Wilson, 2007). These same drugs may also favor oligodendrocyte and pericytes either directly, through protection and maintenance of cellular structure and function, or indirectly, by suppressing glial inflammation and scar formation (Z. Cai, Lin, Fan, Pang, & Rhodes, 2006; Ghareghani et al., 2017; Olivier et al., 2009). Both oligodendrocyte precursor cells and pericytes demonstrate the capability to be reprogrammed into neurons through delivery or stimulation of different transcriptional programs in different pathological conditions (Karow et al., 2018; Karow et al., 2012; Tai et al., 2021; Torper et al., 2015). Using bioactive coatings for the controlled release of these programmable factors into the tissue microenvironment has the potential to increase the number of neurons while simultaneously decreasing the amount of reactive immune cells within the electrode-tissue interface, leading to enhanced longevity and functionality neural electrode interfaces. Finally, anti-inflammatory drugs to reduce neuroinflammation or monoclonal antibodies directed against Aβ have demonstrated some promise in promoting the degradation and clearance of pathological amyloid and tau from the brains of Alzheimer's disease patients (Rivers-Auty, Mather, Peters, Lawrence, & Brough, 2020; Van Dyck, 2018).

Electrical stimulation is an emerging regenerative medicine approach to modulate cellular behavior following brain injury or during neurodegenerative disease (Chen, Stieger, & Kozai, 2021; J. W. Salatino, K. A. Ludwig, T. D. Kozai, & E. K. Purcell, 2017). Both non-neuronal glial and vascular cells express voltage-gated ion channels which indicates their ability to sense and respond to exogenously or endogenously generated electrical signals within the brain (Barres, 1991; Bevan, Chiu, Gray, & Ritchie, 1985; Gautron et al., 1992; Hariharan et al., 2020; Nelson et

al., 2020; Nowak, Ascher, & Berwald-Netter, 1987). Oligodendrocyte precursor cells, oligodendrocytes, and pericytes all either directly interface with neuronal membranes or receive direct input from neuronal synapses. Oligodendrocyte precursor cells are known to form direct synaptic connections with neurons through which bi-directional communication can occur (Paukert & Bergles, 2006; X. Zhang et al., 2021). Known as activity-dependent modulation, oligodendrocyte precursors can respond to different patterns of neuronal activity driving their differentiation and maturation into myelinating oligodendrocytes (E. G. Hughes, Orthmann-Murphy, Langseth, & Bergles, 2018; Thornton & Hughes, 2020). As integrated components of the neurovascular unit pericytes are uniquely positioned to detect and transmit neuronal or astrocyte-derived signals to the brain's blood vessels (Melanie D Sweeney et al., 2016). Direct or indirect activation of pericytes in this manner allows for control of cerebral blood flow both near and far from the site of stimulation due to conducted vascular responses (C. Cai et al., 2018). Finally, neuromodulation is a promising approach for AD therapy (Luo et al., 2021). As a global brain disease, non-invasive approaches to drive brain-wide activity within AD have been pursued, such as transcranial director or magnetic stimulation and gamma entrainment using sensory stimulation (Chang, Lane, & Lin, 2018; Martorell et al., 2019). Alternatively, invasive deep-brain stimulation approaches have been proposed to target specific brain regions or neurotransmitter systems impaired in AD, such as the locus coeruleus to target the noradrenergic system or nucleus basalis of Meynert to modulate cholinergic function (Slater & Wang, 2021; Turnbull, McGeer, Beattie, Calne, & Pate, 1985). The enhanced degradation or clearance of amyloid or tau from the brain has been proposed as a mechanism of action for AD neuromodulation (Chang et al., 2018). Future studies should determine whether Aβ degradation or clearance can be promoted, possibly through enhanced modulation of glial or vascular function, using intracortical stimulating microelectrodes.

The use of innovative biomaterials offer an appealing strategy to modulating brain tissue response outcomes of neural interfaces (Steven M Wellman, James R Eles, et al., 2018b). Systemic delivery of therapeutic drugs can often produce systemic effects on other parts of the body other than the brain or otherwise diluted effects at the intended target site around the microelectrode. Delivery of pharmacological agents directly into the tissue around the electrode can ensure maximum therapeutic efficacy while reducing unintended side effects. Approaches for using functionally modified surfaces, more mechanically compliant substrates, and biodegradable coatings for the controlled release of therapeutic drugs to modulate the behavior and function of oligodendrocytes and their precursors around microelectrode implants have been previously explored (Chen, Wellman, et al., 2021; Steven M Wellman, Franca Cambi, et al., 2018). In general, use of softer, more flexible materials with smaller geometric profiles to reduce the amount of damage incurred to sensitive neuronal and vascular elements (i.e. neuronal soma, axons, and blood vessels) during electrode insertion has the potential to mitigate various glial and vascular neuroimmune responses around implanted microelectrodes (Steven M Wellman, James R Eles, et al., 2018b). The potential of different biomaterials to deliver therapeutic AD drugs has been explored previously (Agrawal et al., 2021), many of which have been explored in the context of neural electrode implants (Fattahi, Yang, Kim, & Abidian, 2014; Steven M Wellman, James R Eles, et al., 2018b; Woeppel, Yang, & Cui, 2017). As with electrical stimulation, modulation of glial and vascular function through bioactive or mechanically compliant interfaces can have therapeutic outcomes on AD-associated neuropathology, such as amyloid or tau, within the vicinity of implanted microelectrodes. Furthermore, electrode surface coatings which deter the biofouling or absorption of harmful pathological proteins, such as Aβ, have demonstrated the ability to improve the bio-integration of implantable microelectrodes possibly due to modulation

of neuroimmune responses within the brain (Puthongkham & Venton, 2019; Tao et al., 2022; Yang et al., 2020). The ability to functionalize various types of biomaterials on the same electrode suggests the potential for modulating multiple different tissue outcomes (i.e. glial reactivity, vascular dysfunction, and aberrant pathological protein accumulation) simultaneously around chronic microelectrodes (Kushwah, Woeppel, Dhawan, Shi, & Cui, 2022; Shi, Dhawan, & Cui, 2021; Vitale et al., 2018).

Bibliography

1. Abd El Mohsen, M. M., Iravani, M. M., Spencer, J. P., Rose, S., Fahim, A. T., Motawi, T. M., . . . Jenner, P. (2005). Age-associated changes in protein oxidation and proteasome activities in rat brain: modulation by antioxidants. *Biochemical and biophysical research communications, 336*(2), 386-391.

2. Acs, P., Selak, M. A., Komoly, S., & Kalman, B. (2013). Distribution of oligodendrocyte loss and mitochondrial toxicity in the cuprizone-induced experimental demyelination model. *Journal of Neuroimmunology, 262*(1), 128-131. doi:https://doi.org/10.1016/j.jneuroim.2013.06.012

3. Adams, R. A., Bauer, J., Flick, M. J., Sikorski, S. L., Nuriel, T., Lassmann, H., . . . Akassoglou, K. (2007). The fibrin-derived gamma377-395 peptide inhibits microglia activation and suppresses relapsing paralysis in central nervous system autoimmune disease. *J Exp Med, 204*(3), 571-582. doi:10.1084/jem.20061931

4. Agrawal, M., Prathyusha, E., Ahmed, H., Dubey, S. K., Kesharwani, P., Singhvi, G., . . . Alexander, A. (2021). Biomaterials in treatment of Alzheimer's disease. *Neurochemistry International, 145*, 105008.

5. Alba, N. A., Du, Z. J., Catt, K. A., Kozai, T. D. Y., & Cui, X. T. (2015). In vivo electrochemical analysis of a PEDOT/MWCNT neural electrode coating. *Biosensors, 5*, 618-646. doi:10.3390/bios5040618

6. Alizadeh, A., Dyck, S. M., & Karimi-Abdolrezaee, S. (2015a). Myelin damage and repair in pathologic CNS: challenges and prospects. *Frontiers in Molecular Neuroscience, 8*, 35. doi:10.3389/fnmol.2015.00035

7. Alizadeh, A., Dyck, S. M., & Karimi-Abdolrezaee, S. (2015b). Myelin damage and repair in pathologic CNS: challenges and prospects. *Frontiers in Molecular Neuroscience, 8*(35). doi:10.3389/fnmol.2015.00035

8. Almeida, R. G., & Lyons, D. A. (2017). On Myelinated Axon Plasticity and Neuronal Circuit Formation and Function. *The Journal of neuroscience : the official journal of the Society for Neuroscience, 37*(42), 10023-10034. doi:10.1523/JNEUROSCI.3185-16.2017

9. Ampofo, E., Schmitt, B. M., Menger, M. D., & Laschke, M. W. (2017). The regulatory mechanisms of NG2/CSPG4 expression. *Cellular & molecular biology letters, 22*, 4.

10. ANDREA, R., DE LA ROCHA, C. I., & REBEKAH, N. (2016). Pathophysiology of NG2-glia: a 'Chicken and Egg'scenario of altered neurotransmission and disruption of NG2-glial cell function. *Opera medica et physiologica*(1).

11. Armulik, A., Genové, G., Mäe, M., Nisancioglu, M. H., Wallgard, E., Niaudet, C., . . . Strittmatter, K. (2010). Pericytes regulate the blood–brain barrier. *Nature, 468*(7323), 557.

12. Arvidsson, A., Collin, T., Kirik, D., Kokaia, Z., & Lindvall, O. (2002). Neuronal replacement from endogenous precursors in the adult brain after stroke. *Nature Medicine, 8*(9), 963-970. doi:10.1038/nm747

13. Attwell, D., Mishra, A., Hall, C. N., O'Farrell, F. M., & Dalkara, T. (2016). What is a pericyte? *Journal of cerebral blood flow and metabolism : official journal of the International Society of Cerebral Blood Flow and Metabolism, 36*(2), 451-455.

14. Attwell, D., Mishra, A., Hall, C. N., O'Farrell, F. M., & Dalkara, T. (2016). What is a pericyte? *Journal of Cerebral Blood Flow & Metabolism, 36*(2), 451-455. doi:10.1177/0271678x15610340

15. Barbier, P., Zejneli, O., Martinho, M., Lasorsa, A., Belle, V., Smet-Nocca, C., . . . Landrieu, I. (2019). Role of tau as a microtubule-associated protein: structural and functional aspects. *Frontiers in aging neuroscience, 11*, 204.

16. Barres, B. A. (1991). Glial ion channels. *Current opinion in neurobiology, 1*(3), 354-359.

17. Barrese, J. C., Rao, N., Paroo, K., Triebwasser, C., Vargas-Irwin, C., Franquemont, L., & Donoghue, J. P. (2013). Failure mode analysis of silicon-based intracortical microelectrode arrays in non-human primates. *Journal of neural engineering, 10*(6), 066014.

18. Barrese, J. C., Rao, N., Paroo, K., Triebwasser, C., Vargas-Irwin, C., Franquemont, L., & Donoghue, J. P. (2013). Failure mode analysis of silicon-based intracortical microelectrode arrays in non-human primates. *J Neural Eng, 10*(6), 066014. doi:10.1088/1741-2560/10/6/066014

19. Barry, R. J., Clarke, A. R., McCarthy, R., Selikowitz, M., Johnstone, S. J., & Rushby, J. A. (2004). Age and gender effects in EEG coherence: I. Developmental trends in normal children. *Clinical Neurophysiology, 115*(10), 2252-2258. doi:https://doi.org/10.1016/j.clinph.2004.05.004

20. Battefeld, A., Klooster, J., & Kole, M. H. P. (2016). Myelinating satellite oligodendrocytes are integrated in a glial syncytium constraining neuronal high-frequency activity. *Nature Communications, 7*, 11298. doi:10.1038/ncomms11298

21. https://www.nature.com/articles/ncomms11298#supplementary-information

22. Baumann, K., Mandelkow, E.-M., Biernat, J., Piwnica-Worms, H., & Mandelkow, E. (1993). Abnormal Alzheimer-like phosphorylation of tau-protein by cyclin-dependent kinases cdk2 and cdk5. *FEBS letters, 336*(3), 417-424.

23. Baumann, N., & Pham-Dinh, D. (2001). Biology of Oligodendrocyte and Myelin in the Mammalian Central Nervous System. *Physiological Reviews, 81*(2), 871-927. doi:10.1152/physrev.2001.81.2.871

24. Baxi, E. G., DeBruin, J., Jin, J., Strasburger, H. J., Smith, M. D., Orthmann-Murphy, J. L., . . . Calabresi, P. A. (2017). Lineage tracing reveals dynamic changes in oligodendrocyte precursor cells following cuprizone-induced demyelination. *Glia, 65*(12), 2087-2098. doi:10.1002/glia.23229

25. Bénardais, K., Kotsiari, A., Škuljec, J., Koutsoudaki, P. N., Gudi, V., Singh, V., . . . Stangel, M. (2013). Cuprizone [bis (cyclohexylidenehydrazide)] is selectively toxic for mature oligodendrocytes. *Neurotoxicity research, 24*(2), 244-250.

26. Benetti, F., Ventura, M., Salmini, B., Ceola, S., Carbonera, D., Mammi, S., . . . Spisni, E. (2010). Cuprizone neurotoxicity, copper deficiency and neurodegeneration. *NeuroToxicology, 31*(5), 509-517. doi:https://doi.org/10.1016/j.neuro.2010.05.008

27. Bergles, D. E., & Richardson, W. D. (2015). Oligodendrocyte Development and Plasticity. *Cold Spring Harbor perspectives in biology, 8*(2), a020453.

28. Berninger, B., Costa, M. R., Koch, U., Schroeder, T., Sutor, B., Grothe, B., & Götz, M. (2007). Functional Properties of Neurons Derived from In Vitro Reprogrammed Postnatal Astroglia. *The Journal of Neuroscience, 27*(32), 8654. doi:10.1523/JNEUROSCI.1615-07.2007

29. Berthiaume, A.-A., Grant, R. I., McDowell, K. P., Underly, R. G., Hartmann, D. A., Levy, M., . . . Shih, A. Y. (2018). Dynamic remodeling of pericytes in vivo maintains capillary coverage in the adult mouse brain. *Cell reports, 22*(1), 8-16.

30. Berthiaume, A.-A., Hartmann, D. A., Majesky, M. W., Bhat, N. R., & Shih, A. Y. (2018). Pericyte structural remodeling in cerebrovascular health and homeostasis. *Frontiers in aging neuroscience, 10*, 210.

31. Bevan, S., Chiu, S., Gray, P., & Ritchie, J. M. (1985). The presence of voltage-gated sodium, potassium and chloride channels in rat cultured astrocytes. *Proceedings of the Royal society of London. Series B. Biological sciences, 225*(1240), 299-313.

32. Biname, F., Sakry, D., Dimou, L., Jolivel, V., & Trotter, J. (2013). NG2 regulates directional migration of oligodendrocyte precursor cells via Rho GTPases and polarity complex proteins. *The Journal of neuroscience : the official journal of the Society for Neuroscience, 33*(26), 10858-10874. doi:10.1523/JNEUROSCI.5010-12.2013

33. Biran, R., Martin, D. C., & Tresco, P. A. (2005). Neuronal cell loss accompanies the brain tissue response to chronically implanted silicon microelectrode arrays. *Experimental Neurology, 195*(1), 115-126. doi:DOI 10.1016/j.expneurol.2005.04.020

34. Birey, F., Kloc, M., Chavali, M., Hussein, I., Wilson, M., Christoffel, D. J., . . . Aguirre, A. (2015). Genetic and Stress-Induced Loss of NG2 Glia Triggers Emergence of Depressive-like Behaviors through Reduced Secretion of FGF2. *Neuron, 88*(5), 941-956.

35. Bowyer, S. M. (2016). Coherence a measure of the brain networks: past and present. *Neuropsychiatric Electrophysiology, 2*(1), 1. doi:10.1186/s40810-015-0015-7

36. Bradl, M., & Lassmann, H. (2010). Oligodendrocytes: biology and pathology. *Acta neuropathologica, 119*(1), 37-53.

37. Busciglio, J., Lorenzo, A., Yeh, J., & Yankner, B. A. (1995). β-Amyloid fibrils induce tau phosphorylation and loss of microtubule binding. *Neuron, 14*(4), 879-888.

38. Buss, A., Pech, K., Kakulas, B. A., Martin, D., Schoenen, J., Noth, J., & Brook, G. A. (2009). NG2 and phosphacan are present in the astroglial scar after human traumatic spinal cord injury. *BMC Neurol, 9*, 32. doi:10.1186/1471-2377-9-32

39. Buzsáki, G., Stark, E., Berényi, A., Khodagholy, D., Kipke, D. R., Yoon, E., & Wise, K. D. (2015). Tools for probing local circuits: high-density silicon probes combined with optogenetics. *Neuron, 86*(1), 92-105.

40. Cai, C., Fordsmann, J. C., Jensen, S. H., Gesslein, B., Lønstrup, M., Hald, B. O., . . . Lauritzen, M. J. (2018). Stimulation-induced increases in cerebral blood flow and local capillary vasoconstriction depend on conducted vascular responses. *Proc Natl Acad Sci U S A, 115*(25), E5796-e5804. doi:10.1073/pnas.1707702115

41. Cai, Z., Lin, S., Fan, L.-W., Pang, Y., & Rhodes, P. (2006). Minocycline alleviates hypoxic–ischemic injury to developing oligodendrocytes in the neonatal rat brain. *Neuroscience, 137*(2), 425-435.

42. Caillé, I., Allinquant, B., Dupont, E., Bouillot, C., Langer, A., Müller, U., & Prochiantz, A. (2004). Soluble form of amyloid precursor protein regulates proliferation of progenitors in the adult subventricular zone.

43. Cations, M., Draper, B., Low, L. F., Radford, K., Trollor, J., Brodaty, H., . . . Withall, A. (2018). Non-Genetic Risk Factors for Degenerative and Vascular Young Onset Dementia: Results from the INSPIRED and KGOW Studies. *J Alzheimers Dis, 62*(4), 1747-1758. doi:10.3233/jad-171027

44. Chan-Ling, T., & Hughes, S. (2005). NG2 can be used to identify arteries versus veins enabling the characterization of the different functional roles of arterioles and venules during microvascular network growth and remodeling. *Microcirculation (New York, N Y : 1994), 12*(7), 539-540; author reply 540-531.

45. Chang, C. H., Lane, H. Y., & Lin, C. H. (2018). Brain Stimulation in Alzheimer's Disease. *Front Psychiatry, 9*, 201. doi:10.3389/fpsyt.2018.00201

46. Chen, K., Stieger, K. C., & Kozai, T. D. (2021). Challenges and opportunities of advanced gliomodulation technologies for excitation-inhibition balance of brain networks. *Current Opinion in Biotechnology, 72*, 112-120.

47. Chen, K., Wellman, S. M., Yaxiaer, Y., Eles, J. R., & Kozai, T. D. (2021). In vivo spatiotemporal patterns of oligodendrocyte and myelin damage at the neural electrode interface. *Biomaterials, 268*, 120526.

48. Chestek, C. A., Gilja, V., Nuyujukian, P., Foster, J. D., Fan, J. M., Kaufman, M. T., . . . Ryu, S. I. (2011). Long-term stability of neural prosthetic control signals from silicon cortical arrays in rhesus macaque motor cortex. *Journal of neural engineering, 8*(4), 045005.

49. Chestek, C. A., Gilja, V., Nuyujukian, P., Foster, J. D., Fan, J. M., Kaufman, M. T., . . . Shenoy, K. V. (2011). Long-term stability of neural prosthetic control signals from silicon cortical arrays in rhesus macaque motor cortex. *J Neural Eng, 8*(4), 045005. doi:10.1088/1741-2560/8/4/045005

50. S1741-2560(11)70539-0 [pii]

51. Clark, G. M., Clark, J., Cardamone, T., Clarke, M., Nielsen, P., Jones, R., . . . Xu, J. (2014). Biomedical studies on temporal bones of the first multi-channel cochlear implant patient at the University of Melbourne. *Cochlear implants international, 15*(sup2), S1-S15.

52. Clark, G. M., Clark, J. C., & Furness, J. B. (2013). The evolving science of cochlear implants. *Jama, 310*(12), 1225-1226.

53. Clarke, A. R., Barry, R. J., Heaven, P. C. L., McCarthy, R., Selikowitz, M., & Byrne, M. K. (2008). EEG coherence in adults with Attention-Deficit/Hyperactivity Disorder. *International Journal of Psychophysiology, 67*(1), 35-40. doi:https://doi.org/10.1016/j.ijpsycho.2007.10.001

54. Clemente, D., Ortega, M. C., Arenzana, F. J., & de Castro, F. (2011). FGF-2 and Anosmin-1 are selectively expressed in different types of multiple sclerosis lesions. *The Journal of neuroscience : the official journal of the Society for Neuroscience, 31*(42), 14899-14909.

55. Cody, P. A., Eles, J. R., Lagenaur, C. F., Kozai, T. D., & Cui, X. T. (2018). Unique electrophysiological and impedance signatures between encapsulation types: An analysis of biological Utah array failure and benefit of a biomimetic coating in a rat model. *Biomaterials, 161*, 117-128.

56. Cogan, S. F., Ludwig, K. A., Welle, C. G., & Takmakov, P. (2016). Tissue damage thresholds during therapeutic electrical stimulation. *Journal of neural engineering, 13*(2), 021001.

57. Collinger, J. L., Kryger, M. A., Barbara, R., Betler, T., Bowsher, K., Brown, E. H., . . . Boninger, M. L. (2014). Collaborative approach in the development of high-performance brain-computer interfaces for a neuroprosthetic arm: translation from animal models to human control. *Clin Transl Sci, 7*(1), 52-59. doi:10.1111/cts.12086

58. Collinger, J. L., Wodlinger, B., Downey, J. E., Wang, W., Tyler-Kabara, E. C., Weber, D. J., . . . Schwartz, A. B. (2013). High-performance neuroprosthetic control by an individual with tetraplegia. *Lancet, 381*(9866), 557-564. doi:10.1016/S0140-6736(12)61816-9

59. Collinger, J. L., Wodlinger, B., Downey, J. E., Wang, W., Tyler-Kabara, E. C., Weber, D. J., . . . Schwartz, A. B. (2013). High-performance neuroprosthetic control by an individual with tetraplegia. *The Lancet, 381*(9866), 557-564.

60. Condello, C., Yuan, P., Schain, A., & Grutzendler, J. (2015). Microglia constitute a barrier that prevents neurotoxic protofibrillar Aβ42 hotspots around plaques. *Nat Commun, 6*, 6176. doi:10.1038/ncomms7176

61. Costa, M. A., Paiva, A. E., Andreotti, J. P., Cardoso, M. V., Cardoso, C. D., Mintz, A., & Birbrair, A. (2018). Pericytes constrict blood vessels after myocardial ischemia. *Journal of molecular and cellular cardiology, 116*, 1-4.

62. Dalkara, T., Alarcon-Martinez, L., & Yemisci, M. (2019). Pericytes in ischemic stroke. In *Pericyte Biology in Disease* (pp. 189-213): Springer.

63. Damisah, E. C., Hill, R. A., Tong, L., Murray, K. N., & Grutzendler, J. (2017). A fluoro-Nissl dye identifies pericytes as distinct vascular mural cells during in vivo brain imaging. *Nat Neurosci, 20*(7), 1023-1032. doi:10.1038/nn.4564

64. Dawson, M. R. L., Polito, A., Levine, J. M., & Reynolds, R. (2003). NG2-expressing glial progenitor cells: an abundant and widespread population of cycling cells in the adult rat CNS. *Molecular and cellular neurosciences, 24*(2), 476-488.

65. Dent, K. A., Christie, K. J., Bye, N., Basrai, H. S., Turbic, A., Habgood, M., . . . Turnley, A. M. (2015). Oligodendrocyte birth and death following traumatic brain injury in adult mice. *PloS one, 10*(3), e0121541-e0121541. doi:10.1371/journal.pone.0121541

66. Dewar, D., Underhill, S. M., & Goldberg, M. P. (2003). Oligodendrocytes and Ischemic Brain Injury. *Journal of Cerebral Blood Flow & Metabolism, 23*(3), 263-274. doi:10.1097/01.WCB.0000053472.41007.F9

67. Di, Z., Wu, X., Xie, W., & Lin, X. (2021). Effect of pericytes on cerebral microvasculature at different time points of stroke. *BioMed Research International, 2021*.

68. Dias Moura Prazeres, P. H., Sena, I. F. G., Borges, I. D. T., de Azevedo, P. O., Andreotti, J. P., de Paiva, A. E., . . . Birbrair, A. (2017). Pericytes are heterogeneous in their origin within the same tissue. *Dev Biol, 427*(1), 6-11. doi:10.1016/j.ydbio.2017.05.001

69. Dimou, L., & Gallo, V. (2015). NG2-glia and their functions in the central nervous system. *Glia, 63*(8), 1429-1451. doi:10.1002/glia.22859

70. Dimou, L., & Gallo, V. (2015). NG 2-glia and their functions in the central nervous system. *Glia, 63*(8), 1429-1451.

71. Dixit, R., Ross, J. L., Goldman, Y. E., & Holzbaur, E. L. (2008). Differential regulation of dynein and kinesin motor proteins by tau. *Science, 319*(5866), 1086-1089.

72. do Carmo Cunha, J., de Freitas Azevedo Levy, B., de Luca, B. A., de Andrade, M. S. R., Gomide, V. C., & Chadi, G. (2007). Responses of reactive astrocytes containing S100beta protein and fibroblast growth factor-2 in the border and in the adjacent preserved tissue after a contusion injury of the spinal cord in rats: implications for wound repair and neuroregeneration. *Wound repair and regeneration : official publication of the Wound Healing Society [and] the European Tissue Repair Society, 15*(1), 134-146.

73. Donkin, J. J., & Vink, R. (2010). Mechanisms of cerebral edema in traumatic brain injury: therapeutic developments. *Curr Opin Neurol, 23*(3), 293-299. doi:10.1097/WCO.0b013e328337f451

74. Dou, C. L., & Levine, J. M. (1994). Inhibition of neurite growth by the NG2 chondroitin sulfate proteoglycan. *The Journal of neuroscience : the official journal of the Society for Neuroscience, 14*(12), 7616-7628. doi:10.1523/JNEUROSCI.14-12-07616.1994

75. Dougherty, K. D., Dreyfus, C. F., & Black, I. B. (2000). Brain-Derived Neurotrophic Factor in Astrocytes, Oligodendrocytes, and Microglia/Macrophages after Spinal Cord Injury. *Neurobiology of Disease, 7*(6), 574-585. doi:https://doi.org/10.1006/nbdi.2000.0318

76. Du, Y., & Dreyfus, C. F. (2002). Oligodendrocytes as providers of growth factors. *Journal of Neuroscience Research, 68*(6), 647-654. doi:10.1002/jnr.10245

77. Du, Z. J., Kolarcik, C. L., Kozai, T. D. Y., Luebben, S. D., Sapp, S. A., Zheng, X. S., . . . Cui, X. T. (2017). Ultrasoft microwire neural electrodes improve chronic tissue integration. *Acta Biomaterialia*. doi:http://dx.doi.org/10.1016/j.actbio.2017.02.010

78. Dziembowska, M., Tham, T. N., Lau, P., Vitry, S., Lazarini, F., & Dubois-Dalcq, M. (2005). A role for CXCR4 signaling in survival and migration of neural and oligodendrocyte precursors. *Glia, 50*(3), 258-269.

79. Eles, J., Vazquez, A., Kozai, T., & Cui, X. (2018). In vivo imaging of neuronal calcium during electrode implantation: Spatial and temporal mapping of damage and recovery. *Biomaterials*.

80. Eles, J. R., & Kozai, T. D. Y. (2020). In vivo imaging of calcium and glutamate responses to intracortical microstimulation reveals distinct temporal responses of the neuropil and somatic compartments in layer II/III neurons. . *Biomaterials*.

81. Eles, J. R., Vazquez, A. L., Kozai, T. D., & Cui, X. T. (2018). In vivo imaging of neuronal calcium during electrode implantation: spatial and temporal mapping of damage and recovery. *Biomaterials, 174*, 79-94.

82. Eles, J. R., Vazquez, A. L., Snyder, N. R., Lagenaur, C., Murphy, M. C., Kozai, T. D., & Cui, X. T. (2017). Neuroadhesive L1 coating attenuates acute microglial attachment to neural electrodes as revealed by live two-photon microscopy. *Biomaterials, 113*, 279-292.

83. Ettle, B., Schlachetzki, J. C. M., & Winkler, J. (2016). Oligodendroglia and Myelin in Neurodegenerative Diseases: More Than Just Bystanders? *Molecular neurobiology, 53*(5), 3046-3062. doi:10.1007/s12035-015-9205-3

84. Faizi, M., Salimi, A., Seydi, E., Naserzadeh, P., Kouhnavard, M., Rahimi, A., & Pourahmad, J. (2016). Toxicity of cuprizone a Cu2+ chelating agent on isolated mouse brain mitochondria: a justification for demyelination and subsequent behavioral dysfunction. *Toxicology mechanisms and methods, 26*(4), 276-283.

85. Falco, A., Pennucci, R., Brambilla, E., & de Curtis, I. (2014). Reduction in parvalbumin-positive interneurons and inhibitory input in the cortex of mice with experimental autoimmune encephalomyelitis. *Experimental brain research, 232*(7), 2439-2449. doi:10.1007/s00221-014-3944-7

86. Fan, Y., Xie, L., & Chung, C. Y. (2017). Signaling Pathways Controlling Microglia Chemotaxis. *Mol Cells, 40*(3), 163-168. doi:10.14348/molcells.2017.0011

87. Fattahi, P., Yang, G., Kim, G., & Abidian, M. R. (2014). A review of organic and inorganic biomaterials for neural interfaces. *Advanced materials, 26*(12), 1846-1885.

88. Fernández-Klett, F., Potas, J. R., Hilpert, D., Blazej, K., Radke, J., Huck, J., . . . Priller, J. (2013). Early loss of pericytes and perivascular stromal cell-induced scar formation after stroke. *Journal of Cerebral Blood Flow & Metabolism, 33*(3), 428-439. doi:10.1038/jcbfm.2012.187

89. Fernández-Klett, F., Potas, J. R., Hilpert, D., Blazej, K., Radke, J., Huck, J., . . . Priller, J. (2013). Early loss of pericytes and perivascular stromal cell-induced scar formation after stroke. *J Cereb Blood Flow Metab, 33*(3), 428-439. doi:10.1038/jcbfm.2012.187

90. Fields, R. D. (2008). Oligodendrocytes Changing the Rules: Action Potentials in Glia and Oligodendrocytes Controlling Action Potentials. *The Neuroscientist : a review journal bringing neurobiology, neurology and psychiatry, 14*(6), 540-543. doi:10.1177/1073858408320294

91. Filley, C. M., & Fields, R. D. (2016). White matter and cognition: making the connection. *Journal of neurophysiology, 116*(5), 2093-2104. doi:10.1152/jn.00221.2016

92. Filous, A. R., Tran, A., Howell, C. J., Busch, S. A., Evans, T. A., Stallcup, W. B., . . . Silver, J. (2014). Entrapment via synaptic-like connections between NG2 proteoglycan+ cells and dystrophic axons in the lesion plays a role in regeneration failure after spinal cord injury. *The Journal of neuroscience : the official journal of the Society for Neuroscience, 34*(49), 16369-16384. doi:10.1523/JNEUROSCI.1309-14.2014

93. Fitch, M. T., & Silver, J. (1997). Glial cell extracellular matrix: boundaries for axon growth in development and regeneration. *Cell Tissue Res, 290*(2), 379-384.

94. Fleck, J. I., Kuti, J., Mercurio, J., Mullen, S., Austin, K., & Pereira, O. (2017). The Impact of Age and Cognitive Reserve on Resting-State Brain Connectivity. *Frontiers in aging neuroscience, 9*, 392-392. doi:10.3389/fnagi.2017.00392

95. Flesher, S. N., Collinger, J. L., Foldes, S. T., Weiss, J. M., Downey, J. E., Tyler-Kabara, E. C., . . . Gaunt, R. A. (2016). Intracortical microstimulation of human somatosensory cortex. *Science Translational Medicine, 8*(361), 361ra141-361ra141. doi:doi:10.1126/scitranslmed.aaf8083

96. Flygt, J., Djupsjö, A., Lenne, F., & Marklund, N. (2013). Myelin loss and oligodendrocyte pathology in white matter tracts following traumatic brain injury in the rat. *European Journal of Neuroscience, 38*(1), 2153-2165. doi:10.1111/ejn.12179

97. Franco-Pons, N., Tomàs, J., Roig, B., Auladell, C., Martorell, L., & Vilella, E. (2009). Discoidin Domain Receptor 1, a Tyrosine Kinase Receptor, is Upregulated in an Experimental Model of Remyelination and During Oligodendrocyte Differentiation In Vitro. *Journal of molecular neuroscience, 38*(1), 2-11. doi:10.1007/s12031-008-9151-x

98. Friedlander, D. R., Milev, P., Karthikeyan, L., Margolis, R. K., Margolis, R. U., & Grumet, M. (1994). The neuronal chondroitin sulfate proteoglycan neurocan binds to the neural cell adhesion molecules Ng-CAM/L1/NILE and N-CAM, and inhibits neuronal adhesion and neurite outgrowth. *The Journal of cell biology, 125*(3), 669-680.

99. Fünfschilling, U., Supplie, L. M., Mahad, D., Boretius, S., Saab, A. S., Edgar, J., . . . Möbius, W. (2012). Glycolytic oligodendrocytes maintain myelin and long-term axonal integrity. *Nature, 485*(7399), 517.

100. Gardner, R. C., Burke, J. F., Nettiksimmons, J., Kaup, A., Barnes, D. E., & Yaffe, K. (2014). Dementia risk after traumatic brain injury vs nonbrain trauma: the role of age and severity. *JAMA neurology, 71*(12), 1490-1497.

101. Gautier, H. O., Evans, K. A., Volbracht, K., James, R., Sitnikov, S., Lundgaard, I., . . . Karadottir, R. T. (2015). Neuronal activity regulates remyelination via glutamate signalling to oligodendrocyte progenitors. *Nat Commun, 6*, 8518. doi:10.1038/ncomms9518

102. Gautron, S., Dos Santos, G., Pinto-Henrique, D., Koulakoff, A., Gros, F., & Berwald-Netter, Y. (1992). The glial voltage-gated sodium channel: cell-and tissue-specific mRNA expression. *Proceedings of the National Academy of Sciences, 89*(15), 7272-7276.

103. Ghareghani, M., Sadeghi, H., Zibara, K., Danaei, N., Azari, H., & Ghanbari, A. (2017). Melatonin increases oligodendrocyte differentiation in cultured neural stem cells. *Cellular and molecular neurobiology, 37*(7), 1319-1324.

104. Gibson, E. M., Purger, D., Mount, C. W., Goldstein, A. K., Lin, G. L., Wood, L. S., . . . Monje, M. (2014). Neuronal activity promotes oligodendrogenesis and adaptive myelination in the mammalian brain. *Science (New York, N Y), 344*(6183), 1252304.

105. Gilgunn, P. J., Xiao Chuan, O., Flesher, S. N., Schwartz, A. B., & Gaunt, R. A. (2013, 6-8 Nov. 2013). *Structural analysis of explanted microelectrode arrays.* Paper presented at the Neural Engineering (NER), 2013 6th International IEEE/EMBS Conference on.

106. Golabchi, A., Wu, B., Li, X., Carlisle, D. L., Kozai, T. D., Friedlander, R. M., & Cui, X. T. (2018a). Melatonin improves quality and longevity of chronic neural recording. *Biomaterials, 180*, 225-239.

107. Golabchi, A., Wu, B., Li, X., Carlisle, D. L., Kozai, T. D. Y., Friedlander, R. M., & Cui, X. T. (2018b). Melatonin improves quality and longevity of chronic neural recording. *Biomaterials, 180*, 225-239. doi:https://doi.org/10.1016/j.biomaterials.2018.07.026

108. Goss-Varley, M., Dona, K. R., McMahon, J. A., Shoffstall, A. J., Ereifej, E. S., Lindner, S. C., & Capadona, J. R. (2017). Microelectrode implantation in motor cortex causes fine motor deficit: Implications on potential considerations to Brain Computer Interfacing and Human Augmentation. *Sci Rep, 7*(1), 15254. doi:10.1038/s41598-017-15623-y

109. Gray, D. A., & Woulfe, J. (2005). Lipofuscin and Aging: A Matter of Toxic Waste. *Science of Aging Knowledge Environment, 2005*(5), re1-re1. doi:doi:10.1126/sageke.2005.5.re1

110. Gudi, V., Gingele, S., Skripuletz, T., & Stangel, M. (2014). Glial response during cuprizone-induced de-and remyelination in the CNS: lessons learned. *Frontiers in cellular neuroscience, 8*, 73.

111. Gudi, V., Moharregh-Khiabani, D., Skripuletz, T., Koutsoudaki, P. N., Kotsiari, A., Skuljec, J., . . . Stangel, M. (2009). Regional differences between grey and white matter in cuprizone induced demyelination. *Brain research, 1283*, 127-138.

112. Guerreiro, R., Wojtas, A., Bras, J., Carrasquillo, M., Rogaeva, E., Majounie, E., . . . Younkin, S. (2013). TREM2 variants in Alzheimer's disease. *New England Journal of Medicine, 368*(2), 117-127.

113. Gybina, A. A., & Prohaska, J. R. (2008). Copper deficiency results in AMP-activated protein kinase activation and acetylCoA carboxylase phosphorylation in rat cerebellum. *Brain research, 1204*, 69-76. doi:https://doi.org/10.1016/j.brainres.2008.01.087

114. Hackett, A. R., Lee, D.-H., Dawood, A., Rodriguez, M., Funk, L., Tsoulfas, P., & Lee, J. K. (2016). STAT3 and SOCS3 regulate NG2 cell proliferation and differentiation after contusive spinal cord injury. *Neurobiology of disease, 89*, 10-22.

115. Hackett, A. R., & Lee, J. K. (2016). Understanding the NG2 Glial Scar after Spinal Cord Injury. *Frontiers in neurology, 7*, 199. doi:10.3389/fneur.2016.00199

116. Hall, C. N., Reynell, C., Gesslein, B., Hamilton, N. B., Mishra, A., Sutherland, B. A., . . . Attwell, D. (2014). Capillary pericytes regulate cerebral blood flow in health and disease. *Nature, 508*(7494), 55-60. doi:10.1038/nature13165

117. Halliday, M. R., Rege, S. V., Ma, Q., Zhao, Z., Miller, C. A., Winkler, E. A., & Zlokovic, B. V. (2016). Accelerated pericyte degeneration and blood-brain barrier breakdown in apolipoprotein E4 carriers with Alzheimer's disease. *J Cereb Blood Flow Metab, 36*(1), 216-227. doi:10.1038/jcbfm.2015.44

118. Hamada, M. S., & Kole, M. H. P. (2015). Myelin loss and axonal ion channel adaptations associated with gray matter neuronal hyperexcitability. *The Journal of neuroscience : the official journal of the Society for Neuroscience, 35*(18), 7272-7286. doi:10.1523/JNEUROSCI.4747-14.2015

119. Hanger, D. P., Hughes, K., Woodgett, J. R., Brion, J.-P., & Anderton, B. H. (1992). Glycogen synthase kinase-3 induces Alzheimer's disease-like phosphorylation of tau: generation of paired helical filament epitopes and neuronal localisation of the kinase. *Neuroscience letters, 147*(1), 58-62.

120. Hansson, E. (2015). Actin filament reorganization in astrocyte networks is a key functional step in neuroinflammation resulting in persistent pain: novel findings on network restoration. *Neurochemical Research, 40*(2), 372-379.

121. Hariharan, A., Weir, N., Robertson, C., He, L., Betsholtz, C., & Longden, T. A. (2020). The ion channel and GPCR toolkit of brain capillary pericytes. *Frontiers in Cellular Neuroscience, 14*, 601324.

122. Hartline, D. K. (2009). What is myelin? *Neuron Glia Biology, 4*(2), 153-163. doi:10.1017/S1740925X09990263

123. Hartmann, D. A., Berthiaume, A.-A., Grant, R. I., Harrill, S. A., Koski, T., Tieu, T., . . . Shih, A. Y. (2021). Brain capillary pericytes exert a substantial but slow influence on blood flow. *Nature neuroscience, 24*(5), 633-645.

124. Hartmann, D. A., Coelho-Santos, V., & Shih, A. Y. (2022). Pericyte Control of Blood Flow Across Microvascular Zones in the Central Nervous System. *Annual Review of Physiology, 84*(1), 331-354. doi:10.1146/annurev-physiol-061121-040127

125. Hatsopoulos, N. G., & Donoghue, J. P. (2009). The science of neural interface systems. *Annual review of neuroscience, 32*, 249-266.

126. Heinrich, C., Bergami, M., Gascon, S., Lepier, A., Vigano, F., Dimou, L., . . . Gotz, M. (2014). Sox2-mediated conversion of NG2 glia into induced neurons in the injured adult cerebral cortex. *Stem cell reports, 3*(6), 1000-1014.

127. Hess, D. C., Abe, T., Hill, W. D., Studdard, A. M., Carothers, J., Masuya, M., . . . Ogawa, M. (2004). Hematopoietic origin of microglial and perivascular cells in brain. *Experimental neurology, 186*(2), 134-144.

128. Hill, R. A., Patel, K. D., Goncalves, C. M., Grutzendler, J., & Nishiyama, A. (2014). Modulation of oligodendrocyte generation during a critical temporal window after NG2 cell division. *Nature neuroscience, 17*(11), 1518-1527.

129. Hochberg, L. R., Bacher, D., Jarosiewicz, B., Masse, N. Y., Simeral, J. D., Vogel, J., . . . Donoghue, J. P. (2012). Reach and grasp by people with tetraplegia using a neurally controlled robotic arm. *Nature, 485*(7398), 372-375.

130. Hochberg, L. R., Serruya, M. D., Friehs, G. M., Mukand, J. A., Saleh, M., Caplan, A. H., . . . Donoghue, J. P. (2006). Neuronal ensemble control of prosthetic devices by a human with tetraplegia. *Nature, 442*(7099), 164-171. doi:nature04970 [pii]

131. 10.1038/nature04970

132. Hoffmann, K., Lindner, M., Gröticke, I., Stangel, M., & Löscher, W. (2008). Epileptic seizures and hippocampal damage after cuprizone-induced demyelination in C57BL/6 mice. *Experimental neurology, 210*(2), 308-321. doi:https://doi.org/10.1016/j.expneurol.2007.11.005

133. Honig, L. S., Vellas, B., Woodward, M., Boada, M., Bullock, R., Borrie, M., . . . Liu-Seifert, H. (2018). Trial of solanezumab for mild dementia due to Alzheimer's disease. *New England Journal of Medicine, 378*(4), 321-330.

134. Howarth, C., Gleeson, P., & Attwell, D. (2012). Updated energy budgets for neural computation in the neocortex and cerebellum. *Journal of Cerebral Blood Flow & Metabolism, 32*(7), 1222-1232.

135. Huang, W., Bai, X., Meyer, E., & Scheller, A. (2020). Acute brain injuries trigger microglia as an additional source of the proteoglycan NG2. *Acta neuropathologica communications, 8*(1), 1-15.

136. Huang, W., Bai, X., Meyer, E., & Scheller, A. (2020). Acute brain injuries trigger microglia as an additional source of the proteoglycan NG2. *Acta Neuropathol Commun, 8*(1), 146. doi:10.1186/s40478-020-01016-2

137. Huber, D., Gutnisky, D. A., Peron, S., O'Connor, D. H., Wiegert, J. S., Tian, L., . . . Svoboda, K. (2012). Multiple dynamic representations in the motor cortex during sensorimotor learning. *Nature, 484*(7395), 473-478. doi:10.1038/nature11039

138. Hughes, C. L., Flesher, S. N., Weiss, J. M., Boninger, M., Collinger, J. L., & Gaunt, R. A. (2021). Perception of microstimulation frequency in human somatosensory cortex. *Elife, 10*, e65128.

139. Hughes, C. L., Flesher, S. N., Weiss, J. M., Downey, J. E., Boninger, M., Collinger, J. L., & Gaunt, R. A. (2021). Neural stimulation and recording performance in human sensorimotor cortex over 1500 days. *Journal of Neural Engineering, 18*(4), 045012.

140. Hughes, E. G., Kang, S. H., Fukaya, M., & Bergles, D. E. (2013a). Oligodendrocyte progenitors balance growth with self-repulsion to achieve homeostasis in the adult brain. *Nat Neurosci, 16*(6), 668-676. doi:10.1038/nn.3390

141. http://www.nature.com/neuro/journal/v16/n6/abs/nn.3390.html#supplementary-information

142. Hughes, E. G., Kang, S. H., Fukaya, M., & Bergles, D. E. (2013). Oligodendrocyte progenitors balance growth with self-repulsion to achieve homeostasis in the adult brain. *Nature neuroscience, 16*(6), 668-676. doi:10.1038/nn.3390

143. Hughes, E. G., Kang, S. H., Fukaya, M., & Bergles, D. E. (2013b). Oligodendrocyte progenitors balance growth with self-repulsion to achieve homeostasis in the adult brain. *Nature neuroscience, 16*(6), 668-676. doi:10.1038/nn.3390

144. Hughes, E. G., Orthmann-Murphy, J. L., Langseth, A. J., & Bergles, D. E. (2018). Myelin remodeling through experience-dependent oligodendrogenesis in the adult somatosensory cortex. *Nat Neurosci, 21*(5), 696-706. doi:10.1038/s41593-018-0121-5

145. Iordanova, B., Vazquez, A. L., Kozai, T. D. Y., Fukuda, M., & Kim, S. G. (2018). Optogenetic investigation of the variable neurovascular coupling along the interhemispheric circuits *Journal of Cerebral Blood Flow & Metabolism, 38*(4), 627-640.

146. Jana, A., Hogan, E. L., & Pahan, K. (2009). Ceramide and neurodegeneration: Susceptibility of neurons and oligodendrocytes to cell damage and death. *Journal of the Neurological Sciences, 278*(1), 5-15. doi:https://doi.org/10.1016/j.jns.2008.12.010

147. Jeffries, M. A., Urbanek, K., Torres, L., Wendell, S. G., Rubio, M. E., & Fyffe-Maricich, S. L. (2016). ERK1/2 Activation in Preexisting Oligodendrocytes of Adult Mice Drives New Myelin Synthesis and Enhanced CNS Function. *The Journal of neuroscience : the official journal of the Society for Neuroscience, 36*(35), 9186-9200. doi:10.1523/JNEUROSCI.1444-16.2016

148. Jeong, J.-W., Shin, G., Park, Sung I., Yu, Ki J., Xu, L., & Rogers, John A. Soft Materials in Neuroengineering for Hard Problems in Neuroscience. *Neuron, 86*(1), 175-186. doi:10.1016/j.neuron.2014.12.035

149. Johnson, V. E., Stewart, W., & Smith, D. H. (2010). Traumatic brain injury and amyloid-β pathology: a link to Alzheimer's disease? *Nat Rev Neurosci, 11*(5), 361-370. doi:10.1038/nrn2808

150. Jones, L. L., Yamaguchi, Y., Stallcup, W. B., & Tuszynski, M. H. (2002). NG2 Is a Major Chondroitin Sulfate Proteoglycan Produced after Spinal Cord Injury and Is Expressed by Macrophages and Oligodendrocyte Progenitors. *The Journal of Neuroscience, 22*(7), 2792.

151. Jorfi, M., Skousen, J. L., Weder, C., & Capadona, J. R. (2015). Progress towards biocompatible intracortical microelectrodes for neural interfacing applications. *J Neural Eng, 12*(1), 011001. doi:10.1088/1741-2560/12/1/011001

152. JUURLINK, B. H. (1997). Response of glial cells to ischemia: roles of reactive oxygen species and glutathione. *Neuroscience & Biobehavioral Reviews, 21*(2), 151-166.

153. Karow, M., Camp, J. G., Falk, S., Gerber, T., Pataskar, A., Gac-Santel, M., . . . Fan, W. (2018). Direct pericyte-to-neuron reprogramming via unfolding of a neural stem cell-like program. *Nature neuroscience, 21*(7), 932-940.

154. Karow, M., Sánchez, R., Schichor, C., Masserdotti, G., Ortega, F., Heinrich, C., . . . Dellavalle, A. (2012). Reprogramming of pericyte-derived cells of the adult human brain into induced neuronal cells. *Cell stem cell, 11*(4), 471-476.

155. Kasischke, K. A., Vishwasrao, H. D., Fisher, P. J., Zipfel, W. R., & Webb, W. W. (2004). Neural activity triggers neuronal oxidative metabolism followed by astrocytic glycolysis. *Science, 305*(5680), 99-103.

156. Kipke, D. R., Shain, W., Buzsaki, G., Fetz, E., Henderson, J. M., Hetke, J. F., & Schalk, G. (2008). Advanced neurotechnologies for chronic neural interfaces: new horizons and clinical opportunities. *The Journal of neuroscience : the official journal of the Society for Neuroscience, 28*(46), 11830-11838.

157. Kipp, M., Clarner, T., Dang, J., Copray, S., & Beyer, C. (2009). The cuprizone animal model: new insights into an old story. *Acta neuropathologica, 118*(6), 723-736.

158. Kıray, H., Lindsay, S. L., Hosseinzadeh, S., & Barnett, S. C. (2016). The multifaceted role of astrocytes in regulating myelination. *Experimental neurology, 283*(Pt B), 541-549. doi:10.1016/j.expneurol.2016.03.009

159. Klunk, W. E., Bacskai, B. J., Mathis, C. A., Kajdasz, S. T., McLellan, M. E., Frosch, M. P., . . . Hyman, B. T. (2002). Imaging Aβ Plaques in Living Transgenic Mice with Multiphoton Microscopy and Methoxy-X04, a Systemically Administered Congo Red Derivative. *Journal of Neuropathology & Experimental Neurology, 61*(9), 797-805. doi:10.1093/jnen/61.9.797

160. Kolarcik, C. L., Luebben, S. D., Sapp, S. A., Hanner, J., Snyder, N., Kozai, T. D. Y., . . . Cui, X. T. (2015). Elastomeric and soft conducting microwires for implantable neural interfaces. *Soft Matter, 11*(24), 4847-4861. doi:10.1039/C5SM00174A

161. Komitova, M., Serwanski, D. R., Lu, Q. R., & Nishiyama, A. (2011). NG2 cells are not a major source of reactive astrocytes after neocortical stab wound injury. *Glia, 59*(5), 800-809.

162. Komitova, M., Serwanski, D. R., Richard Lu, Q., & Nishiyama, A. (2011). NG2 cells are not a major source of reactive astrocytes after neocortical stab wound injury. *Glia, 59*(5), 800-809.

163. Kondo, T., & Raff, M. (2000). Oligodendrocyte precursor cells reprogrammed to become multipotential CNS stem cells. *Science (New York, N Y), 289*(5485), 1754-1757.

164. Kotter, M. R., Li, W.-W., Zhao, C., & Franklin, R. J. (2006). Myelin impairs CNS remyelination by inhibiting oligodendrocyte precursor cell differentiation. *Journal of Neuroscience, 26*(1), 328-332.

165. Kozai, T., Alba, N., Zhang, H., Kotov, N., Gaunt, R., & Cui, X. (2014). Nanostructured Coatings for Improved Charge Delivery to Neurons. In M. D. Vittorio, L. Martiradonna, & J. Assad (Eds.), *Nanotechnology and Neuroscience: Nano-electronic, Photonic and Mechanical Neuronal Interfacing* (pp. 71-134). New York, NY: Springer New York.

166. Kozai, T., Marzullo, T., Hooi, F., Langhals, N., Majewska, A., Brown, E., & Kipke, D. (2010). Reduction of neurovascular damage resulting from microelectrode insertion into the cerebral cortex using in vivo two-photon mapping. *J Neural Eng, 7*(4), 046011.

167. Kozai, T. D., Du, Z., Gugel, Z. V., Smith, M. A., Chase, S. M., Bodily, L. M., . . . Cui, X. T. (2015). Comprehensive chronic laminar single-unit, multi-unit, and local field potential recording performance with planar single shank electrode arrays. *Journal of Neuroscience Methods, 242*, 15-40.

168. Kozai, T. D., Eles, J. R., Vazquez, A. L., & Cui, X. T. (2016). Two-photon imaging of chronically implanted neural electrodes: Sealing methods and new insights. *Journal of neuroscience methods, 258*, 46-55.

169. Kozai, T. D., Gugel, Z., Li, X., Gilgunn, P. J., Khilwani, R., Ozdoganlar, O. B., . . . Cui, X. T. (2014). Chronic tissue response to carboxymethyl cellulose based dissolvable insertion needle for ultra-small neural probes. *Biomaterials, 35*(34), 9255-9268. doi:10.1016/j.biomaterials.2014.07.039

170. Kozai, T. D., Gugel, Z., Li, X., Gilgunn, P. J., Khilwani, R., Ozdoganlar, O. B., . . . Cui, X. T. (2014). Chronic tissue response to carboxymethyl cellulose based dissolvable insertion needle for ultra-small neural probes. *Biomaterials, 35*(34), 9255-9268.

171. Kozai, T. D., Jaquins-Gerstl, A. S., Vazquez, A. L., Michael, A. C., & Cui, X. T. (2015). Brain tissue responses to neural implants impact signal sensitivity and intervention strategies. *ACS Chem Neurosci, 6*(1), 48-67. doi:10.1021/cn500256e

172. Kozai, T. D., Jaquins-Gerstl, A. S., Vazquez, A. L., Michael, A. C., & Cui, X. T. (2015). Brain tissue responses to neural implants impact signal sensitivity and intervention strategies. *ACS chemical neuroscience, 6*(1), 48-67.

173. Kozai, T. D., Jaquins-Gerstl, A. S., Vazquez, A. L., Michael, A. C., & Cui, X. T. (2016). Dexamethasone retrodialysis attenuates microglial response to implanted probes in vivo. *Biomaterials, 87*, 157-169. doi:10.1016/j.biomaterials.2016.02.013

174. Kozai, T. D., Jaquins-Gerstl, A. S., Vazquez, A. L., Michael, A. C., & Cui, X. T. (2016). Dexamethasone retrodialysis attenuates microglial response to implanted probes in vivo. *Biomaterials, 87*, 157-169.

175. Kozai, T. D., Langhals, N. B., Patel, P. R., Deng, X., Zhang, H., Smith, K. L., . . . Kipke, D. R. (2012). Ultrasmall implantable composite microelectrodes with bioactive surfaces for chronic neural interfaces. *Nat Mater, 11*(12), 1065-1073. doi:10.1038/nmat3468

176. Kozai, T. D., Li, X., Bodily, L. M., Caparosa, E. M., Zenonos, G. A., Carlisle, D. L., . . . Cui, X. T. (2014). Effects of caspase-1 knockout on chronic neural recording quality and longevity: insight into cellular and molecular mechanisms of the reactive tissue response. *Biomaterials, 35*(36), 9620-9634.

177. Kozai, T. D., Li, X., Bodily, L. M., Caparosa, E. M., Zenonos, G. A., Carlisle, D. L., . . . Cui, X. T. (2014). Effects of caspase-1 knockout on chronic neural recording quality and longevity: insight into cellular and molecular mechanisms of the reactive tissue response. *Biomaterials, 35*(36), 9620-9634. doi:10.1016/j.biomaterials.2014.08.006

178. Kozai, T. D., Marzullo, T. C., Hooi, F., Langhals, N. B., Majewska, A. K., Brown, E. B., & Kipke, D. R. (2010). Reduction of neurovascular damage resulting from microelectrode insertion into the cerebral cortex using in vivo two-photon mapping. *J Neural Eng, 7*(4), 046011. doi:S1741-2560(10)46092-9 [pii]

179. 10.1088/1741-2560/7/4/046011

180. Kozai, T. D., Vazquez, A. L., Weaver, C. L., Kim, S. G., & Cui, X. T. (2012). In vivo two-photon microscopy reveals immediate microglial reaction to implantation of microelectrode through extension of processes. *J Neural Eng, 9*(6), 066001. doi:10.1088/1741-2560/9/6/066001

181. Kozai, T. D. Y., Catt, K., Du, Z., Na, K., Srivannavit, O., Haque, R.-U. M., . . . Cui, X. T. (2016). Chronic In Vivo Evaluation of PEDOT/CNT for Stable Neural Recordings. *IEEE transactions on bio-medical engineering, 63*, 111-119. doi:10.1109/TBME.2015.2445713

182. Kozai, T. D. Y., Catt, K., Li, X., Gugel, Z. V., Olafsson, V. T., Vazquez, A. L., & Cui, X. T. (2015). Mechanical failure modes of chronically implanted planar silicon-based neural probes for laminar recording. *Biomaterials, 37*, 25–39.

183. Kozai, T. D. Y., Du, Z., Gugel, Z. V., Smith, M. A., Chase, S. M., Bodily, L. M., . . . Cui, X. T. (2015). Comprehensive chronic laminar single-unit, multi-unit, and local field potential recording performance with planar single shank electrode arrays. *Journal of Neuroscience Methods, 242*(1), 15-40. doi:http://dx.doi.org/10.1016/j.jneumeth.2014.12.010

184. Kozai, T. D. Y., Eles, J. R., Vazquez, A. L., & Cui, X. T. (2016). Two-photon imaging of chronically implanted neural electrodes: Sealing methods and new insights. *Journal of Neuroscience Methods, 256*, 46-55. doi:http://dx.doi.org/10.1016/j.jneumeth.2015.10.007

185. Kozai, T. D. Y., Jaquins-Gerstl, A., Vazquez, A. L., Michael, A. C., & Cui, X. T. (2015). Brain Tissue Responses to Neural Implants Impact Signal Sensitivity and Intervention Strategies. *ACS Chemical Neuroscience, 6*(1), 48-67. doi:10.1021/cn500256e

186. Kozai, T. D. Y., Jaquins-Gerstl, A. S., Vazquez, A. L., Michael, A. C., & Cui, X. T. (2015). Brain Tissue Responses to Neural Implants Impact Signal Sensitivity and Intervention Strategies. *ACS Chemical Neuroscience, 6*(1), 48-67. doi:10.1021/cn500256e

187. Kozai, T. D. Y., Jaquins-gerstl, A. S., Vazquez, A. L., Michael, A. C., & Cui, X. T. (2016). Dexamethasone retrodialysis attenuates microglial response to implanted probes in vivo. *Biomaterials, 87*, 157-169. doi:10.1016/j.biomaterials.2016.02.013

188. Kozai, T. D. Y., Li, X., Bodily, L. M., Caparosa, E. M., Zenonos, G. A., Carlisle, D. L., . . . Cui, X. T. (2014). Effects of caspase-1 knockout on chronic neural recording quality and longevity: Insight into cellular and molecular mechanisms of the reactive tissue response. *Biomaterials, 35*(36), 9620-9634.

189. Kozai, T. D. Y., Marzullo, T. C., Hooi, F., Langhals, N. B., Majewska, A., Brown, E., & Kipke, D. R. (2010). Reduction of neurovascular damage resulting from microelectrode insertion into the cerebral cortex using in vivo two-photon mapping. *Journal of Neural Engineering, 7*(4), 046011.

190. Kozai, T. D. Y., Marzullo, T. C., Hooi, F., Langhals, N. B., Majewska, A. K., Brown, E. B., & Kipke, D. R. (2010). Reduction of neurovascular damage resulting from microelectrode insertion into the cerebral cortex using in vivo two-photon mapping. *J Neural Eng, 7*(4), 046011. doi:10.1088/1741-2560/7/4/046011

191. Kozai, T. D. Y., Vazquez, A. L., & Weaver, C. L. (2012). In vivo two-photon microscopy reveals immediate microglial reaction to implantation of microelectrode through. *J Neural Eng, 9*, 1-17. doi:10.1088/1741-2560/9/6/066001

192. Kozai, T. D. Y., Vazquez, A. L., Weaver, C. L., Kim, S.-G., & Cui, X. T. (2012). In vivo two-photon microscopy reveals immediate microglial reaction to implantation of microelectrode through extension of processes. *Journal of Neural Engineering, 9*(6), 066001.

193. Kozberg, M., & Hillman, E. (2016). Neurovascular coupling and energy metabolism in the developing brain. *Progress in brain research, 225*, 213-242.

194. Krahe, D. D., Woeppel, K. M., Yang, Q., Kushwah, N., & Cui, X. T. (2022). Melatonin Decreases Acute Inflammatory Response to Neural Probe Insertion. *Antioxidants, 11*(8), 1628.

195. Krämer, E. M., Schardt, A., & Nave, K. A. (2001). Membrane traffic in myelinating oligodendrocytes. *Microscopy research and technique, 52*(6), 656-671.

196. Kuchibhotla, K. V., Wegmann, S., Kopeikina, K. J., Hawkes, J., Rudinskiy, N., Andermann, M. L., . . . Hyman, B. T. (2014). Neurofibrillary tangle-bearing neurons are functionally integrated in cortical circuits in vivo. *Proc Natl Acad Sci U S A, 111*(1), 510-514. doi:10.1073/pnas.1318807111

197. Kuhlmann, T., Miron, V., Cuo, Q., Wegner, C., Antel, J., & Brück, W. (2008). Differentiation block of oligodendroglial progenitor cells as a cause for remyelination failure in chronic multiple sclerosis. *Brain, 131*(7), 1749-1758. doi:10.1093/brain/awn096

198. Kushwah, N., Woeppel, K., Dhawan, V., Shi, D., & Cui, X. T. (2022). Effects of neuronal cell adhesion molecule L1 and nanoparticle surface modification on microglia. *Acta Biomater, 149*, 273-286. doi:10.1016/j.actbio.2022.06.038

199. Lacour, S. P., Courtine, G., & Guck, J. (2016). Materials and technologies for soft implantable neuroprostheses. *Nature Reviews Materials, 1*, 16063. doi:10.1038/natrevmats.2016.63

200. Lai, A. Y., & McLaurin, J. (2012). Clearance of amyloid-β peptides by microglia and macrophages: the issue of what, when and where. *Future Neurol, 7*(2), 165-176. doi:10.2217/fnl.12.6

201. Lee, C., & Landreth, G. E. (2010). The role of microglia in amyloid clearance from the AD brain. *Journal of neural transmission, 117*(8), 949-960.

202. Lee, J. H., Kim, H., Kim, J. H., & Lee, S.-H. (2016). Soft implantable microelectrodes for future medicine: prosthetics, neural signal recording and neuromodulation. *Lab on a Chip, 16*(6), 959-976. doi:10.1039/C5LC00842E

203. Lee, J. Y., Kang, S. R., & Yune, T. Y. (2015). Fluoxetine prevents oligodendrocyte cell death by inhibiting microglia activation after spinal cord injury. *Journal of Neurotrauma, 32*(9), 633-644.

204. Lee, Y., Morrison, B. M., Li, Y., Lengacher, S., Farah, M. H., Hoffman, P. N., . . . Rothstein, J. D. (2012). Oligodendroglia metabolically support axons and contribute to neurodegeneration. *Nature, 487*(7408), 443-448. doi:10.1038/nature11314

205. Lemons, M. L., Howland, D. R., & Anderson, D. K. (1999). Chondroitin sulfate proteoglycan immunoreactivity increases following spinal cord injury and transplantation. *Exp Neurol, 160*(1), 51-65. doi:10.1006/exnr.1999.7184

206. Levine, J. M. (1994). Increased expression of the NG2 chondroitin-sulfate proteoglycan after brain injury. *The Journal of neuroscience : the official journal of the Society for Neuroscience, 14*(8), 4716-4730.

207. Levine, J. M., & Reynolds, R. (1999). Activation and proliferation of endogenous oligodendrocyte precursor cells during ethidium bromide-induced demyelination. *Experimental neurology, 160*(2), 333-347.

208. Levine, J. M., Reynolds, R., & Fawcett, J. W. (2001). The oligodendrocyte precursor cell in health and disease. *Trends in neurosciences, 24*(1), 39-47.

209. LeVine, S. M., & Torres, M. V. (1993). Satellite oligodendrocytes and myelin are displaced in the cortex of the reeler mouse. *Developmental Brain Research, 75*(2), 279-284. doi:https://doi.org/10.1016/0165-3806(93)90032-6

210. Lewis, C. A., Manning, J., Rossi, F., & Krieger, C. (2012). The Neuroinflammatory Response in ALS: The Roles of Microglia and T Cells. *Neurol Res Int, 2012*, 803701. doi:10.1155/2012/803701

211. Lin, T. N., Te, J., Lee, M., Sun, G. Y., & Hsu, C. Y. (1997). Induction of basic fibroblast growth factor (bFGF) expression following focal cerebral ischemia. *Brain research Molecular brain research, 49*(1-2), 255-265.

212. Lindahl, P., Johansson, B. R., Levéen, P., & Betsholtz, C. (1997). Pericyte loss and microaneurysm formation in PDGF-B-deficient mice. *Science, 277*(5323), 242-245.

213. Liu, F., Grundke-Iqbal, I., Iqbal, K., & Gong, C. X. (2005). Contributions of protein phosphatases PP1, PP2A, PP2B and PP5 to the regulation of tau phosphorylation. *European Journal of Neuroscience, 22*(8), 1942-1950.

214. Liu, L., Liu, Y., Li, N., Huang, R., Zheng, X., Huang, L., . . . Yuan, Q. (2020). Multiple inflammatory profiles of microglia and altered neuroimages in APP/PS1 transgenic AD mice. *Brain research bulletin, 156*, 86-104.

215. Lotocki, G., Vaccari, J. d. R., Alonso, O., Molano, J. S., Nixon, R., Safavi, P., . . . Bramlett, H. M. (2011). Oligodendrocyte vulnerability following traumatic brain injury in rats. *Neuroscience Letters, 499*(3), 143-148. doi:https://doi.org/10.1016/j.neulet.2011.05.056

216. Ludwig, K. A., Miriani, R. M., Langhals, N. B., Joseph, M. D., Anderson, D. J., & Kipke, D. R. (2009). Using a common average reference to improve cortical neuron recordings from microelectrode arrays. *Journal of neurophysiology, 101*(3), 1679-1689.

217. Ludwin, S. K. (1979). The perineuronal satellite oligodendrocyte. *Acta neuropathologica, 47*(1), 49-53. doi:10.1007/BF00698272

218. Luo, Y., Sun, Y., Tian, X., Zheng, X., Wang, X., Li, W., . . . Hou, W. (2021). Deep Brain Stimulation for Alzheimer's Disease: Stimulation Parameters and Potential Mechanisms of Action. *Front Aging Neurosci, 13*, 619543. doi:10.3389/fnagi.2021.619543

219. Maier, A., Adams, G. K., Aura, C., & Leopold, D. A. (2010). Distinct superficial and deep laminar domains of activity in the visual cortex during rest and stimulation. *Frontiers in systems neuroscience, 4*, 31. doi:10.3389/fnsys.2010.00031

220. Marin, C., & Fernandez, E. (2010). Biocompatibility of intracortical microelectrodes: current status and future prospects. *Front Neuroeng, 3*, 8. doi:10.3389/fneng.2010.00008

221. Markoullis, K., Sargiannidou, I., Schiza, N., Roncaroli, F., Reynolds, R., & Kleopa, K. A. (2014). Oligodendrocyte Gap Junction Loss and Disconnection From Reactive Astrocytes in Multiple Sclerosis Gray Matter. *Journal of Neuropathology & Experimental Neurology, 73*(9), 865-879. doi:10.1097/nen.0000000000000106

222. Martin, V., Pavel, H., Eliska, W., Hana, M., Jan, K., Denisa, K., . . . Miroslava, A. A single-cell analysis reveals multiple roles of oligodendroglial lineage cells during post-ischemic regeneration. *Glia*, n/a-n/a. doi:10.1002/glia.23301

223. Martorell, A. J., Paulson, A. L., Suk, H. J., Abdurrob, F., Drummond, G. T., Guan, W., . . . Tsai, L. H. (2019). Multi-sensory Gamma Stimulation Ameliorates Alzheimer's-Associated Pathology and Improves Cognition. *Cell, 177*(2), 256-271.e222. doi:10.1016/j.cell.2019.02.014

224. Matsushima, G. K., & Morell, P. (2001). The neurotoxicant, cuprizone, as a model to study demyelination and remyelination in the central nervous system. *Brain pathology, 11*(1), 107-116.

225. Maysami, S., Nguyen, D., Zobel, F., Heine, S., Hopfner, M., & Stangel, M. (2006). Oligodendrocyte precursor cells express a functional chemokine receptor CCR3: implications for myelination. *Journal of Neuroimmunology, 178*(1-2), 17-23.

226. McConnell, G. C., Butera, R. J., & Bellamkonda, R. V. (2009). Bioimpedance modeling to monitor astrocytic response to chronically implanted electrodes. *J Neural Eng, 6*(5), 055005. doi:10.1088/1741-2560/6/5/055005

227. McConnell, G. C., Rees, H. D., Levey, A. I., Gutekunst, C.-A., Gross, R. E., & Bellamkonda, R. V. (2009). Implanted neural electrodes cause chronic, local inflammation that is correlated with local neurodegeneration. *Journal of Neural Engineering, 6*(5), 056003.

228. McConnell, G. C., Rees, H. D., Levey, A. I., Gutekunst, C. A., Gross, R. E., & Bellamkonda, R. V. (2009). Implanted neural electrodes cause chronic, local inflammation that is correlated with local neurodegeneration. *J Neural Eng, 6*(5), 56003. doi:S1741-2560(09)15685-9 [pii]

229. 10.1088/1741-2560/6/5/056003

230. McCreery, D., Cogan, S., Kane, S., & Pikov, V. (2016). Correlations between histology and neuronal activity recorded by microelectrodes implanted chronically in the cerebral cortex. *Journal of Neural Engineering, 13*(3), 036012.

231. McCreery, D., Cogan, S., Kane, S., & Pikov, V. (2016). Correlations between histology and neuronal activity recorded by microelectrodes implanted chronically in the cerebral cortex. *J Neural Eng, 13*(3), 036012. doi:10.1088/1741-2560/13/3/036012

232. McTigue, D. M., & Tripathi, R. B. (2008). The life, death, and replacement of oligodendrocytes in the adult CNS. *Journal of neurochemistry, 107*(1), 1-19.

233. Mechler, F., & Victor, J. D. (2012). Dipole characterization of single neurons from their extracellular action potentials. *Journal of Computational Neuroscience, 32*(1), 73-100. doi:10.1007/s10827-011-0341-0

234. Mehdi, J., John, L. S., Christoph, W., & Jeffrey, R. C. (2015). Progress towards biocompatible intracortical microelectrodes for neural interfacing applications. *J Neural Eng, 12*(1), 011001.

235. Michelson, N. J., Eles, J. R., Vazquez, A. L., Ludwig, K. A., & Kozai, T. D. Y. (2018). Calcium activation of cortical neurons by continuous electrical stimulation: Frequency-dependence, temporal fidelity and activation density. *Journal of Neuroscience Research*.

236. Michelson, N. J., & Kozai, T. D. Y. (2018). Isoflurane and ketamine differentially influence spontaneous and evoked laminar electrophysiology in mouse V1. *Journal of neurophysiology, 120*(5), 2232-2245. doi:10.1152/jn.00299.2018

237. Michelson, N. J., Vazquez, A. L., Eles, J. R., Salatino, J. W., Purcell, E. K., Williams, J. J., . . . Kozai, T. D. (2018). Multi-scale, multi-modal analysis uncovers complex relationship at the brain tissue-implant neural interface: new emphasis on the biological interface. *Journal of Neural Engineering, 15*(3), 033001.

238. Michelson, N. J., Vazquez, A. L., Eles, J. R., Salatino, J. W., Purcell, E. K., Williams, J. J., . . . Kozai, T. D. Y. (2017). Multi-scale, multi-modal analysis uncovers complex relationship at the brain tissue-implant neural interface: New Emphasis on the Biological Interface. *Journal of neural engineering*. doi:10.1088/1741-2552/aa9dae

239. Michelson, N. J., Vazquez, A. L., Eles, J. R., Salatino, J. W., Purcell, E. K., Williams, J. J., . . . Kozai, T. D. Y. (2018). Multi-scale, multi-modal analysis uncovers complex relationship at the brain tissue-implant neural interface: New Emphasis on the Biological Interface. *Journal of neural engineering, 15*(033001).

240. Micheva, K. D., Wolman, D., Mensh, B. D., Pax, E., Buchanan, J., Smith, S. J., & Bock, D. D. (2016). A large fraction of neocortical myelin ensheathes axons of local inhibitory neurons. *eLife, 5*, e15784. doi:10.7554/eLife.15784

241. Mishra, A., O'Farrell, F. M., Reynell, C., Hamilton, N. B., Hall, C. N., & Attwell, D. (2014). Imaging pericytes and capillary diameter in brain slices and isolated retinae. *Nat Protoc, 9*(2), 323-336. doi:10.1038/nprot.2014.019

242. Morell, P., Barrett, C. V., Mason, J. L., Toews, A. D., Hostettler, J. D., Knapp, G. W., & Matsushima, G. K. (1998). Gene Expression in Brain during Cuprizone-Induced Demyelination and Remyelination. *Molecular and Cellular Neuroscience, 12*(4), 220-227. doi:https://doi.org/10.1006/mcne.1998.0715

243. Muoio, V., Persson, P. B., & Sendeski, M. M. (2014). The neurovascular unit - concept review. *Acta physiologica (Oxford, England), 210*(4), 790-798.

244. Nadol, J. B., Jr., O'Malley, J. T., Burgess, B. J., & Galler, D. (2014). Cellular immunologic responses to cochlear implantation in the human. *Hear Res, 318*, 11-17. doi:10.1016/j.heares.2014.09.007

245. Nakano, M., Tamura, Y., Yamato, M., Kume, S., Eguchi, A., Takata, K., . . . Kataoka, Y. (2017). NG2 glial cells regulate neuroimmunological responses to maintain neuronal function and survival. *Sci Rep, 7*, 42041. doi:10.1038/srep42041

246. Napoli, I., & Neumann, H. (2010). Protective effects of microglia in multiple sclerosis. *Experimental neurology, 225*(1), 24-28.

247. Nelson, A. R., Sagare, M. A., Wang, Y., Kisler, K., Zhao, Z., & Zlokovic, B. V. (2020). Channelrhodopsin excitation contracts brain pericytes and reduces blood flow in the aging mouse brain in vivo. *Frontiers in aging neuroscience, 12*, 108.

248. Neu, S. C., Pa, J., Kukull, W., Beekly, D., Kuzma, A., Gangadharan, P., . . . Redolfi, A. (2017). Apolipoprotein E genotype and sex risk factors for Alzheimer disease: a meta-analysis. *JAMA neurology, 74*(10), 1178-1189.

249. Nguyen, J. K., Jorfi, M., Buchanan, K. L., Park, D. J., Foster, E. J., Tyler, D. J., . . . Capadona, J. R. (2016). Influence of resveratrol release on the tissue response to mechanically adaptive cortical implants. *Acta Biomaterialia, 29*, 81-93.

250. Nicolai, E., Michelson, N., Settell, M., Hara, S., Trevathan, J., Asp, A., . . . Ludwig, K. J. M. (2018). Design choices for next-generation neurotechnology can impact motion artifact in electrophysiological and fast-scan cyclic voltammetry measurements. *9*(10), 494.

251. Nicolai, E. N., Michelson, N. J., Settell, M. L., Hara, S. A., Trevathan, J. K., Asp, A. J., . . . Ludwig, K. A. (2018). Design Choices for Next-Generation Neurotechnology Can Impact Motion Artifact in Electrophysiological and Fast-Scan Cyclic Voltammetry Measurements. *Micromachines, 9*(10), 494.

252. Nielson, C. D., & Shih, A. Y. (2022). In vivo Single Cell Optical Ablation of Brain Pericytes. *Front Neurosci, 16*, 900761. doi:10.3389/fnins.2022.900761

253. Nikolakopoulou, A. M., Montagne, A., Kisler, K., Dai, Z., Wang, Y., Huuskonen, M. T., . . . Kong, P. (2019). Pericyte loss leads to circulatory failure and pleiotrophin depletion causing neuron loss. *Nature neuroscience, 22*(7), 1089-1098.

254. Nishiyama, A., Komitova, M., Suzuki, R., & Zhu, X. (2009). Polydendrocytes (NG2 cells): multifunctional cells with lineage plasticity. *Nature Reviews Neuroscience, 10*(1), 9-22.

255. Nishiyama, A., Yang, Z., & Butt, A. (2005a). Astrocytes and NG2-glia: what's in a name? *Journal of anatomy, 207*(6), 687-693.

256. Nishiyama, A., Yang, Z., & Butt, A. (2005b). Astrocytes and NG2-glia: what's in a name? *Journal of anatomy, 207*(6), 687-693.

257. Noble, W., Hanger, D. P., Miller, C. C., & Lovestone, S. (2013). The importance of tau phosphorylation for neurodegenerative diseases. *Frontiers in neurology, 4*, 83.

258. Nomura, T., Bando, Y., Nakazawa, H., Kanemoto, S., & Yoshida, S. (2019). Pathological changes in mice with long term cuprizone administration. *Neurochemistry International, 126*, 229-238. doi:https://doi.org/10.1016/j.neuint.2019.03.018

259. Nortley, R., Korte, N., Izquierdo, P., Hirunpattarasilp, C., Mishra, A., Jaunmuktane, Z., . . . Madry, C. (2019). Amyloid β oligomers constrict human capillaries in Alzheimer's disease via signaling to pericytes. *Science, 365*(6450), eaav9518.

260. Nowak, L., Ascher, P., & Berwald-Netter, Y. (1987). Ionic channels in mouse astrocytes in culture. *Journal of Neuroscience, 7*(1), 101-109.

261. Nualart-Marti, A., Solsona, C., & Fields, R. D. (2013). Gap junction communication in myelinating glia. *Biochimica et Biophysica Acta (BBA) - Biomembranes, 1828*(1), 69-78. doi:https://doi.org/10.1016/j.bbamem.2012.01.024

262. Olivier, P., Fontaine, R. H., Loron, G., Van Steenwinckel, J., Biran, V., Massonneau, V., . . . Aigrot, M.-S. (2009). Melatonin promotes oligodendroglial maturation of injured white matter in neonatal rats. *PLoS One, 4*(9), e7128.

263. Oxidative Stress, Accumulation of Biological 'Garbage', and Aging. (2006). *Antioxidants & Redox Signaling, 8*(1-2), 197-204. doi:10.1089/ars.2006.8.197

264. Özen, I., Deierborg, T., Miharada, K., Padel, T., Englund, E., Genové, G., & Paul, G. (2014). Brain pericytes acquire a microglial phenotype after stroke. *Acta Neuropathol, 128*(3), 381-396. doi:10.1007/s00401-014-1295-x

265. Özen, I., Deierborg, T., Miharada, K., Padel, T., Englund, E., Genové, G., & Paul, G. (2014). Brain pericytes acquire a microglial phenotype after stroke. *Acta neuropathologica, 128*(3), 381-396.

266. Ozerdem, U., & Stallcup, W. B. (2003). Early contribution of pericytes to angiogenic sprouting and tube formation. *Angiogenesis, 6*(3), 241-249.

267. Pajevic, S., Basser, P. J., & Fields, R. D. (2014). Role of myelin plasticity in oscillations and synchrony of neuronal activity. *Neuroscience, 276*, 135-147. doi:https://doi.org/10.1016/j.neuroscience.2013.11.007

268. Parenti, R., Cicirata, F., Zappalà, A., Catania, A., La Delia, F., Cicirata, V., . . . Willecke, K. (2010). Dynamic expression of Cx47 in mouse brain development and in the cuprizone model of myelin plasticity. *Glia, 58*(13), 1594-1609. doi:10.1002/glia.21032

269. Pasquini, L. A., Calatayud, C. A., Bertone Uña, A. L., Millet, V., Pasquini, J. M., & Soto, E. F. (2007). The Neurotoxic Effect of Cuprizone on Oligodendrocytes Depends on the Presence of Pro-inflammatory Cytokines Secreted by Microglia. *Neurochemical Research, 32*(2), 279-292. doi:10.1007/s11064-006-9165-0

270. Patil, A. C., & Thakor, N. V. (2016). Implantable neurotechnologies: a review of micro- and nanoelectrodes for neural recording. *Medical & Biological Engineering & Computing, 54*(1), 23-44. doi:10.1007/s11517-015-1430-4

271. Paukert, M., & Bergles, D. E. (2006). Synaptic communication between neurons and NG2+ cells. *Current opinion in neurobiology, 16*(5), 515-521.

272. Peña, K., Coblenz, J., & Kiselyov, K. (2015). Brief exposure to copper activates lysosomal exocytosis. *Cell calcium, 57*(4), 257-262.

273. Philips, T., & Rothstein, J. D. (2017). Oligodendroglia: metabolic supporters of neurons. *The Journal of clinical investigation, 127*(9), 3271-3280. doi:10.1172/JCI90610

274. Picture Thresholding Using an Iterative Selection Method. (1978). *IEEE Transactions on Systems, Man, and Cybernetics, 8*(8), 630-632. doi:10.1109/TSMC.1978.4310039

275. Pigino, G., Pelsman, A., Mori, H., & Busciglio, J. (2001). Presenilin-1 mutations reduce cytoskeletal association, deregulate neurite growth, and potentiate neuronal dystrophy and tau phosphorylation. *Journal of Neuroscience, 21*(3), 834-842.

276. Polikov, V. S., Tresco, P. A., & Reichert, W. M. (2005). Response of brain tissue to chronically implanted neural electrodes. *J Neurosci Methods, 148*(1), 1-18. doi:S0165-0270(05)00293-1 [pii]

277. 10.1016/j.jneumeth.2005.08.015

278. PORTA, E. A. (2002). Pigments in Aging: An Overview. *Annals of the New York Academy of Sciences, 959*(1), 57-65. doi:https://doi.org/10.1111/j.1749-6632.2002.tb02083.x

279. Potter-Baker, K. A., Ravikumar, M., Burke, A. A., Meador, W. D., Householder, K. T., Buck, A. C., . . . Tomaszewski, W. H. (2014). A comparison of neuroinflammation to implanted microelectrodes in rat and mouse models. *Biomaterials, 35*(22), 5637-5646.

280. Potter, K. A., Buck, A. C., Self, W. K., Callanan, M. E., Sunil, S., & Capadona, J. R. (2013). The effect of resveratrol on neurodegeneration and blood brain barrier stability surrounding intracortical microelectrodes. *Biomaterials, 34*(29), 7001-7015.

281. Potter, K. A., Buck, A. C., Self, W. K., & Capadona, J. R. (2012). Stab injury and device implantation within the brain results in inversely multiphasic neuroinflammatory and neurodegenerative responses. *J Neural Eng, 9*(4), 046020. doi:10.1088/1741-2560/9/4/046020

282. Praet, J., Guglielmetti, C., Berneman, Z., Van der Linden, A., & Ponsaerts, P. (2014). Cellular and molecular neuropathology of the cuprizone mouse model: Clinical relevance for multiple sclerosis. *Neuroscience & Biobehavioral Reviews, 47*, 485-505. doi:https://doi.org/10.1016/j.neubiorev.2014.10.004

283. Prasad, A., Sankar, V., Dyer, A. T., Knott, E., Xue, Q., Nishida, T., . . . Sanchez, J. C. (2011, 30 Aug.-3 Sept. 2011). *Coupling biotic and abiotic metrics to create a testbed for predicting neural electrode performance.* Paper presented at the 2011 Annual International Conference of the IEEE Engineering in Medicine and Biology Society.

284. Prasad, A., Xue, Q.-S., Sankar, V., Nishida, T., Shaw, G., Streit, W. J., & Sanchez, J. C. (2012). Comprehensive characterization and failure modes of tungsten microwire arrays in chronic neural implants. *Journal of neural engineering, 9*(5), 056015.

285. Price, T. O., Eranki, V., Banks, W. A., Ercal, N., & Shah, G. N. (2012). Topiramate treatment protects blood-brain barrier pericytes from hyperglycemia-induced oxidative damage in diabetic mice. *Endocrinology, 153*(1), 362-372.

286. Puthongkham, P., & Venton, B. J. (2019). Nanodiamond coating improves the sensitivity and antifouling properties of carbon fiber microelectrodes. *ACS sensors, 4*(9), 2403-2411.

287. Ralay Ranaivo, H., & Wainwright, M. S. (2010). Albumin activates astrocytes and microglia through mitogen-activated protein kinase pathways. *Brain research, 1313*, 222-231.

288. Rash, J. E. (2010). Molecular disruptions of the panglial syncytium block potassium siphoning and axonal saltatory conduction: pertinence to neuromyelitis optica and other demyelinating diseases of the central nervous system. *Neuroscience, 168*(4), 982-1008.

289. Ravikumar, M., Sunil, S., Black, J., Barkauskas, D. S., Haung, A. Y., Miller, R. H., . . . Capadona, J. R. (2014). The roles of blood-derived macrophages and resident microglia in the neuroinflammatory response to implanted intracortical microelectrodes. *Biomaterials, 35*(28), 8049-8064. doi:10.1016/j.biomaterials.2014.05.084

290. Rennaker, R., Miller, J., Tang, H., & Wilson, D. (2007). Minocycline increases quality and longevity of chronic neural recordings. *Journal of Neural Engineering, 4*(2), L1.

291. Ribatti, D., Nico, B., & Crivellato, E. (2011). The role of pericytes in angiogenesis. *Int J Dev Biol, 55*(3), 261-268. doi:10.1387/ijdb.103167dr

292. Rivers-Auty, J., Mather, A. E., Peters, R., Lawrence, C. B., & Brough, D. (2020). Anti-inflammatories in Alzheimer's disease—potential therapy or spurious correlate? *Brain communications, 2*(2), fcaa109.

293. Rivers, L. E., Young, K. M., Rizzi, M., Jamen, F., Psachoulia, K., Wade, A., . . . Richardson, W. D. (2008). PDGFRA/NG2 glia generate myelinating oligodendrocytes and piriform projection neurons in adult mice. *Nature neuroscience, 11*(12), 1392-1401.

294. Robel, S., Berninger, B., & Gotz, M. (2011). The stem cell potential of glia: lessons from reactive gliosis. *Nature Reviews Neuroscience, 12*(2), 88-104.

295. Roitbak, T., & Sykova, E. (1999). Diffusion barriers evoked in the rat cortex by reactive astrogliosis. *Glia, 28*(1), 40-48.

296. Rosko, L., Smith, V. N., Yamazaki, R., & Huang, J. K. (2018). Oligodendrocyte Bioenergetics in Health and Disease. *The Neuroscientist*, 1073858418793077. doi:10.1177/1073858418793077

297. Rossi, S., Studer, V., Motta, C., De Chiara, V., Barbieri, F., Bernardi, G., & Centonze, D. (2012). Inflammation inhibits GABA transmission in multiple sclerosis. *Multiple Sclerosis Journal, 18*(11), 1633-1635.

298. Roth, A. D., & Núñez, M. T. (2016). Oligodendrocytes: functioning in a delicate balance between high metabolic requirements and oxidative damage. In *Glial Cells in Health and Disease of the CNS* (pp. 167-181): Springer.

299. Rouget, C. (1873). Memoire sur le develloppment, la structure et les propietes physiologiques des capillaries senguins et lymphatiques. *Arch. Physiol. Norm. Pathol., 5*, 603-663.

300. Rousche, P. J., & Normann, R. A. (1998). Chronic recording capability of the Utah Intracortical Electrode Array in cat sensory cortex. *J Neurosci Methods, 82*(1), 1-15. doi:S0165-0270(98)00031-4 [pii]

301. Rousche, P. J., & Normann, R. A. (1998). Chronic recording capability of the Utah Intracortical Electrode Array in cat sensory cortex. *Journal of Neuroscience Methods, 82*(1), 1-15. doi:https://doi.org/10.1016/S0165-0270(98)00031-4

302. Rousche, P. J., Pellinen, D. S., Pivin, D. P., Jr., Williams, J. C., Vetter, R. J., & Kipke, D. R. (2001). Flexible polyimide-based intracortical electrode arrays with bioactive capability. *IEEE Trans Biomed Eng, 48*(3), 361-371. doi:10.1109/10.914800

303. Rowley, C. D., Bazin, P.-L., Tardif, C. L., Sehmbi, M., Hashim, E., Zaharieva, N., . . . Bock, N. A. (2015). Assessing intracortical myelin in the living human brain using myelinated cortical thickness. *Frontiers in Neuroscience, 9*, 396. doi:10.3389/fnins.2015.00396

304. Sakry, D., Neitz, A., Singh, J., Frischknecht, R., Marongiu, D., Biname, F., . . . Mittmann, T. (2014). Oligodendrocyte precursor cells modulate the neuronal network by activity-dependent ectodomain cleavage of glial NG2. *PLoS biology, 12*(11), e1001993.

305. Sakuma, R., Kawahara, M., Nakano-Doi, A., Takahashi, A., Tanaka, Y., Narita, A., . . . Matsuyama, T. (2016). Brain pericytes serve as microglia-generating multipotent vascular stem cells following ischemic stroke. *Journal of neuroinflammation, 13*(1), 1-13.

306. Sakuma, R., Kawahara, M., Nakano-Doi, A., Takahashi, A., Tanaka, Y., Narita, A., . . . Nakagomi, T. (2016). Brain pericytes serve as microglia-generating multipotent vascular stem cells following ischemic stroke. *J Neuroinflammation, 13*(1), 57. doi:10.1186/s12974-016-0523-9

307. Salatino, J. W., Ludwig, K. A., Kozai, T. D., & Purcell, E. K. (2017). Glial responses to implanted electrodes in the brain. *Nature biomedical engineering, 1*(11), 862-877.

308. Salatino, J. W., Ludwig, K. A., Kozai, T. D. Y., & Purcell, E. K. (2017). Glial responses to implanted electrodes in the brain. *Nature BME*.

309. Salloway, S., Sperling, R., Fox, N. C., Blennow, K., Klunk, W., Raskind, M., . . . Ferris, S. (2014). Two phase 3 trials of bapineuzumab in mild-to-moderate Alzheimer's disease. *New England Journal of Medicine, 370*(4), 322-333.

310. Savya, S. P., Li, F., Lam, S., Wellman, S. M., Stieger, K. C., Chen, K., . . . Kozai, T. D. (2022). In vivo spatiotemporal dynamics of astrocyte reactivity following neural electrode implantation. *Biomaterials, 289*, 121784.

311. Saxena, T., Karumbaiah, L., Gaupp, E. A., Patkar, R., Patil, K., Betancur, M., . . . Bellamkonda, R. V. (2013). The impact of chronic blood-brain barrier breach on intracortical electrode function. *Biomaterials, 34*(20), 4703-4713. doi:10.1016/j.biomaterials.2013.03.007

312. Schwartz, A. B., Cui, X. T., Weber, D. J., & Moran, D. W. (2006). Brain-controlled interfaces: movement restoration with neural prosthetics. *Neuron, 52*(1), 205-220.

313. Schwartz, A. B., Cui, X. T., Weber, D. J., & Moran, D. W. (2006). Brain-controlled interfaces: movement restoration with neural prosthetics. *Neuron, 52*(1), 205-220.

314. Sen, M. K., Mahns, D. A., Coorssen, J. R., & Shortland, P. J. (2019). Behavioural phenotypes in the cuprizone model of central nervous system demyelination. *Neuroscience & Biobehavioral Reviews, 107*, 23-46. doi:https://doi.org/10.1016/j.neubiorev.2019.08.008

315. Seo, J. H., Maki, T., Maeda, M., Miyamoto, N., Liang, A. C., Hayakawa, K., . . . Arai, K. (2014). Oligodendrocyte precursor cells support blood-brain barrier integrity via TGF-beta signaling. *PloS one, 9*(7), e103174.

316. Serlin, Y., Shelef, I., Knyazer, B., & Friedman, A. (2015). Anatomy and physiology of the blood-brain barrier. *Semin Cell Dev Biol, 38*, 2-6. doi:10.1016/j.semcdb.2015.01.002

317. Shah, G. N., Price, T. O., Banks, W. A., Morofuji, Y., Kovac, A., Ercal, N., . . . Sheibani, N. (2013). Pharmacological inhibition of mitochondrial carbonic anhydrases protects mouse cerebral pericytes from high glucose-induced oxidative stress and apoptosis. *Journal of Pharmacology and Experimental Therapeutics, 344*(3), 637-645.

318. Shi, D., Dhawan, V., & Cui, X. T. (2021). Bio-integrative design of the neural tissue-device interface. *Curr Opin Biotechnol, 72*, 54-61. doi:10.1016/j.copbio.2021.10.003

319. Shoffstall, A. J., Ecker, M., Danda, V., Joshi-Imre, A., Stiller, A., Yu, M., . . . Voit, W. E. (2018). Characterization of the neuroinflammatory response to thiol-ene shape memory polymer coated intracortical microelectrodes. *Micromachines, 9*(10), 486.

320. Simon, C., Gotz, M., & Dimou, L. (2011). Progenitors in the adult cerebral cortex: cell cycle properties and regulation by physiological stimuli and injury. *Glia, 59*(6), 869-881. doi:10.1002/glia.21156

321. Sims, R., Van Der Lee, S. J., Naj, A. C., Bellenguez, C., Badarinarayan, N., Jakobsdottir, J., . . . Bis, J. C. (2017). Rare coding variants in PLCG2, ABI3, and TREM2 implicate microglial-mediated innate immunity in Alzheimer's disease. *Nature genetics, 49*(9), 1373-1384.

322. Skripuletz, T., Lindner, M., Kotsiari, A., Garde, N., Fokuhl, J., Linsmeier, F., . . . Stangel, M. (2008). Cortical demyelination is prominent in the murine cuprizone model and is strain-dependent. *The American journal of pathology, 172*(4), 1053-1061. doi:10.2353/ajpath.2008.070850

323. Slater, C., & Wang, Q. (2021). Alzheimer's disease: An evolving understanding of noradrenergic involvement and the promising future of electroceutical therapies. *Clin Transl Med, 11*(4), e397. doi:10.1002/ctm2.397

324. Smith, K. J., & McDonald, W. I. (1999). The pathophysiology of multiple sclerosis: the mechanisms underlying the production of symptoms and the natural history of the disease. *Philosophical transactions of the Royal Society of London. Series B, Biological sciences, 354*(1390), 1649-1673. doi:10.1098/rstb.1999.0510

325. Snaidero, N., & Simons, M. (2017). The logistics of myelin biogenesis in the central nervous system. *Glia, 65*(7), 1021-1031.

326. Song, F. E., Huang, J. L., Lin, S. H., Wang, S., Ma, G. F., & Tong, X. P. (2017). Roles of NG2-glia in ischemic stroke. *CNS Neurosci Ther, 23*(7), 547-553. doi:10.1111/cns.12690

327. Song, J., Tucker, D. M., Gilbert, T., Hou, J., Mattson, C., Luu, P., & Holmes, M. D. (2013). Methods for examining electrophysiological coherence in epileptic networks. *Frontiers in neurology, 4*, 55-55. doi:10.3389/fneur.2013.00055

328. Spaas, J., van Veggel, L., Schepers, M., Tiane, A., van Horssen, J., Wilson, D. M., . . . Eijnde, B. O. (2021). Oxidative stress and impaired oligodendrocyte precursor cell differentiation in neurological disorders. *Cellular and Molecular Life Sciences, 78*(10), 4615-4637.

329. Spiers, K., Cardamone, T., Furness, J. B., Clark, J. C., Patrick, J. F., & Clark, G. M. (2016). An X-ray fluorescence microscopic analysis of the tissue surrounding the multi-channel cochlear implant electrode array. *Cochlear Implants Int, 17*(3), 129-131. doi:10.1080/14670100.2016.1157943

330. Steinmetz, N. A., Aydin, C., Lebedeva, A., Okun, M., Pachitariu, M., Bauza, M., . . . Harris, T. D. (2021). Neuropixels 2.0: A miniaturized high-density probe for stable, long-term brain recordings. *Science, 372*(6539). doi:10.1126/science.abf4588

331. Stocking, K. C., Vazquez, A. L., & Kozai, T. D. Y. (2019). Intracortical neural stimulation with untethered, ultrasmall carbon fiber electrodes mediated by the photoelectric effect. *IEEE Transactions on Biomedical Engineering*.

332. Streit, W. J., Xue, Q., Prasad, A., Sankar, V., Knott, E., Dyer, A., . . . Sanchez, J. C. (2012). Electrode Failure: Tissue, Electrical, and Material Responses. *IEEE Pulse, 3*(1), 30-33. doi:10.1109/MPUL.2011.2175632

333. Susarla, Bala T., Villapol, S., Yi, J.-H., Geller, Herbert M., & Symes, Aviva J. (2014). Temporal patterns of cortical proliferation of glial cell populations after traumatic brain injury in mice. *ASN NEURO, 6*(3), e00143. doi:10.1042/AN20130034

334. Sweeney, M. D., Ayyadurai, S., & Zlokovic, B. V. (2016). Pericytes of the neurovascular unit: key functions and signaling pathways. *Nat Neurosci, 19*(6), 771-783. doi:10.1038/nn.4288

335. Sweeney, M. D., Ayyadurai, S., & Zlokovic, B. V. (2016). Pericytes of the neurovascular unit: key functions and signaling pathways. *Nature neuroscience, 19*(6), 771-783.

336. Szarowski, D. H., Andersen, M. D., Retterer, S., Spence, A. J., Isaacson, M., Craighead, H. G., . . . Shain, W. (2003). Brain responses to micro-machined silicon devices. *Brain Res, 983*(1-2), 23-35. doi:S0006899303030233 [pii]

337. Szögi, T., Borbély, E., Schuster, I., Bozsó, Z., Sántha, M., Tóth, M. E., . . . Fülöp, L. (2022). Examination of Longitudinal Alterations in Alzheimer's Disease-Related Neurogenesis in an APP/PS1 Transgenic Mouse Model, and the Effects of P33, a Putative Neuroprotective Agent Thereon. *International journal of molecular sciences, 23*(18), 10364.

338. Szymanski, L. J., Kellis, S., Liu, C. Y., Jones, K. T., Andersen, R. A., Commins, D., . . . Miller, C. A. (2021). Neuropathological effects of chronically implanted, intracortical microelectrodes in a tetraplegic patient. *Journal of Neural Engineering, 18*(4), 0460b0469.

339. Tai, W., Wu, W., Wang, L.-L., Ni, H., Chen, C., Yang, J., . . . Zhang, C.-L. (2021). In vivo reprogramming of NG2 glia enables adult neurogenesis and functional recovery following spinal cord injury. *Cell stem cell, 28*(5), 923-937. e924.

340. Takasaki, C., Yamasaki, M., Uchigashima, M., Konno, K., Yanagawa, Y., & Watanabe, M. (2010). Cytochemical and cytological properties of perineuronal oligodendrocytes in the mouse cortex. *European Journal of Neuroscience, 32*(8), 1326-1336.

341. Takmakov, P., Ruda, K., Phillips, K. S., Isayeva, I. S., Krauthamer, V., & Welle, C. G. (2015). Rapid evaluation of the durability of cortical neural implants using accelerated aging with reactive oxygen species. *Journal of neural engineering, 12*(2), 026003.

342. Tan, A. M., Zhang, W., & Levine, J. M. (2005). NG2: a component of the glial scar that inhibits axon growth. *Journal of anatomy, 207*(6), 717-725.

343. Taniike, M., Mohri, I., Eguchi, N., Beuckmann, C. T., Suzuki, K., & Urade, Y. (2002). Perineuronal Oligodendrocytes Protect against Neuronal Apoptosis through the Production of Lipocalin-Type Prostaglandin D Synthase in a Genetic Demyelinating Model. *The Journal of Neuroscience, 22*(12), 4885. doi:10.1523/JNEUROSCI.22-12-04885.2002

344. Tao, L., Kong, Y., Xiang, Y., Cao, Y., Ye, X., & Liu, Z. (2022). Implantable optical fiber microelectrode with anti-biofouling ability for in vivo photoelectrochemical analysis. *Chinese Chemical Letters*.

345. Taraboletti, A., Walker, T., Avila, R., Huang, H., Caporoso, J., Manandhar, E., . . . Shriver, L. P. (2017). Cuprizone Intoxication Induces Cell Intrinsic Alterations in Oligodendrocyte Metabolism Independent of Copper Chelation. *Biochemistry, 56*(10), 1518-1528. doi:10.1021/acs.biochem.6b01072

346. Tatsumi, K., Haga, S., Matsuyoshi, H., Inoue, M., Manabe, T., Makinodan, M., & Wanaka, A. (2005). Characterization of cells with proliferative activity after a brain injury. *Neurochem Int, 46*(5), 381-389. doi:10.1016/j.neuint.2004.12.007

347. Tatsumi, K., Takebayashi, H., Manabe, T., Tanaka, K. F., Makinodan, M., Yamauchi, T., . . . Ikenaka, K. (2008). Genetic fate mapping of Olig2 progenitors in the injured adult cerebral cortex reveals preferential differentiation into astrocytes. *Journal of neuroscience research, 86*(16), 3494-3502.

348. Thompson, C. H., Zoratti, M. J., Langhals, N. B., & Purcell, E. K. (2016). Regenerative Electrode Interfaces for Neural Prostheses. *Tissue Eng Part B Rev, 22*(2), 125-135. doi:10.1089/ten.TEB.2015.0279

349. Thorburne, S. K., & Juurlink, B. H. (1996). Low glutathione and high iron govern the susceptibility of oligodendroglial precursors to oxidative stress. *Journal of neurochemistry, 67*(3), 1014-1022.

350. Thornton, M. A., & Hughes, E. G. (2020). Neuron-oligodendroglia interactions: Activity-dependent regulation of cellular signaling. *Neuroscience letters, 727*, 134916.

351. Tomassy, G. S., Berger, D. R., Chen, H.-H., Kasthuri, N., Hayworth, K. J., Vercelli, A., . . . Arlotta, P. (2014). Distinct profiles of myelin distribution along single axons of pyramidal neurons in the neocortex. *Science (New York, N.Y.), 344*(6181), 319-324. doi:10.1126/science.1249766

352. Tomassy, G. S., Berger, D. R., Chen, H. H., Kasthuri, N., Hayworth, K. J., Vercelli, A., . . . Arlotta, P. (2014). Distinct profiles of myelin distribution along single axons of pyramidal neurons in the neocortex. *Science, 344*(6181), 319-324. doi:10.1126/science.1249766

353. Torkildsen, Ø., Brunborg, L. A., Myhr, K. M., & Bø, L. (2008). The cuprizone model for demyelination. *Acta Neurologica Scandinavica, 117*(s188), 72-76. doi:10.1111/j.1600-0404.2008.01036.x

354. Torper, O., Ottosson, D. R., Pereira, M., Lau, S., Cardoso, T., Grealish, S., & Parmar, M. (2015). In vivo reprogramming of striatal NG2 glia into functional neurons that integrate into local host circuitry. *Cell reports, 12*(3), 474-481.

355. Tripathi, R. B., Rivers, L. E., Young, K. M., Jamen, F., & Richardson, W. D. (2010). NG2 glia generate new oligodendrocytes but few astrocytes in a murine experimental autoimmune encephalomyelitis model of demyelinating disease. *The Journal of neuroscience : the official journal of the Society for Neuroscience, 30*(48), 16383-16390.

356. Tsai, H.-H., Frost, E., To, V., Robinson, S., Ffrench-Constant, C., Geertman, R., . . . Miller, R. H. (2002). The chemokine receptor CXCR2 controls positioning of oligodendrocyte precursors in developing spinal cord by arresting their migration. *Cell, 110*(3), 373-383.

357. Turnbull, I. M., McGeer, P. L., Beattie, L., Calne, D., & Pate, B. (1985). Stimulation of the basal nucleus of Meynert in senile dementia of Alzheimer's type. A preliminary report. *Appl Neurophysiol, 48*(1-6), 216-221.

358. Urdaneta, M. E., Kunigk, N. G., Currlin, S., Delgado, F., Fried, S. I., & Otto, K. J. (2022). The long-term stability of intracortical microstimulation and the foreign body response are layer dependent. *Frontiers in Neuroscience, 16*, 908858.

359. Valério-Gomes, B., Guimarães, D. M., Szczupak, D., & Lent, R. (2018). The Absolute Number of Oligodendrocytes in the Adult Mouse Brain. *Frontiers in Neuroanatomy, 12*(90). doi:10.3389/fnana.2018.00090

360. Van Dyck, C. H. (2018). Anti-amyloid-β monoclonal antibodies for Alzheimer's disease: pitfalls and promise. *Biological psychiatry, 83*(4), 311-319.

361. Venkat, P., Chopp, M., & Chen, J. (2017). Blood-Brain Barrier Disruption, Vascular Impairment, and Ischemia/Reperfusion Damage in Diabetic Stroke. *J Am Heart Assoc, 6*(6). doi:10.1161/JAHA.117.005819

362. Vickers, J. C., Chin, D., Edwards, A.-M., Sampson, V., Harper, C., & Morrison, J. (1996). Dystrophic neurite formation associated with age-related β amyloid deposition in the neocortex: clues to the genesis of neurofibrillary pathology. *Experimental neurology, 141*(1), 1-11.

363. Vickers, J. C., Dickson, T. C., Adlard, P. A., Saunders, H. L., King, C. E., & McCormack, G. (2000). The cause of neuronal degeneration in Alzheimer's disease. *Progress in neurobiology, 60*(2), 139-165.

364. Vitale, F., Shen, W., Driscoll, N., Burrell, J. C., Richardson, A. G., Adewole, O., . . . Wang, T. (2018). Biomimetic extracellular matrix coatings improve the chronic biocompatibility of microfabricated subdural microelectrode arrays. *PLoS One, 13*(11), e0206137.

365. Wang, G., Sun, Z., Tao, R., Li, K., Bao, G., & Yan, X. (2016). Epileptic Seizure Detection Based on Partial Directed Coherence Analysis. *IEEE Journal of Biomedical and Health Informatics, 20*(3), 873-879. doi:10.1109/JBHI.2015.2424074

366. Wang, L.-L., & Zhang, C.-L. (2018). Engineering new neurons: in vivo reprogramming in mammalian brain and spinal cord. *Cell and Tissue Research, 371*(1), 201-212.

367. Wang, M.-R., Zhang, X.-J., Liu, H.-C., Ma, W.-D., Zhang, M.-L., Zhang, Y., . . . Chu, Y.-J. (2019). Matrine protects oligodendrocytes by inhibiting their apoptosis and enhancing mitochondrial autophagy. *Brain research bulletin, 153*, 30-38.

368. Wang, W. Y., Tan, M. S., Yu, J. T., & Tan, L. (2015). Role of pro-inflammatory cytokines released from microglia in Alzheimer's disease. *Ann Transl Med, 3*(10), 136. doi:10.3978/j.issn.2305-5839.2015.03.49

369. Wang, X., Huang, T., Bu, G., & Xu, H. (2014). Dysregulation of protein trafficking in neurodegeneration. *Molecular neurodegeneration, 9*(1), 1-9.

370. Ward, M. P., Rajdev, P., Ellison, C., & Irazoqui, P. P. (2009). Toward a comparison of microelectrodes for acute and chronic recordings. *Brain Res, 1282*, 183-200. doi:10.1016/j.brainres.2009.05.052

371. Washington, P. M., Morffy, N., Parsadanian, M., Zapple, D. N., & Burns, M. P. (2014). Experimental traumatic brain injury induces rapid aggregation and oligomerization of amyloid-beta in an Alzheimer's disease mouse model. *J Neurotrauma, 31*(1), 125-134. doi:10.1089/neu.2013.3017

372. Wellman, S. M., Cambi, F., & Kozai, T. D. (2018). The role of oligodendrocytes and their progenitors on neural interface technology: a novel perspective on tissue regeneration and repair. *Biomaterials, 183*, 200-217.

373. Wellman, S. M., Cambi, F., & Kozai, T. D. Y. (2018). The role of oligodendrocytes and their progenitors on neural interface technology: A novel perspective on tissue regeneration and repair. *Biomaterials, 183*, 200-217. doi:https://doi.org/10.1016/j.biomaterials.2018.08.046

374. Wellman, S. M., Eles, J. R., Ludwig, K. A., Seymour, J. P., Michelson, N. J., McFadden, W. E., . . . Kozai, T. D. (2018a). A Materials Roadmap to Functional Neural Interface Design. *Advanced Functional Materials, 28*(12), 201701269. doi:10.1002/adfm.201701269

375. Wellman, S. M., Eles, J. R., Ludwig, K. A., Seymour, J. P., Michelson, N. J., McFadden, W. E., . . . Kozai, T. D. (2018b). A materials roadmap to functional neural interface design. *Advanced functional materials, 28*(12), 1701269.

376. Wellman, S. M., Eles, J. R., Ludwig, K. A., Seymour, J. P., Michelson, N. J., McFadden, W. E., . . . Kozai, T. D. Y. (2017). A Materials Roadmap to Functional Neural Interface Design. *Advanced Functional Materials*, 1701269-n/a. doi:10.1002/adfm.201701269

377. Wellman, S. M., Eles, J. R., Ludwig, K. A., Seymour, J. P., Michelson, N. J., McFadden, W. E., . . . Kozai, T. D. Y. (2018). A Materials Roadmap to Functional Neural Interface Design. *Adv Funct Mater, 28*(12). doi:10.1002/adfm.201701269

378. Wellman, S. M., Guzman, K., Stieger, K. C., Brink, L. E., Sridhar, S., Dubaniewicz, M. T., . . . Kozai, T. D. Y. (2020). Cuprizone-induced oligodendrocyte loss and demyelination impairs recording performance of chronically implanted neural interfaces. *Biomaterials, 239*, 119842. doi:10.1016/j.biomaterials.2020.119842

379. Wellman, S. M., & Kozai, T. D. (2017a). Understanding the inflammatory tissue reaction to brain implants to improve neurochemical sensing performance. In (Vol. 8, pp. 2578-2582): ACS Publications.

380. Wellman, S. M., & Kozai, T. D. (2017b). Understanding the inflammatory tissue reaction to brain implants to improve neurochemical sensing performance. In: ACS Publications.

381. Wellman, S. M., & Kozai, T. D. (2018). In vivo spatiotemporal dynamics of NG2 glia activity caused by neural electrode implantation. *Biomaterials, 164*, 121-133.

382. Wellman, S. M., & Kozai, T. D. Y. (2017). Understanding the Inflammatory Tissue Reaction to Brain Implants To Improve Neurochemical Sensing Performance. *ACS Chemical Neuroscience, 8*(12), 2578-2582. doi:10.1021/acschemneuro.7b00403

383. Wellman, S. M., & Kozai, T. D. Y. (2018). Invivo spatiotemporal dynamics of NG2 glia activity caused by neural electrode implantation. *Biomaterials, 164*, 121-133.

384. Wellman, S. M., Li, L., Yaxiaer, Y., McNamara, I., & Kozai, T. D. (2019a). Revealing spatial and temporal patterns of cell death, glial proliferation, and blood-brain barrier dysfunction around implanted intracortical neural interfaces. *Frontiers in Neuroscience, 13*, 493.

385. Wellman, S. M., Li, L., Yaxiaer, Y., McNamara, I. N., & Kozai, T. D. J. F. i. N. (2019b). Revealing spatial and temporal patterns of cell death, glial proliferation, and blood-brain barrier dysfunction around implanted intracortical neural interfaces. *13*, 493.

386. Werner, S. R., Saha, J. K., Broderick, C. L., Zhen, E. Y., Higgs, R. E., Duffin, K. L., & Smith, R. C. (2010). Proteomic analysis of demyelinated and remyelinating brain tissue following dietary cuprizone administration. *Journal of molecular neuroscience, 42*(2), 210-225.

387. Williams, J. C., Hippensteel, J. A., Dilgen, J., Shain, W., & Kipke, D. R. (2007). Complex impedance spectroscopy for monitoring tissue responses to inserted neural implants. *Journal of neural engineering, 4*(4), 410.

388. Williams, J. C., Hippensteel, J. A., Dilgen, J., Shain, W., & Kipke, D. R. (2007). Complex impedance spectroscopy for monitoring tissue responses to inserted neural implants. *J Neural Eng, 4*(4), 410-423. doi:S1741-2560(07)52611-X [pii]

389. 10.1088/1741-2560/4/4/007

390. Williams, J. C., Rennaker, R. L., & Kipke, D. R. (1999). Long-term neural recording characteristics of wire microelectrode arrays implanted in cerebral cortex. *Brain Res Brain Res Protoc, 4*(3), 303-313. doi:S1385-299X(99)00034-3 [pii]

391. Williams, J. C., Rennaker, R. L., & Kipke, D. R. (1999). Long-term neural recording characteristics of wire microelectrode arrays implanted in cerebral cortex. *Brain Research Protocols, 4*(3), 303-313. doi:https://doi.org/10.1016/S1385-299X(99)00034-3

392. Winkler, E. A., Bell, R. D., & Zlokovic, B. V. (2011). Central nervous system pericytes in health and disease. *Nature neuroscience, 14*(11), 1398-1405. doi:10.1038/nn.2946

393. Winkler, E. A., Bell, R. D., & Zlokovic, B. V. (2011). Central nervous system pericytes in health and disease. *Nature neuroscience, 14*(11), 1398.

394. Winslow, B. D., Christensen, M. B., Yang, W. K., Solzbacher, F., & Tresco, P. A. (2010a). A comparison of the tissue response to chronically implanted Parylene-C-coated and uncoated planar silicon microelectrode arrays in rat cortex. *Biomaterials, 31*(35), 9163-9172. doi:10.1016/j.biomaterials.2010.05.050

395. Winslow, B. D., Christensen, M. B., Yang, W. K., Solzbacher, F., & Tresco, P. A. (2010b). A comparison of the tissue response to chronically implanted Parylene-C-coated and uncoated planar silicon microelectrode arrays in rat cortex. *Biomaterials*. doi:10.1016/j.biomaterials.2010.05.050

396. Winslow, B. D., & Tresco, P. A. (2010). Quantitative analysis of the tissue response to chronically implanted microwire electrodes in rat cortex. *Biomaterials, 31*(7), 1558-1567.

397. Woeppel, K., Yang, Q., & Cui, X. T. (2017). Recent advances in neural electrode–tissue interfaces. *Current opinion in biomedical engineering, 4*, 21-31.

398. Xing, B., Brink, L. E., Maers, K., Sullivan, M. L., Bodnar, R. J., Stolz, D. B., & Cambi, F. (2018a). Conditional depletion of GSK3b protects oligodendrocytes from apoptosis and lessens demyelination *Glia*.

399. Xing, B., Brink, L. E., Maers, K., Sullivan, M. L., Bodnar, R. J., Stolz, D. B., & Cambi, F. (2018b). Conditional depletion of GSK3b protects oligodendrocytes from apoptosis and lessens demyelination in the acute cuprizone model. *Glia, 66*(9), 1999-2012. doi:10.1002/glia.23453

400. Xu, J.-P., Zhao, J., & Li, S. (2011). Roles of NG2 glial cells in diseases of the central nervous system. *Neuroscience Bulletin, 27*(6), 413-421.

401. Yan, P., Bero, A. W., Cirrito, J. R., Xiao, Q., Hu, X., Wang, Y., . . . Lee, J. M. (2009). Characterizing the appearance and growth of amyloid plaques in APP/PS1 mice. *J Neurosci, 29*(34), 10706-10714. doi:10.1523/jneurosci.2637-09.2009

402. Yang, Q., Wu, B., Eles, J. R., Vazquez, A. L., Kozai, T. D. Y., & Cui, X. T. (2020). Zwitterionic Polymer Coating Suppresses Microglial Encapsulation to Neural Implants In Vitro and In Vivo. *Advanced Biosystems, 4*(6), 1900287. doi:https://doi.org/10.1002/adbi.201900287

403. Yemisci, M., Gursoy-Ozdemir, Y., Vural, A., Can, A., Topalkara, K., & Dalkara, T. (2009). Pericyte contraction induced by oxidative-nitrative stress impairs capillary reflow despite successful opening of an occluded cerebral artery. *Nature medicine, 15*(9), 1031-1037.

404. Yuan, P., Condello, C., Keene, C. D., Wang, Y., Bird, T. D., Paul, S. M., . . . Grutzendler, J. (2016). TREM2 Haplodeficiency in Mice and Humans Impairs the Microglia Barrier Function Leading to Decreased Amyloid Compaction and Severe Axonal Dystrophy. *Neuron, 90*(4), 724-739. doi:10.1016/j.neuron.2016.05.003

405. Zambach, S. A., Cai, C., Helms, H. C. C., Hald, B. O., Dong, Y., Fordsmann, J. C., . . . Lauritzen, M. J. (2021). Precapillary sphincters and pericytes at first-order capillaries as key regulators for brain capillary perfusion. *Proceedings of the National Academy of Sciences, 118*(26), e2023749118. doi:doi:10.1073/pnas.2023749118

406. Zehendner, C. M., Sebastiani, A., Hugonnet, A., Bischoff, F., Luhmann, H. J., & Thal, S. C. (2015). Traumatic brain injury results in rapid pericyte loss followed by reactive pericytosis in the cerebral cortex. *Scientific Reports, 5*, 13497. doi:10.1038/srep13497

407. Zhang, J., Guo, Y., Wang, Y., Song, L., Zhang, R., & Du, Y. (2018). Long-term treadmill exercise attenuates Aβ burdens and astrocyte activation in APP/PS1 mouse model of Alzheimer's disease. *Neuroscience letters, 666*, 70-77.

408. Zhang, X., Liu, Y., Hong, X., Li, X., Meshul, C. K., Moore, C., . . . Qi, X. (2021). NG2 glia-derived GABA release tunes inhibitory synapses and contributes to stress-induced anxiety. *Nature communications, 12*(1), 1-18.

409. Zheng, X. S., Snyder, N. R., Woeppel, K., Barengo, J. H., Li, X., Eles, J., . . . Cui, X. T. (2019). A superoxide scavenging coating for improving tissue response to neural implants. *Acta Biomaterialia, 99*, 72-83. doi:https://doi.org/10.1016/j.actbio.2019.08.032

410. Zhong, Y., & Bellamkonda, R. V. (2007). Dexamethasone-coated neural probes elicit attenuated inflammatory response and neuronal loss compared to uncoated neural probes. *Brain research, 1148*, 15-27.

411. Zhu, X., Bergles, D. E., & Nishiyama, A. (2008). NG2 cells generate both oligodendrocytes and gray matter astrocytes. *Development, 135*(1), 145-157. doi:10.1242/dev.004895

412. Zhu, X., Hill, R. A., & Nishiyama, A. (2008). NG2 cells generate oligodendrocytes and gray matter astrocytes in the spinal cord. *Neuron Glia Biology, 4*(1), 19-26.

413. Zlokovic, B. V. (2011). Neurovascular pathways to neurodegeneration in Alzheimer's disease and other disorders. Nature Reviews Neuroscience, 12(12), 723-738.